AD NUMBER

ADB287619

NEW LIMITATION CHANGE

TO

Approved for public release, distribution unlimited

FROM

Distribution authorized to U.S. Gov't. agencies only; Proprietary Info.; Oct 2002. Other requests shall be referred to U.S. Army Medical Research and Materiel Command, 504 Scott St., Ft. Detrick, MD 21702-5012.

AUTHORITY

USAMRMC ltr, DTD 01 Jul 2003

AD_____

Award Number: DAMD17-99-1-9218

TITLE: Frequency-Domain Optical Mammogram

PRINCIPAL INVESTIGATOR: Sergio Fantini, Ph.D.

CONTRACTING ORGANIZATION: Tufts University
                            Medford, Massachusetts   02155

REPORT DATE: October 2002

TYPE OF REPORT: Final

PREPARED FOR: U.S. Army Medical Research and Materiel Command
                Fort Detrick, Maryland   21702-5012

The views, opinions and/or findings contained in this report are those of the author(s) and should not be construed as an official Department of the Army position, policy or decision unless so designated by other documentation.

20030328 384

NOTICE

USING GOVERNMENT DRAWINGS, SPECIFICATIONS, OR OTHER DATA INCLUDED IN THIS DOCUMENT FOR ANY PURPOSE OTHER THAN GOVERNMENT PROCUREMENT DOES NOT IN ANY WAY OBLIGATE THE U.S. GOVERNMENT. THE FACT THAT THE GOVERNMENT FORMULATED OR SUPPLIED THE DRAWINGS, SPECIFICATIONS, OR OTHER DATA DOES NOT LICENSE THE HOLDER OR ANY OTHER PERSON OR CORPORATION; OR CONVEY ANY RIGHTS OR PERMISSION TO MANUFACTURE, USE, OR SELL ANY PATENTED INVENTION THAT MAY RELATE TO THEM.

LIMITED RIGHTS LEGEND

THIS TECHNICAL REPORT HAS BEEN REVIEWED AND IS APPROVED FOR PUBLICATION.

Carol B Christian   _____

_3/12/03_   _____

REPORT DOCUMENTATION PAGE

Public reporting burden for this collection of information is estimated to average 1 hour per response, including the time for reviewing instructions, searching existing data sources, gathering and maintaining the data needed, and completing and reviewing this collection of information. Send comments regarding this burden estimate or any other aspect of this collection of information, including suggestions for reducing this burden to Washington Headquarters Services, Directorate for Information Operations and Reports, 1215 Jefferson Davis Highway, Suite 1204, Arlington, VA 22202-4302, and to the Office of Management and Budget, Paperwork Reduction Project (0704-0188), Washington, DC 20503

1. AGENCY USE ONLY (Leave blank)	2. REPORT DATE October 2002	3. REPORT TYPE AND DATES COVERED Final (1 Oct 99 – 30 Sep 02)	

4. TITLE AND SUBTITLE
Frequency-Domain Optical Mammogram

5. FUNDING NUMBERS
DAMD17-99-1-9218

6. AUTHOR(S)
Sergio Fantini, Ph.D.

7. PERFORMING ORGANIZATION NAME(S) AND ADDRESS(ES)

Tufts University
Medford, Massachusetts   02155

E-Mail: Sergio.fantini@tufts.edu

8. PERFORMING ORGANIZATION REPORT NUMBER

9. SPONSORING / MONITORING AGENCY NAME(S) AND ADDRESS(ES)

U.S. Army Medical Research and Materiel Command
Fort Detrick, Maryland   21702-5012

10. SPONSORING / MONITORING AGENCY REPORT NUMBER

11. SUPPLEMENTARY NOTES
Original contains color plates: All DTIC reproductions will be in black and white.
Report has nonprint media appended to report. A separate document number will be assigned to CD.

12a. DISTRIBUTION / AVAILABILITY STATEMENT
Distribution authorized to U.S. Government agencies only (proprietary information, Oct 02). Other requests for this document shall be referred to U.S. Army Medical Research and Materiel Command, 504 Scott Street, Fort Detrick, Maryland   21702-5012.

12b. DISTRIBUTION CODE

13. ABSTRACT (Maximum 200 Words)

This research project has involved the analysis of a clinical data set of frequency-domain optical mammograms (~150 patients) to maximize the effectiveness of this breast imaging modality for cancer detection and to guide further improvements of this technique.

During the first year, we have computed edge-corrected optical mammograms (N-images) for the whole data set and obtained the corresponding ROC curve. During the second year, we have devised a new approach to tumor oximetry on the basis of spectral data, and we have started developing a second-derivative scheme of image processing. During the third year, we have finalized the second-derivative processing scheme and applied it to the whole set of clinical data. By combining the information provided by the second-derivative optical mammograms at one wavelength, and the oxygenation images computed from data at four wavelengths, we have obtained a new ROC curve that shows a significant improvement upon the ROC curve based on the N-images alone.

In summary, we have completed our broad objectives: (1) maximize the clinically useful information extracted from the existing set of optical mammograms; (2) guide further developments of optical mammography by introducing a new approach to tumor oximetry.

14. SUBJECT TERMS
optical mammography, near-infrared imaging, photon diffusion, optical tomography, near-infrared tissue spectroscopy

15. NUMBER OF PAGES
124

16. PRICE CODE

17. SECURITY CLASSIFICATION OF REPORT Unclassified	18. SECURITY CLASSIFICATION OF THIS PAGE Unclassified	19. SECURITY CLASSIFICATION OF ABSTRACT Unclassified	20. LIMITATION OF ABSTRACT Unlimited

Table of Contents

INTRODUCTION

This research project involved the analysis of an existing clinical set (~150 patients) of frequency-domain optical mammograms to assess the performance of this approach to breast cancer detection. The analysis of the breast images is complemented by theoretical and experimental studies to characterize the proposed algorithms of image processing. The objective of this research is to maximize the clinical information content of the optical images collected with the current instrument design, and to guide the design of new optical instrumentation for breast cancer detection.

BODY

Approved statement of work
The approved statement of work for this project is the following:

Task 1.
Compute and analyze the edge-corrected optical mammograms for all 150 patients **(Months 1-18)**
  a. Install the optical mammography software for the SUN workstation;
  b. Build the edge-effect-corrected images (*N*-images) from the amplitude and phase images;
  c. Carry out a comparison between the *N*-images and the tumor diagnosis for each patient;
  d. Analyze the wavelength dependence of the *N* parameter and the ac amplitude for different kinds of tumors;
  e. Collect a printed summary of all the 2,400 *N*-images (150 patients, 2 breasts, 2 projections, 4 wavelengths) and the spectral features of all the tumors.

Task 2.
Perform the optical measurements on breast-like phantoms **(Months 19-24)**
  a. Prepare the breast-like phantoms (optical inhomogeneities + strongly scattering background);
  b. Collect and analyze the optical data;
  c. Repeat the experiment for a variety of sizes, shapes, optical contrasts, and inhomogeneous backgrounds.

Task 3.
Apply the method for the quantification of the tumor optical properties and construct the spectral chart for benign and malignant tumors **(Months 25-36)**
  a. Find the optical properties, and the hemoglobin-related parameters of the tumors;
  b. Build charts of benign and malignant regions in the μ_a-μ_s' plane at four wavelengths;
  c. Determine whether malignant tumors show a specific spectral signature.

The first Grant period (year 01) was devoted to Task 1, and the results obtained were reported in the first year annual report. The second Grant period (year 02) was devoted to an extension of Tasks 1b and 1d, and to Task 2. Results of the second Grant period were reported in the second annual report. During year 03, we have completed the work initiated in years 01 and 02 (mostly pertaining to Task 1e), and we have performed Task 3. On the basis of the results of years 01 and 02, Tasks 3a and 3b were focused on the hemoglobin oxygenation of tumors rather than on their optical

4

properties (μ_a and μ_s'). By computing an "oxygenation index" on the basis of spectral optical data, we were able to increase the area under the ROC curve based on single-wavelength optical mammograms (Task 3c).

Task 1.e.

During year 01, we have obtained the so-called N-images for the whole dataset of optical mammograms. We briefly recall that the N-images are the result of an algorithm of image processing previously developed by us to minimize the effect of the breast thickness variability on the optical mammograms. The resulting images display a dimensionless parameter (called N) that is indicative of the optical density of the breast. We have found that N-images enhance the tumor detectability with respect to amplitude or phase images (i.e. with respect to images obtained from the raw optical data). After having examined the results for the whole dataset, we have found that all of the outstanding image regions associated with cancer, benign tumors, and blood vessels are characterized by an increased value of N. Such an increased value (peak) is always associated with a negative second spatial derivative. On the contrary, we have observed that areas that introduce edge effects (i.e. the artifacts associated with the breast thickness reduction by the edge of the breast image) are usually associated with a positive second spatial derivative of N.

As a result of the above findings, during year 02, we have started developing a new scheme of image processing based on the second derivative of N. This image processing approach consists of the following steps:

I)   Smooth the original N image by a low-pass spatial filter;
II)   Calculate the average of the second spatial derivative along eight directions through each image pixel (N'');
III)   Set all of the image pixels corresponding to a positive value of N'' to white;
IV)   Set all of the pixels out of the breast to black;
V)   Display the image pixels with N''<0 using a gray scale palette where white corresponds to N''=0 and black corresponds to the maximum value of N''.

This algorithm of data processing keeps all of the strengths of the N-imaging and further improves on the quality of the image display. During year 03, we have taken full advantage of this new image processing scheme in two ways: (1) We have applied it to all of the clinical data to compile second-derivative images of the whole clinical data set; (2) We have used these images to identify a subset of pixels of interest (those with a negative second derivative) for which we have applied the spectral analysis of Task 1d to compute a spatially-resolved oxygenation index. As a result, we obtained two new sets of optical images, namely second-derivative images and oxygenation images. The complete set of these images, as well as the complete set of the N-images obtained during year 01 as part of Task 1b, is included in a CD-ROM that is part of the Appendix. The Appendix also contains a color-coded list of the classification for all patient numbers. A complete hardcopy set of printed images is available upon request (we opted not to include a hard copy of all the images with this final report because it consists of two large binders containing several hundreds pages each).

Task 3.

During year 03, we have studied the most effective way to combine the 4-wavelength optical mammograms to obtain information on the hemoglobin saturation of detected breast lesions. After a number of tests, we have chosen to proceed according to the following two-step procedure:

1) Identify regions of interest as those with a negative second derivative in the N'' images;

1) Identify regions of interest as those with a negative second derivative in the N'' images;
2) For each pixel in these regions of interest, calculate an oxygenation index using the N values at the four wavelengths (690, 756, 788, 856 nm).

N (690 nm) 2nd derivative (690 nm) Oxygenation index
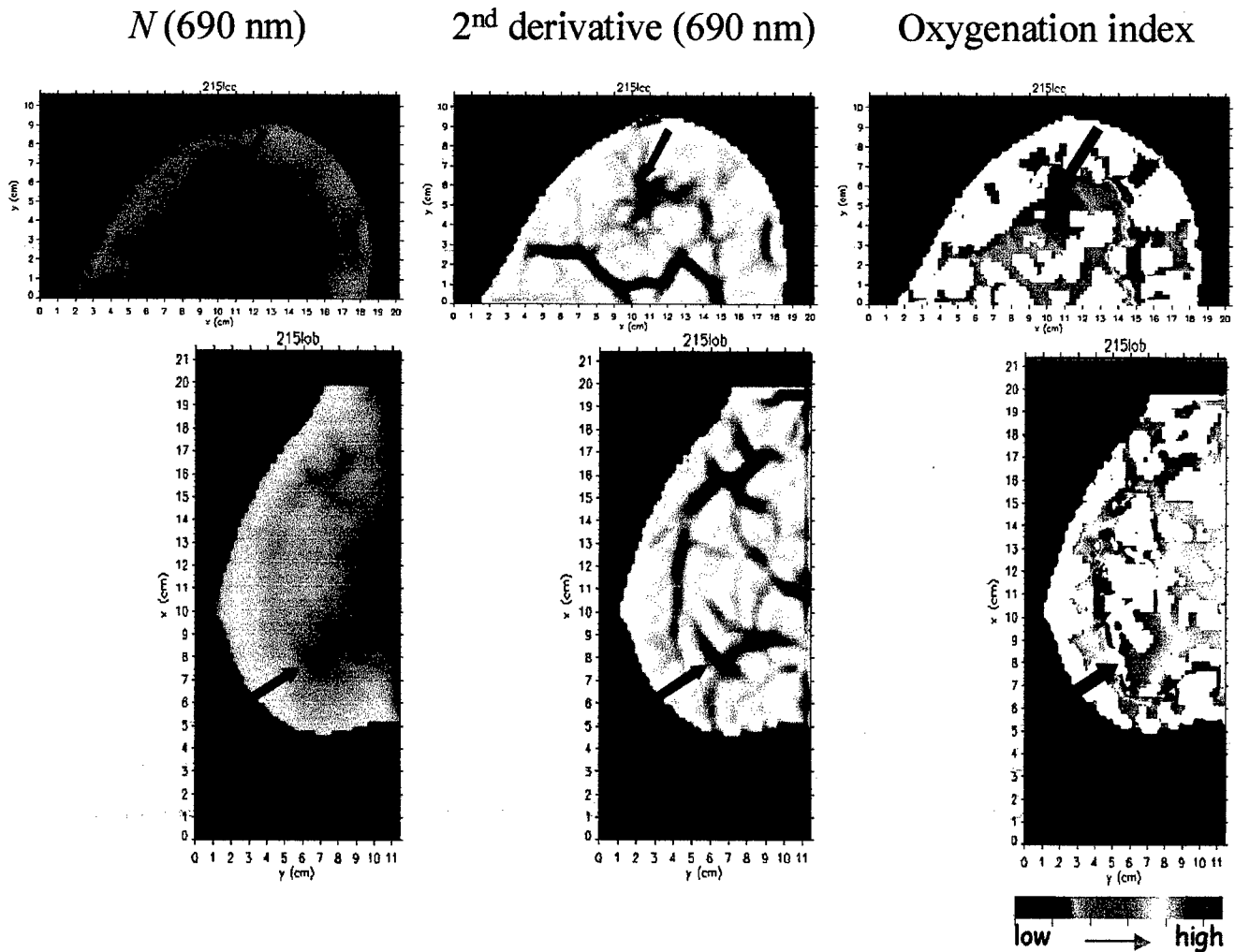
Fig. 1. Representative N-images, N'' images, and oxygenation index images of a cancerous breast in craniocaudal view (top images) and oblique view (bottom images). The cancer location (invasive ductal carcinoma), known from x-ray mammography, is indicated by the arrow. This patient (#215) is 53 years old.

During year 02, we used the second-derivative of N to calculate the oxygenation index, but we found N (rather than its second derivative) to be a better choice in order to extend the calculation of the oxygenation index beyond the pixel corresponding to the peak value of N. We stress that the new spectral method developed during year 02 for quantitative tissue oximetry, which requires data over a broad continuous spectral band, cannot be used on our clinical images that contain data at only four wavelengths. Therefore, we have calculated the oxygenation index (OI) at each pixel of the regions of interest by fitting the N values at the four wavelengths λ_i with a linear combination of the extinction spectra of oxy-hemoglobin and deoxy-hemoglobin. The analytical expression for the oxygenation index is the following:

$$OI = \frac{\left(\sum_i N(\lambda_i)\varepsilon_{HbO2}(\lambda_i)\right)\left(\sum_i \varepsilon_{Hb}^2(\lambda_i)\right) - \left(\sum_i N(\lambda_i)\varepsilon_{Hb}(\lambda_i)\right)\left(\sum_i \varepsilon_{HbO2}(\lambda_i)\varepsilon_{Hb}(\lambda_i)\right)}{\left(\sum_i N(\lambda_i)\varepsilon_{HbO2}(\lambda_i)\right)\left(\sum_i \varepsilon_{Hb}^2(\lambda_i)\right) + \left(\sum_i N(\lambda_i)\varepsilon_{Hb}(\lambda_i)\right)\left(\sum_i \varepsilon_{HbO2}^2(\lambda_i)\right) - \left(\sum_i N(\lambda_i)[\varepsilon_{Hb}(\lambda_i) + \varepsilon_{HbO2}(\lambda_i)]\right)\left(\sum_i \varepsilon_{HbO2}(\lambda_i)\varepsilon_{Hb}(\lambda_i)\right)}$$

where i is the wavelength index (ranging from 1 to 4), while ε_{Hb} and ε_{HbO2} are the molar extinction coefficients of deoxy-hemoglobin and oxy-hemoglobin, respectively. An example of an oxygenation index (OI) image is shown in Fig. 1, where the false colors indicate the level of oxygenation. In the example of Fig. 1, it can be seen that the cancer location (known from x-ray mammography) correspond to lower values of the oxygenation index, i.e. blue color in the top panel (craniocaudal view) and green-blue color in the bottom panel (oblique view). We have used the second-derivative (N'') images in combination with the oxygenation index (OI) images to build an ROC curve to be compared with the ROC curve based solely on N images that we obtained during year 01. The new ROC curve for the N'' & OI images was developed by assigning a score of 3, 2, 1, or 0 to lesions detected in the N'' and OI images. Specifically, the criteria for scoring were the following.

Score 3: A score of 3 was given to areas that had high contrast in the N'' image and a low OI value relative to other areas in the image.

Score 2: A score of 2 was given to (a) areas that had high contrast in the N'' image and an OI value that was not the lowest in the image; (b) areas that had lower contrast in the N'' image but that had the lowest OI value in the image.

Score 1: A score of 1 was given to (a) areas with a low OI value that appeared symmetrically in the N'' images of the right and left breasts regardless of their contrast; (b) areas that showed low contrast in the N'' image but showed the lowest OI value in the image; (c) areas with high contrast in the N'' image and high OI values.

Score 0: A value of 0 was given to (a) spatially extended areas of low contrast in the N'' image with high OI values; (b) thread-like structures in the N'' image with high OI value.

When a breast lesion appeared in both breast views, we averaged the scores assigned to the individual breast views (craniocaudal and oblique).

The new ROC curve was obtained by setting threshold values of 2.5, 2, 1.5, and 1 to the score of positive lesions. The sensitivity and specificity corresponding to these four threshold values are given in Table I.

Table I. Sensitivity and specificity for the four threshold values applied to the scoring based on N'' and oxygenation images.

Threshold	Sensitivity	Specificity
2.5	20%	97%
2.0	41%	94%
1.5	72%	80%
1.0	86%	63%

The new ROC curve extrapolated from the four points corresponding to the four threshold values is shown in Fig. 2, where it is compared with the ROC curve based on N-images that was reported in the first annual report. The improvement obtained with the new ROC curve is apparent. The reviewer of our first annual report suggested that more than one examiner scored the optical mammograms. We agree that this is important, and we are now performing this multi-examiner process. We intend to confirm the findings reported in Fig. 2 and quantify the deviations between ROC curves obtained by different examiners. These results will be reported in a scientific publication that is currently in preparation and that will summarize the key results of this three-year project. Such key results are briefly summarized in the Conclusion section.
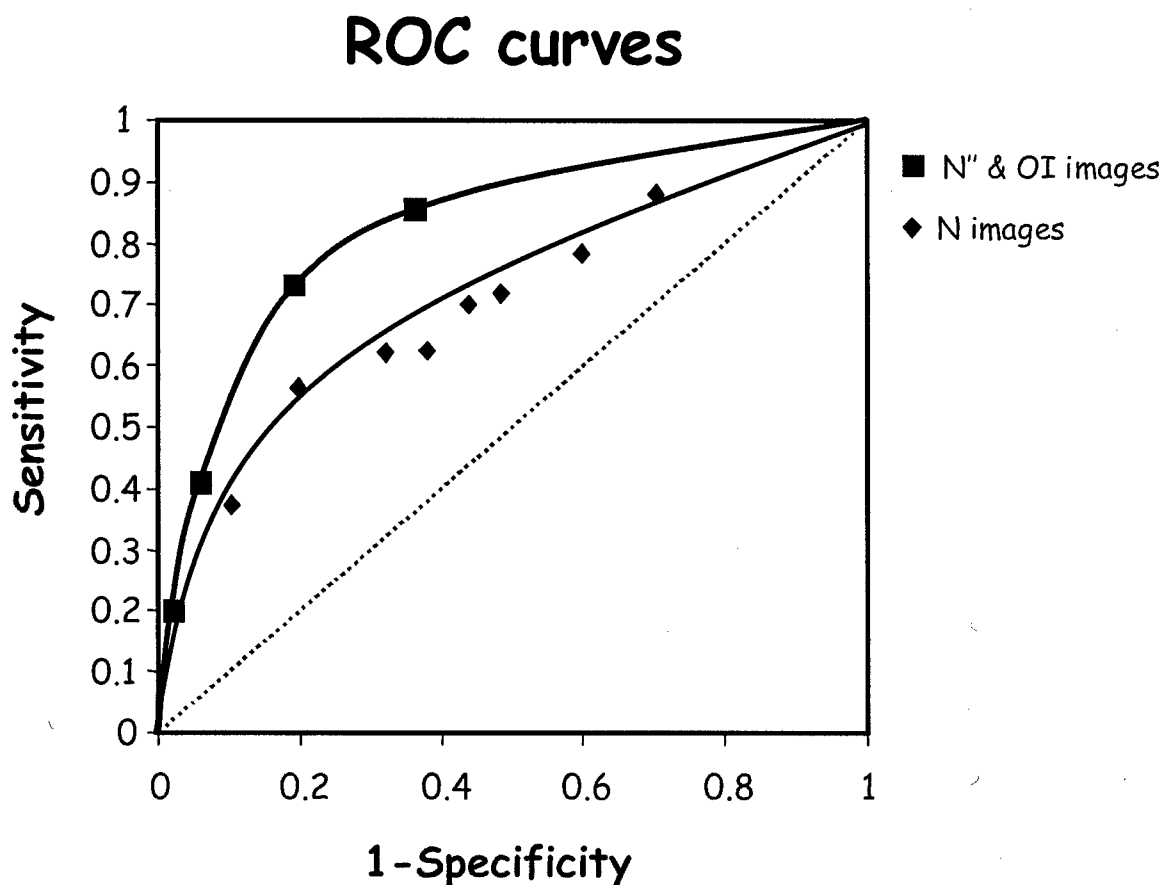
ROC curves

Fig. 2. ROC curve based on N'' & OI images (squares) obtained during year 03, and ROC curve based on N-images (diamonds) obtained during year 01.

Additional research
In year 03, the PI has published a manuscript [Phys. Med. Biol. **47**, N249 (2002)] that reports a hemodynamic model to guide the physiological interpretation of near-infrared spectroscopy data. This model has wide applicability and can also be used to help interpret the data collected with optical mammography.

KEY RESEARCH ACCOMPLISHMENTS

YEAR 01:

- Implemented modifications to the software for the computation of N-images and for the computation of the tumor contrast for each optical mammogram.
- Computation of the N-images for the whole data set of ~150 patients.
- Determination of the ROC diagram based on one-wavelength N images for the 131 patients with complete pathology report.
- Development of a perturbation approach for the spectral analysis of the optically detected breast lesions.
- Determination of the effectiveness of the spectral perturbation approach to discriminating benign and malignant breast lesions on a subset of 19 patients.

YEAR 02:

- Development of a new scheme of image processing based on the second spatial derivative of the N images.
- Computation of a tumor oxygenation index (OI) based on the spectral dependence of the second derivative of N at the tumor.
- Combination of the above two points into a composite false-color breast image containing structural information (from the second derivative of N) and functional information (OI).
- Development of a new method to measure the tumor oxygenation from an appropriate choice of a wavelength pair that depends on the tumor oxygenation.
- Theoretical tests of the new method using the analytical solution for a spherical inclusion (tumor) embedded in a turbid medium (breast tissue).
- Experimental tests of the new method on breast-simulating turbid media.

YEAR 03:

- Application of the second-derivative image-processing scheme to the whole clinical data set of optical mammograms.
- Generation of tumor oxygenation index (OI) images by computing the value of OI at pixels identified as regions of interest by the second-derivative images.
- Generation of an ROC curve based on the combination of second-derivative images and oxygenation index images.

REPORTABLE OUTCOMES

Manuscripts

1. V. E. Pera, E. L. Heffer, H. Siebold, O. Schütz, S. Heywang-Köbrunner, L. Götz, A. Heinig, and S. Fantini, "Spatial second-derivative image processing: An application to optical mammography to enhance the detection of breast tumors," J. Biomed. Opt. (*submitted 7/18/2002*).
2. S. Fantini, "A haemodynamic model for the physiological interpretation of *in vivo* measurements of the concentration and oxygen saturation of haemoglobin," Phys. Med. Biol. **47**, N249-N257 (2002).

3. E. L. Heffer and S. Fantini, "Quantitative oximetry of breast tumors: A novel near-infrared method that identifies two optimal wavelengths for each tumor," Appl. Opt. **41**, 3827-3839 (2002).

4. M. A. Franceschini, D. A. Boas, A. Zourabian, S. G. Diamond, S. Nadgir, D. W. Lin, J. B. Moore, and S. Fantini, "Near-Infrared Spiroximetry: Non-Invasive Measurement of Venous Saturation in Piglets and Human Subjects," J. Appl. Physiol. **92**, 372-384 (2002).

5. S. Fantini and M. A. Franceschini, "Frequency-Domain Techniques for Tissue Spectroscopy and Imaging," in *Handbook of Optical Biomedical Diagnostics*, V. V. Tuchin, Ed., (SPIE Press, Bellingham, WA, 2002), Chapter 7, pp.405-453.

6. S. Fantini, E. L. Heffer, M. A. Franceschini, L. Götz, A. Heinig, S. Heywang-Köbrunner, Oliver Schütz, and Horst Siebold, "Optical Mammography with Intensity-Modulated Light," Proceedings of Inter-Institute Workshop on In Vivo Optical Imaging at the NIH, A. H. Gandjbakhche, Ed. (Optical Society of America, Washington, DC 2000), pp. 111-117. **(Invited).**

7. M. A. Franceschini, S. Fantini, V. Toronov, M. E. Filiaci, and E. Gratton, "Cerebral Hemodynamics Measured by Near-Infrared Spectroscopy at Rest and During Motor Activation," Proceedings of Inter-Institute Workshop on In Vivo Optical Imaging at the NIH, A. H. Gandjbakhche, Ed. (Optical Society of America, Washington, DC 2000), pp. 73-80. **(Invited).**

Abstracts/Presentations

1. S. Fantini, E. L. Heffer, V. E. Pera, S. Heywang-Köbrunner, L. Götz, A. Heinig, O. Schütz, and H. Siebold, "Near-Infrared Oximetry of Breast Lesions Detected with Second-Derivative Image Processing of Optical Mammograms," Proceedings of *Third Inter-Institute Workshop on Diagnostic Optical Imaging and Spectroscopy: The Clinical Adventure*, Bethesda, MD, September 26-27, 2002. **(Invited).**

2. S. Fantini, M. A. Franceschini, F. Fabbri, S. Nadgir, P. F. Renshaw, and M. E. Henry, "Bilateral near-infrared measurements of the cerebral hemodynamics and oxygenation during unilateral electro-convulsive therapy," Proceedings of *Third Inter-Institute Workshop on Diagnostic Optical Imaging and Spectroscopy: The Clinical Adventure*, Bethesda, MD, September 26-27, 2002.

3. S. Fantini, E. L. Heffer, V. E. Pera, O. Schütz, H. Siebold, S. Heywang-Köbrunner, L. Götz, and A. Heinig, "Structural and functional near-infrared imaging of the human breast," Proceedings of *Asian Symposium on Biomedical Optics and Photomedicine*, October 21-23, 2002, Sapporo, Japan.

4. M. A. Franceschini, S. Nadgir, F. Fabbri, S. Fantini, P. F. Renshaw, and M. Henry, "Cerebral near-infrared spectroscopy during electro-convulsive therapy," Proceedings of *Asian Symposium on Biomedical Optics and Photomedicine*, October 21-23, 2002, Sapporo, Japan.

5. S. Fantini, V. E. Pera, E. L. Heffer, L. Götz, A. Heinig, S. Heywang-Köbrunner, O. Schütz, and H. Siebold, "Frequency-domain optical mammography: A novel imaging technique to detect breast cancer," Proceedings of *Progress in Electromagnetics Research Symposium* (PIERS) 2002, Cambridge, MA, July 1-5, 2002. **(Invited).**

6. S. Fantini and E. L. Heffer, "Spectral imaging of the human breast for cancer detection," in *OSA Biomedical Topical Meetings*, OSA Technical Digest, (Optical Society of America, Washington, DC, 2002), pp. 435-437. **(Invited).**

7. V. E. Pera, E. L. Heffer, O. Schütz, H. Siebold, S. Heywang-Köbrunner, L. Götz, A. Heinig, and S. Fantini, "Second-derivative optical mammography," in *OSA Biomedical Topical Meetings*, OSA Technical Digest, (Optical Society of America, Washington, DC, 2002), pp. 671-673.

8. E. L. Heffer and S. Fantini, "Novel approach to quantitative oximetry of breast lesions using two *ad hoc* near-infrared wavelengths," in *OSA Biomedical Topical Meetings*, OSA Technical Digest, (Optical Society of America, Washington, DC, 2002), pp. 99-101.

9. S. Fantini, "Optical Mammography," Department of Electrical Engineering and Computer Science, Tufts University, Medford, MA, November 10, 1999.

10. S. Fantini, "Using intensity-modulated light to detect breast cancer," Center for Innovative Minimally Invasive Therapy (CIMIT), Massachusetts General Hospital, Boston, MA, May 2, 2000.

11. E. L. Heffer, "Spectral Analysis of Frequency-Domain Optical Mammograms," Beckman Laser Institute, University of California at Irvine, May 12, 2000.

12. E. L. Heffer, M. A. Franceschini, O. Schütz, H. Siebold, L. Götz, A. Heinig, S. Heywang-Köbrunner, and S. Fantini "Analysis of Frequency-Domain Optical Mammograms Using Spectral Information," Gordon Conference on *Lasers in Medicine and Biology*, New London, CT, June 10-15, 2000.

Patents

1. "Optical imaging and oximetry of tissue," Inventor: S. Fantini, Filed: 3/13/2002.

Funding applied for based on work supported by this award:

Title:	"Near-infrared oximetry of breast tumors"
PI:	Sergio Fantini
Period:	10/2002 – 9/2006;
Agency:	NIH/NCI (R21 CA95885);
Total amount:	$1,068,805;
Status:	Pending

LIST OF PERSONNEL

Sergio Fantini, Asst. Prof, Department of Electrical Engineering and Computer Science, Tufts University

Erica L. Heffer, Grad. Student, Department of Electrical Engineering and Computer Science, Tufts University

Vivian Pera, Grad. Student, Department of Electrical Engineering and Computer Science, Tufts University

CONCLUSIONS

We have performed the proposed analysis of frequency-domain optical mammograms for a clinical population of about 150 patients. This analysis has led to the compilation of edge-effect-corrected images (N-images), second-derivative images (N''-images), and oxygenation index images (OI images). The ROC curve obtained from the combination of N'' and OI images is significantly improved with respect to the ROC curve obtained from N-images (see Fig. 2). This result indicate that multi-wavelength data can significantly improve the clinical effectiveness of optical mammography. To further exploit the spectral information available with optical mammography, we have developed a novel approach to the oximetry of breast lesions, which requires broad band spectral imaging.

The relevance of our results is twofold: (1) they show that optical mammography can be a useful imaging modality to help detect breast cancer, and (2) they pose the basis for further developments in optical mammography. In particular, we found the instrumental design based on a parallel plate geometry and slight breast compression to be a robust, reliable, and reproducible approach, which we will continue to employ. Furthermore, our 4-wavelength results (OI images) indicate the importance of using spectral information, and the novel oximetry approach developed as part of this project is a specific new idea that points to new directions in instrument design.

REFERENCES
N/A

APPENDIX

The appendix contains:

1) A CD-ROM with all the images compiled as part of this project, namely N-images, N''-images, and oxygenation index (OI) images.

2) A color-coded list of all patient numbers and the corresponding diagnostic information provided by our clinical collaborators in Germany.

3) A copy of the articles published during year 03 of this project. These are manuscripts numbers 1, 2, 3, 4, and 5 listed in the "Reportable Outcomes" section.

147L	204R	244L	277R	312R
161L	205L	245L	278R	313L
162R	206L	246L	279R	314R
163R	207L	247R	280R mast in L	315R
164L	210R	248L	280L carc in R	316L
165R also other	211L	249R	281L	317R
166R	212R	250L	283R carc in L	318R
171L	213R	251L	283L mast in R	319L
173R	214L	252L	284a	321R
174L	215L	253R	285aR fibr in L	323L
175L	216R	254R	285aL carc in R	331L
176L	217R	255R	286L	335R
177R	218L	256L	287R	343L
181R	219L	257R	288R	344R
183R	220R	258R also mast	289L	344aL
184R	222L	259L also other	291L	
185R	223L also fibr	261R mast in L	293R	
187R	224R	261L fibr in R	294L	
188L	225L	262L	295R	
189R	227R	263R	296R	
192L	228L	264R also fibr	297R	
193R mast in L	229L	265R	298L	
193L carc in R	230L	266L	299R	
194R	231L	267R	301R	
195R	233R	268L	302R	
196R	234R	269R	303R	
197L	235L	270L	304R	
198L	236R	271L	305R	
199L	237R	272L	307R	
200R	239L	273L	308L	
201L	240L	274L	309L	
202R	241R	275L	310L	
203R	243R	276R	311L	

Color codes:
Carcinoma
Fibroadenoma
Mastopathy
DCIS
Other

Spatial second-derivative image processing: An application to optical mammography to enhance the detection of breast tumors

Vivian E. Pera[1], Erica L. Heffer[1], Horst Siebold[2], Oliver Schütz[2],

Sylvia Heywang-Köbrunner[3], Linda Götz[3], Anke Heinig[3], and Sergio Fantini[1*]

[1] Bioengineering Center, Department of Electrical Engineering and Computer Science,

Tufts University, 4 Colby Street, Medford, MA 02155

Ph: (617) 627-4356, Fax: (617) 627-3151, E-mail: sergio.fantini@tufts.edu

[2] Siemens AG, Medical Engineering, Erlangen, Germany

[3] Martin Luther Universitaet Halle/Wittenberg,

Institut für Diagnostische Radiologie und CT, Halle, Germany

[*] To whom all correspondence should be addressed

Abstract

We present an image processing method that enhances the detection of regions of higher absorbance in optical mammograms. At the heart of this method lies a second-derivative operator, which is commonly employed in edge-detection algorithms. The resulting images possess a high contrast, an automatic display scale, and a greater sensitivity to smaller departures from the local background absorbance. Moreover, the images are free of artifacts near the breast edge. This second-derivative method enhances the display of structural information in optical mammograms, and may be used to robustly select areas of interest to be further analyzed spectrally to determine the oxygenation level of breast lesions.

Keywords: Optical mammography, breast cancer, photon migration, digital image processing

1. Introduction

Optical mammography is a technique that employs near-infrared light in the wavelength range of 630-1000 nm to image the human breast. In this wavelength range, the main source of image contrast is the absorption of hemoglobin. Angiogenesis, or increased blood vessel formation, and other hemodynamic and oxygenation changes are often associated with the presence of breast tumors.[1] These changes typically produce a local increase in the optical absorption that allows near-infrared methods to detect the presence of breast tumors. Our goal is to find a way of enhancing the detection of those areas in the breast image that exhibit a local maximum in absorption and might therefore correspond to the location of tumors. We show that

2

a robust way of accomplishing this is by employing the spatial second derivative, an operator commonly used in edge-detection algorithms.[2]

2. Background

We have previously reported "edge-corrected" optical mammograms, that we call N-images, which enhance the image contrast and detectability of breast tumors in transillumination images.[3] An N-image is constructed from raw phase and amplitude data acquired by a frequency-domain instrument that operates in a planar projection geometry. Examples of frequency-domain instruments operating in this geometry are the research prototypes previously developed by Zeiss[4,5] and Siemens.[6] Figure 1 shows a schematic diagram of the Siemens prototype, whose technical specifications have been reported elsewhere.[7] The need for an edge correction is due primarily to the variable thickness of the breast between the two glass plates that slightly compress it. The N-parameter is defined as:

$$N(x,y) = \frac{r_0 ac_0}{r(x,y)ac(x,y)},\qquad(1)$$

where r_0 is the separation of the plates, ac_0 is the amplitude of the intensity modulated signal at a pixel where the breast thickness is r_0, $ac(x,y)$ is the amplitude measured at pixel (x,y), and $r(x,y)$ is the breast thickness at that pixel derived from the phase information available in the frequency domain. A representative N-image of the left breast, craniocaudal projection, for a 58-year-old patient affected by invasive ductal carcinoma is reported in Fig. 2(a). A line graph of N at $y = 3.2$ cm is shown in Fig. 2(b).

Although N-images represent a significant improvement in quality over the images based on raw intensity data, it is nevertheless often difficult to discern much structure in them. For example, the secondary peak around $x = 8.8$ cm along the line y = 3.2 cm is visible in Fig. 2(b),

but it is almost completely hidden in the N-image of Fig. 2(a) by the large dynamic range due to the main peak at $x = 12$ cm. However, we have found that by calculating the spatial second derivative (N'') and considering only those pixels where the second derivative is negative, we can isolate areas in the N-image characterized by a local maximum in absorption. The resulting N'' image is presented in Fig. 2(c). In Fig. 2(d) we have plotted the negative of the second derivative along the line $y = 3.2$ cm and set a threshold at $N'' = 0$. Notice how the feature around $x = 8.8$ cm, which is likely due to a blood vessel, is now much more visible, both in the line graph and in the N''-image. It is also evident from Fig. 2(d) that there is additional structure around $x = 6$ cm, and this, too, is visible in the second-derivative image, even if with relatively low contrast. Overall, the N''-image is a higher contrast image that makes it easier to spot those areas in the breast where there is a local maximum in absorption, and therefore potentially smaller tumors that might have been eclipsed by other features.

3. Second-derivative method

Our method of generating second-derivative images from edge-corrected optical mammograms (N-images) is summarized in Fig. 3. Below we discuss each step in detail. All of the processing was carried out in IDL (Interactive Data Language, a higher-level programming language developed by Research Systems, Inc.) on a Pentium IV personal computer.

3.1. Input N-image

We have used the second-derivative method to analyze images collected with a frequency-domain instrument designed and built by Siemens Medical Engineering[6,7] (Fig. 1). The instrument consists of four laser diodes (690, 750, 788, and 856 nm) used as optical sources

modulated at a frequency of ~70 MHz. The source and detector fibers are located on opposite sides of the breast, which is slightly compressed between two parallel glass plates. The fibers are scanned in tandem across the breast to yield two-dimensional projection images of the phase and amplitude of the intensity-modulated light. Two projections of each breast were typically acquired, craniocaudal (the geometry illustrated in Fig. 1) and oblique, obtained by rotating the glass plates by 45 degrees. The raw data at each wavelength was converted into an N-image according to Eq. (1). It is necessary to remove edge effects prior to processing with the second derivative in order to avoid the introduction of artifacts near the breast edge.

3.2. Convolve with smoothing function

Before taking the second derivative, we smoothed the N-image with the 5x5 weighted average matrix shown in Fig. 3 to reduce the effects of noise. Any significant noise spikes or anomalies in the data should be removed prior to smoothing, e.g. by employing traditional image processing techniques like median filtering.[2] Our 5x5 weighted average function is the result of cascading two 3x3 uniformly weighted average functions. The amount of smoothing necessary will, of course, depend on the characteristics of the input data. In our case, the pixel size in the input N-image was 2 mm × 2 mm, and smoothing over a 1 cm^2 area worked well.

3.3. Calculate second derivative in four directions

We calculated the second derivative of N at each pixel by considering the N values at its nearest neighbors in four directions: horizontal, vertical, and along the two diagonals. Including other intermediate directions in the calculation did not significantly alter the results. We have used a standard forward-difference discrete approximation of the second derivative, but for

completeness we define our second-derivative operator in the horizontal direction as follows. Consider three pixels in an N-image that lie in the same row, and denote them left (l), center (c), and right (r). The value of N at each pixel is N_l, N_c, and N_r, respectively. Let Δw represent the center-to-center pixel separation in the horizontal direction. Then the first derivatives (N') to the left and right of the center pixel, respectively, are given by:

$$N'_{cl} = \frac{N_c - N_l}{\Delta w},$$
(2)

and

$$N'_{rc} = \frac{N_r - N_c}{\Delta w}.$$
(3)

From Eqs. (2) and (3), it follows that the second derivative at the center pixel is:

$$N''_c = \frac{N'_{rc} - N'_{cl}}{\Delta w} = \frac{1}{\Delta w}\left(\frac{N_r - N_c}{\Delta w} - \frac{N_c - N_l}{\Delta w}\right) = \frac{N_r - 2N_c + N_l}{\Delta w^2}.$$
(4)

The second derivative in the vertical and diagonal directions is defined analogously. In the case of the diagonal directions, the center-to-center pixel separation is $\sqrt{2}\Delta w$, so the horizontal and vertical second-derivative coefficients differ from the diagonal ones by a factor of 2. In the matrices of Fig. 3, Δw has been normalized to one, so only the factor of 2 remains.

When implementing the second-derivative calculation as a convolution with the functions of Fig. 3, one must take into account the transition between the image background (area outside the breast) and the breast. In our N-image, the background pixels contain zeros while the breast pixels contain positive N-values. So simply filtering an N-image (or a smoothed version of it) with the second-derivative functions of Fig. 3 yields artifacts along the breast edge whenever background pixels are included in the calculation. One way of correcting this problem is to use an edge-detection algorithm to flag pixels near the breast edge and write a convolution routine

that excludes background pixels in this region. A simpler, albeit cruder, solution is to segment the image into inside-breast/outside-breast regions and set the outside-breast region to a value higher than the average inside-breast N-value during the second-derivative calculation. We employed the latter approach in our analysis.

To a lesser degree, this same issue arises when convolving the N-image with the smoothing function of Section 3.2. To avoid artificially lowering the N-values along the breast edge, we set the outside-breast region to the average inside-breast N-value during this step.

3.4. Take minimum

We took the minimum of the second derivative along the four directions and assigned that value to the corresponding pixel in the N''-image. We used the minimum, as opposed to the average, in order to avoid missing areas that have a negative second derivative in one direction but are relatively flat or concave in the other directions. This procedure enhances the visualization of directional structures such as blood vessels.

3.5. Display

The second-derivative images are normalized by introducing a uniform multiplicative factor that sets to -1 the pixel value corresponding to the most negative second derivative. The normalized second-derivative values are indicated with N''_{norm}. We set a threshold at zero such that pixels with $N''_{norm} \geq 0$ are displayed in white. Pixels with a negative second derivative ($-1 \leq N''_{norm} < 0$) are displayed in grayscale, with darker corresponding to more negative. We performed a linear contrast stretch[2] on the gray levels of the image pixels for which the second derivative is negative. This contrast stretch procedure consists of linearly scaling the gray levels

7

for $(100-x)\%$ of the pixels with a negative second derivative, where the $x\%$ pixels, which are those with the most negative second derivative, are set to the darkest gray level. The percentage x of the pixels excluded from the contrast stretch is given by:

$$
\begin{aligned}
x &= 5 && \text{if} \quad 5747\!\left(\sigma^2\right)-161 < 5; \\
x &= 5747\!\left(\sigma^2\right)-161 && \text{if} \quad 5 \le 5747\!\left(\sigma^2\right)-161 \le 10; \\
x &= 10 && \text{if} \quad 5747\!\left(\sigma^2\right)-161 > 10,
\end{aligned}
\tag{5}
$$

where σ^2 is the variance of N''_{norm} for the pixels with a negative N''_{norm}. For example, consider an N''_{norm}-image with a variance such that $x = 7\%$ which we wish to display in 256 gray levels (0 to 255). Then the 7% of the negative-N''_{norm} pixels with the most negative values of N''_{norm} would be set to 0 in the contrast-stretched image, and the gray levels of the remaining 93% of the negative-N''_{norm} pixels would be linearly scaled into the range 0 (black) to 255 (white). The lower and upper limits of 5 and 10%, respectively, for x, along with the coefficients of 5747 and 161 in Eq. (5) were chosen empirically from a subset of images and then successfully applied to others without a need for adjustments for individual images.

This contrast stretch is asymmetric and therefore somewhat unusual. However, in our case this asymmetry is justified, since we lose little by making the darkest features in our images black, while we would be compromising the detectability of the dimmest structures if we made them lighter. With this process, we are, in effect, using the variance of N''_{norm} for those pixels with a negative second derivative to set a new threshold; the pixels whose N''_{norm} values are below this threshold (most negative) are set to 0 (black), and those whose N''_{norm} values are above it (less negative) are linearly scaled into the range 0 to 255. The motivation for using the variance of N''_{norm} at the negative-N''_{norm} pixels to determine the amount of contrast stretching is

simple. Typically, images with the largest variance are ones that possess a dark dominant feature and many light areas. Setting a higher threshold in this situation makes the lighter features that much darker, thereby potentially revealing other structures in addition to the most salient one.

4. Results

We present four cases that illustrate the advantages of second-derivative images over N-images (Figs. 4-7). On the left side of each figure is the N-image, with the craniocaudal projection on the top and the oblique projection on the bottom. On the right side, Figs. 4-7 show the corresponding craniocaudal and oblique projections of the N''-image. Arrows indicate the location of the lesion, which we know from x-ray mammography, and whether it is cancer or a benign mastopathy, which we know from the pathology report.

4.1. Figure 4: Case 197, 2.5 cm cancer

Patient 197 is a 72-year-old woman with a 2.5 cm tumor (invasive ductal carcinoma) in the left breast. In this case, the tumor is clearly visible in both projections of the N-image, but notice the additional structural information, likely due to the vasculature, that emerges in the second-derivative image. Some of the blood vessels were faintly visible in the N-image, but they appear as high-contrast features in the N''-image. We also see that the areas near the edge of the breast in the N''-image are mostly white, i.e. they correspond to a positive second derivative, so it appears that taking the second derivative does not result in the introduction of artifacts in this region. We have found this to be the case with all N''-images that we have examined.

9

4.2. Figure 5: Case 267, 2 cm cancer

The case of Patient 267, a 76-year-old woman with invasive ductal carcinoma in the right breast, is an example of a low-contrast N-image without much visible structure. The tumor is barely discernible in the craniocaudal projection of the N-image (Fig. 5(a)) and cannot be easily differentiated from other dark areas in the image. In the oblique projection (Fig. 5(b)), the tumor is altogether eclipsed by another feature (circle). The N''-image, however, clearly reveals the location of the tumor in the craniocaudal projection (Fig. 5(c)), while the other dark areas in the N-image now appear to be due to blood vessels. Although the oblique projection (Fig. 5(d)) continues to be dominated by the circled structure, the area corresponding to the location of the tumor is not white (i.e. it has a negative second derivative) and can therefore be distinguished from the background.

4.3. Figure 6: Case 165, mastopathy

Patient 165, a 52-year-old woman, has a benign lesion in the right breast. This feature dominates the N-image and as a result, not much else is visible. But in the N''-image, we see finer structure likely due to blood vessels emerge. In particular, in the oblique projection, we can see that what appeared to be a rather murky and undifferentiated feature in the N-image shows up as a combination of two resolved structures in the N''-image.

4.4. Figure 7: Case 215, 3 cm cancer

The case of Patient 215, a 53 year-old woman with invasive ductal carcinoma in the left breast, is particularly interesting. In the craniocaudal projection of the N-image (Fig. 7(a)), the cancer is readily apparent, as is another structure: a blood vessel. But even in this situation there is a

substantial improvement in the contrast and level of detail visible in the N''-image (Fig. 7(c)). For example, in the N''-image we can now make out what seems to be a network of blood vessels at the tumor site. The N-image oblique projection (Fig. 7(b)) has a lower contrast, and the improvement in the N''-image (Fig. 7(d)) is therefore more pronounced. The visibility of the tumor in this projection is much greater in the N''-image than in its counterpart.

5. Discussion

From the examples presented, it is clear that applying the second-derivative method enhances the structural information content of N-images. N''-images reveal attributes that were just barely visible in N-images or, in some cases, not really visible at all. In those images that are dominated by one feature (Figs. 4 and 6), we are now able to see additional structure away from the dominant feature and to better resolve finer details of the dominant feature. In cases where the N-image has a low contrast (Figs. 5(a) and 7(b)), or when the lesion is not the dominant structure (Fig. 5(b)), applying this method can lead to the detection of a previously missed tumor. Moreover, since we normalize the N''-images and select the linear contrast stretch parameters once for all, the N''-images can be generated without any user input. The detectability of a particular lesion does not depend on a fortunate choice of threshold or contrast level.

As Fig. 2 illustrates, the second derivative is more sensitive to smaller departures from the local background absorbance. Furthermore, it is insensitive to the breast edge. The net result is a process capable of bringing out "buried" features (like the peak at $x = 8.8$ cm in Fig. 2(a)) without introducing artifacts close to the breast edge.

The greater detail visible in N''-images improves the sensitivity of tumor detection, but this may come at the price of a reduced specificity, and Fig. 7(d) brings home this point nicely. Were

it not for the arrow indicating the location of the tumor in this image, one would be hard-pressed to argue that this structure is a lesion and not just part of a blood vessel. Structural information alone will not allow us to properly classify the various features visible in an N'' image. For this we must make use of data at multiple wavelengths and exploit the potential of optical mammography to provide functional information (in the form of a measurement of oxygenation) from spectral information.

There are several groups currently working to develop an accurate way of measuring the oxygenation level of breast lesions *in vivo* by combining data from two or more wavelengths.[8-13] Our second-derivative method can play an important role in the interpretation of optical mammograms by robustly selecting areas of interest to be analyzed spectrally in order to discriminate benign from malignant lesions. The second-derivative operator is an ideal choice for this pre-filtering step. By setting a threshold at zero and considering only pixels with a negative second derivative, one is, by definition, picking out any area that represents a local absorption maximum, irrespective of its magnitude, size or shape. It is for this reason that we have elected to use the minimum value of N'' instead of the average (Section 3.4). Although this tends to emphasize narrow, elongated features (e.g. blood vessels), we felt it best to err on the side of being more inclusive and not to rely on the assumption that breast lesions would be largely symmetric. The second derivative is analytically straightforward and easy to implement; it is the driving mechanism behind many edge-detection algorithms in use today.

Finally, we should comment on the issues of depth discrimination and resolution. From a planar projection, it is not possible to determine the depth of structures visible in N'' images. But because these images possess a relatively high contrast, they may be particularly well-suited for multi-source and/or multi-detector approaches to depth discrimination.[14,15] As for resolution, we

should point out that the second-derivative method does not improve the quality of the data available. It does, however, improve the display of the data thereby allowing for the discrimination of nearby structures that are not visibly resolved in the original images.

6. Conclusion

We have developed an image processing method based on a spatial second-derivative operator to enhance the detection of breast tumors in optical mammograms. Applying this method has revealed the presence of breast tumors and of fine structures, likely blood vessels, that were not visible in the original images. As a result, this second-derivative method enhances the structural imaging capability of optical mammography, thus leading to a potentially higher sensitivity in the detection of breast cancer. In fact, in addition to the direct visualization of breast tumors, a modified spatial pattern of the vascularization may also provide an indirect indication of the presence of cancer. Furthermore, the identification of suspicious areas of interest provided by second-derivative images may guide the selection of image pixels for a spectral analysis aimed at the assessment of the local oxygen saturation of hemoglobin. This second step, which provides functional information, may improve the specificity of optical mammography by possibly allowing for the discrimination of benign and malignant breast lesions.

References

1. P. Vaupel, F. Kallinioski, and P. Okunieff, "Blood flow, oxygen and nutrient supply, and metabolic microenvironment of human tumors: a review," *Cancer Research* **49**, 6449-6465 (1989).

2. R. C. Gonzalez and R. E. Woods, *Digital Image Processing*, Addison-Wesley, Reading, MA (1992).

3. S. Fantini, M.A. Franceschini, G. Gaida, E. Gratton, H. Jess, W. W. Mantulin, K. T. Moesta, P. M. Schlag, and M. Kaschke, "Frequency-domain optical mammography: edge-effect corrections," *Med. Phys.* **23**, 149-157 (1996).

4. M. Kaschke, H. Jess, G. Gaida, J. M. Kaltenbach, and W. Wrobel, "Transillumination Imaging of Tissue by Phase Modulation Techniques," in *Advances in Optical Imaging and Photon Migration*, Editor R. R. Alfano, Proc. OSA **21**, 88-92 (1994).

5. M. A. Franceschini, K. T. Moesta, S. Fantini, G. Gaida, E. Gratton, H. Jess, W. W. Mantulin, M. Seeber, P. M. Schlag, and M. Kaschke, "Frequency-Domain Techniques Enhance Optical Mammography: Initial Clinical Results," *Proc. Natl. Acad. Sci. USA* **94**, 6468-6473 (1997).

6. L. Götz, S. H. Heywang-Köbrunner, O. Schütz, and H. Siebold, "Optische Mammographie an präoperativen Patientinnen," *Akt. Radiol.* **8**, 31-33 (1998).

7. S. Fantini, E. L. Heffer, M. A. Franceschini, L. Götz, A. Heinig, S. Heywang-Köbrunner, Oliver Schütz, and Horst Siebold, "Optical Mammography with Intensity-Modulated Light," *Proceedings of Inter-Institute Workshop on In Vivo Optical Imaging at the NIH*, A. H. Gandjbakhche, Ed. (Optical Society of America, Washington, DC 2000), pp. 111-117.

8. S. Zhou, C. Xie, S. Nioka, H. Liu, Y. Zhang, and B. Chance, "Phased Array Instrumentation Appropriate to High Precision Detection and Localization of Breast Tumor," in *Optical*

Tomography and Spectroscopy of Tissue: Theory, Instrumentation, Model, and Human Studies II, B. Chance and R. R. Alfano, eds., Proc. SPIE **2979**, 98-106 (1997).

9. B. W. Pogue, M. Testorf, T. McBride, U. Osterberg, and K. Paulsen, "Instrumentation and design of a frequency-domain diffuse optical tomography imager for breast cancer detection," *Optics Express* **1,** 391-403 (1997).

10. D. Grosenick, H. Wabnitz, H. H. Rinneberg, K. T. Moesta, and P. M. Schlag, "Development of a time-domain optical mammography and first *in vivo* applications," *Appl. Opt.* **38,** 2927-2943 (1999).

11. V. Ntziachristos, A. G. Yodh, M. Schnall, and B. Chance, "Concurrent MRI and diffuse optical tomography of breast after indocyanine green enhancement," *Proc. Natl. Acad. Sci. USA* **97,** 2767-2772 (2000).

12. N. Shah, A. Cerussi, C. Eker, J. Espinoza, J. Butler, J. Fishkin, R. Hornung, and B. Tromberg, "Noninvasive functional optical spectroscopy of human breast tissue," *Proc. Natl. Acad. Sci. USA* **98,** 4420-4425 (2001).

13. E. L. Heffer and S. Fantini, "Quantitative oximetry of breast tumors: A novel near-infrared method that identifies two optimal wavelengths," *Appl. Opt.* **41,** 3827-3839 (2002).

14. X. D. Li, T. Durduran, A. G. Yodh, B. Chance, and D. N. Pattanayak "Diffraction tomography for biochemical imaging with diffuse-photon density waves," *Opt. Lett.* **22,** 573-575 (1997).

15. H. Wabnitz, A. Liebert, M. Möller, D. Grosenick, R. Model, and H. Rinneberg, "Scanning Laser-Pulse Mammography: Matching Fluid and Off-Axis Measurements," in *OSA Biomedical Topical Meetings*, OSA Technical Digest, (Optical Society of America, Washington DC, 2002), pp. 686-688.

Figure captions

Fig. 1. Schematic diagram of the frequency-domain research prototype developed by Siemens Medical Engineering, Erlangen, Germany, for optical mammography. PMT: photomultiplier tube.

Fig. 2. (a) Edge corrected N-image at 690 nm of the left breast, craniocaudal view (lcc), of 58-year-old Patient 310. (b) Graph of the N data vs. x along the line $y = 3.2$ cm shown in panel (a). (c) Second-derivative image at 690 nm of the same breast shown in panel (a). (d) Graph of the negative second derivative of N ($-N''$) vs. x along the line $y = 3.2$ cm shown in panel (c). The arrow in panels (a) and (c) indicates the location of a 3-cm invasive ductal carcinoma.

Fig. 3. Conceptual representation of the steps involved in the second-derivative image processing scheme that converts the input N-image into the second-derivative N''-image.

Fig. 4. N-images at 690 nm of the left breast of 72-year-old Patient 197 in craniocaudal projection (panel (a)) and oblique projection (panel (b)), and corresponding second-derivative images (panels (c) and (d)). The arrows indicate the location of a 2.5-cm invasive ductal carcinoma.

Fig. 5. N-images at 690 nm of the right breast of 76-year-old Patient 267 in craniocaudal projection (panel (a)) and oblique projection (panel (b)), and corresponding second-derivative
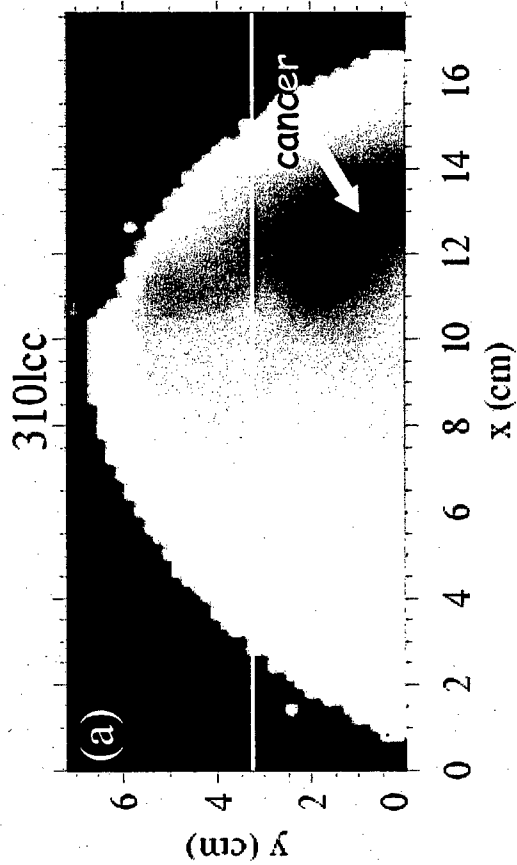
images (panels (c) and (d)). The arrows indicate the location of a 2.0-cm invasive ductal carcinoma.

Fig. 6. *N*-images at 690 nm of the right breast of 52-year-old Patient 165 in craniocaudal projection (panel (a)) and oblique projection (panel (b)), and corresponding second-derivative images (panels (c) and (d)). The arrows indicate the location of a benign mastopathy.
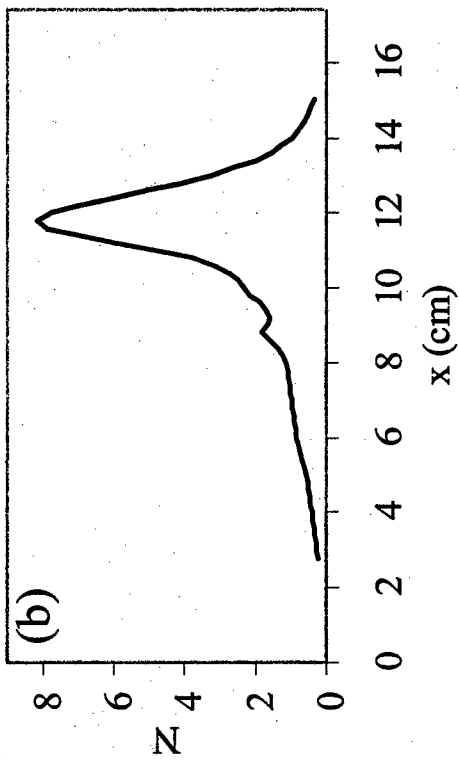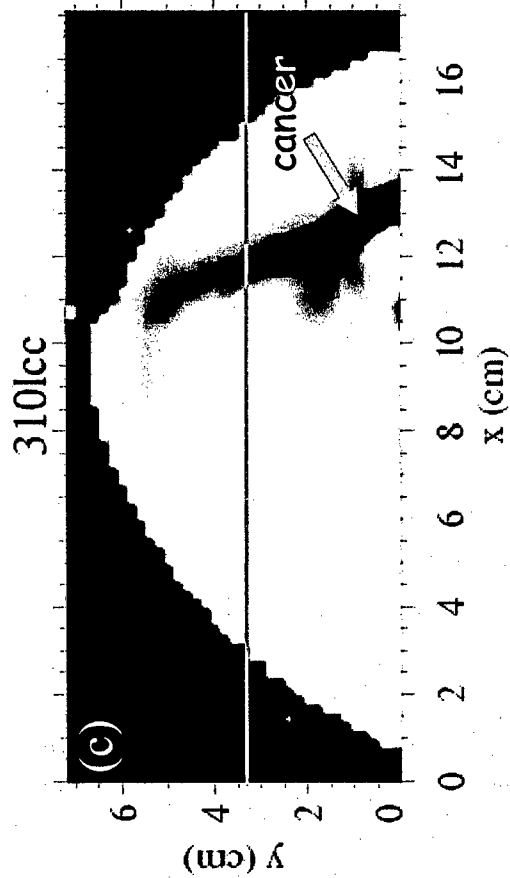
Fig. 7. *N*-images at 690 nm of the left breast of 53-year-old Patient 215 in craniocaudal projection (panel (a)) and oblique projection (panel (b)), and corresponding second-derivative images (panels (c) and (d)). The arrows indicate the location of a 3.0-cm invasive ductal carcinoma.

Display

Laser diodes
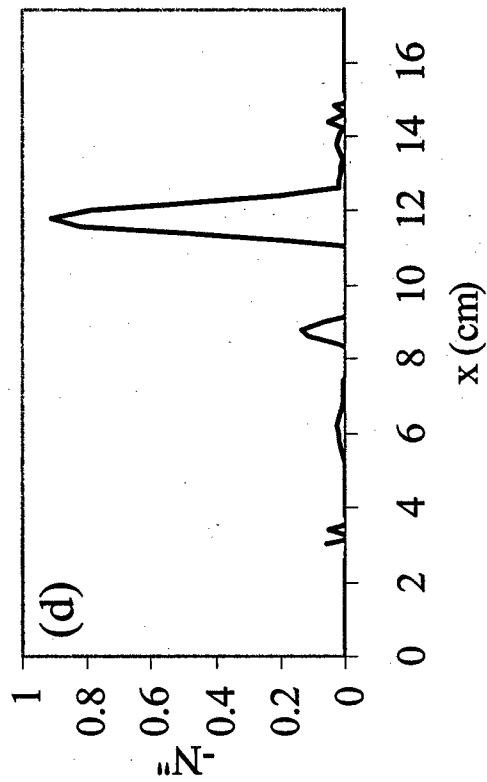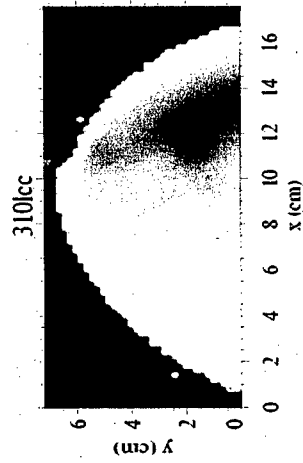Wavelength (nm):

69.50 MHz
69.80 MHz
70.20 MHz
70.45 MHz

Synch.

Data
processing

690
750
788
856

Optical fibers

Fiber coupler

Compressed
breast

PMT

Optical fiber

N-image (690 nm)

(a)

310lcc

cancer

y (cm)

x (cm)

(b)

N along y = 3.2 cm

N

x (cm)

2nd derivative image (690 nm)

(c)

310lcc

cancer

y (cm)

x (cm)

(d)

-N" along y = 3.2 cm

-N"

x (cm)

310lcc

y (cm)
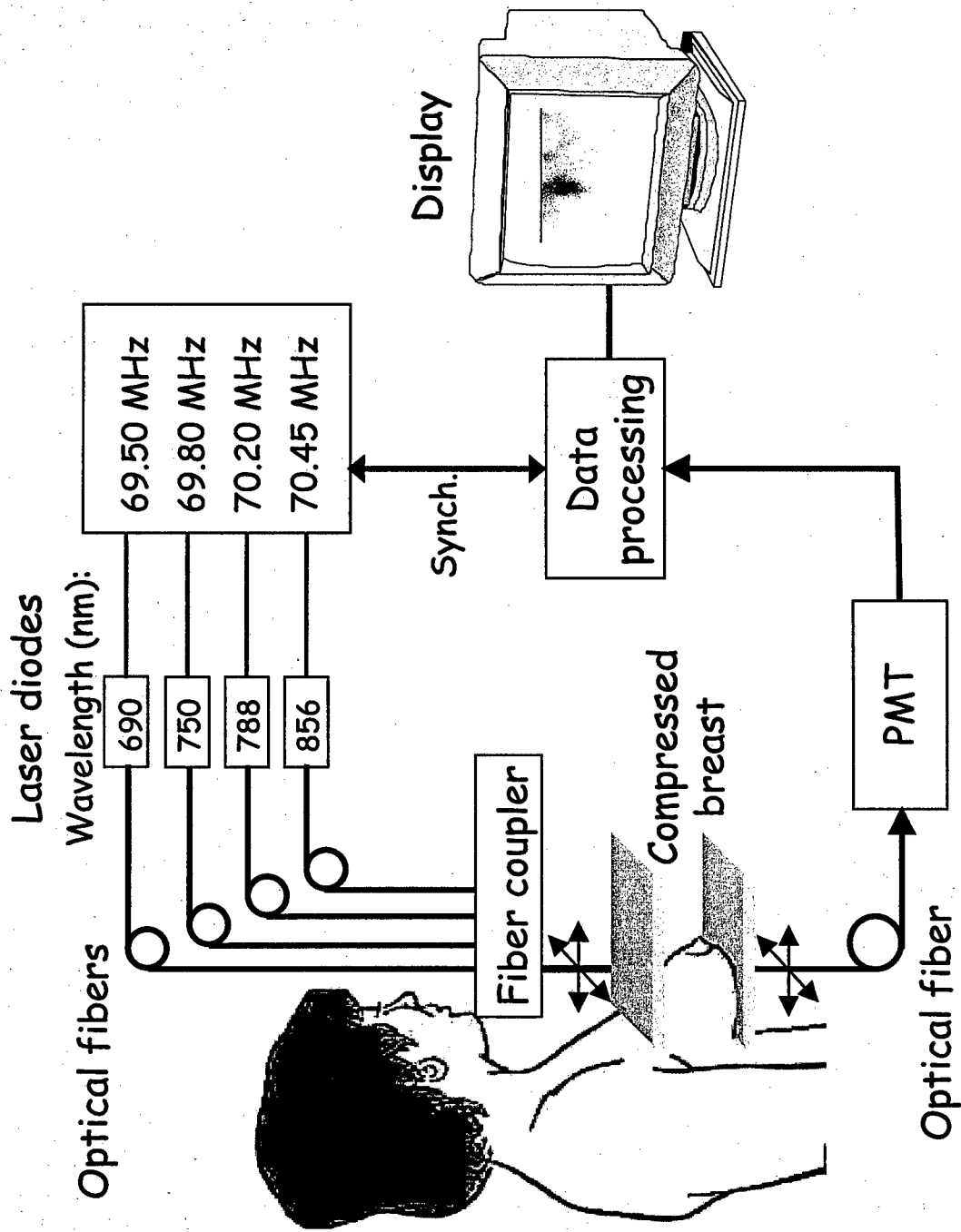
x (cm)

① Input *N*-image

② Convolve with smoothing function

1	2	3	2	1
2	4	6	4	2
3	6	9	6	3
2	4	6	4	2
1	2	3	2	1

⊗

| 2 | -4 | 2 |

| 2 |
| -4 |
| 2 |
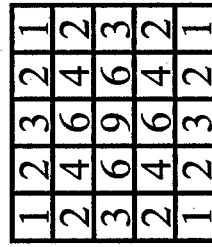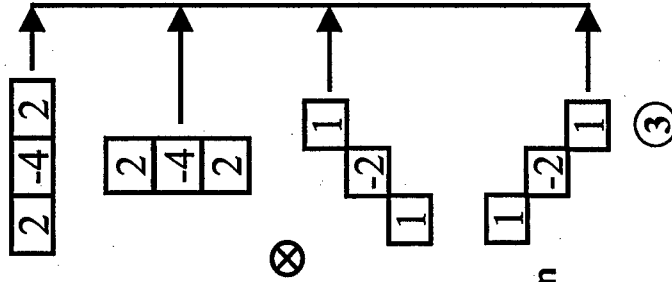
③

Calculate 2ⁿᵈ derivative in four directions

min ( )

④ Take minimum

310lcc

y (cm)

x (cm)

⑤ Display

N″< 0: grayscale
N″≥ 0: white
Outside breast: black

N-image (690 nm)

2ⁿᵈ derivative image (690 nm)
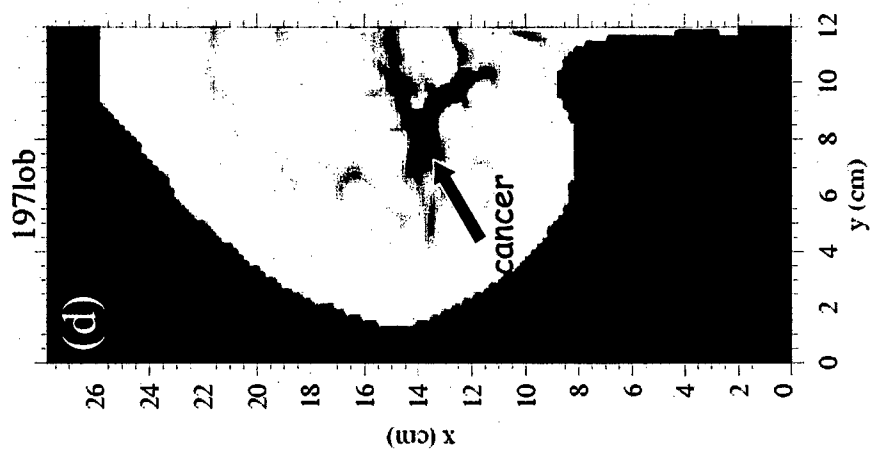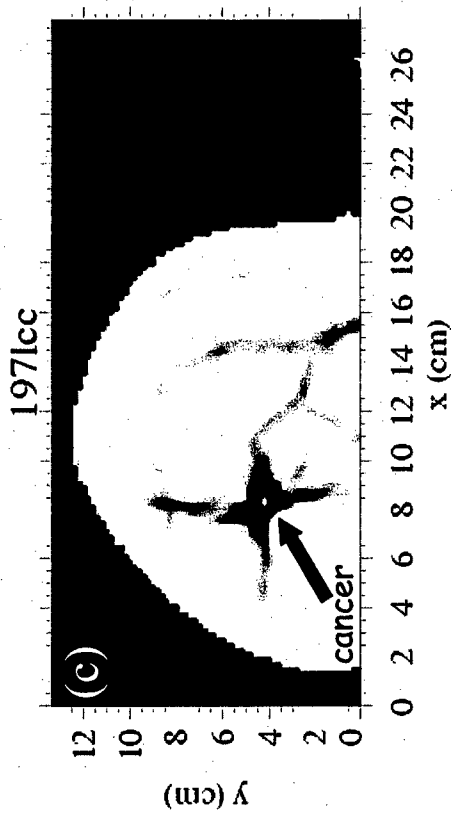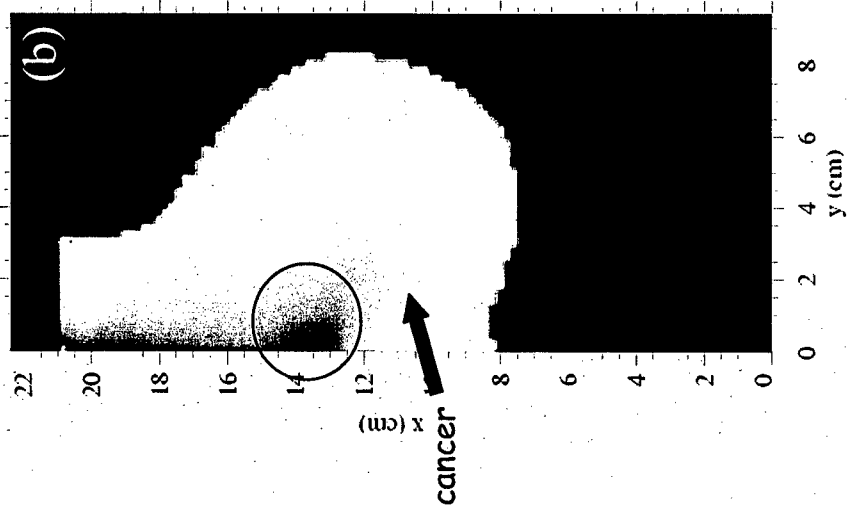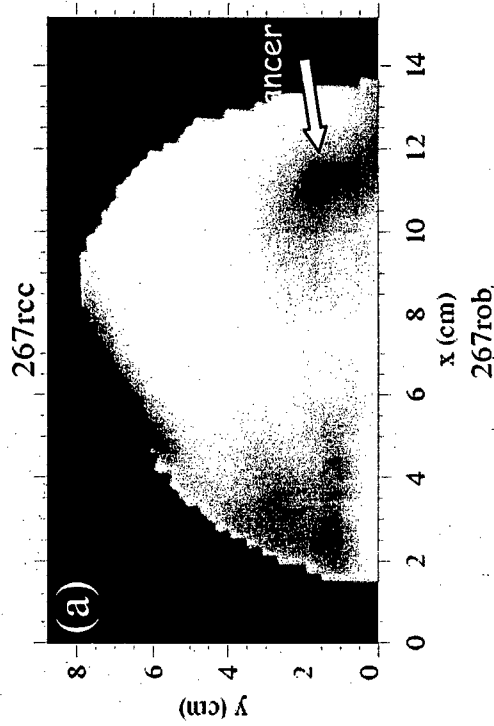
2nd derivative image (690 nm)

2nd derivative image (690 nm)

267rcc

(c) cancer

267rob

(d) cancer

N-image (690 nm)

267rcc

(a) cancer

267rob

(b) cancer

2nd derivative image (690 nm)

N-image (690 nm)

N-image (690 nm)

(a)

215lcc

cancer

y (cm)

x (cm)

(b)

215lob

cancer

x (cm)

y (cm)

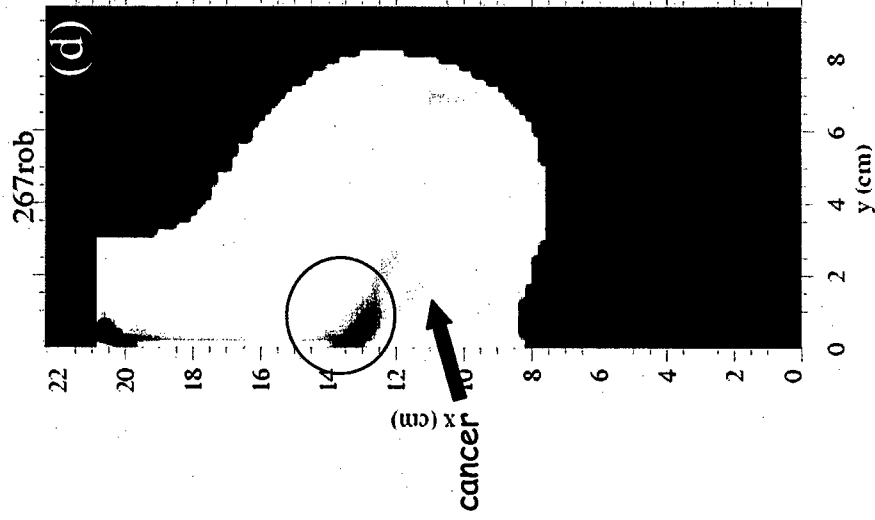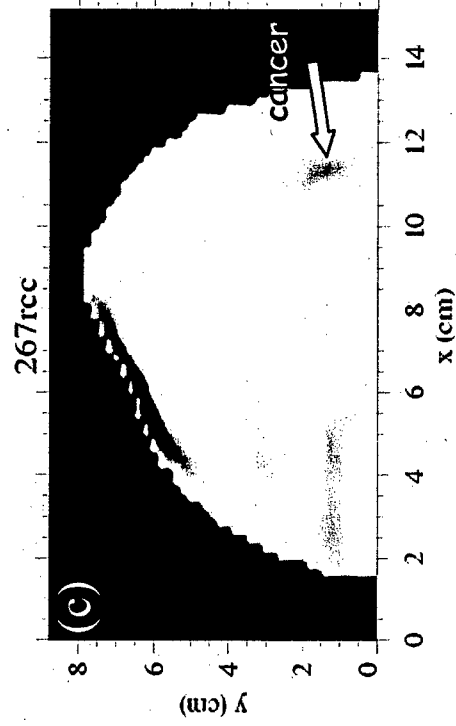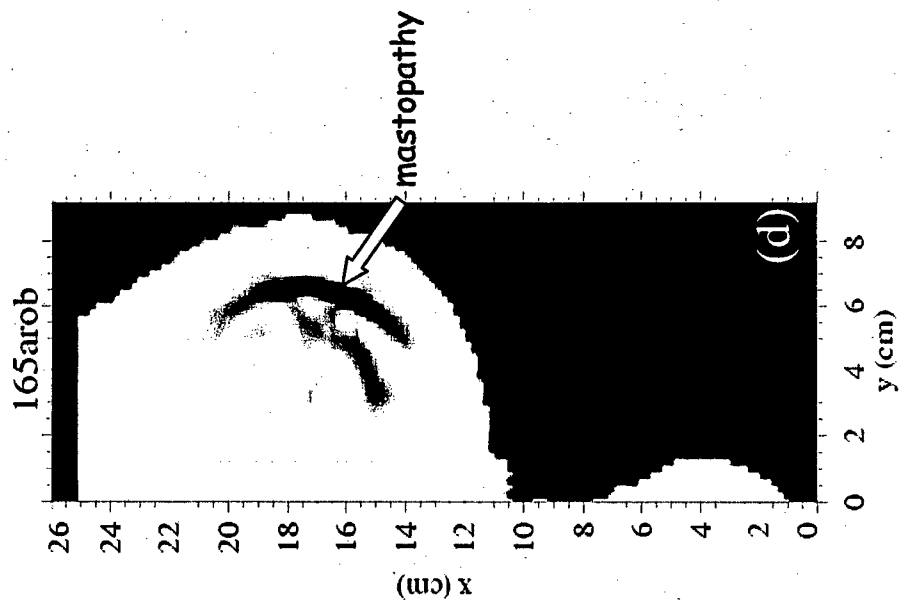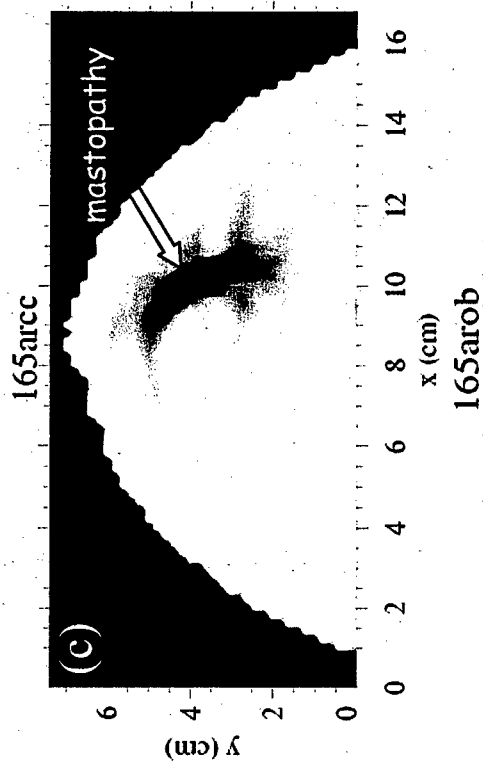# 2nd derivative image (690 nm)

(c)

215lcc

cancer

y (cm)

x (cm)

(d)

215lob

cancer

x (cm)
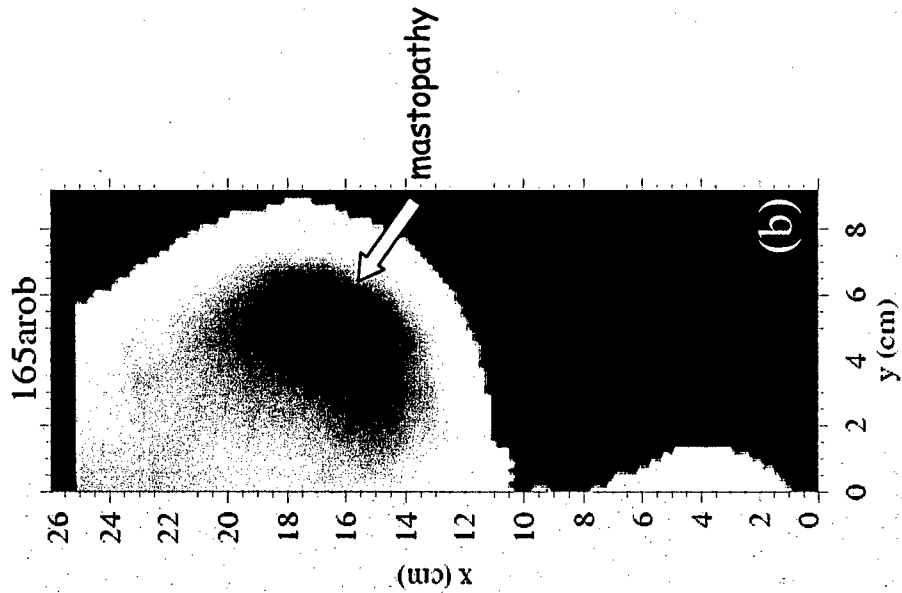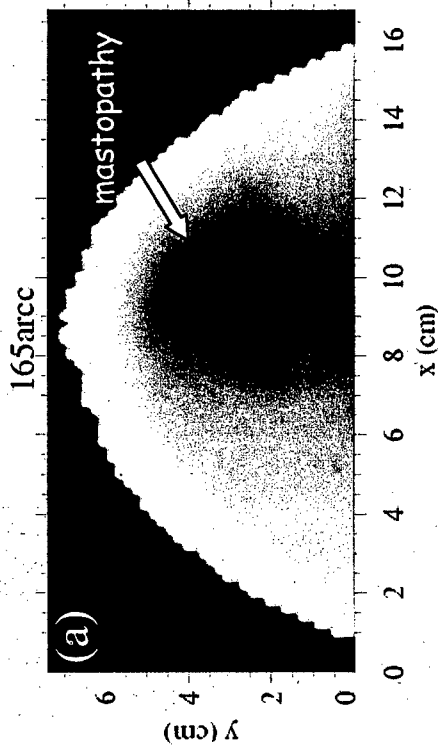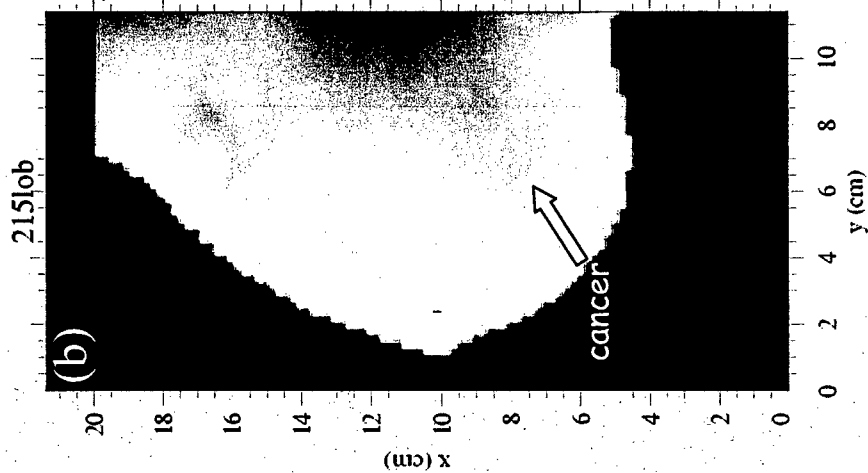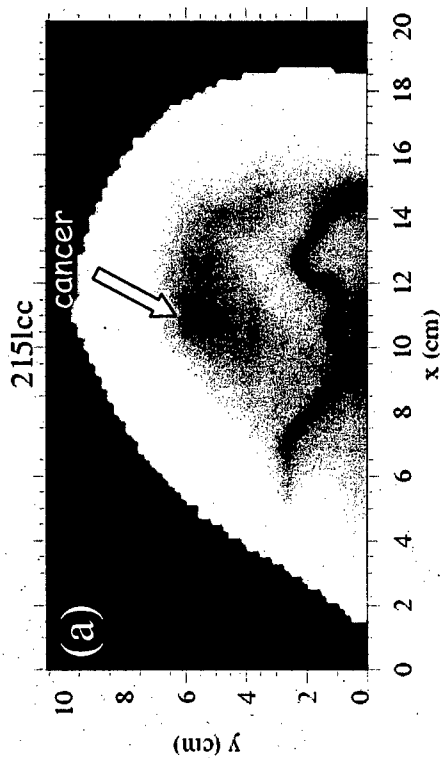
y (cm)
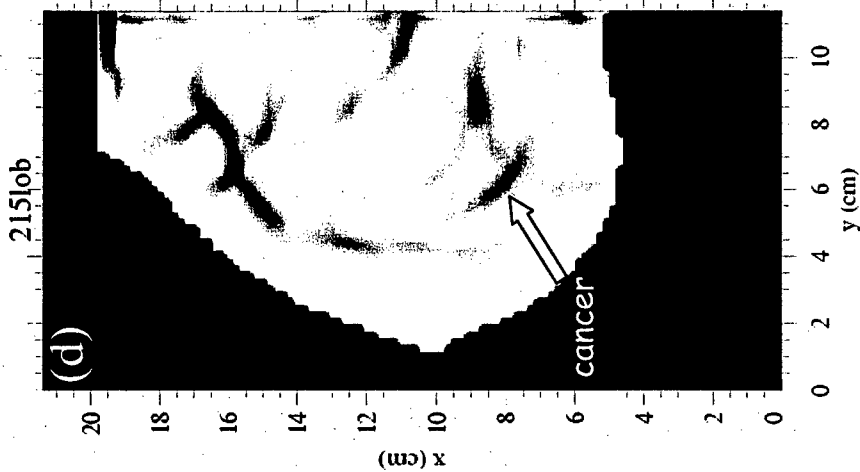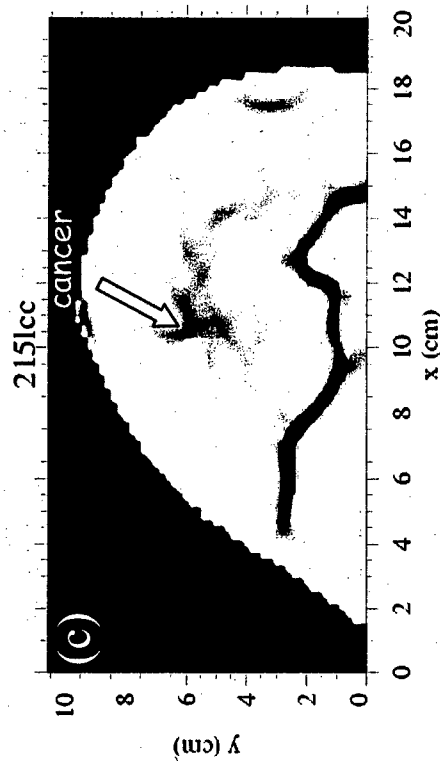
Quantitative oximetry of breast tumors: a near-infrared method that identifies two optimal wavelengths for each tumor

Erica L. Heffer and Sergio Fantini

We present a noninvasive optical method to measure the oxygen saturation of hemoglobin in breast lesions. This method introduces the novel concept that the best choice of near-infrared wavelengths for noninvasive tumor oximetry consists of a wavelength pair (λ_1, λ_2) within the range 680–880 nm, where the specific values of λ_1 and λ_2 depend on the optical properties of the specific tumor under examination. Our method involves two steps: (1) identify the optimal wavelength pair for each tumor and (2) measure the tumor oxygenation using the optical data at the two selected wavelengths. We have tested our method by acquiring experimental optical data from turbid media containing cylindrical or irregularly shaped inhomogeneities and by computing theoretical data for the case of spherical lesions embedded in a highly scattering medium. We have found that our optical method can provide accurate and quantitative measurements of the oxygenation of embedded lesions without requiring knowledge of their size, shape, and depth. © 2002 Optical Society of America

OCIS codes: 110.7050, 170.3830, 170.6510, 170.7050, 300.1030.

1. Introduction

Breast cancer is the most common cancer diagnosed and the second leading cause of cancer death among women in the United States.[1] The current method for screening is x-ray mammography, which provides high-resolution images but uses ionizing radiation, thus presenting the risk of inducing cancer. Furthermore, significant variations in interpreter performance have been observed that are due to the qualitative nature of the image analysis.[2] Other possible methods of breast cancer detection are computed tomography, which is used to detect abnormalities that are difficult to pinpoint with conventional mammography (i.e., in cases in which tumors are close to the chest wall); ultrasound, which is used to distinguish fluid-filled cysts from other types of lesion; and magnetic resonance imaging and positron emission tomography which are used to determine abnormally active tissues.[3]

The authors are with the Department of Electrical Engineering and Computer Science, Bioengineering Center, Tufts University, 4 Colby Street, Medford, Massachusetts 02155. E. L. Heffer's e-mail address is eheffe01@tufts.edu.

Magnetic resonance imaging and positron emission tomography are being studied as supplementary tests to x-ray mammography to distinguish benign from malignant lesions in high-risk patients.[4] In addition, thermography and immunodetection have been mentioned as additional detection modalities.[5-7]

Optical techniques have been proposed for many years as an alternative breast imaging modality that provides a safe and noninvasive study of the human breast. The initial investigation of optical methods for detection of breast cancer began in 1929, when Cutler proposed transillumination of the breast with broad-beam continuous-wave (cw) light,[8] a technique for which the terms diaphanography[9] and light scanning[10] were later adopted. Eventually diaphanography and light scanning were abandoned after clinical studies reported inferior performance with respect to x-ray mammography.[11-13] Recently, however, technical advances and the application of diffusion theory to model the propagation of light in tissue[14-20] have led to new approaches to optical mammography. As a result, new time-domain (based on pulsed light sources),[21-25] frequency-domain (based on intensity-modulated light sources),[26-30] and cw methods[31-33] for the optical study of the human breast have emerged.

Optical imaging in the near infrared relies mainly on the absorption of hemoglobin for the source of

image contrast. Hemodynamic changes such as an increase in the vascular density (resulting from angiogenesis) and changes in the blood flow and oxygenation typically occur at tumor sites.[34] The increase in vascular density induces a local increase in the optical absorption that may allow for the detection of breast lesions but does not necessarily provide indications on the nature (benign or malignant) of the lesion. The oxygenation level of the lesion, however, may provide this distinction. Measurements of the partial pressure of oxygen in tumors have shown that hypoxic or anoxic conditions often exist in malignant tumors but not in benign lesions.[35–38] Therefore a measurement of the oxygenation level *in vivo* has the potential to distinguish benign from malignant lesions in the human breast. As a result of these findings, several groups have attempted to obtain measurements of tumor oxygen saturation. Zhu *et al.* have reported deoxyhemoglobin and oxyhemoglobin concentration differences between tumors and background tissue, but did not obtain quantitative assessments of oxygen saturation (SO_2).[39] Holboke *et al.* have reported tumor oxygen saturation measurements where ultrasound is used for localization and the optical methods are used purely for spectroscopic measurements.[40] In a measurement on a single patient, they found a value of tumor oxygenation (63%) significantly lower than the values measured in the surrounding tissue (73% and 68%).[40] Using a nonimaging method on relatively large (approximately 2 cm × 1 cm) and superficial tumors, Tromberg *et al.*[41,42] have also reported a lower hemoglobin oxygenation in tumor with respect to normal tissue [$SO_{2(tumor)} \sim 65\%$ and $SO_{2(normal)} \sim 80\%$]. McBride *et al.* have been able to obtain oxygen saturation measurements to within 15% of the actual values in phantoms and have reported similar oxygenation values in normal human breast tissue as found in the research of Tromberg *et al.* [$SO_{2(normal)} = 84\% \pm 11\%$].[43] Fantini *et al.*[44] have performed similar measurements in which oxygen saturation of a papillary cancer was measured to be 71% ± 9%.

In this paper we present a novel spectral imaging approach that is aimed at quantifying the oxygen saturation of the hemoglobin in breast lesions. The strength of our new approach is its insensitivity to the tumor size, shape, and depth within the breast. We report experimental results on tissuelike phantoms and theoretical results for an idealized case that illustrate the capability of our method to provide accurate and quantitative oxygenation measurements of embedded tumors. The basic idea is that an appropriate choice of a pair of wavelengths (λ_1, λ_2), which depends on the oxygenation level of the tumor and on the optical properties of the background healthy breast tissue, leads to a measurement of the tumor oxygenation that is largely independent of the tumor size, shape, and location inside the breast. The fact that the best choice of wavelengths for the near-infrared measurement of tumor oxygenation is not fixed, but rather depends on the tumor oxygen-
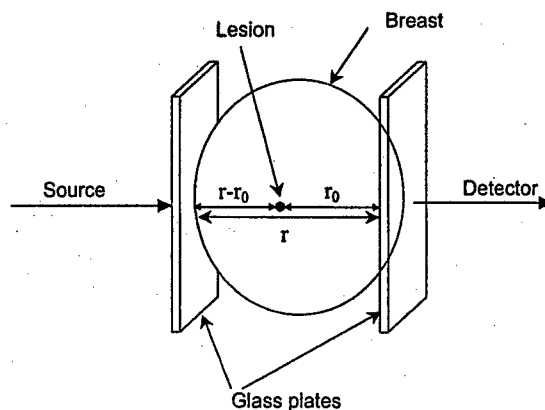
Fig. 1. Schematic representation of the perturbation approach. A small optical perturbation (lesion) causes a maximal reduction in intensity at the detector when the source, detector, and lesion are collinear. The distance from the center of the lesion to the detector is r_0, and the source–detector separation is r.

ation itself, is the most significant new concept introduced by our spectral imaging approach.

2. Methods

A. Mathematical Model

Our starting point is to treat the tumor as an optical perturbation within a highly scattering background medium (breast tissue). To a first approximation, a localized optical perturbation embedded in a turbid medium can be modeled with the first-order perturbative solution to the diffusion equation. First-order perturbation applies to small optical perturbations, where small means that the linear dimensions of the perturbation are much smaller than the distance r between the illumination and the collection points, that induce a small (with respect to 1) relative change in the optical signal. This case is schematically illustrated in Fig. 1 for a lesion embedded in a transilluminated human breast.

Let us denote the absorption and reduced scattering coefficient of the background medium (healthy breast tissue) with μ_{a0} and μ_{s0}', respectively, and the absorption and scattering perturbations (associated with the tumor) with $\Delta\mu_a$ and $\Delta\mu_s'$, respectively. This means that the absorption and reduced scattering coefficients at the location of the optical perturbation (tumor) are given by $\mu_{a0} + \Delta\mu_a$ and $\mu_{s0}' + \Delta\mu_s'$, respectively. The relative intensity change $\Delta I/I_0$ (where I_0 is the unperturbed intensity measured in the background medium) induced by the optical perturbation is maximized (in absolute value) when the source, detector, and the perturbation are collinear as shown in Fig. 1. The first-order perturbative solution to the diffusion

equation leads to the following expression for this maximal intensity change:[45]

$$\frac{\Delta I^{(\text{pert})}}{I_0}\bigg|_{\text{max}} = -\left(\frac{3\mu_{s0}{}'}{4\pi}\right)\frac{rV}{r_0(r - r_0)}\left\{\Delta\mu_a\right.$$

$$+ \frac{\Delta\mu_s{}'}{3\mu_{s0}{}'^2}\left[(3\mu_{a0}\mu_{s0}{}')^{1/2} + \frac{1}{r_0}\right]$$

$$\left.\times\left[(3\mu_{a0}\mu_{s0}{}')^{1/2} + \frac{1}{(r - r_0)}\right]\right\}. \quad (1)$$

Here V is the volume of the lesion, and the geometric parameters r and r_0 are defined in Fig. 1. The second term inside the braces in Eq. (1), the scattering perturbation term, is neglected on the basis of in vivo studies that have shown that the scattering tumor-to-background contrast is much smaller than the absorption contrast.[24,42,44] Therefore Eq. (1) is reduced to

$$\frac{\Delta I^{(\text{pert})}}{I_0}\bigg|_{\text{max}} = -\left[\frac{3rV}{4\pi r_0(r - r_0)}\right](\mu_{s0}{}'\Delta\mu_a). \quad (2)$$

As shown by Eq. (2), first-order perturbation theory predicts that the maximal intensity effect of an optical inclusion (for the case $\Delta\mu_s{}' = 0$) is given by the product of a wavelength-independent geometric factor and a wavelength-dependent factor given by $\mu_{s0}{}'\Delta\mu_a$. Chernomordik et al. have extended the limit of validity of Eq. (2) to larger inclusions by adding a multiplicative factor equal to $\exp[-\mu_{s0}{}'\Delta\mu_a V^{2/3}/2]$ to the right-hand side of Eq. (2).[46]

We now proceed on the hypothesis that Eq. (2) can be generalized to correctly predict the functional dependence of $\Delta I/I_0|_{\text{max}}$ on μ_{a0}, $\mu_{s0}{}'$, and $\Delta\mu_a$ beyond the limits of validity of the first-order perturbation analysis. Specifically, we hypothesize that, in the case of $\Delta\mu_s{}' = 0$, we can generalize Eq. (2) to the case of spatially extended objects that induce significant changes in the optical intensity by saying that $\Delta I/I_0|_{\text{max}}$ depends only on the product $\mu_{s0}{}'\Delta\mu_a$ and on wavelength-independent parameters that are related to the source–detector separation r and to the object–detector distance r_0, size V, and shape s of the object. Therefore we write

$$\frac{\Delta I}{I_0}\bigg|_{\text{max}} = f[r, r_0, V, s, (\mu_{s0}{}'\Delta\mu_a)], \quad (3)$$

implicitly in the argument $\mu_{s0}{}'\Delta\mu_a$ because the geometric parameters r, r_0, V, and s are independent of the wavelength. Consequently, because of the monotonicity of $\Delta I/I_0|_{\text{max}}$ on $\mu_{s0}{}'\Delta\mu_a$, if two wavelengths λ_1 and λ_2 are such that $\Delta I/I_0|_{\text{max}}^{(\lambda_1)} = \Delta I/I_0|_{\text{max}}^{(\lambda_2)}$, then we can conclude that $\mu_{s0}{}'(\lambda_1)\Delta\mu_a(\lambda_1) = \mu_{s0}{}'(\lambda_2)\Delta\mu_a(\lambda_2)$. Therefore the ratio of the absorption perturbations at these two wavelengths is just given by the inverse of the ratio of the background reduced scattering coefficients at the same two wavelengths:

$$\frac{\Delta\mu_a(\lambda_2)}{\Delta\mu_a(\lambda_1)} = \frac{\mu_{s0}{}'(\lambda_1)}{\mu_{s0}{}'(\lambda_2)}. \quad (4)$$

This analysis indicates that, by appropriately choosing the two wavelengths λ_1 and λ_2, one can translate a measurement of the background scattering ratio into a measurement of the absorption-perturbation ratio associated with the embedded inclusion. This result is relevant for the near-infrared determination of the oxygen saturation of hemoglobin in breast lesions because (1) the near-infrared spectral properties of hemoglobin and breast tissue are such that it is usually possible to identify two wavelengths at which the tumor-induced intensity perturbations are similar and because (2) the oxygen saturation of hemoglobin is only a function of the ratio of the optical absorption at two wavelengths.[47] If the absorption at the tumor location is given by the sum of the contributions from the background (μ_{a0}) and from the tumor [$\mu_a^{(t)}$], then $\Delta\mu_a$ can be identified with the tumor absorption [$\mu_a^{(t)} = \Delta\mu_a$]. If, instead, the absorption at the tumor location is due only to the tumor, then $\mu_a^{(t)} = \mu_{a0} + \Delta\mu_a$. However, if $\Delta\mu_a \gg \mu_{a0}$ (high-contrast tumor), one can still argue that $\Delta\mu_a$ is representative of the tumor absorption [$\mu_a^{(t)} \approx \Delta\mu_a$]. Here we consider the oxygen saturation (SO_2) of hemoglobin that is associated with the additional absorption $\Delta\mu_a$. At least in the two cases mentioned above, SO_2 is representative of the tumor oxygenation. When we assume that $\Delta\mu_a$ is solely due to hemoglobin, the expression for SO_2 in terms of $\Delta\mu_a(\lambda_1)$ and $\Delta\mu_a(\lambda_2)$ is the following:

$$SO_2 = \frac{\varepsilon_{\text{Hb}}(\lambda_2) - \varepsilon_{\text{Hb}}(\lambda_1)\Delta\mu_a(\lambda_2)/\Delta\mu_a(\lambda_1)}{[\varepsilon_{\text{Hb}}(\lambda_2) - \varepsilon_{\text{HbO}_2}(\lambda_2)] + [\varepsilon_{\text{HbO}_2}(\lambda_1) - \varepsilon_{\text{Hb}}(\lambda_1)]\Delta\mu_a(\lambda_2)/\Delta\mu_a(\lambda_1)}, \quad (5)$$

where f indicates an unknown function of its arguments. We further hypothesize that, as in the perturbation case, $\Delta I/I_0|_{\text{max}}$ is a monotonic function of the product $\mu_{s0}{}'\Delta\mu_a$. These two hypotheses are consistent with Eq. (2) and with its extension to larger inclusions reported by Chernomordik et al.[46] At this point, it is important to observe that the wavelength dependence of $\Delta I/I_0|_{\text{max}}$ appears only

where ε_{Hb} and $\varepsilon_{\text{HbO}_2}$ are the molar extinction coefficients of deoxyhemoglobin and oxyhemoglobin, respectively.

In practice, it may not be possible to identify two wavelengths λ_1 and λ_2 that exactly satisfy the requirement that $\Delta I/I_0|_{\text{max}}^{(\lambda_1)} = \Delta I/I_0|_{\text{max}}^{(\lambda_2)}$. In this case, we select the wavelength pair (λ_1, λ_2) that minimizes the absolute value of the difference $\Delta I/I_0|_{\text{max}}^{(\lambda_1)} - \Delta I/I_0|_{\text{max}}^{(\lambda_2)}$.

To correct, at least in part, for a difference between $\Delta I/I_0|_{\text{max}}^{(\lambda_1)}$ and $\Delta I/I_0|_{\text{max}}^{(\lambda_2)}$, we assume, on the basis of Eq. (2), that $\Delta I/I_0|_{\text{max}}^{(\lambda)} \propto \mu_{s0}'(\lambda)\Delta\mu_a(\lambda)$ so that

$$\frac{\Delta\mu_a(\lambda_2)}{\Delta\mu_a(\lambda_1)} = \frac{\mu_{s0}'(\lambda_1)}{\mu_{s0}'(\lambda_2)} \frac{\Delta I/I_0|_{\text{max}}^{(\lambda_2)}}{\Delta I/I|_{\text{max}}^{(\lambda_1)}}. \qquad (6)$$

When we combine Eqs. (5) and (6), the lesion saturation is given by

$$\text{SO}_2 = \frac{\varepsilon_{\text{Hb}}(\lambda_2) - \varepsilon_{\text{Hb}}(\lambda_1)\dfrac{\mu_{s0}'(\lambda_1)}{\mu_{s0}'(\lambda_2)}\dfrac{\Delta I/I_0|_{\text{max}}^{(\lambda_2)}}{\Delta I/I_0|_{\text{max}}^{(\lambda_1)}}}{[\varepsilon_{\text{Hb}}(\lambda_2) - \varepsilon_{\text{HbO}_2}(\lambda_2)] + [\varepsilon_{\text{HbO}_2}(\lambda_1) - \varepsilon_{\text{Hb}}(\lambda_1)]\dfrac{\mu_{s0}'(\lambda_1)}{\mu_{s0}'(\lambda_2)}\dfrac{\Delta I/I_0|_{\text{max}}^{(\lambda_2)}}{\Delta I/I_0|_{\text{max}}^{(\lambda_1)}}}, \qquad (7)$$

which is the equation we use to quantify the tumor oxygenation from measurements of (1) the background (healthy tissue) reduced scattering coefficient $[\mu_{s0}'(\lambda)]$ and (2) the maximal relative change in the intensity caused by the tumor $[\Delta I/I_0|_{\text{max}}^{(\lambda)}]$.

As a final comment on our mathematical model, we observe that, in addition to requiring that the intensity change induced by the inclusion is similar (ideally equal) at the two wavelengths, we also need to impose that these wavelengths are not too close to one another. In fact, Sevick et al. have shown that the sensitivity of the oxygenation measurement is degraded if the two near-infrared wavelengths are too close to each other.[48] In fact, a sensitivity analysis shows that $\lim_{\lambda_1 \to \lambda_2} \partial(\Delta\mu_a^{\lambda_1}/\Delta\mu_a^{\lambda_2})/\partial(\text{SO}_2) = 0$, because if $\lambda_1 = \lambda_2$, the ratio $\Delta\mu_a(\lambda_1)/\Delta\mu_a(\lambda_2)$ is equal to 1 independent of the value of SO_2. It can also be shown that the sensitivity of near-infrared hemoglobin oximetry is higher if the two wavelengths λ_1 and λ_2 are on the opposite sides of the $\sim$800-nm isosbestic point.

We adopt the criterion that $|\lambda_2 - \lambda_1| > 40$ nm to guarantee that the minimization of the absolute value of the difference $\Delta I/I_0|_{\text{max}}^{(\lambda_1)} - \Delta I/I_0|_{\text{max}}^{(\lambda_2)}$ yields an appropriate pair of wavelengths.

B. Experimental Procedures

The experimental portion of this study was divided into three segments: (1) preparation and optical characterization of inclusions to simulate tumors, (2) preparation and optical characterization of the background material (a highly scattering, liquid, effectively infinite medium), and (3) experimental procedures to investigate the dependence of $\Delta I/I_0|_{\text{max}}$ on $\mu_{s0}'\Delta\mu_a$ for the case of cylindrical and irregularly shaped objects embedded in a uniform turbid medium.

1. Optical Inclusions

Inclusions were comprised of a mixture of General Electric silicones, Model RTV615 (clear) and Model RTV11 (white). The white silicone was used as the scattering material, and black India ink was used as the absorber. Two different mixtures were prepared

with different optical properties (the first with $\mu_a \sim 0.05$–0.06 cm^{-1} and $\mu_s' \sim 9$–10 cm^{-1} and the second with $\mu_a \sim 0.11$–0.15 cm^{-1} and $\mu_s' \sim 9$–10 cm^{-1} over the wavelength range of 752–840 nm considered here) to cover a range of $\Delta\mu_a$ that is representative of the expected absorption contrast of breast lesions in vivo. We performed the optical characterization of the inclusions using the arrangement shown in Fig. 2. The silicone mixtures were formed into two cy-lindrically shaped blocks (one to characterize each mixture) of 11 cm in diameter and 9 cm in height. A frequency-domain, near-infrared spectrometer (Oxi-PlexTS, ISS, Inc., Champaign, Ill.) housed and controlled the laser sources and optical detectors used to obtain the measurements. The sources were laser diodes at six discrete wavelengths (752, 778, 786, 813, 830, and 840 nm), and the optical detector was a photomultiplier tube (Hamamatsu Photonics R928). The sources were intensity modulated at a frequency
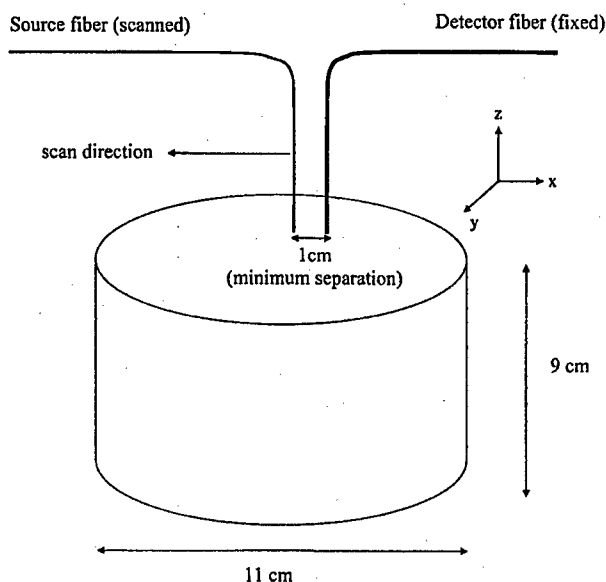
Fig. 2. Experimental arrangement for the optical characterization of the material used to cast the optical inclusions. Each silicone mixture was formed into a cylindrically shaped block that is 11 cm in diameter and 9 cm in height. The initial source–detector separation was 1 cm. The detector fiber bundle remained stationary and was in contact with the surface of the block. The end of the source fiber bundle was placed close to the surface without touching (<0.25 mm) and was translated in the negative x direction at a rate of 0.65 mm/s. Intensity and phase were acquired every 0.5 s. We determined the optical properties at six wavelengths (752, 778, 786, 813, 830, and 840 nm) using the diffusion model for light propagation in a semi-infinite medium.

of 110 MHz, electronically multiplexed at a rate of approximately 10 Hz to time share the detector, and were coupled to 400-μm core-diameter optical fibers that were collected into a fiber bundle with a rectangular cross section of 1.2 mm in width and 3 mm in length. The detector was coupled to another fiber bundle of circular cross section (3-mm internal diameter). The detector fiber bundle remained fixed and was in contact with the surface of the silicone blocks, whereas the end of the source bundle was brought close to the surface of the blocks (<0.25 mm away). The starting distance between the source and the detector fibers was 1 cm (x direction). The source fiber was then moved in the negative x direction defined in Fig. 2 (away from the detector fiber) at a rate of 0.65 mm/s. Data were acquired at every 0.5 s providing a measurement every 325 μm over a total traveled distance of 2 cm. We recorded and translated the amplitude (ac), average value (dc), and phase of the detected modulated intensity into measurements of the reduced scattering and absorption coefficients by employing a multidistance method based on the diffusion equation and semi-infinite boundary conditions.[16]

2. Background Turbid Medium

The background medium was comprised of 1 liter of Liposyn 10% (Abbott Laboratories, North Chicago, Ill.) to 8 liters of deionized water and was contained in a rectangular vessel with dimensions of 27 cm in width, 32 cm in length, and 13 cm in height. Again, the ISS frequency-domain spectrometer was used to perform the measurements. The experimental arrangement was similar to that used in Fig. 2 except that the ends of the source and fiber bundles were fully immersed in the Liposyn mixture to simulate an infinite medium. Acquisition times, laser multiplexing rate, and source-displacement speed (with the detector remaining fixed) were also the same as in the inclusion characterization. The ac, dc, and phase data were used in the diffusion model for light propagation in an infinite, highly scattering medium to determine the background reduced scattering (μ_{s0}') and absorption coefficients (μ_{a0}). Measurements of μ_{a0} over the wavelengths used ranged from 0.02 to 0.04 cm^{-1} and those of μ_{s0}' ranged from 10 to 12 cm^{-1} and were chosen to match typical absorption and scattering coefficients in breast tissue for this wavelength range [μ_a(breast) $\sim$ 0.03 cm^{-1} and μ_s'(breast) $\sim$ 12 cm^{-1}].[49–51]

3. Optical Measurements of Inclusions Embedded in a Turbid Medium

The experimental procedure to investigate the dependence of $\Delta I/I_0|_{max}$ on $\mu_{s0}'\Delta\mu_a$ was based on the arrangement shown in Fig. 3. The ISS frequency-domain tissue spectrometer was employed at the same six wavelengths used above to determine the optical properties of the inclusion material and the background. In this arrangement, the source and detector fiber bundles were arranged collinearly, and their ends were fully immersed in the formerly
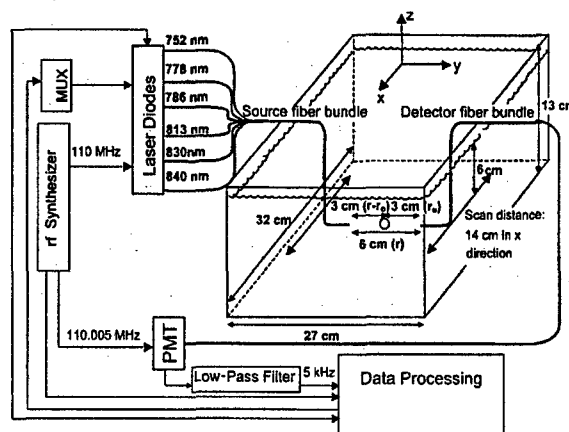

Fig. 3. Experimental setup for the optical measurements of inclusions embedded in a turbid medium. Six laser diodes from the frequency-domain near-infrared spectrometer were coupled to the source fiber bundle, and the photomultiplier tube (PMT) was coupled to the detector fiber. The lasers were multiplexed (MUX) to time share the optical detector. The radio frequency (rf) synthesizer provided the 110-MHz intensity modulation of the sources and the 110.005-MHz modulation of the PMT gain. The PMT output is low-pass filtered to isolate the downconverted 5-kHz frequency that is then digitally converted and processed. Source and detector fibers are arranged collinearly and are fully immersed in the Liposyn aqueous suspension. Source and detector separation was 6 cm and remained constant. The inclusions (either irregular or cylindrical) were suspended in the Liposyn mixture halfway between the source and the detector (inclusion center was 3 cm from the source and detector) by use of Pasteur pipets filled with the background medium. The source and detector were scanned together at a rate of 0.65 mm/s over a total distance of 14 cm starting at 7 cm away from the center of the inclusion in the x direction. Optical data were acquired every 0.88 s during the scan.

characterized background medium to simulate an infinite geometry. The source–detector separation for these experiments remained a constant 6 cm, which is representative of the thickness of a slightly compressed breast. Inclusions of different sizes and shapes were then suspended in the medium equidistant from the source and detector by use of Pasteur pipets to hold them in place. The pipets were filled with a background medium to reduce the optical perturbation they might cause.

We formed the inclusion material into irregular shapes (by cutting cylindrical shapes with razor blades) and into a 10-cm-long cylinder using the two different mixtures, thus creating two different sets of the same sizes and shapes. The cylinder had a diameter of 1.0 cm, whereas the irregular shapes were created to have the same volumes as the spheres with a 0.9-cm diameter ($V = 0.43$ cm^3) and a 1.4-cm diameter ($V = 1.31$ cm^3), respectively. The source and detector optical fibers were scanned together over a 14-cm distance in the x direction (as shown in Fig. 3) beginning at a distance of approximately 7 cm from the center of the inclusion in the x direction. Scanning was performed at a rate of 0.65 mm/s, and data were acquired every 0.88 s, providing a data point every 572 μm.

C. Theoretical Computation of Optical Data for a Spherical Inclusion

We calculated the theoretical estimates of the optical signals using an analytical solution to the diffusion equation for a spherical inclusion embedded in an infinite turbid medium.[15] This solution was implemented in a photon migration imaging software package developed by Boas *et al.* at Massachusetts General Hospital, Charlestown, Mass., as part of publicly available software.[52] Two types of theoretical analysis were performed.

Our first analysis was aimed at testing the hypothesis that the dependence of $\Delta I/I_0|_{max}$ on μ_{a0}, μ_{s0}', and $\Delta\mu_a$ is well approximated by a function of the product $\mu_{s0}'\Delta\mu_a$ even outside of the perturbation regime as in the cases of spheres having a diameter that is not much smaller than the source–detector separation and for values of $\Delta\mu_a$ that are not much smaller than μ_{a0}. This means that $\Delta I/I_0|_{max}$, for the case of $\Delta\mu_s' = 0$ considered here, is independent of μ_{a0} and is not affected by μ_{s0}' and $\Delta\mu_a$ separately, but only by their product $\mu_{s0}'\Delta\mu_a$. We carried out this theoretical analysis for two sphere diameters (1.4 and 3.0 cm) for the case in which the sphere is equidistant from the source and detector scanning lines (sphere center is 3.0 cm from either fiber in the collinear case). For the smaller sphere (1.4 cm in diameter), we also considered a 1.5-cm off-center position, where the distances from the sphere center to the source and detector fibers were 1.5 and 4.5 cm, respectively, in the collinear condition.

Our second theoretical analysis was aimed at testing the effectiveness of our new method for the measurement of tumor oxygenation. In this analysis, we set the background absorption and scattering spectra $\mu_{a0}(\lambda)$ and $\mu_{s0}'(\lambda)$, respectively, equal to typical absorption and reduced scattering spectra for breast tissue. We determined the absorption spectra by combining the absorption contributions from typical concentrations of oxyhemoglobin (~4.4 μM), deoxyhemoglobin (~2.7 μM), water (~39.5% volume by volume), and lipids (~60.5% volume by volume) in healthy breast tissue, as reported by Quaresima *et al.*[53] In the spectral region that we considered (680–880 nm), μ_{a0} ranged from 0.023 cm^{-1} (at 680 nm) to 0.076 cm^{-1} (at 880 nm). The background-scattering spectrum was estimated from data reported by Cubeddu *et al.* on two healthy human subjects.[25] In the

spectral region that we considered (680–880 nm), μ_{s0}' ranged from 10.0 cm^{-1} (at 680 nm) to 7.8 cm^{-1} (at 880 nm). We then considered spherical lesions with no scattering contrast ($\Delta\mu_s' = 0$) and with an absorption contrast provided by a hemoglobin concentration of 60 μM (corresponding to $\Delta\mu_a = 0.12$ cm^{-1} at 800 nm). As in the first analysis, we considered two sphere diameters (1.4 and 3.0 cm) in the centered case (sphere halfway between the source and the detector scanning lines) and one sphere diameter (1.4 cm) in the off-center case (sphere 1.5-cm off center). The maximum relative change in the optical signal induced by the spherical lesion ($\Delta I/I_0|_{max}$) was calculated at nine wavelengths (680, 720, 730, 758, 768, 776, 800, 840, and 880 nm) as a function of hemoglobin saturation values within the sphere over the range 0–100%. This choice of wavelengths covered the 680–880-nm diagnostic window and included the local maxima and minima in the deoxyhemoglobin absorption spectrum (730 and 758 nm, respectively) and the local minimum in the oxyhemoglobin absorption spectrum (680 nm).

3. Results

A. Measurement of the Optical Properties of the Inclusions and Background Medium

Table 1 shows the results of the measurements of the optical properties of the inclusions and background medium. The range of $\Delta\mu_a$ is from 0.014 to 0.12 cm^{-1} when we consider both silicone mixtures, whereas the range of $\Delta\mu_s'$ is from −0.5 to −2.9 cm^{-1}. Given the background optical properties of the order of 0.02 cm^{-1} for μ_{a0} and 9 cm^{-1} for μ_{s0}', the absorption perturbations are approximately 70–600% of the background absorption, whereas the scattering perturbations, in absolute value, do not exceed 31% of the background-reduced scattering coefficient. These conditions are representative of the range of optical contrast offered by tumors in the human breast *in vivo*.[24,41,42,44]

B. Experimental Measurements of $\Delta I/I_0|_{max}$ for Cylindrical and Irregularly Shaped Inclusions

Figure 4 shows a typical result of the optical intensity I measured during a linear scan across the object location at $x = 0$. Because $\Delta\mu_a > 0$, there is a decrease in detected intensity as the source–detector

---

Table 1. Summary of the Optical Properties of the Background Material (Liposyn Suspension) and Inclusions (Silicone Mixtures A and B) Used in the Experiments

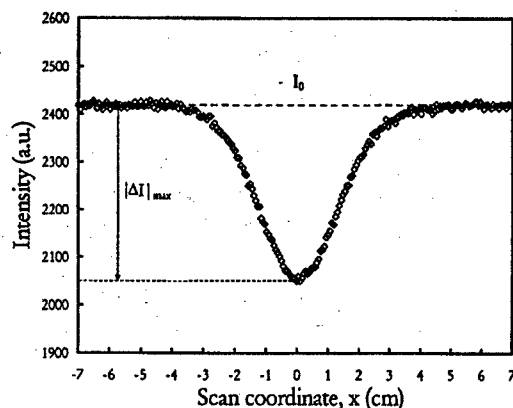| λ (nm)	Silicone Mixture A μ_a (cm^{-1})	Silicone Mixture A μ_s' (cm^{-1})	Silicone Mixture B μ_a (cm^{-1})	Silicone Mixture B μ_s' (cm^{-1})	Liposyn Suspension μ_a (cm^{-1})	Liposyn Suspension μ_s' (cm^{-1})
752	0.062(3)	9.8(4)	0.148(6)	9.3(4)	0.029(1)	12.2(6)
778	0.055(2)	9.7(4)	0.127(5)	9.8(4)	0.028(1)	11.7(6)
786	0.058(2)	9.8(4)	0.130(5)	9.8(4)	0.026(1)	11.6(6)
813	0.055(2)	9.3(4)	0.119(5)	9.6(4)	0.024(1)	11.1(5)
830	0.054(2)	9.4(4)	0.117(5)	9.6(4)	0.031(2)	10.5(5)
840	0.053(2)	8.9(4)	0.111(5)	9.4(4)	0.039(2)	10.2(5)

Fig. 4. Intensity data collected at 813 nm during a tandem scan of the source and detector optical fibers in the turbid medium containing an irregular inclusion (volume of 1.3 cm^3). The absorption and the reduced scattering coefficients of the inclusion were 0.119 and 9.6 cm^{-1}, respectively. Background absorption μ_{a0} was 0.024 cm^{-1}, and background-reduced scattering μ_{s0}' was 11.1 cm^{-1}. The scan coordinate $x = 0$ corresponds to the location of the center of the inclusion in the scan. The maximum intensity change $|\Delta I|_{max}$ caused by the inclusion and the background intensity I_0 are indicated.

pair approaches the inclusion during the scan. The background value I_0 and the maximum (in absolute value) intensity change $|\Delta I|_{max}$ are indicated in Fig. 4. The spectrum of $(\Delta I)_{max}/I_0(\lambda)$ is then used by our method to guide the choice of the two wavelengths λ_1 and λ_2 that are used to measure the oxygenation of the embedded object according to Eq. (7).

The experimental results for $-\Delta I/I_0|_{max}$ as a function of the product $\mu_{s0}'\Delta\mu_a$ are reported in Fig. 5(a) for the irregularly shaped inclusions and in Fig. 5(b) for the cylindrical inclusion. In both cases, the fact that the experimental data of $\Delta I/I_0|_{max}$ for a range of values of μ_{s0}' and $\Delta\mu_a$ (see Table 1) are distributed along a single curve as a function of the product $\mu_{s0}'\Delta\mu_a$ is indicative of the dependence of $\Delta I/I_0|_{max}$ on $\mu_{s0}'\Delta\mu_a$. In Figs. 5(a) and 5(b), the functions of $\mu_{s0}'\Delta\mu_a$ are represented by continuous curves. The deviations of the experimental points from the smooth lines are assigned to experimental errors and to the approximate fulfillment of the condition $\Delta\mu_s' = 0$ (see Table 1). These experiments confirm our hypothesis that $\Delta I/I_0|_{max}$ is only a function of the product $\mu_{s0}'\Delta\mu_a$ [as hypothesized in Eq. (3)] even for objects with a relatively large size, cylindrical or irregular shape, and relatively high-absorption contrast. Furthermore, as also hypothesized, $\Delta I/I_0|_{max}$ varies monotonically with $\mu_{s0}'\Delta\mu_a$.

C. Theoretical Calculations of $\Delta I/I_0|_{max}$ for Spherical Inclusions

Figure 6(a) shows the calculated dependence of $-\Delta I/I_0|_{max}$ on the product $\mu_{s0}'\Delta\mu_a$ for a spherical object embedded in a uniform turbid medium. As described in Subsection 2.C, we considered two sphere diameters (1.4 and 3.0 cm) for the case in which the
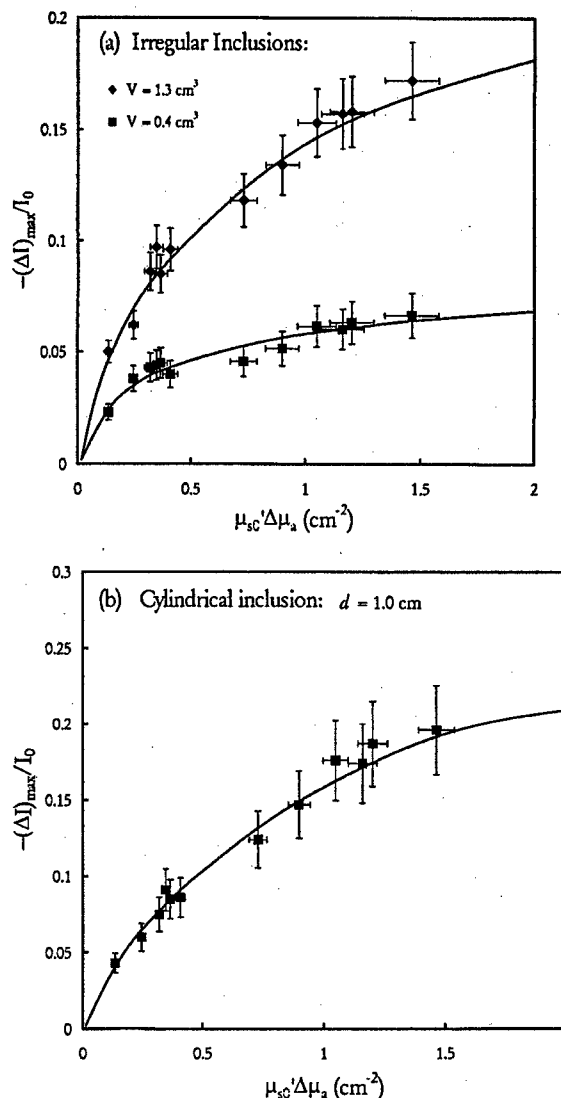

Fig. 5. Experimental results for $-\Delta I/I_0|_{max}$ as a function of $\mu_{s0}'\Delta\mu_a$ for (a) irregular inclusions and (b) a cylindrical inclusion. The volume V of the irregular inclusions and the diameter d of the cylindrical inclusion are indicated in (a) and (b), respectively.

sphere is equidistant from the source and detector fibers and one sphere diameter (1.4 cm) for the off-axis case in which the sphere is 1.5 cm off the midline between the source and the detector. The absorption coefficient of the background medium (μ_{a0}) is 0.06 cm^{-1}, and the scattering perturbation ($\Delta\mu_s'$) is set to zero. In all three cases considered, we found that $\Delta I/I_0|_{max}$ is not separately dependent on μ_{s0}' and $\Delta\mu_a$, but it only depends, monotonically, on their product [see Fig. 6(a)]. Furthermore, Fig. 6(b) shows that $\Delta I/I_0|_{max}$ is weakly dependent on μ_{a0} over the range of optical properties of interest.

D. Theoretical Test of the New Method to Measure the Oxygenation of Optical Inclusions

To test the effectiveness of our new method, we computed the values of $-\Delta I/I_0|_{max}$ at nine wavelengths (680, 720, 730, 758, 768, 776, 800, 840, and 880 nm)
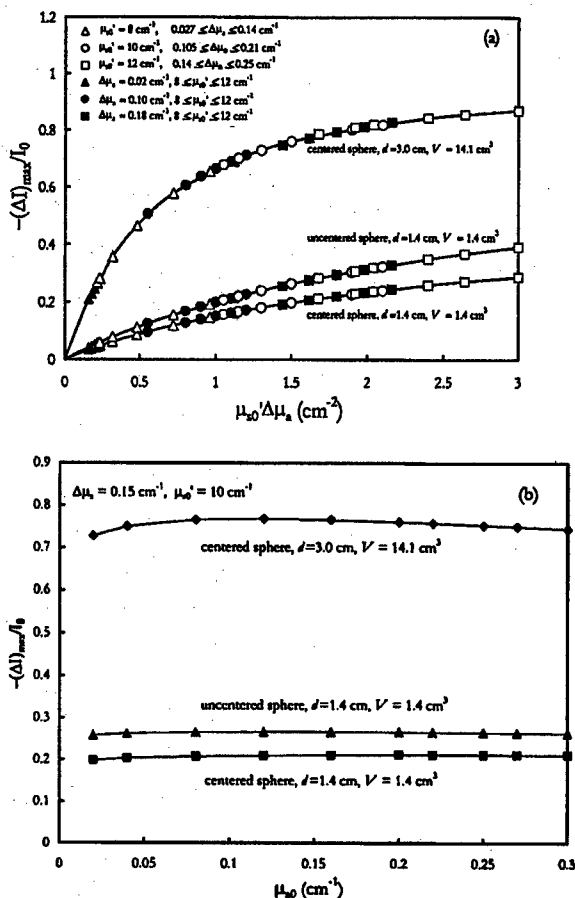
Fig. 7. Spectra of $\mu_{s0}'\Delta\mu_a$ used in the theoretical test of our method for SO_2 values of 0, 20, 40, 60, 80, and 100%. The wavelengths used in our theoretical calculations are shown by dashed lines. The symbols (matching the symbols of Fig. 8) identify the wavelength pairs that minimize the difference between $\Delta I/I_0|_{max}^{(\lambda_1)}$ and $\Delta I/I_0|_{max}^{(\lambda_2)}$ (which is the criterion used in our method to select the particular wavelength pair) for each value of SO_2.

Fig. 6. Dependence of $-\Delta I/I_0|_{max}$ versus (a) $\mu_{s0}'\Delta\mu_a$ and (b) μ_{a0} calculated by the diffusion theory for a spherical object in an infinite turbid medium. In (a) $\mu_{a0} = 0.06$ cm^{-1}; in (b) $\mu_{s0}'\Delta\mu_a = 1.5$ cm^{-1}; in both (a) and (b) $\Delta\mu_s' = 0$. Two sphere diameters d were considered (1.4 and 3.0 cm) for the case in which the sphere is centered between the source and the detector, and one sphere diameter (1.4 cm) was considered for the case in which the sphere is 1.5 cm off center (uncentered case). The volume V of the spheres was also indicated—the open (closed) symbols in (a) refer to constant values of $\mu_{s0}'(\Delta\mu_a)$.

for a spherical inclusion in a case that mimics a realistic condition in optical mammography. As described in Subsection 2.C, we set the background scattering and absorption spectra equal to representative spectra for healthy breast tissue obtained from literature data.[25,53] We observe that, because of the results of Fig. 6(b), the background absorption spectrum plays a minor role in the determination of $\Delta I/I_0|_{max}$. We set the hemoglobin concentration of the embedded lesion to a value 60 μM higher than that in the background, and we varied the hemoglobin saturation of the sphere over the range 0–100%. The resulting spectra of the product $\mu_{s0}'\Delta\mu_a$ for SO_2 values of 0, 20, 40, 60, 80, and 100% are reported in Fig. 7, where we also indicate with dashed lines the wavelengths used in our calculations. On the basis of our key hypothesis [Eq. (3)], the spectra of Fig. 7 are representative of the spectra of $\Delta I/I_0|_{max}$. We compared the measurements of the hemoglobin satura-
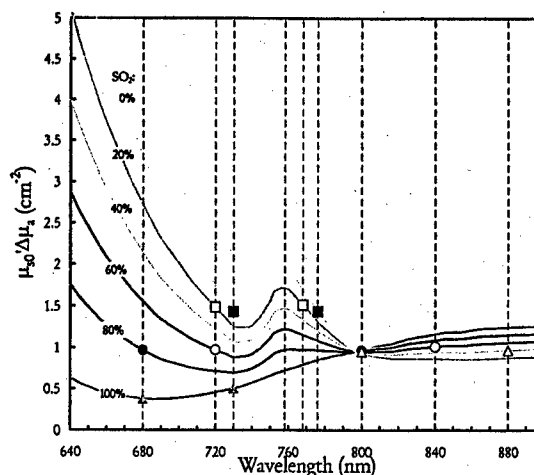
tion in the lesion obtained (1) by using Eq. (5) and a ratio $\Delta\mu_a(\lambda_2)/\Delta\mu_a(\lambda_1)$ computed with the perturbation theory [Eq. (2)] from the intensity change $\Delta I/I_0|_{max}$ measured at two fixed wavelengths and (2) by using our new method [Eq. (7)] at two wavelengths that are at least 40 nm apart and that minimize the absolute value of the difference $\Delta I/I_0|_{max}(\lambda_2) - \Delta I/I_0|_{max}(\lambda_1)$. Both approaches require knowledge of the background-reduced scattering coefficient, which was known in our theoretical computations and which can be measured with time-resolved methods in a practical implementation to the human breast. The results of the perturbation analysis for a number of wavelength pairs are shown in Fig. 8(a) for a 1.4-cm-diameter sphere (on the midline between the source and the detector), in Fig. 8(c) for a 3.0-cm-diameter sphere (on the midline between the source and the detector), and in Fig. 8(e) for a 1.4-cm-diameter sphere off the midline by 1.5 cm. The results of our new method are shown in Fig. 8(b) (sphere diameter of 1.4 cm, on the midline), Fig. 8(d) (sphere diameter of 3.0 cm, on the midline), and Fig. 8(f) (sphere diameter of 1.4 cm, 1.5 cm off the midline). These results show that our new method can achieve accurate measurements of the oxygenation of spherical regions over the full range of oxygenation values and independent of the size and location of the sphere. The wavelength pairs that minimize the difference between $\Delta I/I_0|_{max}^{(\lambda_1)}$ and $\Delta I/I_0|_{max}^{(\lambda_2)}$ [which is the criterion used to select the particular wavelength pairs in Figs. 8(b), 8(d), and 8(f)] for the cases of SO_2 equal to 0, 20, 40, 60, 80, and 100% are indicated in Fig. 7. We also computed SO_2 using all nine wavelengths [by fitting a linear combination of the oxyhemoglobin and deoxyhemoglobin extinction spectra to $\Delta\mu_a(\lambda_i)$ from Eq. (2)] (data not shown), and we found
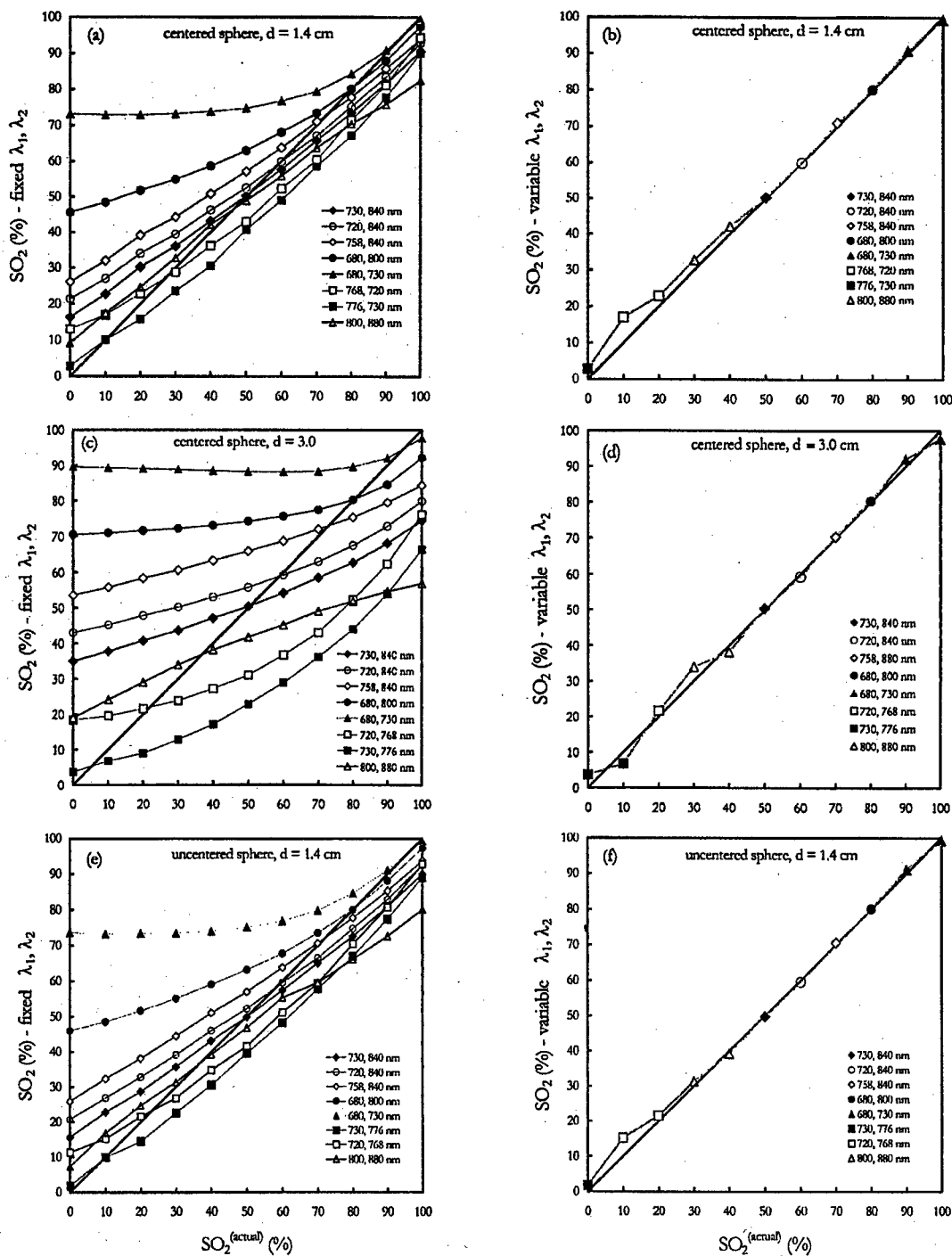
Fig. 8. Calculations of the oxygen saturation (SO_2) of spherical inclusions versus their actual value [$SO_2^{(actual)}$] used to compute the optical data from diffusion theory. (a), (c), and (e) show the perturbation approximation method when two fixed wavelengths were used to calculate SO_2. (b), (d), and (f) use the new method, which uses appropriately chosen wavelength pairs to determine SO_2. (a) and (b) are calculations for a centered 1.4-cm-diameter sphere; (c) and (d) are calculations for a centered 3.0-cm-diameter sphere; and (e) and (f) are calculations for an uncentered (1.5-cm off center) 1.4-cm-diameter sphere. The criterion to choose the most appropriate wavelength pair from the measured optical intensity is given in the text (Subsection 2.A).

no improvement on the fixed-wavelength pair results of Figs. 8(a), 8(c), and 8(e).

4. Discussion

We used first-order perturbation theory as a guide to develop our new method. In fact, our major hypothesis (namely, that in the case $\Delta\mu_s' = 0$, the ratio $\Delta I/I_0|_{max}$ depends only on wavelength through the product $\mu_{s0}'\Delta\mu_a$) is suggested by the proportionality between $\Delta I/I_0|_{max}^{(pert)}$ and $\mu_{s0}'\Delta\mu_a$ found in the perturbation limit [see Eq. (2)]. Furthermore, the expression for the ratio $\Delta\mu_a(\lambda_2)/\Delta\mu_a(\lambda_1)$ [Eq. (6)] that we use to compute the tumor saturation according to Eq. (5) is the same as the one provided by first-order perturbation theory [Eq. (2)]. Therefore it may appear that our approach is exclusively based on first-order perturbation theory. This is not the case because one key feature of our new method, namely, the criterion to select the two wavelengths λ_1 and λ_2, is based on the results of Fig. 6, which refer to situations that are beyond the limits of applicability of first-order perturbation theory. As a result, even if $\Delta I/I_0|_{max}$ does not show a linear dependence on $\mu_{s0}'\Delta\mu_a$ as predicted by first-order perturbation theory, our method still provides accurate readings of the tumor saturation, provided that one can identify two wavelengths λ_1 and λ_2 such that $\Delta I/I_0|_{max}^{(\lambda_1)} \approx \Delta I/I_0|_{max}^{(\lambda_2)}$. Of course, this latter requirement becomes redundant in the perturbation limit, where $\Delta I/I_0|_{max}$ is indeed proportional to $\mu_{s0}'\Delta\mu_a$, and less critical in a regime of quasi-proportionality between $\Delta I/I_0|_{max}$ and $\mu_{s0}'\Delta\mu_a$. As shown by Figs. 5 and 6(a), this proportionality occurs approximately for values of $\mu_{s0}'\Delta\mu_a$ that are smaller than ~0.5 cm^{-2} (i.e., for values of $\Delta\mu_a < 0.05$ cm^{-1} if $\mu_{s0}' \sim 10$ cm^{-1}), even though the size of the inclusion also affects the extent of the quasi-proportionality range. In summary, the success of our method depends on the fulfillment of at least one of the three following conditions:

1. relatively small tumors;
2. relatively small tumor background absorption contrast; or
3. identification of two wavelengths, at least 40 nm apart, such that $\Delta I/I_0|_{max}^{(\lambda_1)} \approx \Delta I/I_0|_{max}^{(\lambda_2)}$.

The fulfillment of conditions 1 and 2 allows the applicability of the perturbative relationship given in Eq. (2), whereas the fulfillment of condition 3 enables the application of Eq. (7) on the basis of Eq. (3). In general, if condition 3 above cannot be fulfilled, the most accurate measurement of SO$_2$ will come from the wavelengths where the optical signal is least affected by the tumor, i.e., for the wavelengths at which the absolute value of $\Delta I/I_0|_{max}$ is the smallest.

The idea behind the development of our new method is that a robust approach to the optical oximetry of breast cancers will improve the diagnostic value of optical mammography. Instead of trying to obtain a full solution of the inverse imaging problem to determine the size, shape, location, and optical properties of the tumor, we aim at measuring one physiological parameter, namely, the tumor oxygenation, using a method that is insensitive to the size, shape, and location of the tumor. The insensitivity to the shape of the inclusion is shown by the experimental results of Fig. 5, whereas the insensitivity to the size and location of the inclusion is shown by the theoretical results of Figs. 6 and 8. This approach has the potential of being more robust in practical clinical measurements with respect to full reconstruction schemes. The only information required by our method is (1) the spectrum of the background-scattering coefficient $\mu_{s0}'(\lambda)$, (2) the background intensity $I_0(\lambda)$, and (3) the maximum intensity change $(\Delta I)_{max}$ caused by the tumor. To best apply our method, the spectral measurements should be conducted at a large number of wavelengths in the range 680–880 nm, possibly continuously over this spectral band.

In view of the actual implementation of this new method to clinical optical mammography, it is worth commenting on the required measurements of $\mu_{s0}'(\lambda)$ and $I_0(\lambda)$. What is really required by our method is the ratio $\mu_{s0}'(\lambda_1)/\mu_{s0}'(\lambda_2)$ so that the spectral shape of μ_{s0}', rather than its absolute value, is the critical quantity. This fact minimizes the influence of tissue inhomogeneity because it has been reported that the spectral shape of μ_{s0}', but not its absolute value, is relatively constant at different breast locations.[25] As a result, $\mu_{s0}'(\lambda)$ can be measured when time-resolved measurements are averaged at several breast locations. Because of the featureless scattering spectrum, measurements at a few discrete wavelengths λ_i can be effectively extrapolated to yield a continuous spectrum of $\mu_{s0}'(\lambda)$, as demonstrated by Bevilacqua et al.[54] With respect to the measurement of the background intensity $I_0(\lambda)$, in the presence of a heterogeneous background such as breast tissue, it may be appropriate to consider an average background intensity over a specifically selected breast area rather than the intensity measured at a particular breast location.

Our method is expected to be insensitive to boundary conditions. In fact, it has been reported that measurements based on comparing or ratioing data at two wavelengths [our method is based on a condition that involves the ratios $\Delta I/I_0|_{max}^{(\lambda_1)}$ and $\Delta I/I_0|_{max}^{(\lambda_2)}$ to assess the ratio $\Delta\mu_a(\lambda_1)/\Delta\mu_a(\lambda_2)$] are highly insensitive to boundary conditions.[55,56] For this reason, we believe that the experimental and theoretical results presented here, which we obtained using effectively infinite media, are applicable to the bounded breast case of Fig. 1.

The new method that we present in this paper is aimed at quantifying the oxygen saturation associated with $\Delta\mu_a$, i.e., with the additional absorption at the tumor location with respect to the background tissue [see Eq. (5)]. We have argued that $\Delta\mu_a$ is indeed representative of the tumor absorption [$\mu_a^{(t)}$] if (1) the absorption at the tumor location results from the sum of the background (healthy tissue) absorption (μ_{a0}) plus the tumor contribution [$\mu_a^{(t)} \equiv \Delta\mu_a$] or if (2) the tumor absorption $\mu_a^{(t)}$ is equal to $\mu_{a0} + \Delta\mu_a$

and $\Delta\mu_a \gg \mu_{a0}$ (high-contrast tumor). For the case in which $\mu_a^{(t)} = \mu_{a0} + \Delta\mu_a$, but $\Delta\mu_a$ is not much greater than μ_{a0}, the tumor saturation $SO_2^{(t)}$ may not be accurately represented by SO_2 of Eq. (5). In this case, the tumor saturation is given by

$$SO_2^{(t)} = \frac{\varepsilon_{Hb}(\lambda_2) - \varepsilon_{Hb}(\lambda_1)\dfrac{\mu_{a0}(\lambda_2) + R\Delta\mu_a(\lambda_1)}{\mu_{a0}(\lambda_1) + \Delta\mu_a(\lambda_1)}}{[\varepsilon_{Hb}(\lambda_2) - \varepsilon_{HbO_2}(\lambda_2)] + [\varepsilon_{HbO_2}(\lambda_1) - \varepsilon_{Hb}(\lambda_1)]\dfrac{\mu_{a0}(\lambda_2) + R\Delta\mu_a(\lambda_1)}{\mu_{a0}(\lambda_1) + \Delta\mu_a(\lambda_1)}}, \tag{8}$$

where $R = \Delta\mu_a(\lambda_2)/\Delta\mu_a(\lambda_1)$ is the ratio used in our method to calculate SO_2. Because R is of the order of $\mu_{s0}'(\lambda_1)/\mu_{s0}'(\lambda_2)$, it is typically close to 1. As expected, $SO_2^{(t)}$ given by Eq. (8) tends to the background saturation $[SO_2^{(0)}]$ in the limit $\Delta\mu_a \to 0$ and to the saturation based on $\Delta\mu_a$ (SO_2) in the limit $\Delta\mu_a \gg \mu_{a0}$. The derivative of $SO_2^{(t)}$ with respect to $\Delta\mu_a(\lambda_1)$ at constant R is given by

is independent of $\Delta\mu_a(\lambda_1)$. As a result, $SO_2^{(t)}$ monotonically increases (or decreases) from $SO_2^{(0)}$ to SO_2 as the tumor contrast increases. This is graphically shown in Fig. 9 for the case $SO_2^{(0)} = 70\%$, $\mu_{a0}(800\ nm) = 0.02\ cm^{-1}$ (a reasonable estimate of the back-ground hemoglobin absorption in breast tissue), and SO_2 values of 0, 20, 40, 60, 80, and 100%. Therefore we can conclude that the sign of $SO_2^{(t)} - SO_2^{(0)}$, which indicates whether the tumor is more oxygenated or less oxygenated than the background healthy tissue, is accurately given by the sign of $SO_2 - SO_2^{(0)}$ independent of the tumor contrast. Furthermore, Fig. 9 indicates that, for $\Delta\mu_a > 0.1\ cm^{-1}$ and tumor satu-

$$\left[\frac{\partial SO_2^{(t)}}{\partial\Delta\mu_a^{(\lambda_1)}}\right]_R = \frac{[\mu_{a0}(\lambda_2) - R\mu_{a0}(\lambda_1)][\varepsilon_{Hb}(\lambda_2)\varepsilon_{HbO_2}(\lambda_1) - \varepsilon_{Hb}(\lambda_1)\varepsilon_{HbO_2}(\lambda_2)]}{\{[\varepsilon_{Hb}(\lambda_2) - \varepsilon_{HbO_2}(\lambda_2)][\mu_{a0}(\lambda_1) + \Delta\mu_a(\lambda_1)] + [\varepsilon_{HbO_2}(\lambda_1) - \varepsilon_{Hb}(\lambda_1)][\mu_{a0}(\lambda_2) + R\Delta\mu_a(\lambda_1)]\}^2}. \tag{9}$$

Equation (9) shows that, for any given value of R, the sign of the derivative of $SO_2^{(t)}$ with respect to $\Delta\mu_a(\lambda_1)$

ration values greater than 40%, $SO_2^{(t)}$ and SO_2 differ by no more than ~5%. An estimate of $\Delta\mu_a(\lambda_1)$, for example, on the basis of Eq. (2), may lead to a refinement of the tumor saturation measurement from the values of SO_2 (with our new method) and $SO_2^{(0)}$ (measurable on healthy breast tissue). We conclude by stressing that this latter discussion based on Eqs. (8) and (9) pertains only to the cases in which the tumor absorption is better represented by $\mu_{a0} + \Delta\mu_a$ then by $\Delta\mu_a$. If $\mu_a^{(t)} \approx \Delta\mu_a$, then SO_2 provides an accurate measurement of the tumor saturation.

5. Conclusion

We have presented a novel optical method to quantitatively measure the oxygen saturation of breast tumors. In the field of optical mammography, the most appropriate number of wavelengths to be used and the choice of those wavelengths are commonly questioned. According to our method, the optimal number of wavelengths to measure the tumor oxygenation is two (within the range 680–880 nm), but the two specific wavelengths depend on the particular value of the tumor oxygenation. Therefore our method requires the collection of optical data at multiple wavelengths, ideally a continuum, and then selection of the two optimal near-infrared wavelengths for each tumor on the basis of a specific criterion [namely, the minimization of the absolute value of the difference $\Delta I/I_0|_{max}(\lambda_2) - \Delta I/I_0|_{max}(\lambda_1)$]. After the optimal wavelength pair has been selected, our
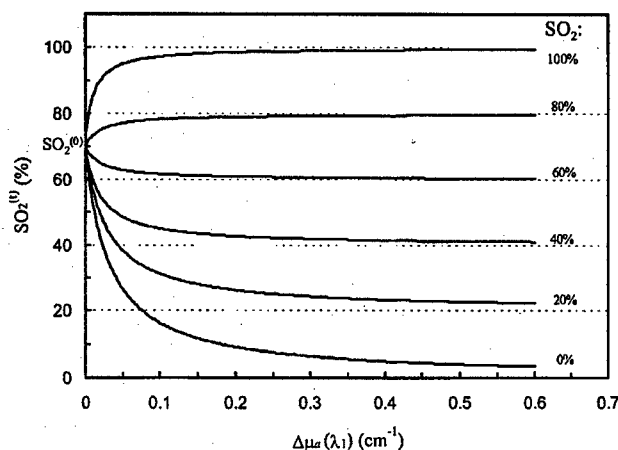

Fig. 9. Schematic for the case in which the tumor absorption is better represented by $\mu_{a0} + \Delta\mu_a$ then by $\Delta\mu_a$ and showing the dependence of the tumor saturation $[SO_2^{(t)}]$ on $\Delta\mu_a(\lambda_1)$ for a background saturation $SO_2^{(0)} = 70\%$ and six different values (0, 20, 40, 60, 80, 100%) of SO_2. SO_2 is the saturation based on $\Delta\mu_a(\lambda_1)$ and $\Delta\mu_a(\lambda_2)$ that is provided by our new method. For each value of SO_2, we considered the corresponding optimal wavelength pair that is given in Figs. 7 and 8. If $\mu_a^{(t)} \approx \Delta\mu_a$, then SO_2 provides an accurate measurement of the tumor saturation $[SO_2^{(t)} \approx SO_2]$, and the curves in this figure are replaced by horizontal lines independent of $\Delta\mu_a$.

method describes the way to process the optical data at these two wavelengths to obtain the tumor oxygenation. From laboratory experiments and theoretical calculations, we have found that we can accurately measure the oxygenation of embedded lesions over the full range 0–100% independently of their size, shape, and depth. This method offers the potential to improve the diagnostic capability of optical mammography.

We conclude by observing that, even if we have described an application to the oximetry of breast tumors, our method lends itself to measuring the oxygenation of other hemoglobin-rich localized tissue areas as well. For example, the focal increase in cerebral hemoglobin concentration induced by selected cerebral activity, a localized hematoma, or relatively large blood vessels can be investigated by some of the basic ideas presented here to measure their oxygenation levels.

References

1. P. A. Wingo, T. Tong, and S. Bolden, "Cancer statistics, 1995," CA Cancer J. Clin. **45**, 8–30 (1995).
2. J. G. Elmore, C. K. Wells, C. H. Lee, D. H. Howard, and A. R. Feinstein, "Variability in radiologists' interpretation of mammograms," N. Engl. J. Med. **331**, 1493–1499 (1994).
3. National Cancer Institute, "Understanding breast changes—a health guide for all women," http://www.cancer.gov/cancer_information/doc_img.aspx?viewid=1cf1a0cb-cdfe-4e6e-8ad1-73bb376232aa (2001).
4. Medical College of Wisconsin Physicians & Clinics, "MRI highly effective for breast cancer detection," http://healthlink.mcw.edu/article/956629092.html (2000).
5. Breast Thermography Physician's Review, "A review of breast thermography," http://www.breastthermography.com/infra-red_imaging_review_mf.htm (2001).
6. J. R. Keyserlingk, P. D. Ahlgren, E. Yu, and N. Belliveau, "Infrared imaging of the breast: initial reappraisal using high-resolution digital technology in 100 successive cases of stage I and stage II breast cancer," Breast J. **4**, 245–251 (1998).
7. D. B. Kopans, " 'Early' breast cancer detection using techniques other than mammography," Am. J. Roentgenol. **143**, 465–468 (1984).
8. M. Cutler, "Transillumination of the breast," Surg. Gynecol. Obstet. **48**, 721–727 (1929).
9. C. M. Gros, Y. Quenneville, and Y. Hummel, "Diaphanologie mammaire," J. Radiol. Electrol. Med. Nucl. **53**, 297–306 (1972).
10. E. Carlsen, "Transillumination light scanning," Diagn. Imaging **4**, 28–34 (1982).
11. E. A. Sickles, "Breast cancer detection with transillumination and mammography," Am. J. Roentgenol. **142**, 841–844 (1984).
12. J. J. Gisvold, L. R. Brown, R. G. Swee, D. J. Raygor, N. Dick-

erson, and M. K. Ranfranz, "Comparison of mammography and transillumination light scanning in the detection of breast lesions," Am. J. Roentgenol. **147**, 191–194 (1986).
13. A. Alveryd, I. Andersson, K. Aspegren, G. Balldin, N. Bjurstam, G. Edström, G. Fagerberg, U. Glas, O. Jarlman, S. A. Larsson, E. Lidbrink, H. Lingaas, M. Löfgren, C.-M. Rudenstam, L. Strender, L. Samuelsson, L. Tabàr, A. Taube, H. Wallberg, P. Åkesson, and D. Hallberg, "Lightscanning versus mammography for the detection of breast cancer in screening and clinical practice," Cancer **65**, 1671–1677 (1990).
14. T. J. Farrell, M. S. Patterson, and B. Wilson, "A diffusion theory model of spatially resolved, steady-state diffuse reflectance for the noninvasive determination of tissue optical properties in vivo," Med. Phys. **19**, 879–888 (1992).
15. D. A. Boas, M. A. O'Leary, B. Chance, and A. G. Yodh, "Scattering of diffuse photon density waves by spherical inhomogeneities within turbid media: analytic solution and applications," Proc. Natl. Acad. Sci. USA **51**, 4887–4891 (1994).
16. S. Fantini, M. A. Franceschini, and E. Gratton, "Semi-infinite geometry boundary problem for light migration in highly scattering media: a frequency-domain study in the diffusion approximation," J. Opt. Soc. Am. B **11**, 2128–2138 (1994).
17. R. C. Haskell, L. O. Svaasand, T. T. Tsay, T. C. Feng, M. S. McAdams, and B. J. Tromberg, "Boundary conditions for the diffusion equation in radiative transfer," J. Opt. Soc. Am. A **11**, 2727–2741 (1994).
18. M. S. Patterson, S. Andersson-Engels, B. C. Wilson, and E. K. Osei, "Absorption spectroscopy in tissue-simulating materials: a theoretical and experimental study of photon paths," Appl. Opt. **34**, 22–30 (1995).
19. J. B. Fishkin, S. Fantini, M. J. vandeVen, and E. Gratton, "Gigahertz photon density waves in a turbid medium: theory and experiments," Phys. Rev. E **53**, 2307–2319 (1996).
20. M. R. Ostermeyer and S. L. Jacques, "Perturbation theory for diffuse light transport in complex biological tissues," J. Opt. Soc. Am. A **14**, 255–261 (1997).
21. K. Wells, J. C. Hebden, F. E. W. Schmidt, and D. T. Delpy, "The UCL multichannel time-resolved system for optical tomography," in *Optical Tomography and Spectroscopy of Tissue: Theory, Instrumentation, Model, and Human Studies II*, B. Chance and R. R. Alfano, eds., Proc. SPIE **2979**, 599–607 (1997).
22. V. Ntziachristos, X. H. Ma, and B. Chance, "Time-correlated single photon counting imager for simultaneous magnetic resonance and near-infrared mammography," Rev. Sci. Instrum. **69**, 4221–4223 (1998).
23. V. Ntziachristos, A. G. Yodh, M. Schnall, and B. Chance, "Concurrent MRI and diffuse optical tomography of breast after indocyanine green enhancement," Proc. Natl. Acad. Sci. USA **97**, 2767–2772 (2000).
24. D. Grosenick, H. Wabnitz, H. H. Rinneberg, K. T. Moesta, and P. M. Schlag, "Development of a time-domain optical mammography and first *in vivo* applications," Appl. Opt. **38**, 2927–2943 (1999).
25. R. Cubeddu, A. Pifferi, P. Taroni, A. Torricelli, and G. Valentini, "Noninvasive absorption and scattering spectroscopy of bulk diffusive media: an application to the optical characterization of human breast," Appl. Phys. Lett. **74**, 874–876 (1999).
26. S. Fantini, M. A. Franceschini, G. Gaida, E. Gratton, H. Jess, W. W. Mantulin, K. T. Moesta, P. M. Schlag, and M. Kaschke, "Frequency-domain optical mammography: edge-effect corrections," Med. Phys. **23**, 149–157 (1996).
27. S. Zhou, C. Xie, S. Nioka, H. Liu, Y. Zhang, and B. Chance, "Phase array instrumentation appropriate to high precision detection and localization of breast tumor," in *Optical Tomography and Spectroscopy of Tissue: Theory, Instrumentation,*

Model, and Human Studies II, B. Chance and R. R. Alfano, eds., Proc. SPIE **2979**, 98–106 (1997).

28. M. A. Franceschini, K. T. Moesta, S. Fantini, G. Gaida, E. Gratton, H. Jess, W. W. Mantulin, M. Seeber, P. M. Schlag, and M. Kaschke, "Frequency-domain techniques enhance optical mammography: initial clinical results," Proc. Natl. Acad. Sci. USA **94**, 6468–6473 (1997).

29. B. W. Pogue, M. Testorf, T. McBride, U. Osterberg, and K. Paulsen, "Instrumentation and design of a frequency-domain diffuse optical tomography imager for breast cancer detection," Opt. Exp. **1**, 391–403 (1997), http://www.opticsexpress.org/issue.cfm?issue_id20.

30. N. Shah, A. Cerussi, C. Eker, J. Espinoza, J. Butler, J. Fishkin, R. Hornung, and B. Tromberg, "Noninvasive functional optical spectroscopy of human breast tissue," Proc. Natl. Acad. Sci. USA **98**, 4420–4425 (2001).

31. Y. Yamashita and M. Kaneko, "Visible and infrared diaphanography for medical diagnosis," in *Medical Optical Tomography: Functional Imaging and Monitoring*, J. Beuthan, O. Minet, G. J. Mueller, and V. Praparat, eds., Vol. IS11 of the SPIE Institute Series (SPIE, Bellingham, Wash., 1993), pp. 283–316.

32. J. H. Hoogenrad, M. B. van der Mark, S. B. Colak, G. W.'t Hooft, and E. S. van der Linden, "First results from the Philips optical mammoscope," in *Photon Propagation in Tissues III*, D. Benaron, B. Chance, and M. Ferrari, eds., Proc. SPIE **3194**, 184–190 (1998).

33. R. L. Barbour, H. L. Graber, C. H. Schmitz, Y. Pei, A. Zhong, S. S. Barbour, S. Blattman, and T. Panetta, "Spatio-temporal imaging of vascular reactivity by optical tomography," *Proceedings of the Inter-Institute Workshop on In Vivo Optical Imaging at the NIH, 1999*, A. H. Gandjbakhche, ed. (Optical Society of America, Washington, D.C., 2000), pp. 161–166.

34. P. Vaupel, F. Kallinowski, and P. Okunieff, "Blood flow, oxygen and nutrient supply, and metabolic microenvironment of human tumors: a review," Cancer Res. **49**, 6449–6465 (1989).

35. P. Vaupel, K. Schlenger, C. Knoop, and M. Hockel, "Oxygenation of human tumors: evaluation of tissue oxygen distribution in breast cancer by computerized O_2 tension measurements," Cancer Res. **51**, 3316–3322 (1991).

36. P. Hohenberger, C. Flegner, W. Haensch, and P. M. Schlag, "Tumor oxygenation correlates with molecular growth determinants in breast cancer," Breast Cancer Res. Treat. **48**, 97–106 (1998).

37. P. Vaupel, D. K. Kelleher, and M. Hockel, "Oxygen status of malignant tumors: pathogenesis of hypoxia and significance for tumor therapy," Semin. Oncol. **28**, 29–35 (2001).

38. M. Hockel and P. Vaupel, "Biological consequences of tumor hypoxia," Semin. Oncol. **28**, 36–41 (2001).

39. Q. Zhu, E. Conant, and B. Chance, "Optical imaging as an adjunct to sonograph in differentiating benign from malignant breast lesions," J. Biomed. Opt. **5**, 229–236 (2000).

40. M. J. Holboke, B. J. Tromberg, X. Li, N. Shah, J. Fishkin, D. Kidney, J. Butler, B. Chance, and A. G. Yodh, "Three dimensional diffuse optical mammography with ultrasound localization in a human subject," J. Biomed. Opt. **5**, 237–247 (2000).

41. B. J. Tromberg, O. Coquez, J. B. Fishkin, T. Pham, E. R. Anderson, J. Butler, M. Cahn, J. D. Gross, V. Venugopalan, and D. Pham, "Non-invasive measurements of breast tissue optical properties using frequency-domain photon migration," Philos. Trans. R. Soc. London Ser. B **352**, 661–668 (1997).

42. B. J. Tromberg, N. Shah, R. Lanning, A. Cerussi, J. Espinoza, T. Pham, L. Svaasand, and J. Butler, "Non-invasive *in vivo* characterization of breast tumors using photon migration spectroscopy," Neoplasia **2**, 26–40 (2000).

43. T. O. McBride, B. W. Pogue, E. D. Gerety, S. B. Poplack, U. L. Osterberg, and K. D. Paulsen, "Spectroscopic diffuse optical tomography for quantitatively assessing hemoglobin concentration and oxygen saturation in breast tissue," Appl. Opt. **38**, 1–11 (1999).

44. S. Fantini, S. A. Walker, M. A. Franceschini, M. Kaschke, P. M. Schlag, and K. T. Moesta, "Assessment of the size, position, and optical properties of breast tumors *in vivo* by noninvasive optical methods," Appl. Opt. **37**, 1982–1989 (1998).

45. D. A. Boas, M. A. O'Leary, B. Chance, and A. G. Yodh, "Detection and characterization of optical inhomogeneities with diffuse photon density waves: a signal-to-noise analysis," Appl. Opt. **36**, 75–92 (1997).

46. V. Chernomordik, D. Hattery, A. Gandjbakhche, A. Pifferi, P. Taroni, A. Torricelli, G. Valentini, and R. Cubeddu, "Quantification by random walk of the optical parameters of nonlocalized abnormalities embedded within tissuelike phantoms," Opt. Lett. **25**, 951–953 (2000).

47. S. Fantini, M. A. Franceschini-Fantini, J. S. Maier, and S. A. Walker, "Frequency-domain multichannel optical detector for noninvasive tissue spectroscopy and oximetry," Opt. Eng. **34**, 32–42 (1995).

48. E. M. Sevick, B. Chance, J. Leigh, S. Nioka, and M. Maris, "Quantitation of time-space and frequency-resolved optical spectra for the determination of tissue oxygenation," Anal. Biochem. **195**, 330–351 (1991).

49. H. Heusmann, J. Kölzer, and G. Mitic, "Characterization of female breasts *in vivo* by time resolved and spectroscopic measurements in near infrared spectroscopy," J. Biomed. Opt. **1**, 425–434 (1996).

50. H. Heusmann, J. Kölzer, R. Puls, J. Otto, S. Heywang-Köbrunner, and W. Zinth, "Spectral transillumination of human breast tissue," in *Optical Tomography, Photon Migration, and Spectroscopy of Tissue and Model Media: Theory, Human Studies, and Instrumentation*, B. Chance and R. R. Alfano, eds., Proc. SPIE **2389**, 788–808 (1995).

51. J. Kölzer, G. Mitic, J. Otto, and W. Zinth, "Measurements of the optical properties of breast tissue using time-resolved transillumination," in *Photon Transport in Highly Scattering Tissue*, S. Arrillier, B. Chance, G. J. Mueller, A. V. Priezzhev, and V. V. Tuchin, eds., Proc. SPIE **2326**, 143–152 (1995).

52. D. A. Boas, R. Gaudette, and T. Gaudette, PMI software, http://www.nmr.mgh.harvard.edu/DOT/resources/toolbox.htm.

53. V. Quaresima, S. J. Matcher, and M. Ferrari, "Identification and quantification of intrinsic optical contrast for near-infrared mammography," Photochem. Photobiol. **67**, 4–14 (1998).

54. F. Bevilacqua, A. J. Berger, A. E. Cerussi, D. Jakubowski, and B. J. Tromberg, "Broadband absorption spectroscopy in turbid media by combined frequency-domain and steady-state methods," Appl. Opt. **39**, 6498–6507 (2000).

55. S. Fantini, M. A. Franceschini, G. Gaida, H. Jess, H. Erdl, W. W. Mantulin, E. Gratton, K. T. Moesta, P. M. Schlag, and M. Kaschke, "Contrast-enhancement by edge effect corrections in frequency-domain optical mammography," in *Advances in Optical Imaging and Photon Migration*, R. R. Alfano and J. G. Fujimoto, eds., Vol. 2 of 1996 OSA Trends in Optics and Photonics Series (Optical Society of America, Washington, D.C., 1996), pp. 160–163.

56. Q. Zhang, T. J. Brukilacchio, J. Stott, A. Li, and D. A. Boas, "Spectroscopic difference tomography for breast lesion detection," Opt. Lett. (submitted for publication).

NOTE

A haemodynamic model for the physiological interpretation of *in vivo* measurements of the concentration and oxygen saturation of haemoglobin

Sergio Fantini

Bioengineering Center, Department of Electrical Engineering and Computer Science,
Tufts University, 4 Colby Street, Medford, MA 02155, USA

Abstract

We present a model that describes the effect of physiological parameters such as the speed of blood flow, local oxygen consumption, capillary recruitment, and vascular dilation/constriction on the concentration and oxygen saturation of haemoglobin in tissue. This model can be used to guide the physiological interpretation of haemodynamic and oximetric data collected *in vivo* with techniques such as optical imaging, near-infrared spectroscopy and functional magnetic resonance imaging. In addition to providing a formal description of well-established results (exercise-induced hyperemia, reperfusion hyperoxia, decrease in the concentration of deoxyhaemoglobin induced by brain activity, measurement of arterial saturation by pulse oximetry, etc.), this model suggests that the superposition of asynchronous contributions from the arterial, capillary and venous haemoglobin compartments may be at the origin of observed out-of-phase oscillations of the oxyhaemoglobin and deoxyhaemoglobin concentrations in tissue.

1. Introduction

Several medical imaging, diagnostic and research tools are sensitive to the haemoglobin, in its oxygenated and/or deoxygenated forms, that is present in the blood. For example, near-infrared spectroscopy (NIRS) measures the optical absorption associated with oxyhaemoglobin and deoxyhaemoglobin, and BOLD (blood oxygen level-dependent) functional magnetic resonance imaging (fMRI) is based on magnetic susceptibility changes induced by paramagnetic deoxyhaemoglobin. NIRS measurements of the concentration and oxygen saturation of haemoglobin in tissue, the fMRI BOLD signal and any measurement of blood oxygenation *in vivo* are the result of the interplay among a number of physiological parameters such as blood volume, blood flow and metabolic rate of oxygen. Several models have been developed for the coupling between cerebral blood flow and oxygen metabolism (Buxton and Frank 1997, Hyder *et al* 1998), for the relationship between the BOLD signal
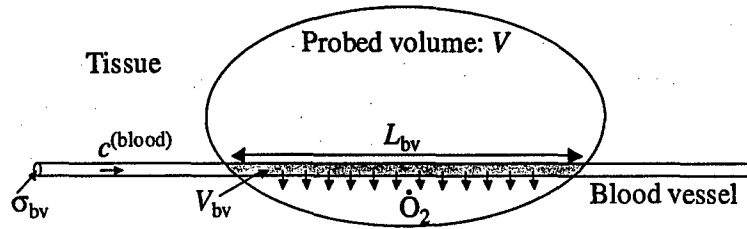
Figure 1. Schematic representation of our model. A blood vessel of cross section σ_{bv} intersects for a length L_{bv} the volume V probed by the measurement technique of interest. The average blood speed within the vessel is indicated with $c^{(blood)}$, while $\dot{O}_2$ represents the rate of oxygen diffusion from the blood vessel to the tissue within volume V.

and the cerebral blood volume, blood flow and oxygen consumption (Ogawa *et al* 1993, Mandeville *et al* 1999, Hoge *et al* 1999), and for the dynamic bioenergetic relationship between the deoxyhaemoglobin concentration measured by NIRS and muscle oxygen consumption (Binzoni *et al* 1999). It has been shown that the interpretation of optical data can be guided by the same haemodynamic modelling principles used for the fMRI BOLD signal (Mayhew *et al* 2001). In this note, we present a general haemodynamic model that relates the concentration and oxygen saturation of haemoglobin in tissue to a number of physiological parameters such as the speed of blood flow, the local oxygen consumption, capillary recruitment and vascular dilation/constriction. This model specifies the conditions that determine a higher or lower sensitivity of the concentration and saturation of haemoglobin in tissue to these physiological parameters. The analytical relationships derived here can be used to guide the physiological interpretation of haemoglobin-related measurements in living tissue.

2. The model

The schematic representation of the problem is illustrated in figure 1. A blood vessel of cross section σ_{bv}, in which blood flows with an average speed $c^{(blood)}$, intersects for a length L_{bv} the volume V of interest. For instance, V may be a voxel in fMRI or optical imaging, or the tissue region probed by NIRS, i.e. the volume that contains most of the photon migration paths from the illumination point to the collection optical fibre. As the blood flows within volume V, the concentration of oxygen in the blood $\left([O_2]^{(blood)}\right)$ may decrease as a result of oxygen diffusion to tissue cells, where the decrease rate is proportional to the difference between the oxygen concentrations in the plasma $\left([O_2]^{(plasma)}\right)$ and in the tissue $\left([O_2]^{(tissue)}\right)$. This diffusion process may be described by assigning to each oxygen molecule a probability of extraction per unit time (k), which depends on the permeability and surface area of the blood vessel wall (Buxton and Frank 1997). By using the speed of blood flow $c^{(blood)}$, the probability of oxygen extraction per unit length along the blood vessel can be written as $k/c^{(blood)}$. As a result, if l is the line coordinate along the blood vessel, one can write

$$\frac{d[O_2]^{(blood)}}{dl} = -\frac{k}{c^{(blood)}}\left([O_2]^{(plasma)} - [O_2]^{(tissue)}\right) = -\frac{kr}{c^{(blood)}}[O_2]^{(blood)} \quad (1)$$

where $r = \left([O_2]^{(plasma)} - [O_2]^{(tissue)}\right)/[O_2]^{(blood)}$. By defining $\alpha_{\dot{O}_2} = kr$, and assuming that $\alpha_{\dot{O}_2}$ and $c^{(blood)}$ are independent of l

$$[O_2]^{(blood)}(l) = [O_2]_0^{(blood)}e^{-\frac{\alpha_{\dot{O}_2}}{c^{(blood)}}l} \quad (2)$$

where the subscript 0 in $[O_2]_0^{\text{(blood)}}$ indicates the oxygen concentration in the blood at $l = 0$, i.e. before any oxygen extraction occurs within volume V. From equation (2), the total rate of oxygen extraction $(\dot{O}_2)$ over the length L_{bv} of the blood vessel is given by $\dot{O}_2 = [O_2]_0^{\text{(blood)}}\left[1 - \exp\left(-\alpha_{\dot{O}_2}L_{bv}/c^{\text{(blood)}}\right)\right]c^{\text{(blood)}}\sigma_{bv}$ which shows the dependence of the oxygen extraction rate on $\alpha_{\dot{O}_2}$ and $c^{\text{(blood)}}$. The average value of $[O_2]^{\text{(blood)}}$ within volume V can be easily calculated as follows:

$$\left\langle [O_2]^{\text{(blood)}}\right\rangle_V = \frac{1}{L_{bv}}\int_0^{L_{bv}} [O_2]^{\text{(blood)}}(l)\,\mathrm{d}l = [O_2]_0^{\text{(blood)}}\left(1 - e^{-\frac{\alpha_{\dot{O}_2}L_{bv}}{c^{\text{(blood)}}}}\right)\frac{c^{\text{(blood)}}}{\alpha_{\dot{O}_2}L_{bv}}. \tag{3}$$

The derivation of equation (2) is based on the assumption that $\alpha_{\dot{O}_2}$ is not a function of l. If $[O_2]^{\text{(plasma)}} \gg [O_2]^{\text{(tissue)}}$, which is an approximation that has been used for brain tissue (Buxton and Frank 1997, Hyder *et al* 1998) the spatial uniformity of $\alpha_{\dot{O}_2}$ implies that the ratio $[O_2]^{\text{(plasma)}}/[O_2]^{\text{(blood)}}$ is not a function of the blood oxygenation. Because of the nonlinear oxygen equilibrium curve of haemoglobin, this assumption is not strictly correct, but Buxton and Frank found that the nonlinear correction to equation (2) is not significant (Buxton and Frank 1997). However, Hyder *et al*, who also used $r \approx [O_2]^{\text{(plasma)}}/[O_2]^{\text{(blood)}}$, allowed for a variable diffusivity $\alpha_{\dot{O}_2}$ in their model for the regulation of cerebral oxygen delivery (Hyder *et al* 1998). Mayhew *et al* proposed that $[O_2]^{\text{(tissue)}}$ should not be neglected in r (Mayhew *et al* 2001), so that an increased cellular utilization rate of oxygen can directly increase the probability of oxygen extraction $\alpha_{\dot{O}_2}$ by decreasing $[O_2]^{\text{(tissue)}}$ and thereby increasing the $[O_2]$ gradient across the blood vessel wall. Here, we proceed on the assumption that $\alpha_{\dot{O}_2}$ is uniform over the length L_{bv} of the blood vessel, but we allow for temporal changes of $\alpha_{\dot{O}_2}$ associated with changes in $[O_2]^{\text{(tissue)}}$ that reflect changes in the cellular metabolic rate of oxygen. The concentration of oxygen in the blood $[O_2]^{\text{(blood)}}$ results from two contributions; from dissolved oxygen in the plasma $\left([O_2]^{\text{(plasma)}}\right)$ and from oxygen bound to haemoglobin $([O_2]^{\text{(haemoglobin)}})$. Because $[O_2]^{\text{(plasma)}}$ normally accounts for only 1–3% of $[O_2]^{\text{(blood)}}$ (Guyton and Hall 2000), we will consider $[O_2]^{\text{(blood)}} \approx [O_2]^{\text{(haemoglobin)}}$, so that the concentration of oxyhaemoglobin in the blood $[HbO_2]^{\text{(blood)}} \approx \frac{1}{4}[O_2]^{\text{(blood)}}$ (where the factor 1/4 accounts for the four binding sites for oxygen at each haemoglobin molecule). The concentration of oxyhaemoglobin in the tissue volume $V([HbO_2]^{\text{(tissue)}})$ can be written as the average concentration of oxyhaemoglobin in the blood times the blood-volume fraction V_{bv}/V. Using equation (2) and the approximate proportionality between $[HbO_2]^{\text{(blood)}}$ and $[O_2]^{\text{(blood)}}$, $[HbO_2]^{\text{(tissue)}}$ can be expressed as follows:

$$\begin{aligned}
[HbO_2]^{\text{(tissue)}} &= \left\langle [HbO_2]^{\text{(blood)}}\right\rangle_V \frac{V_{bv}}{V} \\
&= [HbO_2]_0^{\text{(blood)}}\left(1 - e^{-\frac{\alpha_{\dot{O}_2}L_{bv}}{c^{\text{(blood)}}}}\right)\frac{c^{\text{(blood)}}}{\alpha_{\dot{O}_2}L_{bv}}\frac{V_{bv}}{V} \\
&= \left. SO_2\right|_0^{\text{(blood)}}[HbT]^{\text{(blood)}}\left(1 - e^{-\frac{\alpha_{\dot{O}_2}L_{bv}}{c^{\text{(blood)}}}}\right)\frac{c^{\text{(blood)}}\sigma_{bv}}{\alpha_{\dot{O}_2}V}
\end{aligned} \tag{4}$$

where the subscript 0 indicates the initial value at $l = 0$, before any oxygen extraction occurs in volume V, $[HbT]^{\text{(blood)}} = [HbO_2]_0^{\text{(blood)}} + [Hb]_0^{\text{(blood)}}$ is the total haemoglobin concentration in the blood (we drop the subscript 0 in $[HbT]^{\text{(blood)}}$ because the total concentration of haemoglobin is not a function of l), and $\left.SO_2\right|_0^{\text{(blood)}} = \frac{[HbO_2]_0^{\text{(blood)}}}{[HbT]^{\text{(blood)}}}$ is the oxygen saturation of haemoglobin at $l = 0$. From equation (4) it is straightforward to derive the following expressions for the concentrations of deoxyhaemoglobin and total haemoglobin in tissue

($[Hb]^{(tissue)}$ and $[HbT]^{(tissue)} = [HbO_2]^{(tissue)} + [Hb]^{(tissue)}$, respectively), and for the tissue saturation ($StO_2 = [HbO_2]^{(tissue)}/[HbT]^{(tissue)}$):

$$[Hb]^{(tissue)} = [HbT]^{(tissue)} - [HbO_2]^{(tissue)}$$

$$= [HbT]^{(blood)} \frac{V_{bv}}{V} \left[1 - SO_2\big|_0^{(blood)} \left(1 - e^{-\frac{\alpha_{O_2} L_{bv}}{c^{(blood)}}} \right) \frac{c^{(blood)}}{\alpha_{O_2} L_{bv}} \right] \tag{5}$$

$$[HbT]^{(tissue)} = [HbT]^{(blood)} \frac{V_{bv}}{V} \tag{6}$$

$$StO_2 = SO_2\big|_0^{(blood)} \left(1 - e^{-\frac{\alpha_{O_2} L_{bv}}{c^{(blood)}}} \right) \frac{c^{(blood)}}{\alpha_{O_2} L_{bv}}. \tag{7}$$

Equations (4)–(7) provide analytical relationships that relate the concentration and oxygen saturation of haemoglobin in the tissue to physiological parameters such as the local rate of oxygen extraction, the blood oxygenation and the speed of blood flow.

During a measurement, depending on the particular protocol and the individual physiological response, there may be variations in $SO_2\big|_0^{(blood)}$, $[HbT]^{(blood)}$, σ_{bv}, α_{O_2} or $c^{(blood)}$. We assume that L_{bv} and V remain constant and we also continue to consider the case of a single blood vessel. The assumption of constant L_{bv} and V is based on the fact that changes in V and L_{bv} (caused for instance by changes in the tissue optical properties in the case of NIRS) are likely to induce smaller effects in the measurements of concentration and saturation of haemoglobin with respect to the effects of the other mentioned parameters. The changes in $[HbO_2]^{(tissue)}$, $[Hb]^{(tissue)}$, $[HbT]^{(tissue)}$ and StO_2 can be expressed as follows by differentiation:

$$\Delta[HbO_2]^{(tissue)} = SO_2\big|_0^{(blood)} [HbT]^{(blood)} \frac{c^{(blood)}\sigma_{bv}}{\alpha_{O_2} V} \left(1 - e^{-\frac{\alpha_{O_2} L_{bv}}{c^{(blood)}}} \right) \left(\frac{\Delta SO_2\big|_0^{(blood)}}{SO_2\big|_0^{(blood)}} \right.$$

$$\left. + \frac{\Delta[HbT]^{(blood)}}{[HbT]^{(blood)}} + \frac{\Delta\sigma_{bv}}{\sigma_{bv}} \right) + SO_2\big|_0^{(blood)} [HbT]^{(blood)} \frac{c^{(blood)}\sigma_{bv}}{\alpha_{O_2} V}$$

$$\times \left[1 - e^{-\frac{\alpha_{O_2} L_{bv}}{c^{(blood)}}} \left(\frac{\alpha_{O_2} L_{bv}}{c^{(blood)}} + 1 \right) \right] \left(-\frac{\Delta\alpha_{O_2}}{\alpha_{O_2}} + \frac{\Delta c^{(blood)}}{c^{(blood)}} \right) \tag{8}$$

$$\Delta[Hb]^{(tissue)} = [HbT]^{(blood)} \frac{V_{bv}}{V} \left[1 - SO_2\big|_0^{(blood)} \frac{c^{(blood)}}{\alpha_{O_2} L_{bv}} \left(1 - e^{-\frac{\alpha_{O_2} L_{bv}}{c^{(blood)}}} \right) \right]$$

$$\times \left(\frac{\Delta[HbT]^{(blood)}}{[HbT]^{(blood)}} + \frac{\Delta\sigma_{bv}}{\sigma_{bv}} \right) + SO_2\big|_0^{(blood)} [HbT]^{(blood)} \frac{c^{(blood)}\sigma_{bv}}{\alpha_{O_2} V}$$

$$\times \left(1 - e^{-\frac{\alpha_{O_2} L_{bv}}{c^{(blood)}}} \right) \left(-\frac{\Delta SO_2\big|_0^{(blood)}}{SO_2\big|_0^{(blood)}} \right) + SO_2\big|_0^{(blood)} [HbT]^{(blood)} \frac{c^{(blood)}\sigma_{bv}}{\alpha_{O_2} V}$$

$$\times \left[1 - e^{-\frac{\alpha_{O_2} L_{bv}}{c^{(blood)}}} \left(\frac{\alpha_{O_2} L_{bv}}{c^{(blood)}} + 1 \right) \right] \left(\frac{\Delta\alpha_{O_2}}{\alpha_{O_2}} - \frac{\Delta c^{(blood)}}{c^{(blood)}} \right) \tag{9}$$

$$\Delta[HbT]^{(tissue)} = [HbT]^{(blood)} \frac{V_{bv}}{V} \left(\frac{\Delta[HbT]^{(blood)}}{[HbT]^{(blood)}} + \frac{\Delta\sigma_{bv}}{\sigma_{bv}} \right) \tag{10}$$

$$\Delta StO_2 = SO_2\big|_0^{(blood)} \frac{c^{(blood)}}{\alpha_{\dot{O}_2} L_{bv}} \left(1 - e^{-\frac{\alpha_{\dot{O}_2} L_{bv}}{c^{(blood)}}}\right) \frac{\Delta SO_2\big|_0^{(blood)}}{SO_2\big|_0^{(blood)}}$$

$$+ SO_2\big|_0^{(blood)} \frac{c^{(blood)}}{\alpha_{\dot{O}_2} L_{bv}} \left[1 - e^{-\frac{\alpha_{\dot{O}_2} L_{bv}}{c^{(blood)}}} \left(\frac{\alpha_{\dot{O}_2} L_{bv}}{c^{(blood)}} + 1\right)\right] \left(-\frac{\Delta\alpha_{\dot{O}_2}}{\alpha_{\dot{O}_2}} + \frac{\Delta c^{(blood)}}{c^{(blood)}}\right).$$

$$(11)$$

Because the factors that multiply the parentheses containing the relative changes $\Delta x/x$ are all positive (where x stands for any physiological parameter), the sign in front of any relative change $\Delta x/x$ indicates the direction of the change (plus: increase; minus: decrease) in $[HbO_2]^{(tissue)}$, $[Hb]^{(tissue)}$, $[HbT]^{(tissue)}$ or StO_2 associated with an increase in the physiological parameter x.

The case of multiple blood vessels within the probed volume V requires a summation of the corresponding single-blood-vessel terms on the right hand side of equations (4) and (5) to obtain $[HbO_2]^{(tissue)MV}$ and $[Hb]^{(tissue)MV}$ (the superscript MV indicates the multi-vessel case). $[HbT]^{(tissue)MV}$ and StO_2^{MV} are then computed from $[HbO_2]^{(tissue)MV}$ and $[Hb]^{(tissue)MV}$. The more general case where the blood vessels within volume V include arteries, capillaries and veins can be examined by generalizing equations (4)–(7) as follows:

$$[HbO_2]^{(tissue)MV} = \left[SO_2\big|^{(a-blood)} V_{bv}^{(a)} + SO_2\big|_0^{(c-blood)} \left(1 - e^{-\frac{\alpha_{\dot{O}_2} L_{bv}^{(c)}}{c^{(c-blood)}}}\right) \frac{c^{(c-blood)} \sigma_{bv}^{(c)}}{\alpha_{\dot{O}_2}} \right.$$

$$\left. + SO_2\big|^{(v-blood)} V_{bv}^{(v)}\right] \frac{[HbT]^{(blood)}}{V} \tag{12}$$

$$[Hb]^{(tissue)MV} = \left\{\left(1 - SO_2\big|^{(a-blood)}\right) V_{bv}^{(a)} + \left[1 - SO_2\big|_0^{(c-blood)} \left(1 - e^{-\frac{\alpha_{\dot{O}_2} L_{bv}^{(c)}}{c^{(c-blood)}}}\right) \frac{c^{(c-blood)}}{\alpha_{\dot{O}_2} L_{bv}^{(c)}}\right]\right.$$

$$\left. \times V_{bv}^{(c)} + \left(1 - SO_2\big|^{(v-blood)}\right) V_{bv}^{(v)}\right\} \frac{[HbT]^{(blood)}}{V} \tag{13}$$

$$[HbT]^{(tissue)MV} = \left(V_{bv}^{(a)} + V_{bv}^{(c)} + V_{bv}^{(v)}\right) \frac{[HbT]^{(blood)}}{V} \tag{14}$$

$$StO_2^{MV} = \frac{SO_2\big|^{(a-blood)} V_{bv}^{(a)} + SO_2\big|_0^{(c-blood)} \left(1 - e^{-\frac{\alpha_{\dot{O}_2} L_{bv}^{(c)}}{c^{(c-blood)}}}\right) \frac{c^{(c-blood)} \sigma_{bv}^{(c)}}{\alpha_{\dot{O}_2}} + SO_2\big|^{(v-blood)} V_{bv}^{(v)}}{V_{bv}^{(a)} + V_{bv}^{(c)} + V_{bv}^{(v)}}$$

$$(15)$$

where the superscripts (a), (c), and (v) indicate the arterial, capillary and venous haemoglobin compartments, respectively, and we have considered that the oxygen extraction occurs only in the capillaries (i.e. $\alpha_{\dot{O}_2} = 0$ for arteries and veins) so that we have dropped the subscript 0 in $SO_2\big|^{(a-blood)}$ and $SO_2\big|^{(v-blood)}$, and we have set $[HbT]^{(blood)}$ to be the same for all blood vessels for simplicity. The fact that the small-vessel haematocrit is typically lower than the large-vessel haematocrit can be accommodated in the model by using different values for $[HbT]^{(a-blood)}$, $[HbT]^{(c-blood)}$ and $[HbT]^{(v-blood)}$ rather than factorize a common value for $[HbT]^{(blood)}$ as done in equations (12)–(14). However, the regional difference between the haematocrit in small and large vessels is hard to estimate *in vivo*. Data in the literature indicate that the small-vessel to large-vessel haematocrit is on the order of 0.8–0.9 (Grubb *et al* 1974).

3. Discussion

.The relationships derived here provide indications on the relative contributions of $SO_2|_0^{(blood)}$, $[HbT]^{(blood)}$, σ_{bv}, $\alpha_{\dot{O}_2}$ and $c^{(blood)}$ to the average concentration and saturation of haemoglobin in tissue, and on the conditions that affect such contributions. The quantitative predictions of this model, however, should be used with caution and their applicability evaluated for each particular case. In fact, in addition to the assumptions already mentioned (uniform $c^{(blood)}$ and $\alpha_{\dot{O}_2}$ over the length of the blood vessel, time-independent V and L_{bv}) our model simplifies the treatment of the partial contributions within the volume V by assuming that all volume elements within V contribute equally to the measurement of the haemoglobin-related parameters (see equation (3)). This may not always be the case, for example, because of the non-uniform density of the photon migration paths within V in NIRS. In this case, a quantitative treatment of the problem would require the introduction of spatially dependent weight functions (Graber *et al* 1993) or a more rigorous treatment of photon transport in tissue (Arridge and Hebden 1997). Furthermore, the size of individual blood vessels also plays a role in determining their relative contribution to the optical measurements (Liu *et al* 1995). When the size of V is smaller, as may be the case for optical imaging and fMRI voxels, this problem is minimized but one has to consider that $SO_2|_0^{(c-blood)}$ for small portions of capillaries may depend on $\alpha_{\dot{O}_2}$ and $c^{(blood)}$, thus introducing an additional variable in the model. Nevertheless, our model provides simple analytical relationships of general applicability, at least for qualitative analyses, which would not be available with more complex, quantitative models.

Our model is applicable to the description of equilibrium states or changes induced by transitions from one equilibrium state to another. However, this model is not restricted to stationary conditions but it is also applicable to dynamical processes, provided that the variations associated with these processes occur on a time scale that is longer than the time needed to reach equilibrium. Examples of such processes are the pressure-induced volume oscillations of the arterial and venous compartments, which occur on a time scale of seconds, much longer than the essentially instantaneous pressure–volume equilibrium process determined by the incompressibility of blood. In the case of changes associated with the blood flow, with the cellular metabolic rate of oxygen, or with a vascular bolus of oxyhaemoglobin or deoxyhaemoglobin, the time needed to reach equilibrium is determined by the vascular transit time across volume V. This time depends on the size of V and on the speed of blood flow. An *in vivo* study on rhesus monkeys has found a cerebral vascular mean transit time in the range 2–6 s (Grubb *et al* 1974), which can be considered as an upper limit for the vascular transit time through the volume of interest V ($\sim mm^3$ to $\sim cm^3$) considered here. These equilibrium requirements should be considered when using this model for quantitative analyses. However, qualitative analyses of the relative contributions to $[HbO_2]^{(tissue)}$, $[Hb]^{(tissue)}$, $[HbT]^{(tissue)}$ and StO_2 from the physiological parameters considered here can be performed on a more general basis.

A number of results reported in the literature find a formal description in the model presented here. For example, equations (10) and (14) account for the observed increase in $[HbT]^{(tissue)}$ as a result of the dilation of blood vessels (i.e. positive $\Delta\sigma_{bv}$ in equation (10)) and capillary recruitment (i.e. increase in $V_{bv}^{(c)}$ in equation (14)) during muscle exercise (Quaresima *et al* 1995). Equation (11) describes how an increase in the speed of blood flow (positive $\Delta c^{(blood)}$) may exactly compensate a moderate increase in the oxygen consumption (positive $\Delta\alpha_{\dot{O}_2}$) (walking exercise (Quaresima *et al* 1995)), undercompensate a significant increase in oxygen consumption (running exercise (Quaresima *et al* 1995)) or overcompensate the local oxygen demand (reperfusion hyperoxia (Smith *et al* 1990, Hampson and Piantadosi 1988)). In fact, the term with $\Delta c^{(blood)}$ has a positive sign in equation (11) (so that an increase

in the blood speed cause an increase in StO_2), while the term with $\Delta\alpha_{O_2}$ has a negative sign (so that an increase in the oxygen consumption causes a decrease in StO_2). Furthermore, equation (11) indicates that the relative increase in $c^{(blood)}$ should match the relative increase in α_{O_2} to exactly compensate its effect on StO_2.

An important point of equation (10) is that a change in the speed of blood flow ($c^{(blood)}$), by itself, does not modify $[HbT]^{(tissue)}$, which is only affected by the partial volume of blood in the tissue (which is proportional to σ_{bv}) and by the total haemoglobin concentration in the blood (see also, equation (6)). By contrast, if $\alpha_{O_2} \neq 0$, the speed of blood flow does have an effect on the concentrations of oxyhaemoglobin and deoxyhaemoglobin in tissue (if $\alpha_{O_2} = 0$, the terms that multiply $\Delta c^{(blood)}/c^{(blood)}$ in equations (8) and (9) become zero). As can be seen in equations (8) and (9), the contributions from $\Delta\alpha_{O_2}$ to $\Delta[HbO_2]^{(tissue)}$ and $\Delta[Hb]^{(tissue)}$ have opposite signs with respect to the corresponding contributions from $\Delta c^{(blood)}$. An increase in $c^{(blood)}$ (i.e., a positive $\Delta c^{(blood)}$) induces an increase in $[HbO_2]^{(tissue)}$ and a decrease in $[Hb]^{(tissue)}$. This accounts for the fact that the increase in the cerebral $[HbO_2]^{(tissue)}$ and the decrease in $[Hb]^{(tissue)}$ observed during brain activation result from a greater increase in blood flow with respect to the increase in the oxygen consumption induced by neuronal activation (Fox and Raichle 1986, Villringer and Chance 1997). Studies on animal models have shown that cerebral blood flow increases are mostly determined by increased flow velocity rather than by capillary recruitment (Bereczki *et al* 1993), so that $c^{(blood)}$ is the relevant parameter to describe blood flow in this case.

Equations (8) and (9) only predict in-phase (same sign) or 180° out-of-phase (opposite signs) changes in $[HbO_2]^{(tissue)}$ and $[Hb]^{(tissue)}$. In particular, in-phase changes are associated with modifications to the total haemoglobin concentration in the blood ($\Delta[HbT]^{(blood)}$) or blood partial volume ($\sim\Delta\sigma_{bv}$), while 180° out-of-phase changes are associated with modifications to the initial blood oxygen saturation ($\Delta SO_2|_0^{(blood)}$), oxygen utilization rate ($\Delta\alpha_{O_2}$) or speed of blood flow ($\Delta c^{(blood)}$). While either in-phase (Wolf *et al* 1997) or 180° out-of-phase (Elwell *et al* 1994) oscillations in $[HbO_2]^{(tissue)}$ and $[Hb]^{(tissue)}$ are typically recorded, intermediate phase shifts have also been observed (Taga *et al* 2000). These intermediate phase shifts can result from the superposition of out-of-phase contributions from different blood vessels, for instance arteries, capillaries and veins, as considered in equations (12) and (13). For example, if the partial blood volumes associated with arteries and veins, $V_{bv}^{(a)}$ and $V_{bv}^{(v)}$, respectively, oscillate with an arbitrary phase difference, then $[HbO_2]^{(tissue)MV}$ and $[Hb]^{(tissue)MV}$ may also oscillate with an arbitrary phase difference because of the different relative contributions of $V_{bv}^{(a)}$ and $V_{bv}^{(v)}$ to $[HbO_2]^{(tissue)MV}$ and $[Hb]^{(tissue)MV}$ (see equations (12) and (13)). In fact, the arterial/venous partial volume contribution ratio is $SO_2|^{(a-blood)}/SO_2|^{(v-blood)}$ in equation (12), while it is $\left(1 - SO_2|^{(a-blood)}\right)\big/\left(1 - SO_2|^{(v-blood)}\right)$ in equation (13). Equations (12)–(14) also illustrate how the volume oscillations of the arterial and venous compartments can be used to measure the arterial saturation (pulse oximetry) (Mendelson 1992) and the venous saturation (spiroximetry) (Franceschini *et al* 2002), respectively. In fact, by assuming that $V_{bv}^{(a)}$ oscillates at the heartbeat frequency and that $V_{bv}^{(v)}$ oscillates at the respiratory frequency, equations (12) and (14) show that the ratio of the amplitudes of the $[HbO_2]^{(tissue)MV}$ and $[HbT]^{(tissue)MV}$ oscillations at the heart rate and respiratory frequency are equal to $SO_2|^{(a-blood)}$ (the arterial saturation or SaO$_2$) and $SO_2|^{(v-blood)}$ (the venous saturation or SvO$_2$), respectively.

4. Conclusion

We have presented a haemodynamic model that can be used to guide the physiological interpretation of oxyhaemoglobin and deoxyhaemoglobin concentration measurements in

living tissue with techniques such as optical imaging, NIRS and functional MRI. In particular, this model elucidates the role played by the partial blood volume, local oxygen consumption, speed of blood flow and vascular dilation/contraction, on the measurements of concentration and oxygen saturation of haemoglobin in tissue. Our model also indicates the possible sources of oscillatory components of the oxyhaemoglobin and deoxyhaemoglobin concentrations that are in-phase, 180° out-of-phase, or out-of-phase by an arbitrary angle.

Acknowledgments

References

Arridge S R and Hebden J C 1997 Optical imaging in medicine: II. Modelling and reconstruction *Phys. Med. Biol.* **42** 841–53

Bereczki D, Wei L, Otsuka T, Acuff V, Pettigrew K, Patlak C and Fenstermacher J 1993 Hypoxia increases velocity of blood flow through parenchymal microvascular systems in rat brain *J. Cereb. Blood. Flow Metab.* **13** 475–86

Binzoni T, Colier W, Hiltbrand E, Hoofd L and Cerretelli P 1999 Muscle oxygen consumption by NIRS: a theoretical model *J. Appl. Physiol.* **87** 683–8

Buxton R B and Frank L R 1997 A model for the coupling between cerebral blood flow and oxygen metabolism during neural stimulation *J. Cereb. Blood Flow Metab.* **17** 64–72

Elwell C E, Owen-Reece H, Cope M, Edwards A D, Wyatt J S, Reynolds E O R and Delpy D T 1994 Measurement of changes in cerebral hemodynamics during inspiration and expiration using near infrared spectroscopy *Adv. Exp. Med. Biol.* **388** 619–26

Fox P T and Raichle M E 1986 Focal physiological uncoupling of cerebral blood flow and oxidative metabolism during somatosensory stimulation in human subjects *Proc. Natl. Acad. Sci. USA* **83** 1140–4

Franceschini M A, Boas D A, Zourabian A, Diamond S G, Nadgir S, Lin D W, Moore J B and Fantini S 2002 Near-infrared spiroximetry: non-invasive measurement of venous saturation in piglets and human subjects *J. Appl. Physiol.* **92** 372–84

Graber H L, Chang J, Aronson R and Barbour R L 1993 A perturbation model for imaging in dense scattering media: derivation and evaluation of imaging operators *Medical Optical Tomography: Functional Imaging and Monitoring* vol IS11, ed G J Müller *et al* (Bellingham, WA: SPIE) pp 65–86

Grubb R L, Raichle M E, Eichling J O and Ter-Pogossian M M 1974 The effects of changes in $PaCO_2$ on cerebral blood volume, blood flow and vascular mean transit time *Stroke* **5** 630–9

Guyton A C and Hall J E 2000 *Textbook of Medical Physiology* 10th edn (Philadelphia, PA: Saunders) ch 40, p 469

Hampson N B and Piantadosi C A 1988 Near infrared monitoring of human skeletal muscle oxygenation during forearm ischemia *J. Appl. Physiol.* **64** 2449–57

Hoge R D, Atkinson J, Gill B, Crelier G R, Marrett S and Pike G B 1999 Investigation of BOLD signal dependence on cerebral blood flow and oxygen consumption: the deoxyhemoglobin dilution model *Magn. Reson. Med.* **42** 849–63

Hyder F, Shulman R G and Rothman D L 1998 A model for the regulation of cerebral oxygen delivery *J. Appl. Physiol.* **85** 554–64

Liu H, Chance B, Hielscher A H, Jacques S L and Tittel F K 1995 Influence of blood vessels on the measurement of hemoglobin oxygenation as determined by time-resolved reflectance spectroscopy *Med. Phys.* **22** 1209–17

Mandeville J B, Marota J J A, Ayata C, Moskowitz M A, Weisskoff R M and Rosen B 1999 MRI measurement of the temporal evolution of relative $CMRO_2$ during rat forepaw stimulation *Magn. Reson. Med.* **42** 944–51

Mayhew J, Johnston D, Martindale J, Jones M, Berwick J and Zheng Y 2001 Increased oxygen consumption following activation of brain: theoretical footnotes using spectroscopic data from barrel cortex *Neuroimage* **13** 975–87

Mendelson Y 1992 Pulse oximetry: theory and applications for noninvasive monitoring *Clin. Chem.* **38** 1601–7

Ogawa S, Lee R M and Barrere B 1993 The sensitivity of magnetic resonance image signals of a rat brain to changes in the cerebral venous blood oxygenation *Magn. Reson. Med.* **29** 205–10

Quaresima V, Pizzi A, De Blasi R A, Ferrari A, De Angelis M and Ferrari M 1995 Quadriceps oxygenation changes during walking and running on a treadmill *Proc. SPIE* **2387** 249–56

Smith D S, Levy W, Maris M and Chance B 1990 Reperfusion hyperoxia in brain after circulatory arrest in humans *Anesthesiology* **73** 12–9

Taga G, Konishi Y, Maki A, Tachibana T, Fujiwara M and Koizumi H 2000 Spontaneous oscillation of oxy- and deoxy-hemoglobin changes with a phase difference throughout the occipital cortex of newborn infants observed using non-invasive optical topography *Neurosci. Lett.* **282** 101–4

Villringer A and Chance B 1997 Non-invasive optical spectroscopy and imaging of human brain function *Trends Neurosci.* **20** 435–42

Wolf M, Duc G, Keel M and Niederer P 1997 Continuous noninvasive measurement of cerebral arterial and venous oxygen saturation at the bedside in mechanically ventilated neonates *Crit. Care Med.* **9** 1579–82

innovative techniques

Near-infrared spiroximetry: noninvasive measurements of venous saturation in piglets and human subjects

MARIA ANGELA FRANCESCHINI,[1,2] DAVID A. BOAS,[2] ANNA ZOURABIAN,[2]
SOLOMON G. DIAMOND,[2] SHALINI NADGIR,[1] DAVID W. LIN,[1]
JOHN B. MOORE,[2] AND SERGIO FANTINI[1]
[1]Bioengineering Center, Department of Electrical Engineering and Computer Science
Tufts University, Medford 02155-6013; and [2]NMR Center, Massachusetts General
Hospital, Harvard Medical School, Charlestown, Massachusetts 02129

Franceschini, Maria Angela, David A. Boas, Anna Zourabian, Solomon G. Diamond, Shalini Nadgir, David W. Lin, John B. Moore, and Sergio Fantini. Near-infrared spiroximetry: noninvasive measurements of venous saturation in piglets and human subjects. J Appl Physiol 92: 372–384, 2002.—We present a noninvasive method to measure the venous oxygen saturation (Sv_{O_2}) in tissues using near-infrared spectroscopy (NIRS). This method is based on the respiration-induced oscillations of the near-infrared absorption in tissues, and we call it spiroximetry (the prefix spiro means respiration). We have tested this method in three piglets (hind leg) and in eight human subjects (vastus medialis and vastus lateralis muscles). In the piglet study, we compared our NIRS measurements of the Sv_{O_2} (Sv_{O_2}-$NIRS_{resp}$) with the Sv_{O_2} of blood samples. Sv_{O_2}-$NIRS_{resp}$ and Sv_{O_2} of blood samples agreed well over the whole range of Sv_{O_2} considered (20–95%). The two measurements showed an average difference of 1.0% and a standard deviation of the difference of 5.8%. In the human study, we found a good agreement between Sv_{O_2}-$NIRS_{resp}$ and the Sv_{O_2} values measured with the NIRS venous occlusion method. Finally, in a preliminary test involving muscle exercise, Sv_{O_2}-$NIRS_{resp}$ showed an expected postexercise decrease from the initial baseline value and a subsequent recovery to baseline.

tissue spectroscopy; frequency-domain; pulse oximetry; hemoglobin saturation

THE POSSIBILITY OF USING LIGHT to measure the oxygen saturation of hemoglobin in vivo has been explored since the 1940s (37). The feasibility of optical blood oximetry stems from the oxygenation dependence of the optical spectrum of hemoglobin. This is illustrated in Fig. 1, which shows the absorption spectra of 100 μM hemoglobin for oxygen saturation values of 0, 20, 40, 60, 80, and 100%. The spectra of Fig. 1 were calculated from published values of the molar extinction coefficients of oxyhemoglobin (HbO_2) and deoxyhemoglobin (Hb) (43, 53).

Oxygen saturation of the pulmonary capillary blood in rabbits has been measured by using dynamic invasive techniques (48). Near-infrared light in the wavelength range from 700 to 900 nm results in a sufficient penetration depth for the noninvasive optical monitoring of skeletal muscle, cerebral gray matter, and breast tissue. As a result, near-infrared techniques allow a noninvasive assessment of hemoglobin saturation for a wide range of applications, such as the study of muscle metabolism (7, 9, 12, 29, 45), the diagnosis of vascular disorders (2, 20, 32, 33, 44, 49), functional brain imaging (3, 10, 24, 30, 35, 50), and breast cancer detection (23, 28, 40, 42, 46).

If near-infrared light is highly sensitive to the oxygen saturation of hemoglobin, then its large penetration depth inside tissues implies that the arterial, venous, and capillary compartments all contribute to the optical signal. The average hemoglobin oxygenation measured with near-infrared spectroscopy (NIRS) (19, 34, 41) is usually referred to as tissue oxygen saturation (St_{O_2}). St_{O_2} values are assumed to be in between arterial and local venous saturation values (Sa_{O_2} and Sv_{O_2}, respectively). A number of research studies have investigated the relationship between the near-infrared (noninvasive) measurement of St_{O_2} and the values of Sa_{O_2} and local Sv_{O_2} measured invasively from drawn blood samples (31, 51). The contribution of the arterial compartment to the noninvasive optical signal can be isolated because of its unique temporal dynamics associated with the systolic-diastolic blood pressure variation at the heartbeat frequency (1). The
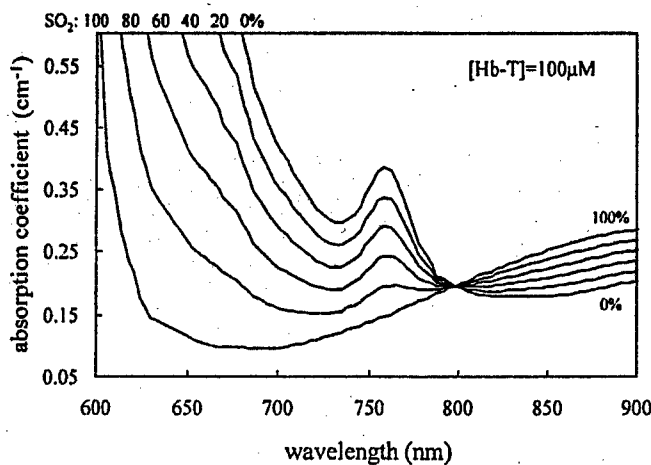

Fig. 1. Near-infrared absorption spectra of 100 μM hemoglobin concentration ([Hb-T], where T stands for total) for different values of the oxygen saturation (So$_2$) in the range of 0–100%. The curve for So$_2$ = 0% corresponds to the deoxyhemoglobin (Hb) absorption spectrum, whereas the curve for So$_2$ = 100% corresponds to the oxyhemoglobin (HbO$_2$) absorption spectrum. These spectra have been computed from published spectra of the molar extinction coefficients of HbO$_2$ and Hb (43, 53).

pulsatile component of the optical signals at two or more wavelengths at the heartbeat frequency is used by conventional (1, 36) or self-calibrated (21) pulse oximeters to measure the Sao$_2$. Sao$_2$ is a parameter that provides information about the ventilation and the oxygen exchange in the lungs. In contrast, Svo$_2$ is a parameter that reflects the local balance between blood flow and oxygen consumption. The noninvasive optical measurement of Svo$_2$ is complicated by the fact that the isolation of the contribution of the venous compartment to the noninvasive optical signal is not straightforward. There are no clinical devices presently capable of monitoring Svo$_2$ noninvasively.

A number of experimental approaches have been proposed to measure Svo$_2$ from induced local changes in the venous blood volume. For instance, proposed approaches involve a venous occlusion in a limb (13, 39, 55, 56), tilting the patient's head down by 15 degrees (47), a partial jugular vein occlusion (15, 54), or mechanical ventilation (52). In all these approaches, Svo$_2$ is optically measured as the ratio between the increases in the HbO$_2$ concentration ([HbO$_2$]) and the total hemoglobin concentration (equal to [HbO$_2$] + [Hb], where [Hb] is deoxyhemoglobin concentration) induced by the local increase in venous blood volume. To overcome the limitations of these methods, which can either be applied only to the limbs (venous occlusion method) or require an external perturbation (partial jugular vein occlusion, mechanical ventilation, and tilting methods), we propose an alternative approach that is an extension of the method of Wolf et al. (52). This approach involves no external perturbations and is applicable to subjects who are breathing either spontaneously or synchronously with a metronome set at their average respiratory frequency. Furthermore, this method can provide continuous and real-time monitoring of Svo$_2$. The basic idea is to measure Svo$_2$ from the amplitude of the optically measured [HbO$_2$] and [Hb] oscillations at the respiratory frequency. The basic hypothesis, originally formulated in this context and tested on the brain of mechanically ventilated infants by Wolf et al., is that the oscillatory components of [HbO$_2$] and [Hb] at the breathing rate are mostly representative of the venous compartment. Because the venous compliance is ~20 times as large as the arterial compliance (4), a given change in the blood pressure in the veins causes a venous volume change ~20 times as large as the arterial volume change corresponding to the same pressure change in the arteries. During normal breathing, the inspiration phase involves a decrease in the intrathoracic pressure and an increased pressure gradient between the peripheral venous system and the intrathoracic veins. This causes blood to be drawn from the extrathoracic veins into the intrathoracic vessels and heart (26). Because of the vein valves, venous return is increased more by inspiration than it is decreased by expiration (38). The net effect is the so-called respiratory pump that facilitates the venous return from the periphery by the respiration-induced periodic fluctuations in the central venous pressure (38). As a result of the respiratory pump, the peripheral venous blood volume oscillates at the respiratory frequency, decreasing during inspiration and increasing during expiration.

It is on this oscillatory component at the respiratory frequency that we base our near-infrared measurement of the Svo$_2$. We coin the term spiroximeter to indicate an instrument for measuring the Svo$_2$ from respiration-induced oscillations in the venous blood pressure and in the venous volume fraction in tissues. It must be observed that respiration may also induce perturbations to the heart rate (respiratory sinus arrhythmia) and consequently to the cardiac output and arterial blood pressure. As a result, the arterial compartment volume may, in general, also oscillate at the respiratory frequency; thus near-infrared spiroximetry data must be carefully examined to guarantee a reliable reading of Svo$_2$.

We report a validation study conducted on the hind leg of three piglets, in which we compared the near-infrared measurements of Svo$_2$ (Svo$_2$-NIRS) with the Svo$_2$ values obtained by the gas analysis of venous blood samples (Svo$_2$-blood). To show the applicability of spiroximetry to human subjects, we also conducted a preliminary test on the vastus medialis and vastus lateralis muscles of healthy volunteers at rest and postexercise.

MATERIALS AND METHODS

Tissue spectrometer. The near-infrared measurements were performed with a frequency-domain tissue spectrometer (model 96208, ISS, Champaign, IL) (18, 25). This instrument uses two parallel photomultiplier tube detectors that are time shared by eight multiplexed laser diodes emitting at 636, 675, 691, 752, 780, 788, 830, and 840 nm, respectively. The frequency of intensity modulation is 110 MHz, and heterodyne detection is performed with a cross-correlation frequency of 5 kHz. The multiplexing rate, i.e., the frequency

of sequential laser switching, is 100 Hz. As a result, 50 cross-correlation periods are acquired during the on time of each laser diode, and a complete acquisition cycle over the eight wavelengths is completed every 80 ms. The laser diodes and the photomultiplier tubes are all coupled to fiber optics. The eight individual illumination fibers, each 400 μm in internal diameter, are arranged into a fiber bundle having a rectangular cross-section of 3.5×2.0 mm^2. The collecting circular fiber bundles are 3.0 mm in internal diameter. The optical fibers are placed in contact with the skin by means of a flexible plastic probe. The optical probe arranges the tips of the illuminating and collecting fiber bundles along a line, with the two collecting fiber bundles at distances of 1.0 and 2.0 cm from the single illuminating bundle. In some cases, we have used a second tissue spectrometer to perform simultaneous measurements on both legs (*piglets 2* and *3*) or at different locations on the same leg (human subjects). In the second tissue spectrometer (which used the optical *probes PL* and *HVL* defined below), the 840-nm laser diode was replaced by a laser diode emitting at 814 nm.

Measurements on piglets. We performed measurements on three piglets that were 15 ± 1 days old and weighed 5 ± 1 kg. The experimental arrangement for the piglet measurements is schematically illustrated in Fig. 2. The piglets were anesthetized by inhalation of 3–4% isoflurane administered by means of a breathing mask applied to the piglet's snout. The animals were not mechanically ventilated, and they breathed freely throughout the experiment. A strain-gauge belt (Sleepmate/Newlife Technologies, Resp-EZ) was placed around the piglet's thorax to continuously monitor the respiratory excursion. A pulse oximeter (Nellcor, N-200) continuously recorded the heart rate at the foot of the right hind leg. The analog outputs from the strain gauge and the pulse oximeter were fed to the auxiliary input ports of the tissue spectrometer for continuous coregistration of optical and physiological data. A femoral cutdown was performed into the left inferior femoral vein to insert a catheter for periodic blood sampling. The femoral venous blood samples were run through a commercial blood-gas analyzer (Instrumentation Laboratory, model

1304 pH/blood-gas analyzer) to obtain invasive readings of Sv_{O_2}-blood. One optical probe (identified as *probe PR*) was always located on the right (noncatheterized) hind leg. In *piglets 2* and *3*, a second probe (*probe PL*) was placed on the catheterized (left) leg. The protocol consisted of varying the femoral Sv_{O_2} over the approximate range of 20–95% by modulating the volume fraction of oxygen inspired by the piglet ($F_{I_{O_2}}$) over the range of 10–100%. The oxygenation cycles performed on the three piglets are illustrated in Fig. 3. Each cycle consisted of varying the $F_{I_{O_2}}$ approximately every 4–6 min through the values of ~40, 15, 10, and 100% (*piglets 1* and *2*) or ~40, 20, 17.5, 15, 12.5, 10, and 100% (*piglet 3*). We performed two $F_{I_{O_2}}$ cycles on *piglet 1*, four on *piglet 2*, and three on *piglet 3*. For each specific value of $F_{I_{O_2}}$, we acquired about 3,000 optical data points [4 min $\times$ (60 s/min)/(80 ms/data point)] or more. During *cycles C* and *D* on *piglet 2*, the optical *probe PR* was slightly moved with respect to the location examined during *cycles A* and *B*, to collect data on two different muscle volumes during the two cycle pairs *A-B* and *C-D*. Optical *probe PR* always collected data on the right hind leg, whereas *probe PL* was placed on the left hind leg during *cycles A* and *B* of *piglet 2* and *cycles A* and *B* of *piglet 3* (we did not collect data with the optical *probe PL* on *piglet 1*, during *cycles C-D* on *piglet 2*, and during *cycle C* on *piglet 3*). In all three piglets, the invasive measurement of Sv_{O_2} from a femoral vein blood sample was performed at the end of each $F_{I_{O_2}}$ interval, as shown in Fig. 3. Motion artifacts were minimized in the optical data by securing the piglet's legs to the operating table. The protocol was approved by the Institutional Review Board of the Massachusetts General Hospital, where the piglet experiments were performed.

Measurements on human subjects. We performed measurements on eight healthy human subjects (6 men and 2 women; mean age of 24.5 yr, age range of 20–35 yr). The subjects sat on a comfortable chair and rested for 10–15 min before the experimental protocol was started. A pneumatic cuff was placed around the right thigh of the subject to later induce a venous occlusion by inflating the cuff to a pressure of 70 mmHg. A pulse oximeter probe (Nellcor, N-200) was placed
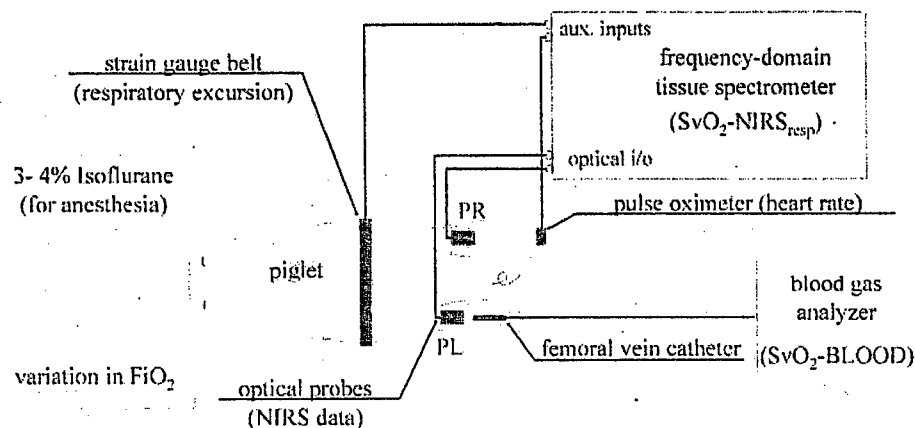

Fig. 2. Experimental arrangement for the piglet study. A breathing mask applied to the piglet's snout provided the 3–4% isoflurane anesthetic and was connected to the oxygen line for variations in the fraction of inspired oxygen ($F_{I_{O_2}}$). A strain-gauge belt and a pulse oximeter monitored the respiratory excursion and the heart rate, respectively, and their analog outputs were directed to the auxiliary inputs of the frequency-domain tissue spectrometer (ISS, Champaign, IL, model 96208). One or two optical probes (PR on the right hind leg and PL on the left hind leg) of the tissue spectrometer were used to measure the near-infrared tissue absorption with a time resolution of 80 ms. The absorption oscillations at the respiratory frequency were processed to provide measurement of the venous O_2 saturation (Sv_{O_2}-NIRS$_{resp}$) (NIRS is near-infrared spectroscopy). Invasive measurements of the venous O_2 saturation (designated Sv_{O_2}-blood) were obtained by gas analysis of venous blood samples collected by a femoral vein catheter. aux, Auxiliary; optical I/O, optical input/output.
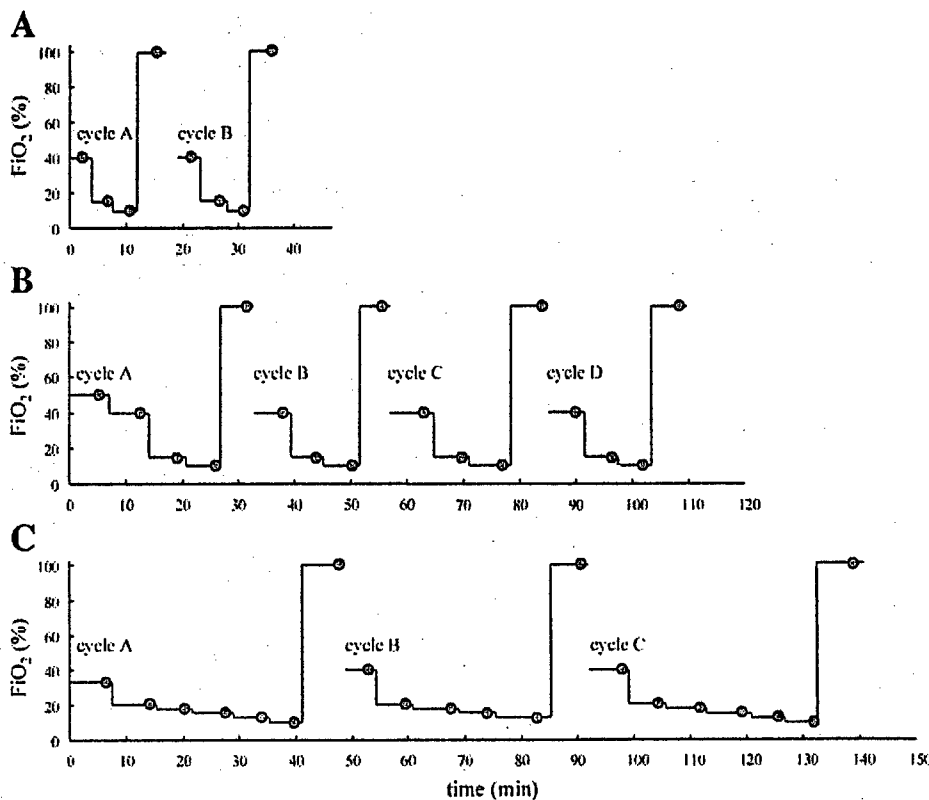
Fig. 3. Schematic representation of FI_{O_2} cycles for *piglet 1* (*A*), *piglet 2* (*B*), and *piglet 3* (*C*). ●, Time at which venous blood samples were run through the blood-gas analyzer for Sv_{O_2}-blood measurements.

on the index finger of the left hand. A strain-gauge belt (Sleepmate/Newlife Technologies, Resp-EZ) was placed around the subject's upper abdomen to monitor the respiratory excursion. As in the piglet experiment, we used the analog outputs of the pulse oximeter and strain gauge for continuous coregistration of the physiological and near-infrared data. Two optical probes were placed on the right thigh; the first probe (*probe HVM*) was positioned on top of a visible superficial vein of the vastus medialis muscle, and the second probe (*probe HVL*) was placed on the vastus lateralis muscle, far from visible superficial veins. During the measurements, we asked the subject to breathe regularly, following a metronome whose frequency was set to the average breathing rate of the subject at rest (typically 14–15 breaths/min). During the whole experiment, the subject was asked to breathe at the same frequency as the metronome pace. No subjects experienced any discomfort or difficulties with this procedure. The measurement protocol consisted of 2 min of baseline (we acquired 1,535 optical data points at 80 ms/point), followed by 40 s of venous occlusion, and a final recovery period of a few minutes. A few subjects performed an additional exercise routine to test the effect of exercise on the measured value of Sv_{O_2}-$NIRS_{resp}$ on the muscle. The exercise consisted of raising the right foot, voluntarily contracting the leg muscles (isometric contraction), until the subject felt tired. The human study was approved by the Institutional Review Board of Tufts University, where the human experiments were performed; all subjects gave their written, informed consent.

Near-infrared data processing for the measurement of Sv_{O_2}. We used a modified Beer-Lambert law approach (14) to translate the temporal intensity ratio collected at each wavelength [$I(\lambda, t)/I(\lambda, 0)$, where I is intensity, λ is wavelength, and t is time] at a distance of 1.0 cm from the illumination point, into a time variation in the tissue absorption [$\Delta\mu_a(\lambda, t)$,

where μ_a is the tissue absorption coefficient]. This approach was implemented by applying the following equation (14)

$$\Delta\mu_a(\lambda, t) = \frac{1}{L_{eff}} \ln\left[\frac{I(\lambda, 0)}{I(\lambda, t)}\right] \quad (1)$$

where L_{eff} is the effective optical pathlength from the illuminating point to the light collection point. We measured L_{eff} by quantifying μ_a and the reduced scattering coefficient (μ_s') using the frequency-domain multidistance method (17). The diffusion-theory relationship that gives L_{eff} in terms of μ_a, μ_s', and the source-detector separation (r) in a semi-infinite turbid medium (where the illumination and collection points are at the boundary of the turbid medium) is the following (17)

$$L_{eff} = \frac{3\mu_s' r^2}{2(r\sqrt{3\mu_a\mu_s'} + 1)} \quad (2)$$

More details on this hybrid frequency-domain [to measure $L_{eff}(\lambda)$] and continuous wave (modified Beer-Lambert law) approach are given in Refs. 14, 17, 21, and 22. *Equation 2* shows that for typical values of the near-infrared μ_a and μ_s', say $\mu_a = 0.1$ cm^{-1} and $\mu_s' = 10$ cm^{-1}, the value of L_{eff} is ~5.5 cm for $r = 1$ cm. The multi-distance scheme was implemented by considering the data collected by the two fiber bundles located at two different distances (1.0 and 2.0 cm) from the source fiber bundle. At these source detector distances, the diffusion regime of light propagation in tissues is already established (18). As an alternative to the diffusion equation model to describe the spatial dependence of the optical signal, empirical approaches have been proposed (6). The different sensitivity of the two detector channels was accounted for by a preliminary calibration measurement on a synthetic tissue-like sample. The applicability of the initial calibration to the

whole data set was verified at the end of each measurement session by repositioning the optical probe on the calibration sample. We typically reproduced the calibration values of the block optical coefficients to within 10%. In the piglet experiments, we updated the measured values of L_{eff} at each wavelength every time the F_{IO_2} was changed. Specifically, L_{eff} was computed, according to *Eq. 2*, from average measurements of μ_a and μ_s' over the last 80 s of each period corresponding to a specific F_{IO_2} value. For the measurements on human subjects, we computed an initial value of L_{eff} (at each wavelength) over the first 2 min of baseline, and we used this value for the analysis of the data over the whole measurement session. The long integration time for the mean pathlength measurements (80 s in the piglet experiment, 120 s in the human subjects measurements) realized a low-pass filter that minimized the time-varying contributions from the Hb oscillations caused by the arterial pulsation and breathing. Furthermore, the two-distance measurement scheme for the mean pathlength measurement also provided some level of spatial averaging. In contrast, the optical data for the measurement of Sv_{O_2} were acquired with an 80-ms temporal resolution and with the use of a single source-detector distance (1 cm).

To measure the Sv_{O_2}, we followed a two-step procedure. First, we computed the amplitude of the absorption oscillations at the respiratory frequency at each of the eight wavelengths considered. Second, we fit the spectrum of the experimental absorption amplitude with the hemoglobin absorption spectrum. We have used two alternative methods to quantify the absorption oscillations at the respiratory frequency. The first method is based on the fast Fourier transform (FFT) of $\Delta\mu_a(t)$. The sum of the amplitudes of the FFT of $\Delta\mu_a$ over the respiratory frequency band yields a measure of the amplitude of the respiration-induced absorption oscillations. This method assumes that the Fourier spectrum of $\Delta\mu_a$ clearly shows a discernable peak at the respiratory frequency. The second method is based on a band-pass (BP) filter of $\Delta\mu_a(t)$ and on a modeling algorithm (MA) (sine-wave fit). The BP filter serves the purpose of isolating the absorption oscillations at the respiratory frequency by suppressing higher and lower frequency components in $\Delta\mu_a(t)$. The MA consists of fitting a sine wave to $\Delta\mu_a(BP)$ over each respiratory cycle. The amplitude of the fitted sine wave gives an estimate of the absorption oscillation amplitude at the respiratory frequency. As a result, the second method (BP + MA) achieves a reading of Sv_{O_2} from each individual respiration cycle, whereas the first method (FFT) requires multiple respiration cycles to produce a Sv_{O_2} reading. Both methods provide phase readings that can be used to verify that the respiration-induced absorption oscillations at different wavelengths are in phase with each other. We indicate the Sv_{O_2} measurement according to the FFT and BP + MA methods with Sv_{O_2}-NIRS$_{resp}$(FFT) and Sv_{O_2}-NIRS$_{resp}$(BP), respectively.

In the piglet experiments, we evaluated the FFT of $\Delta\mu_a$ over 256 data points, corresponding to a time trace of 20.5 s, to achieve reliable spectra from a number of breathing periods (typically 13–16). Furthermore, we averaged about 800 successive FFTs (each computed from a data set shifted by one data point with respect to the previous one), so that the total number of data points resulting in a single Sv_{O_2} reading was on the order of 1,000, corresponding to a train of data 80 s long. This 80-s-long data set was chosen to be at the end of each F_{IO_2} period, and it coincides with the 80-s period over which we measured L_{eff}. In the human subject experiment, we used 512 points for the FFT because the breathing frequency was lower (0.22–0.26 Hz) than that of the piglets

(0.6–0.9 Hz) and we wanted to have a similar number of breathing periods. As in the piglets experiment, we averaged the results from multiple (500–1,000) successive FFTs.

The spectrum of the amplitude of the absorption oscillations at the respiratory frequency $[\Delta\mu_a^{resp}(\lambda_i)]$ was fitted with a linear combination of the HbO$_2$ and Hb extinction spectra, $\varepsilon_{HbO_2}(\lambda_i)\Delta[HbO_2]^{resp} + \varepsilon_{Hb}(\lambda_i)\Delta[Hb]^{resp}$, where $\varepsilon_{HbO_2}(\lambda_i)$ and $\varepsilon_{Hb}(\lambda_i)$ are the extinction coefficients of HbO$_2$ and Hb, respectively (43, 53). The fitting parameters were the amplitudes of the oscillatory concentration of oxyhemoglobin ($\Delta[HbO_2]^{resp}$) and deoxyhemoglobin ($\Delta[Hb]^{resp}$) at the respiratory frequency. The minimization of the sum of the squares of the residuals, i.e., $\Sigma_i[\Delta\mu_a^{fit}(\lambda_i) - \Delta\mu_a^{resp}(\lambda_i)]^2$, yields a linear system whose solution gives the following best fit concentrations of amplitude of the oscillatory [HbO$_2$] and [Hb] (11)

$$\Delta[HbO_2]^{resp} = \frac{\begin{array}{c}[\Sigma_i \Delta\mu_a^{resp}(\lambda_i)\varepsilon_{HbO_2}(\lambda_i)][\Sigma_i \varepsilon_{Hb}^2(\lambda_i)] \\ - [\Sigma_i \Delta\mu_a^{resp}(\lambda_i)\varepsilon_{Hb}(\lambda_i)][\Sigma_i \varepsilon_{HbO_2}(\lambda_i)\varepsilon_{Hb}(\lambda_i)]\end{array}}{[\Sigma_i \varepsilon_{HbO_2}^2(\lambda_i)][\Sigma_i \varepsilon_{Hb}^2(\lambda_i)] - [\Sigma_i \varepsilon_{HbO_2}(\lambda_i)\varepsilon_{Hb}(\lambda_i)]^2}$$

$$(3)$$

$$\Delta[Hb]^{resp} = \frac{\begin{array}{c}[\Sigma_i \Delta\mu_a^{resp}(\lambda_i)\varepsilon_{Hb}(\lambda_i)][\Sigma_i \varepsilon_{HbO_2}^2(\lambda_i)] \\ - [\Sigma_i \Delta\mu_a^{resp}(\lambda_i)\varepsilon_{HbO_2}(\lambda_i)][\Sigma_i \varepsilon_{HbO_2}(\lambda_i)\varepsilon_{Hb}(\lambda_i)]\end{array}}{[\Sigma_i \varepsilon_{HbO_2}^2(\lambda_i)][\Sigma_i \varepsilon_{Hb}^2(\lambda_i)] - [\Sigma_i \varepsilon_{HbO_2}(\lambda_i)\varepsilon_{Hb}(\lambda_i)]^2}$$

$$(4)$$

The oxygen saturation of the hemoglobin compartment oscillating synchronously with respiration (Sv_{O_2}-NIRS$_{resp}$) is then given by

$$Sv_{O_2} - NIRS_{resp} = \frac{\Delta[HbO_2]^{resp}}{\Delta[HbO_2]^{resp} + \Delta[Hb]^{resp}}$$

$$= \frac{\begin{array}{c}[\Sigma_i \Delta\mu_a^{resp}(\lambda_i)\varepsilon_{HbO_2}(\lambda_i)][\Sigma_i \varepsilon_{Hb}^2(\lambda_i)] \\ - [\Sigma_i \Delta\mu_a^{resp}(\lambda_i)\varepsilon_{Hb}(\lambda_i)][\Sigma_i \varepsilon_{HbO_2}(\lambda_i)\varepsilon_{Hb}(\lambda_i)]\end{array}}{\begin{array}{c}[\Sigma_i \Delta\mu_a^{resp}(\lambda_i)\varepsilon_{HbO_2}(\lambda_i)]\{\Sigma_i \varepsilon_{Hb}(\lambda_i)[\varepsilon_{Hb}(\lambda_i) - \varepsilon_{HbO_2}(\lambda_i)]\} \\ - [\Sigma_i \Delta\mu_a^{resp}(\lambda_i)\varepsilon_{Hb}(\lambda_i)]\{\Sigma_i \varepsilon_{HbO_2}(\lambda_i)[\varepsilon_{Hb}(\lambda_i) - \varepsilon_{HbO_2}(\lambda_i)]\}\end{array}} \quad (5)$$

It is important to note that for the determination of Sv_{O_2}-NIRS$_{resp}$ one only needs to know L_{eff} to within a wavelength-independent factor. In fact, *Eq. 5* shows that a common, wavelength-independent multiplicative factor in $\Delta\mu_a(\lambda_i)$ cancels out in the expression for Sv_{O_2}-NIRS$_{resp}$. In contrast, the wavelength dependence of L_{eff} is important for the measurement of Sv_{O_2} with our method, and this is why we have opted to measure L_{eff} at each wavelength using the multidistance, frequency-domain technique. It is also important to observe that our method requires *1*) oscillations of μ_a at the respiratory frequency to be reliably attributed to hemoglobin (and not, for instance, to motion artifacts), *2*) the hemoglobin concentration fluctuations to result from the volume oscillation of a hemoglobin compartment rather than from periodic fluctuations in the blood flow, and *3*) the fluctuating hemoglobin compartment responsible for the measured $\Delta\mu_a$ to be mainly the venous compartment. In our measurements, we have considered each one of the three above points. The assignment of the absorption oscillations to hemoglobin (*point 1*) was done by requiring that the hemoglobin spectrum fits the absorption data relatively well. To this aim, we requested that the average absolute value of the relative residuals, defined as $\varepsilon^{fit} = 1/N\Sigma_{i=1}^{N} |\Delta\mu_a^{fit}(\lambda_i) - \Delta\mu_a^{resp}(\lambda_i)| / \Delta\mu_a^{fit}(\lambda_i)$, where N is the number of wavelengths considered, be at most twice the experimental percent error in $\Delta\mu_a^{resp}$. We also used the standard deviation of the Sv_{O_2}-NIRS$_{resp}$(FFT) values obtained with the 800 (piglet experiment) or 500–1,000 (human experiment) successive FFTs to estimate the

error in Sv_{O_2}-NIRS$_{resp}$(FFT). We discarded the cases having a standard deviation error in Sv_{O_2}-NIRS$_{resp}$ greater than 15%. The assignment of the absorption oscillations to volume rather than blood flow fluctuations (*point 2*) is achieved by verifying that the absorption oscillations at the eight wavelengths are in phase. In fact, blood flow fluctuations induce out-of-phase oscillations in the [HbO$_2$] and [Hb] (because of the increased rates of inflow of HbO$_2$ and washout of Hb), as opposed to the in-phase oscillations of HbO$_2$ and Hb that result from volume pulsations. The third point, namely the requirement that the absorption oscillations at the respiratory frequency are representative of venous blood, is investigated by *1*) comparing the Sv_{O_2}-NIRS from the respiratory hemoglobin oscillations (Sv_{O_2}-NIRS$_{resp}$) with the corresponding values measured by gas analysis of Sv_{O_2}-blood (piglet experiments) or by the NIRS venous occlusion method (Sv_{O_2}-NIRS$_{vo}$) (human subject experiments), *2*) studying the effect on the [Hb] and [HbO$_2$] oscillations at the respiratory frequency of a venous occlusion induced between the lungs and the peripheral measurement area (the thigh muscles in human subject experiments), and *3*) by recording the effect of muscle exercise on the near-infrared measurements of Sv_{O_2} [Sv_{O_2}-NIRS$_{resp}$(BP)] in human subjects.

RESULTS

Figure 4 reports average spectra of L_{eff} measured for a source-detector separation of 1 cm. Figure 4A refers to piglet measurements conducted at two different values of F_{IO_2}, whereas Fig. 4B refers to human measurements with *probes HVM* and *HVL*. The error bars in
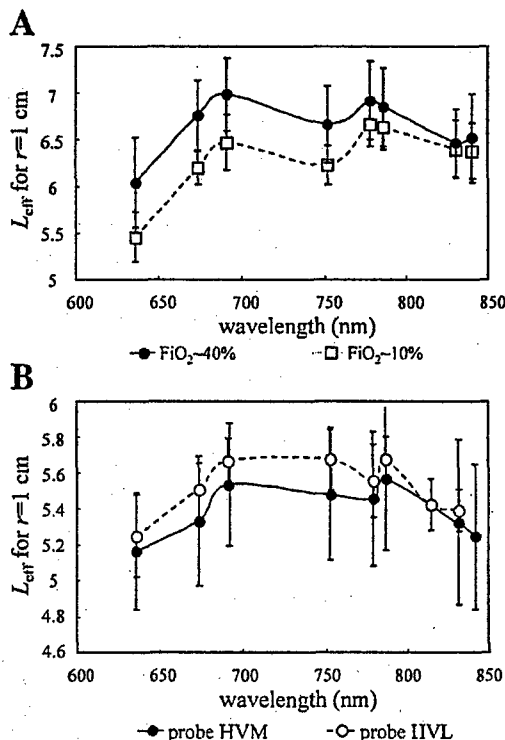
Fig. 4. Near-infrared spectra of the effective optical pathlength (L_{eff}) measured on the piglet's leg (A) and a human thigh muscle (B) for a source-detector separation (r) of 1 cm. In A, different symbols refer to 2 different values of F_{IO_2}. In B, different symbols refer to 2 different thigh muscles (vastus medialis for *probe HVM* and vastus lateralis for *probe HVL*). The lines join the points as an aid to the eye.

Fig. 4 represent the standard deviations over multiple measurements (multiple F_{IO_2} cycles and piglets for Fig. 4A and multiple subjects for Fig. 4B).

In the piglet experiment, we discarded 11 (from a total of 67) Sv_{O_2}-NIRS$_{resp}$(FFT) measurements because the standard deviation over 800 FFTs exceeded 15%. These discarded Sv_{O_2}-NIRS$_{resp}$(FFT) readings occurred as follows: one (of 8) in *piglet 1*, two (of 26) in *piglet 2*, and eight (of 33) in *piglet 3*. One discarded reading was assigned to motion artifacts, whereas the other ten discarded measurements all occurred at low-F_{IO_2} values (10–17.5%) corresponding to Sv_{O_2}-blood values of 20–50%. We were not able to apply the BP method to *piglet 2* and to the F_{IO_2} cycles A and B of *piglet 3* because of irregular absorption oscillation waveforms that were not reliably processed by the BP + MA approach.

Figure 5 shows typical temporal traces of the relative [HbO$_2$] and [Hb] measured on the piglet's leg (with optical *probe PR*) (Fig. 5A) and on the human vastus medialis muscle at rest (Fig. 5B) and during venous occlusion on the upper thigh (optical *probe HVM*) (Fig. 5C). The temporal traces of [Hb] and [HbO$_2$] are obtained by fitting the measured spectrum of $\Delta\mu_a(\lambda,t)$ (whose value at each wavelength was obtained from *Eq. 2*) with a linear combination of the HbO$_2$ and Hb extinction spectra. This procedure results in the application of *Eqs. 3* and *4* without the superscript "resp" on $\Delta\mu_a$, Δ[HbO$_2$], and Δ[Hb]. Two oscillatory components are clearly visible in the relative [HbO$_2$] and [Hb] traces of Fig. 5A: the first one, associated with the heartbeat (as shown by the pulse oximeter data; top trace in Fig. 5) is at a frequency of ~2.5 Hz, whereas the second one, associated with respiration (as shown by the strain gauge signal; second trace from the top in Fig. 5), is at a frequency of ~0.65 Hz. Only the latter oscillatory component (at a frequency of ~0.23 Hz in human subjects) is clearly visible in Fig. 5B, whereas neither is present in Fig. 5C. Figure 5, B and C, shows additional low-frequency oscillations associated with changes in blood pressure and heart rate. We observe that the strain-gauge signal (second trace from the top in Fig. 5) increases during inspiration and decreases during expiration. The BP filter described in the previous section aims at isolating the oscillatory component at the respiratory frequency by filtering out higher and lower frequency components. The relative [HbO$_2$] and [Hb] traces after BP filtering are shown in Fig. 5, *bottom*. In the case reported in Fig. 5, which is representative of the results reported in this article for Sv_{O_2}-NIRS$_{resp}$, the oscillatory components of [HbO$_2$] and [Hb] at the respiratory frequency are in phase with each other and disappear during venous occlusion.

Figure 6 illustrates representative $\Delta\mu_a^{resp}$ spectra measured on the piglet's leg (*probe PR*) (Fig. 6A) and on the human vastus medialis muscle at rest (Fig. 6B) and during venous occlusion on the upper thigh (*probe HVM*) (Fig. 6C). The y-axis of each panel of Fig. 6 refers to the values of $\Delta\mu_a^{resp}$ obtained with the BP filter method. The values of $\Delta\mu_a^{resp}$ computed with the FFT method are normalized by a wavelength-independent
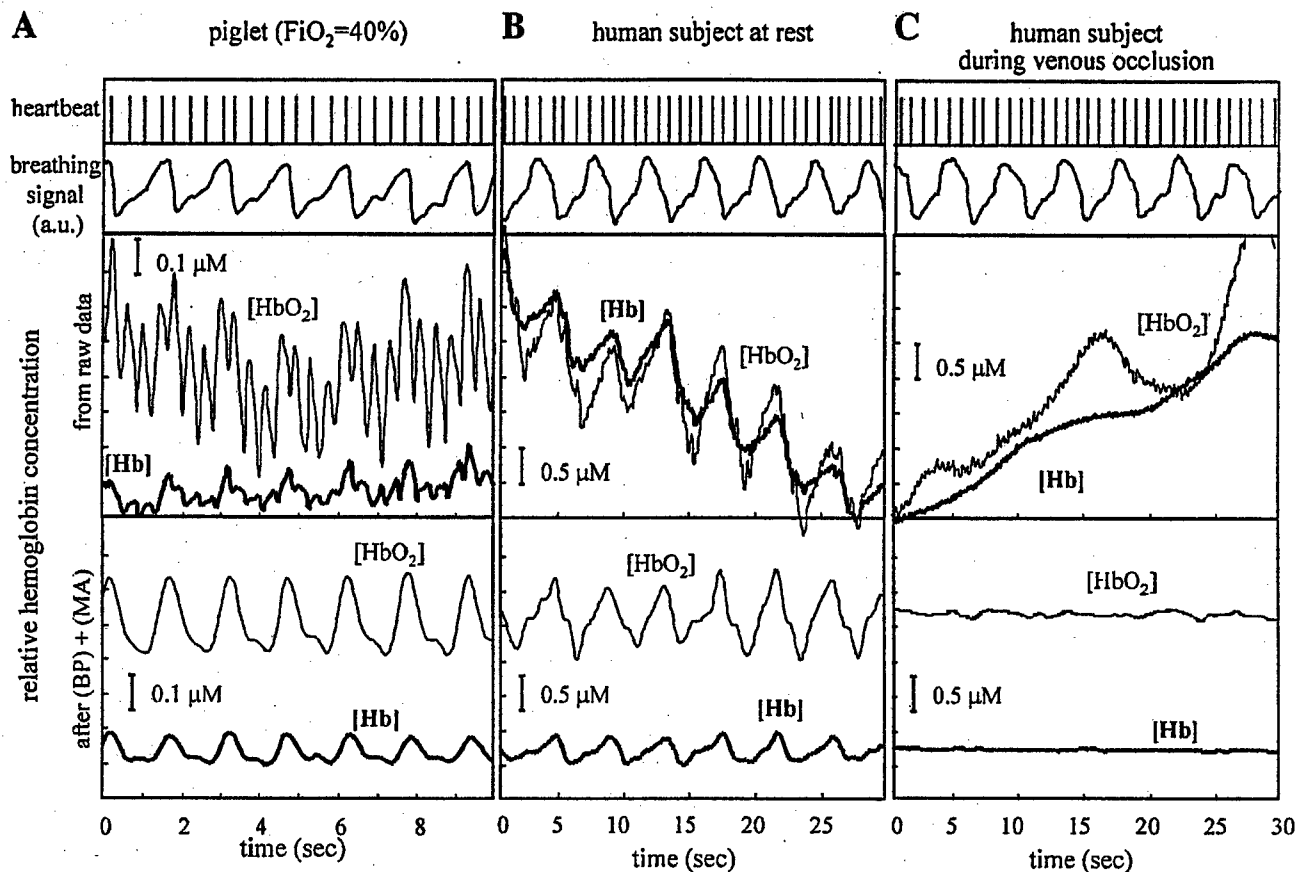
Fig. 5. Representative traces of the relative HbO₂ concentrations ([HbO₂]) and Hb concentrations ([Hb]) measured on the piglet's leg (with optical *probe PR*) (*A*) and on the human vastus medialis muscle at rest (*B*) and during venous occlusion on the upper thigh (optical *probe HVM*) (*C*). *Bottom panels* report the [Hb] traces after processing with the digital band-pass filter [band pass (BP) + modeling algorithm (MA)] designed to isolate the oscillations at the respiratory frequency. *Top trace* represents the piglet's heartbeat monitored by the pulse oximeter. *Second trace* from the top is the strain gauge signal that monitors the respiratory excursion. The strain gauge signal increases during inspiration and decreases during expiration. a.u., Arbitrary units.

factor to match the BP value of $\Delta\mu_a^{resp}$ at 636 nm. The relatively high value of ϵ^{fit} during venous occlusion (Fig. 6*C*) is an indication of the poor fit, which in turn results from the lack of hemoglobin oscillations at the respiratory frequency (see Fig. 5*C*, *bottom*, and the *y*-axis values of Fig. 5*C* compared with those of Fig. 5*B*). Figure 6 also shows the best fit of the hemoglobin absorption spectrum to the BP $\Delta\mu_a^{resp}$ and to the FFT $\Delta\mu_a^{resp}$. The best-fit hemoglobin spectra represent the oxygen saturation of hemoglobin, as illustrated in Fig. 1. The value of Sv_{O_2}-NIRS$_{resp}$ is given by *Eq. 5*.

Figure 7 compares the measurements of Sv_{O_2}-NIRS$_{resp}$(BP), Sv_{O_2}-NIRS$_{resp}$(FFT), and Sv_{O_2}-blood during *cycle A* of *piglet 1* and during *cycle C* of *piglet 3*. The Sv_{O_2}-NIRS$_{resp}$(BP) traces reported in Fig. 7 were obtained by performing a running average of the breath-to-breath values obtained with the BP method. In Fig. 7, the averaging procedure consists of a 5-point (in Fig. 7*A*) or 15-point (in Fig. 7*B*) running average. The assessment of the agreement between the measurements of Sv_{O_2}-NIRS$_{resp}$(FFT) and Sv_{O_2}-blood in the full piglet study is carried out according to the procedure described by Bland and Altman (5). Figure 8*A* plots the

results of the NIRS method based on the respiratory oscillations of the tissue absorption against the invasive measurement of Sv_{O_2}-blood. The shape of the symbols in Fig. 8*A* indicates the piglet number, whereas the type of fill indicates the location of the NIRS measurement. The range of Sv_{O_2}-blood values considered in this study is ~20–95%. The error bars in Fig. 8*A* are the standard deviations (SD) computed from the results of ~800 successive FFTs (as described in MATERIALS AND METHODS). Figure 8*B* displays the difference between the two readings vs. their average, and it quantifies the discrepancy between the two methods and the possible dependence of such a difference on the level of Sv_{O_2}. The mean difference between Sv_{O_2}-NIRS$_{resp}$ and Sv_{O_2}-blood over the full oxygenation range considered in this study is 1.0% (a measurement of the bias of the Sv_{O_2}-NIRS$_{resp}$ measurement), and the SD of the difference is 5.8%. Figure 8*B* does not show any striking dependence of the difference on the mean. If we take the values of mean difference ± 2 SD as the limits of agreement of the two methods (5), we get an estimate of the maximal discrepancies between Sv_{O_2}-NIRS$_{resp}$(FFT) and Sv_{O_2}-blood of −10.6% and +12.6%.

A

piglet (FiO$_2$=40%)

$\varepsilon_{(BP)}^{(fit)} = \varepsilon_{(FFT)}^{(fit)} = 6\%$

B

human subject at rest

$\varepsilon_{(BP)}^{(fit)} = \varepsilon_{(FFT)}^{(fit)} = 4\%$

C

human subject during venous occlusion

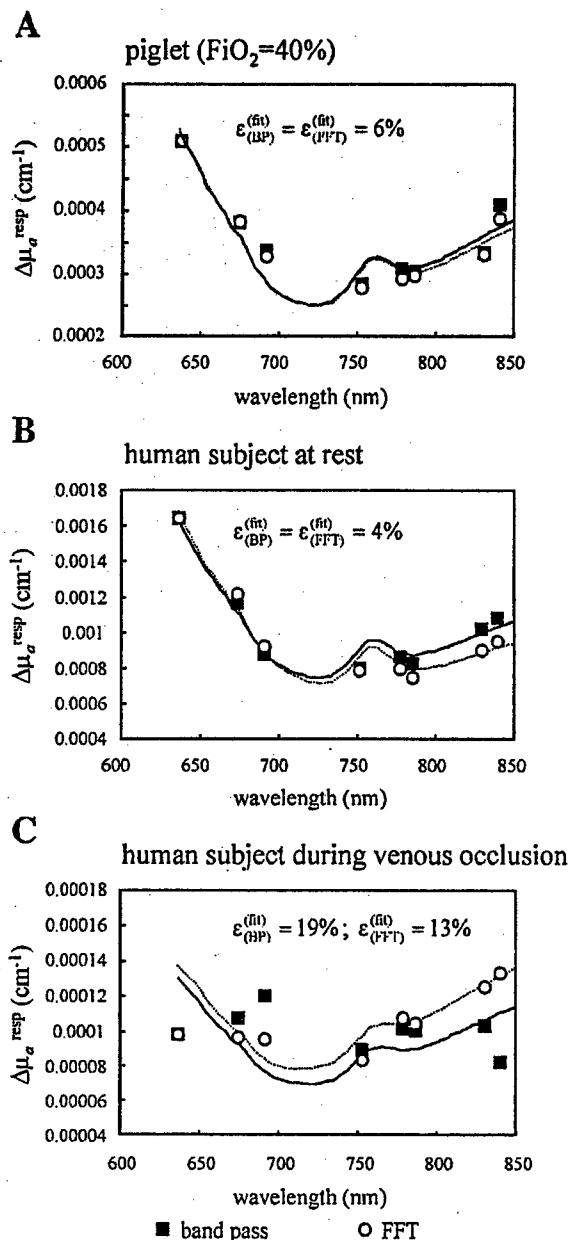$\varepsilon_{(BP)}^{(fit)} = 19\%$; $\varepsilon_{(FFT)}^{(fit)} = 13\%$

■ band pass   O FFT

Fig. 6. Representative change in respiratory tissue absorption coefficient ($\Delta\mu_a^{resp}$) spectra measured with the BP and fast Fourier transform (FFT) methods on the piglet's leg (probe PR) (A) and on the human vastus medialis muscle at rest (B) and during venous occlusion on the upper thigh (probe HVM) (C). The experimental 8-point $\Delta\mu_a^{resp}$ spectra were fitted with the hemoglobin absorption spectrum (with the oxy- and deoxyhemoglobin concentrations as fitting parameters). The values of ε^{fit} (defined in the text) for the BP and FFT spectra give a measure of the quality of the fit.

In the human experiment, we found that the NIRS values of Sv$_{O_2}$ measured with probe HVM (placed on top of a visible vein) were typically smaller than those measured with probe HVL (placed far from any visible vein). Furthermore, the amplitude of the oscillatory absorption at the respiration (heartbeat) frequency was typically greater (smaller) for the data collected with probe HVM than with probe HVL. Of the 16 Sv$_{O_2}$-NIRS$_{resp}$ measurements (8 subjects, 2 locations),

we discarded only 2 measurements (because of a value of Σ^{fit} greater than twice the error in $\Delta\mu_a^{resp}$), both collected with probe HVL. Figure 9 compares the Sv$_{O_2}$-NIRS$_{resp}$ values measured in the human subjects at rest in which the FFT method and the BP filtering approach were used. Figure 9A shows the good agreement of the two measurements, and Fig. 9B quantifies the average difference (0.9%) and the maximum discrepancies of −5.1 and +6.9%, as given by the mean ± 2 SD of the differences. Figure 10 reports a similar comparison between Sv$_{O_2}$-NIRS$_{resp}$(FFT) and Sv$_{O_2}$-NIRS$_{vo}$. As described by Yoxall and Weindling (56), under the assumption that a venous occlusion induces an initial increase in the venous blood volume, Sv$_{O_2}$-NIRS$_{vo}$ is given by [H̊bO$_2$]$_0$/[H̊b −T]$_0$, where the dots indicate a time derivative and the subscript 0 indicates the initial time that immediately follows the onset of venous occlusion. The agreement between Sv$_{O_2}$-NIRS$_{resp}$(FFT) and Sv$_{O_2}$-NIRS$_{vo}$ is good, with an average deviation of 0.8% and maximum discrepancies of −4.2 and +5.8%. Two horizontal lines in Figs. 8B and 9B indicate the range given by the mean difference ± 2 SD. The maximum discrepancy among Sv$_{O_2}$-NIRS$_{resp}$(FFT), Sv$_{O_2}$-NIRS$_{resp}$(BP), and Sv$_{O_2}$-NIRS$_{vo}$ is less than the maximum deviation between Sv$_{O_2}$-NIRS$_{resp}$(FFT) and Sv$_{O_2}$-blood found in piglets (see Fig. 8B).

The effect of muscle exercise on the measurement of Sv$_{O_2}$-NIRS$_{resp}$(BP) on top of a visible superficial vein (probe HVM) is illustrated in Fig. 11. Although Sa$_{O_2}$ (measured with a pulse oximeter) is unaffected by the exercise, Sv$_{O_2}$-NIRS$_{resp}$(BP) shows a significant postexercise decrease from a baseline value of 75–78% down to a minimum value of ~54%. The recovery to the baseline value of Sv$_{O_2}$-NIRS$_{resp}$(BP) occurs after ~30 s. By using the BP approach, we could monitor Sv$_{O_2}$-NIRS$_{resp}$ at every breathing period, i.e., every ~5 s, thus achieving a real-time monitoring of Sv$_{O_2}$. We observe that we could not obtain meaningful measurements of Sv$_{O_2}$-NIRS$_{resp}$ during exercise because of motion artifacts.

DISCUSSION

Various methods for measuring Sv$_{O_2}$. The method presented in this article to measure Sv$_{O_2}$ from the near-infrared absorption oscillations at the respiratory frequency (spiroximetry) can be implemented by using a FFT or a digital BP filter in conjunction with a MA. We have indicated the measurements of Sv$_{O_2}$ obtained with these two approaches with the notations Sv$_{O_2}$-NIRS$_{resp}$(FFT) and Sv$_{O_2}$-NIRS$_{resp}$(BP), respectively. An alternative method for measuring Sv$_{O_2}$ with NIRS is based on a previously described venous occlusion protocol (13, 39, 55, 56). We have identified the results of this measurement procedure with the notation Sv$_{O_2}$-NIRS$_{vo}$. In the human study, the NIRS measurements were conducted at two locations on the thigh. One location was on top of a visible superficial vein of the vastus medialis muscle (probe HVM), and the second location was far from visible superficial veins on the vastus lateralis muscle (probe HVL). Finally, the inva-

Fig. 7. Comparison between the continuous measurement of Sv_{O_2}-$NIRS_{resp}$ (BP) and the discontinuous measurements of Sv_{O_2}-$NIRS_{resp}$(FFT) and Sv_{O_2}-blood. *A* refers to *cycle A* of *piglet 1*, whereas *B* refers to *cycle C* of *piglet 3*. The values of FI_{O_2} (%, left *y*-axes) during the experiment are indicated by the shaded profiles.

O Sv_{O_2}-BLOOD   ▣ Sv_{O_2}-$NIRS_{resp}$(FFT)   — Sv_{O_2}-$NIRS_{resp}$(BP)
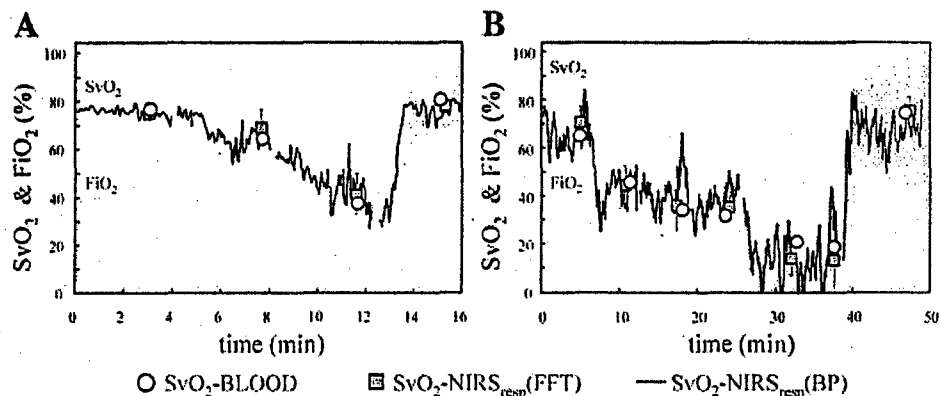
sive measurement of Sv_{O_2} performed by the gas analysis of venous blood samples is indicated with Sv_{O_2}-blood. In this section, we discuss the different features of these measurements of Sv_{O_2}, and the comparison of their results, as reported in Figs. 7–9.

The FFT and BP filter approaches to near-infrared spiroximetry. The major advantage of the BP approach is that it allows for a real-time measurement of Sv_{O_2} by providing a reading of Sv_{O_2}-$NIRS_{resp}$(BP) at every respiration cycle. Consequently, this method is particularly effective during transients, as illustrated by the recovery of the Sv_{O_2}-$NIRS_{resp}$(BP) traces corresponding to the sudden increase of FI_{O_2} to 100% in piglets (see Fig. 6, *A* and *B*), or to the end of the exercise period in human subjects (see Fig. 11). On the other hand, the BP filter + MA method is susceptible to fluctuations in the respiratory frequency and to irregular respiration patterns. This accounts for the fact that we did not get reliable readings of Sv_{O_2}-$NIRS_{resp}$(BP) in *piglet 2* and in FI_{O_2} *cycles A* and *B* of *piglet 3*. The FFT method was more robust, producing reliable readings in 56 of 67 cases (84%) in the piglet study and in 14 of 16 cases (87%) in the human study. It is important to observe that 10 of the 11 discarded readings in piglets occurred at low-Sv_{O_2}-NIRS-blood values (20–50%), and one was

assigned to motion artifacts. Both discarded readings in the human study were collected with *probe HVL*, which was placed far from visible veins. Therefore, we have found indications that the measurement of Sv_{O_2}-$NIRS_{resp}$(FFT) is particularly robust at Sv_{O_2} values >50% (in piglets) and when the optical probe is placed on top of a visible superficial vein (in human subjects). Although the FFT method, which is based on a measurement of the integrated peak at the respiratory frequency, is less sensitive than the BP method to irregular respiration patterns, it is not applicable during transients. In fact, we did not obtain reliable readings of Sv_{O_2} when the time frame used to compute Sv_{O_2}-$NIRS_{resp}$(FFT) (80 s in piglets, 80–120 s in human subjects) included significant changes in the Sv_{O_2}. When both the FFT and the BP methods can be applied, they provide Sv_{O_2}-$NIRS_{resp}$ measurements that are in excellent agreement, as shown in Figs. 6 and 9. The differences between the two measurements (SD of 3.0%) are comparable with measurement errors and significantly less than the maximum deviation between Sv_{O_2}-$NIRS_{resp}$(FFT) and Sv_{O_2}-blood (approximately ±10%) observed in the piglet study (see Fig. 8*B*).
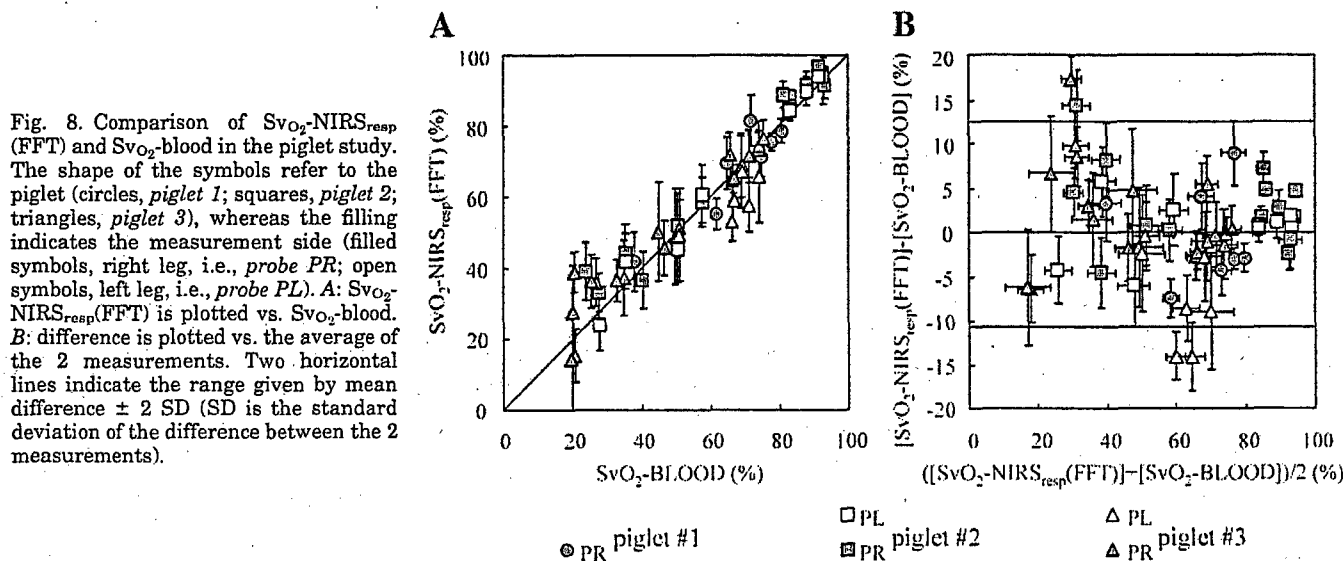

Fig. 8. Comparison of Sv_{O_2}-$NIRS_{resp}$ (FFT) and Sv_{O_2}-blood in the piglet study. The shape of the symbols refer to the piglet (circles, *piglet 1*; squares, *piglet 2*; triangles, *piglet 3*), whereas the filling indicates the measurement side (filled symbols, right leg, i.e., *probe PR*; open symbols, left leg, i.e., *probe PL*). *A*: Sv_{O_2}-$NIRS_{resp}$(FFT) is plotted vs. Sv_{O_2}-blood. *B*: difference is plotted vs. the average of the 2 measurements. Two horizontal lines indicate the range given by mean difference ± 2 SD (SD is the standard deviation of the difference between the 2 measurements).
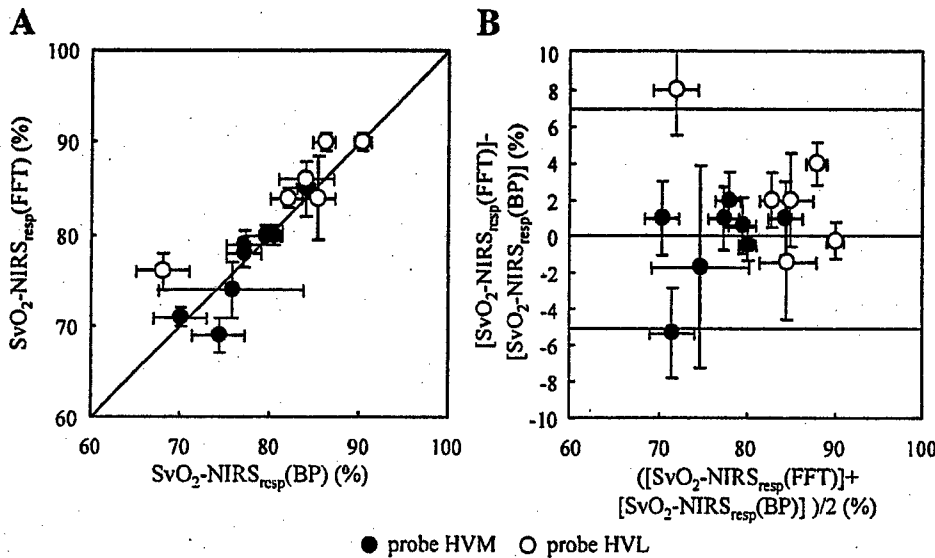
⊕ PR ⊙ PL piglet #1   □ PL ▣ PR piglet #2   △ PL ▲ PR piglet #3

A

B

Fig. 9. Comparison of Sv_{O_2}-$NIRS_{resp}$ (FFT) and Sv_{O_2}-$NIRS_{resp}$(BP) in the human study. ●, Vastus medialis muscle; i.e., *probe HVM*. ○, Vastus lateralis muscle; i.e., *probe HVL*. Probe HVM was place on top of a visible superficial vein, whereas *probe HVL* was far from visible veins. A: Sv_{O_2}-$NIRS_{resp}$- (FFT) is plotted vs. Sv_{O_2}-$NIRS_{resp}$(BP). B: difference is plotted vs. the average of the 2 measurements. Two horizontal lines in B indicate the range given by mean difference ± 2 SD.

● probe HVM   ○ probe HVL

Measurements of Sv_{O_2}-$NIRS_{resp}$ and Sv_{O_2}-$NIRS_{vo}$. Both of these NIRS methods to measure the Sv_{O_2} (resp and vo) rely on a change in the volume fraction of venous blood in the tissue. The two major differences between the two methods are as follows. *1*) The vo method requires an external perturbation consisting of a pneumatic-cuff-induced venous occlusion, whereas the resp method is only based on the intrinsic blood pressure oscillations induced by normal respiration and can be applied continuously. *2*) The vo method can be applied only to limbs, whereas the resp method can, in principle, be applied to any tissue and in particular to the brain, as already shown by Wolf et al. (52). However, we stress that it is always important to verify that the [HbO_2] and [Hb] oscillate in phase at the respiratory frequency for the resp method to provide reliable measurements of Sv_{O_2}. For instance, Elwell et al. (16) reported out-of-phase oscillations of [Hb] and [HbO_2] in the human brain, which would indicate a blood

flow rather than volume oscillations, thus rendering the resp method inapplicable. In our human study, we found an excellent agreement between Sv_{O_2}-$NIRS_{resp}$(FFT) and Sv_{O_2}-$NIRS_{vo}$, with a maximum deviation on the order of ±4–5% (see Fig. 10).

Optical probes PR, PL, HVM, and HVL. In the piglet study, we have found no significant difference between the Sv_{O_2}-$NIRS_{resp}$(FFT) data collected with *probes PR* (on the right leg) and *PL* (on the left leg, where the venous catheter was inserted) (see Fig. *8A*). This result indicates that noninvasive measurements of Sv_{O_2} on one leg can be meaningfully compared with invasive measurements of Sv_{O_2} on the other leg. In the human study, we found some differences between the Sv_{O_2}-NIRS measurements with *probe HVM* (placed on top of a visible superficial vein in the vastus medialis muscle) and with *probe HVL* (placed far from visible veins on the vastus lateralis muscle). As shown in Figs. 8 and 9, the Sv_{O_2}-NIRS readings (with both the $NIRS_{resp}$ and $NIRS_{vo}$
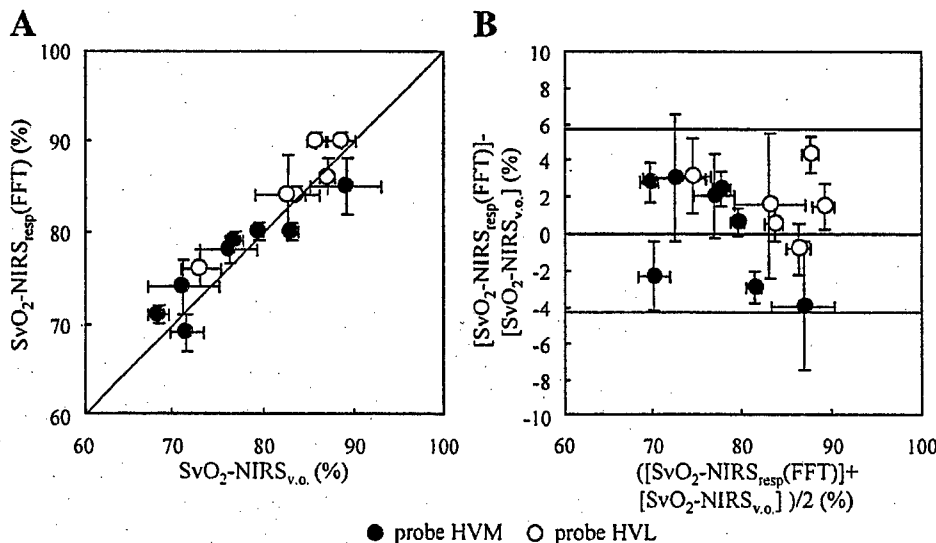
A

B

Fig. 10. Comparison of Sv_{O_2}-$NIRS_{resp}$ (FFT) and Sv_{O_2}-$NIRS_{vo}$ (venous occlusion) in the human study. ●, Vastus medialis muscle; i.e., *probe HVM*. ○, Vastus lateralis muscle; i.e., *probe HVL*. Probe HVM was place on top of a visible superficial vein, whereas *probe HVL* was far from visible veins. A: Sv_{O_2}-$NIRS_{resp}$(FFT) is plotted vs. Sv_{O_2}-$NIRS_{vo}$. B: difference is plotted vs. the average of the 2 measurements. Two horizontal lines in B indicate the range given by mean difference ± 2 SD.
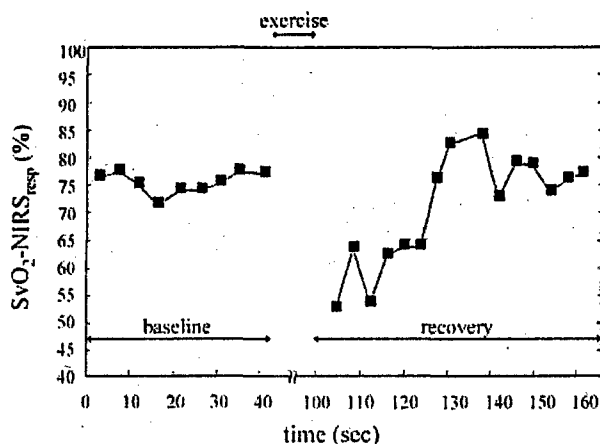
● probe HVM   ○ probe HVL

Fig. 11. Continuous measurement of Sv_{O_2}-NIRS$_{resp}$(BP) with optical *probe HVM* (vastus medialis muscle, on top of a visible superficial vein) on a healthy human subject during baseline and after isometric muscle exercise (recovery).

method) of *probe HVM* (see Figs. 8 and 9) were typically smaller than the readings of *probe HVL* (see Figs. 8 and 9). We assign this result to a partial contribution from the capillary and/or arterial compartments picked up by *probe HVL*. In fact, although the optical data from probe HVM shown in Fig. 4, *B* and *C*, do not show any visible contribution from the arterial pulsation, data from *probe HVL* (not shown) do contain pulsatile components at the heartbeat frequency. As a result, we believe that the optical probe should be placed on top of visible superficial veins for more accurate readings of Sv_{O_2}-NIRS$_{resp}$ on human subjects. We believe that the reason that Sv_{O_2}-NIRS$_{resp}$ readings in the piglet study were in close agreement with the invasive measurement of Sv_{O_2}, despite the evident arterial pulsation in Fig. 5*A*, is related to the smaller extent of respiratory sinus arrhythmia in piglets with respect to humans. In fact, respiratory sinus arrhythmia is the main origin of the arterial oscillations at the respiratory frequency (38). The larger role played by respiratory sinus arrhythmia in human subjects with respect to piglets will probably require a more careful interpretation of the optical data for spiroximetry. However, the results of Fig. 11 show the practical applicability of spiroximetry to human subjects, so that we do not expect respiratory sinus arrhythmia to introduce an intrinsic limitation of the method.

Noninvasive vs. invasive measurements of Sv_{O_2}. The comparison between Sv_{O_2}-NIRS$_{resp}$(FFT) and Sv_{O_2}-blood in the piglet study shows a maximum deviation range of -10.6% to $+12.6\%$. The local character of the Sv_{O_2} (as opposed to the systemic nature of the Sa_{O_2}) requires some caution in the comparison of invasive (Sv_{O_2}-blood) and noninvasive (Sv_{O_2}-NIRS) measurements of Sv_{O_2}. In fact, in our piglet study, Sv_{O_2}-blood was measured from blood samples drawn from the femoral vein, whereas Sv_{O_2}-NIRS$_{resp}$ was measured with an optical probe placed on the leg muscle. It is likely that the NIRS oscillatory signal

(at the respiratory frequency) is not just representative of the femoral vein and may therefore be indicative of the oxygen consumption at different tissue areas than those affecting the femoral vein saturation. This fact may not lead to significant differences under rest conditions, but it may be important under stress. Although we found a good agreement between Sv_{O_2}-NIRS$_{resp}$(FFT) and Sv_{O_2}-blood over the whole range of $F_{I_{O_2}}$ values considered (see Fig. 8), we observed a meaningfully greater SD of the differences over the 20–55% Sv_{O_2}-blood range (SD = 7.8%) than in the 55–95% range (SD = 3.6%).

Effect of muscle exercise on Sv_{O_2}-NIRS$_{resp}$(BP). The result reported in Fig. 11 serves the purpose of further illustrating the potential of the Sv_{O_2}-NIRS$_{resp}$(BP) measurement approach. In fact, Fig. 11 shows the feasibility of monitoring the Sv_{O_2} in real time on a breath-to-breath basis (one data point every 4–5 s). Furthermore, the baseline Sv_{O_2}-NIRS$_{resp}$(BP) value of 75–78% and the exercise-induced drop indicate the venous origin of the saturation measurement, since the Sa_{O_2} measurement provided by the pulse oximeter stayed constant at 98 ± 1% for the whole measurement period. On the other hand, Fig. 11 reports only one representative case, and more studies are required to quantify the effect of muscle exercise on the measurement of Sv_{O_2}-NIRS$_{resp}$.

In conclusion, we have presented a noninvasive approach to measure the Sv_{O_2} in tissues from the near-infrared spectrum of the amplitude of respiration-induced absorption oscillations. We have implemented this approach, which we call near-infrared spiroximetry, by processing the optical data with a FFT method or with a digital BP filter in conjunction with a MA. More sophisticated data processing schemes may further improve the effectiveness and the range of applicability of spiroximetry. The Sv_{O_2} measurements reported in this article complement previously demonstrated NIRS measurements of St_{O_2} (8, 27) and Sa_{O_2} (21). Therefore, our results may lead to the design of a noninvasive optical instrument capable of providing simultaneous and real-time measurements of local Sa_{O_2}, St_{O_2}, and Sv_{O_2}.

REFERENCES

1. **Aoyagi T, Kishi M, Yamaguchi K, and Watanabe S.** Improvement of the earpiece oximeter. In: *Abstracts of the Japanese*

Society of Medical Electronics and Biological Engineering, Tokyo, Japan, 1974, p. 90–91.

2. **Bank W, Park J, Lech G, and Chance B.** Near-infrared spectroscopy in the diagnosis of mitochondrial disorders. *Biofactors* 7: 243–245, 1998.

3. **Benaron DA, Hintz SR, Villringer A, Boas D, Kleinschmidt A, Frahm J, Hirth C, Obrig H, van Houten JC, Kermit EL, Cheong WF, and Stevenson DK.** Noninvasive functional imaging of human brain using light. *J Cereb Blood Flow Metab* 20: 469–477, 2000.

4. **Berne RM and Levy MN.** *Cardiovascular Physiology* (7th ed.). St. Louis, MO: Mosby Year Book, 1997, p. 196.

5. **Bland JM and Altman DG.** Statistical methods for assessing agreement between two methods of clinical measurement. *Lancet* 1: 307–310, 1986.

6. **Butler JP, Miki H, Suzuki S, and Takishima T.** Step response of lung surface-to-volume ratio by light-scattering stereology. *J Appl Physiol* 67: 1873–1880, 1989.

7. **Casavola C, Paunescu LA, Fantini S, and Gratton E.** Blood flow and oxygen consumption with near-infrared spectroscopy and venous occlusion: spatial maps and the effect of time and pressure of inflation. *J Biomed Opt* 5: 269–276, 2000.

8. **Chance B, Cope M, Gratton E, Ramanujam N, and Tromberg BJ.** Phase measurement of light absorption and scatter in human tissues. *Rev Sci Instrum* 689: 3457–3481, 1998.

9. **Chance B, Dait M, Zhang C, Hamaoka T, and Hagerman F.** Recovery from exercise-induced desaturation in the quadriceps muscle of elite competitive rowers. *Am J Physiol Cell Physiol* 262: C766–C775, 1992.

10. **Colier WN, Quaresima V, Wenzel R, van der Sluijs MC, Oeseburg B, Ferrari M, and Villringer A.** Simultaneous near-infrared spectroscopy monitoring of left and right occipital areas reveals contralateral hemodynamic changes upon hemifield paradigm. *Vision Res* 41: 97–102, 2001.

11. **Cope M.** *The Application of Near-Infrared Spectroscopy to Non-Invasive Monitoring of Cerebral Oxygenation in the Newborn Infant* (PhD thesis). London: Biomedical Optics Research Group, University College, 1991, p. 263–269. [Online] http://www.medphys.ucl.ac.uk/research/borg/homepages/mcope/index.htm [2001, May 10]

12. **De Blasi R, Cope M, Elwell C, Safoue F, and Ferrari M.** Noninvasive measurement of human forearm oxygen consumption by near infrared spectroscopy. *Eur J Appl Physiol* 67: 20–25, 1993.

13. **De Blasi RA, Ferrari M, Natali A, Conti G, Mega A, and Gasparetto A.** Noninvasive measurement of forearm blood flow and oxygen consumption by near-infrared spectroscopy. *J Appl Physiol* 76: 1388–1393, 1994.

14. **Delpy DT, Cope M, van der Zee P, Arridge S, Wray S, and Wyatt JS.** Estimation of optical pathlength through tissue from direct time of flight measurement. *Phys Med Biol* 33: 1433–1442, 1988.

15. **Elwell CE, Matcher SJ, Tyszczuk L, Meek JH, and Delpy DT.** Measurement of cerebral venous saturation in adults using near infrared spectroscopy. *Adv Exp Med Biol* 411: 453–460, 1997.

16. **Elwell CE, Owen-Reece H, Cope M, Edwards AD, Wyatt JS, Reynolds EOR, and Delpy DT.** Measurement of changes in cerebral heamodynamic during inspiration and expiration using near infrared spectroscopy. *Adv Exp Med Biol* 388: 619–626, 1994.

17. **Fantini S, Franceschini MA, Fishkin JB, Barbieri B, and Gratton E.** Quantitative determination of the absorption spectra of chromophores in strongly scattering media: a light-emitting-diode based technique. *Appl Opt* 33: 5204–5213, 1994.

18. **Fantini S, Franceschini MA, and Gratton E.** Effective source term in the diffusion equation for photon transport in turbid media. *Appl Opt* 36: 156–163, 1997.

19. **Fantini S, Franceschini MA, Maier JS, Walker SA, Barbieri B, and Gratton E.** Frequency-domain multichannel optical detector for non-invasive tissue spectroscopy and oximetry. *Opt Eng* 34: 32–42, 1995.

20. **Franceschini MA, Fantini S, Palumbo R, Pasqualini L, Vaudo G, Franceschini E, Gratton E, Palumbo B, Inno-**cente S, **and Mannarino E.** Quantitative near-infrared spectroscopy on patients with peripheral vascular disease. *Proc SPIE* 3194: 112–115, 1998.

21. **Franceschini MA, Gratton E, and Fantini S.** Non-invasive optical method to measure tissue and arterial saturation: an application to absolute pulse oximetry of the brain. *Opt Lett* 24: 829–831, 1999.

22. **Fantini S, Hueber D, Franceschini MA, Gratton E, Rosenfeld W, Stubblefield PG, Maulik D, and Stankovic MR.** Non-invasive optical monitoring of the newborn piglet brain using continuous-wave and frequency-domain methods. *Phys Med Biol* 44: 1543–1563, 1999.

23. **Franceschini MA, Moesta KT, Fantini S, Gaida G, Gratton E, Jess H, Mantulin WW, Seeber M, Schlag PM, and Kaschke M.** Frequency-domain instrumentation enhances optical mammography: initial clinical results. *Proc Natl Acad Sci USA* 94: 6468–6473, 1997.

24. **Franceschini MA, Toronov V, Filiaci ME, Gratton E, and Fantini S.** On-line optical imaging of the human brain with 160-ms temporal resolution. *Opt Express* 6: 49–57, 2000.

25. **Franceschini MA, Wallace D, Barbieri B, Fantini S, Mantulin WW, Pratesi S, Donzelli GP, and Gratton E.** Optical study of the skeletal muscle during exercise with a second generation frequency-domain tissue oximeter. *Proc SPIE* 2979: 807–814, 1997.

26. **Fung YC.** *Biomechanics—Circulation* (2nd ed.). New York: Springer-Verlag, 1997, p. 243.

27. **Gratton E, Fantini S, Franceschini MA, Gratton G, and Fabiani M.** Measurements of scattering and absorption changes in muscle and brain. *Philos Trans R Soc Lond B Biol Sci* 352: 727–735, 1997.

28. **Grosenick D, Wabnitz H, and Rinneberg H.** Time-resolved imaging of solid phantoms for optical mammography. *Appl Opt* 36: 221–231, 1997.

29. **Hamaoka T, Iwane H, Shimomitsu T, Katsumura T, Murase N, Nishio S, Osada T, Kurosawa Y, and Chance B.** Noninvasive measures of oxidative metabolism on working human muscles by near-infrared spectroscopy. *J Appl Physiol* 81: 1410–1417, 1996.

30. **Hoshi Y and Tamura M.** Near-infrared optical detection of sequential brain activation in the prefrontal cortex during mental tasks. *Neuroimage* 5: 292–297, 1997.

31. **Hueber DM, Franceschini MA, Ma HY, Xu Q, Ballesteros JR, Fantini S, Wallace D, Ntziachristos V, and Chance B.** Non-invasive and quantitative near-infrared hemoglobin spectrometry in the piglet brain during hypoxic stress, using a frequency-domain multi-distance instrument. *Phys Med Biol* 46: 41–62, 2001.

32. **Komiyama T, Shigematsu H, Yasuhara H, and Muto T.** Near-infrared spectroscopy grades the severity of intermittent claudication in diabetics more accurately than ankle pressure measurement. *Br J Surg* 87: 459–466, 2000.

33. **Kooijman HM, Hopman MT, Colier WN, van der Vliet JA, and Oeseburg B.** Near infrared spectroscopy for noninvasive assessment of claudication. *J Surg Res* 72: 1–7, 1997.

34. **Liu H, Boas DA, Zhang Y, Yodh AG, and Chance B.** Determination of optical properties and blood oxygenation in tissue using continuous NIR light. *Phys Med Biol* 40: 1983–1993, 1995.

35. **Meek JH, Elwell CE, Khan MJ, Romaya J, Wyatt JS, Delpy DT, and Zeki S.** Regional changes in cerebral haemodynamics as a result of a visual stimulus measured by near infrared spectroscopy. *Proc R Soc Lond B Biol Sci* 261: 351–356, 1995.

36. **Mendelson Y.** Pulse oximetry: theory and applications for non-invasive monitoring. *Clin Chem* 38: 1601–1607, 1992.

37. **Millikan GA.** The oximeter, an instrument for measuring continuously the oxygen saturation of arterial blood in man. *Rev Sci Instrum* 13: 434–444, 1942.

38. **Mohrman DE and Heller LJ.** *Cardiovascular Physiology* (4th ed.). New York: McGraw-Hill, Health Professions Division, 1997, p. 177.

39. **Nitzan M, Babchenko A, Khanokh B, and Taitelbaum H.** Measurement of oxygen saturation in venous blood by dynamic near infrared spectroscopy. *J Biomed Opt* 5: 155–162, 2000.

40. Ntziachristos V, Yodh AG, Schnall M, and Chance B. Concurrent MRI and diffuse optical tomography of breast after indocyanine green enhancement. *Proc Natl Acad Sci USA* 97: 2767–2772, 2000.

41. Patterson MS, Chance B, and Wilson BC. Time resolved reflectance and transmittance for the non-invasive measurement of optical properties. *Appl Opt* 28: 2331–2336, 1989.

42. Pogue BW, Poplack SP, McBride TO, Wells WA, Osterman KS, Osterberg UL, and Paulsen KD. Quantitative hemoglobin tomography with diffuse near-infrared spectroscopy: pilot results in the breast. *Radiology* 218: 261–266, 2001.

43. Prahl S. *Optical Absorption of Hemoglobin.* [Online] Oregon Medical Laser Center http://omlc.ogi.edu/spectra/hemoglobin/index.html [2001, May 10]

44. Quaresima V and Ferrari M. Assessment of quadriceps oxygenation in patients with myopathies by near infrared spectroscopy. *Neurology* 51: 1238–1239, 1998.

45. Sako T, Hamaoka T, Higuchi H, Kurosawa Y, and Katsumura T. Validity of NIR spectroscopy for quantitatively measuring muscle oxidative metabolic rate in exercise. *J Appl Physiol* 90: 338–344, 2001.

46. Shah N, Cerussi A, Eker C, Espinoza J, Butler J, Fishkin J, Hornung R, and Tromberg B. Noninvasive functional optical spectroscopy of human breast tissue. *Proc Natl Acad Sci USA* 98: 4420–4425, 2001.

47. Skov L, Pryds O, Greisen G, and Lou H. Estimation of cerebral venous saturation in newborn infants by near infrared spectroscopy. *Pediatr Res* 33: 52–55, 1993.

48. Topulos GP, Lipsky NR, Lehr JL, Rogers RA, and Butler JP. Fractional changes in lung capillary blood volume and oxygen saturation during the cardiac cycle in rabbits. *J Appl Physiol* 82: 1668–1676, 1997.

49. Varela JE, Cohn SM, Giannotti GD, Dolich MO, Ramon H, Wiseberg JA, and McKenney M. Near-infrared spectroscopy reflects changes in mesenteric and systemic perfusion during abdominal compartment syndrome. *Surgery* 129: 363–370, 2001.

50. Villringer A and Chance B. Non-invasive optical spectroscopy and imaging of human brain function. *Trends Neurosci* 20: 435–442, 1997.

51. Watzman HM, Kurth CD, Montenegro LM, Rome J, Steven JM, and Nicolson SC. Arterial and venous contributions to near-infrared cerebral oximetry. *Anesthesiology* 93: 947–953, 2000.

52. Wolf M, Duc G, Keel M, and Niederer P. Continuous noninvasive measurement of cerebral arterial and venous oxygen saturation at the bedside in mechanically ventilated neonates. *Crit Care Med* 9: 1579–1582, 1997.

53. Wray S, Cope M, Delpy DT, Wyatt JS, and Reynolds EOR. Characterization of the near infrared absorption spectra of cytochrome aa₃ and haemoglobin for the non-invasive monitoring of cerebral oxygenation. *Biochim Biophys Acta* 933: 184–192, 1988.

54. Yoxall CW, Weindling AM, Dawani NH, and Peart I. Measurement of cerebral venous oxyhemoglobin saturation in children by near-infrared spectroscopy and partial jugular venous occlusion. *Pediatr Res* 38: 319–323, 1995.

55. Yoxall CW and Weindling AM. The measurement of peripheral venous oxyhemoglobin saturation in newborn infants by near infrared spectroscopy with venous occlusion. *Pediatr Res* 39: 1103–1106, 1996.

56. Yoxall CW and Weindling AM. Measurement of venous oxyhaemoglobin saturation in the adult human forearm by near infrared spectroscopy with venous occlusion. *Med Biol Eng Comput* 35: 331–336, 1997.

HANDBOOK OF
Optical Biomedical Diagnostics

Valery V. Tuchin
Editor

Published by

Printed in the United States of America.

FREQUENCY-DOMAIN TECHNIQUES FOR TISSUE SPECTROSCOPY AND IMAGING

Sergio Fantini
Maria Angela Franceschini
Tufts University, USA

CONTENTS

7.1 INTRODUCTION

In frequency-domain spectroscopy, the intensity of the light source is sinusoidally modulated at a frequency f. One can fully describe the modulated intensity using three parameters: namely, the average intensity (DC intensity), the amplitude of the intensity oscillations (AC amplitude), and the phase (Φ) of the intensity wave. The modulation is defined by the ratio AC/DC. Because the phase measurement and the intensity modulation are the key features of frequency-domain spectroscopy, the term *phase modulation* is sometimes used interchangeably with *frequency domain*. The phase measurement is related to the time-delay experienced by the probing intensity wave. If τ is a typical time delay, the phase is of the order of $\omega\tau$, where $\omega = 2\pi f$ is the angular modulation frequency. To obtain phase measurements with good signal-to-noise ratio, it is required that $\omega\tau \sim 1$, which is the condition that guides the choice of the modulation frequency, f. In the case of near-infrared spectroscopy and imaging of tissues, $\tau \sim 1$ ns for source-detector separations on the order of a few centimeters.[1,2] Consequently, the condition $\omega\tau \sim 1$ determines $f \sim 100$ MHz, which falls within the radio-frequency range. The 100-MHz frequency range is the one typically used for frequency-domain optical studies of biological tissues.

In this chapter, we describe the frequency-domain instrumentation (Section 7.2), the theoretical modeling of light propagation in tissue (Section 7.3), and *in vivo* applications of frequency-domain spectroscopy (Section 7.4) and imaging (Section 7.5). We have tried to make this chapter self-contained, while providing extensive reference to the literature as a guide for additional reading and for in-depth coverage of topics that are only briefly mentioned here.

7.2 INSTRUMENTATION, MODULATION METHODS, AND SIGNAL DETECTION

Frequency-domain spectroscopy can be implemented using several instrumental schemes. For instance, homodyne techniques [in-phase quadrature (IQ), or zero-cross detection] perform amplitude and phase measurements without down-converting the radio frequency, while heterodyne detection (using two oscillators) relies on down conversion of the radio frequency from the 100-MHz range to the kilohertz range. Furthermore, signal processing may involve zero crossing detectors and analog filters, or analog-to-digital conversion and Fourier filters. A comprehensive review of the instrumentation for optical studies of tissue in the frequency domain can be found in Ref. [3]. In Sections 7.2.1–7.2.5, we describe the various light sources and modulation methods, and the principles of heterodyne detection with digital signal processing and Fourier filtering. In Section 7.2.6, we describe a specific frequency-domain instrument for near-infrared tissue spectroscopy.

7.2.1 Lasers and Arc Lamps

The emission of continuous-wave lasers and arc lamps can be modulated using devices based on the electro-optical (Pockels cells)[4] or acousto-optical[5,6] effect. A Pockels cell is a birefringent crystal whose indices of refraction can be varied by applying an electric field. The application of a time-varying voltage to the Pockels cell modulates the relative phase delay of the light components polarized along the two principal axes of the cell. If this relative phase delay, or retardation, oscillates between 0 and π when the modulated Pockels cell is sandwiched between two crossed linear polarizers, each at an angle of 45 deg with respect to the principal axes of the cell, one achieves an intensity modulator. In fact, no light is transmitted when the retardation is 0, while all light is transmitted when the retardation is π. An acousto-optic modulator is a material that uses piezoelectric and photoelastic effects to convert an oscillating electric field into mechanical vibrations, which in turn induce a spatially dependent index of refraction. When a standing acoustic wave is established, the acousto-optic crystal behaves as an oscillating refractive index grating that modulates the transmitted light by time-varying diffraction. Both electro-optic and acousto-optic devices require the light beam to be collimated. In the case of arc lamps, appropriate collimation optics are required. Pockels cells provide effective modulations up to about 500 MHz, and acousto-optic modulators up to about 300 MHz.

The wavelength of the laser is chosen on the basis of the requirements of the particular application (absorption band of a chromophore, optimal penetration depth in tissues, etc.). Examples of externally modulated CW lasers suitable for optical studies of tissues include the krypton ion (647 nm) and He-Ne (633 nm) lasers. Dye lasers pumped by either argon or krypton lasers afford continuous tunability over a wide spectral range that covers the whole visible band. Arc lamps (Xe, Xe-Hg, etc.) provide continuous spectral emission from the UV (230 nm) to the near-infrared (1100 nm). Therefore, they are ideal sources for spectroscopic studies when a wide and continuous spectral range is required.

7.2.2 Pulsed Sources

It is possible to achieve a large modulation bandwidth by exploiting the harmonic content of pulsed sources with high repetition rates. These sources can be either mode-locked pulsed lasers (Nd:YAG, Ti:sapphire, dye lasers, etc.)[7] or synchrotron radiation.[8,9] The repetition rate of the pulses gives the fundamental frequency, whereas the pulse width determines the width of the power spectrum band. The power spectrum of mode-locked lasers extends well above 10 GHz, an upper limit in frequency-domain spectroscopy imposed by the optical detectors rather than the light sources. The wavelengths of the above-mentioned lasers are 1064 nm for the Nd:YAG, 660–1180 nm (tunable) for the Ti:sapphire, and 625–780 nm (tunable) for dye lasers using DCM or oxanine 1 dyes. A unique pulsed source is provided by synchrotron radiation, which continuously covers the UV/visible/near-infrared spectrum.

7.2.3 LASER DIODES AND LIGHT-EMITTING DIODES (LEDs)

Semiconductor lasers and LEDs can be intensity modulated by driving them with an oscillating current. As a result of the relatively fast response time of laser diodes, they can be modulated at frequencies up to the gigahertz range. The LEDs' modulation frequency bandwidth is typically limited to 150 MHz, and they emit light over a spectral bandwidth of about 50–80 nm. Consequently, LEDs can be used to measure continuous spectra.[10] For frequency-domain tissue spectroscopy, one can find a number of laser diodes and LEDs emitting in the wavelength region of interest extending from 600 to 1300 nm. Laser diodes are the most commonly used light sources in frequency-domain optical studies of tissue because of their cost-effectiveness, ease of modulation, and effective coupling to fiber optics, in addition to the fact that tissue spectroscopy can be effectively performed using a few discrete wavelengths (see Sections 7.4.2 and 7.4.3).

7.2.4 OPTICAL DETECTORS

Optical detectors employed in frequency-domain spectroscopy include photomultiplier tubes (PMTs),[11–14] microchannel plate photomultipliers (MCP-PMT),[15,16] avalanche photodiodes (APD),[17,18] and charge-coupled device (CCD) cameras in conjunction with a gated image intensifier.[19,20] In all cases, the down-conversion from the source modulation frequency f to the cross-correlation frequency Δf (see Section 7.2.5) can occur either internally to the detector by modulating the detector gain at frequency $f + \Delta f$, or externally by electronically mixing the detector output at frequency f with the down-conversion signal at frequency $f + \Delta f$. Photomultiplier tubes are very sensitive detectors. The cathode sensitivity is typically 50 mA/W, and a current amplification by about 10^7 determines an anode sensitivity as high as 1 A/μW. PMTs can operate in the visible and in the near-infrared up to about 1000 nm. For internal down-conversion, their gain is modulated by a signal applied to the second dynode of the amplification chain. The typical rise time of a PMT, which is in the nanosecond range, allows for a modulation bandwidth of several hundred megahertz. The faster response of microchannel plates makes them suitable devices for modulation frequencies of up to several gigahertz. The frequency down-conversion can be performed by modulating the grid of the MCP-PMT[15] or by feeding the MCP-PMT output into an electronic mixer.[16] CCD cameras with modulated image intensifiers are powerful tools for frequency-domain spectroscopy, microscopy, and imaging. Finally, avalanche photodiodes can work at higher modulation frequencies and/or longer wavelengths than those allowed by PMTs. The APD output is usually directed to an electronic mixer for frequency down-conversion.

7.2.5 HETERODYNE DETECTION, DIGITAL SIGNAL PROCESSING, AND FOURIER FILTERING

Heterodyne detection consists of down-converting the frequency f of the detected signal to a lower-frequency Δf. In the digital acquisition method,[21] after current-

to-voltage conversion and low-pass filtering, the low-frequency signal is digitized. The A/D sampling rate is an integer multiple of $\Delta f (n \Delta f)$, so that the digital sampling is synchronous with the cross-correlation signal. The sampling theorem[22] states that n must be equal to at least 2 for the complete determination of the harmonic at frequency Δf. A higher sampling rate allows for the discrimination of higher harmonics. Typical values of n range from 4 to 256. The digital signal processing consists of a preliminary average of the data sampled over a number of cross-correlation periods, followed by the discrimination of the frequency harmonic at Δf by discrete Fourier transform. The first filter (averaging) causes destructive interference of all the frequencies that are not multiples of Δf, while the discrete Fourier transform resolves each harmonic of Δf. The rejection of higher harmonics is accomplished by a factor greater than 2000 (Ref. [21]). Figure 7.1 shows a schematic illustration of the heterodyne detection and digital acquisition.

7.2.6 A FREQUENCY-DOMAIN TISSUE SPECTROMETER

We now describe a specific frequency-domain instrument for near-infrared spectroscopy and imaging of tissues. After the initial design and the implementation of a working prototype at the University of Illinois,[23] this instrument has undergone engineering and software development at ISS, Inc., Champaign, IL. A schematic diagram of the instrument is shown in Fig. 7.2. The light sources are laser diodes that are DC biased near threshold for laser operation. A superimposed 110-MHz radio-frequency current signal modulates the optical output of the laser diodes with a modulation depth close to 100%. The optical detectors are photomultiplier
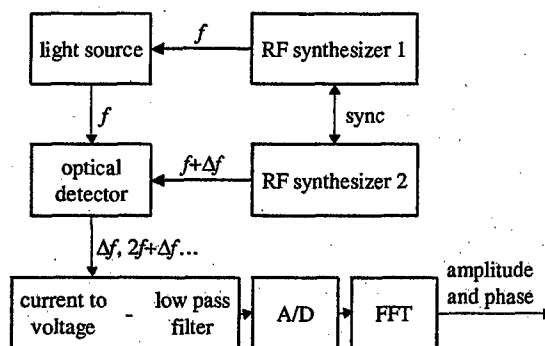
Figure 7.1 Heterodyne detection scheme and digital signal processing with Fourier filter. The intensity of the light source is modulated at a radio-frequency (RF) f, typically on the order of 100 MHz. The beating between the detected signal at frequency f and the down-conversion signal at frequency $f + \Delta f$ determines a low frequency component Δf that is filtered, digitized (A/D), and fast Fourier transformed (FFT) to yield the amplitude and phase readings. The two radio-frequency synthesizers are synchronized (sync).
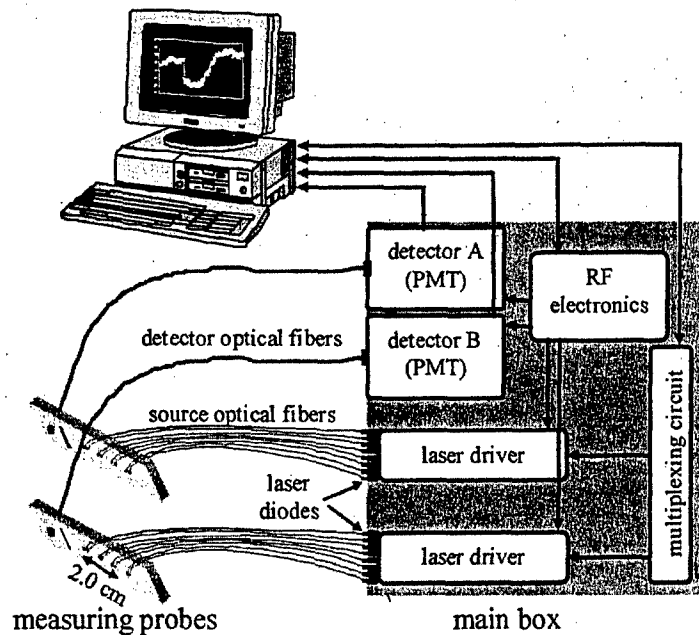
Figure 7.2 Schematic diagram of a frequency-domain tissue spectrometer (Model 96208, ISS, Inc., Champaign, IL). In the configuration for tissue oximetry (shown here), each optical probe contains eight illuminating optical fibers and one detecting optical fiber. These fibers are coupled to eight laser diodes (four emitting at 690 nm and four at 830 nm) and to a photomultiplier tube (PMT) detector, respectively. RF electronics modulate the output of the light sources at a frequency of 110 MHz, and the PMT gain at a frequency of 110.005 MHz. A multiplexing circuit turns the lasers on and off in sequence at an adjustable rate controlled by the software (a typical multiplexing rate of 100 Hz corresponds to a 10-ms on-time per laser). The two optical probes can operate in parallel at two different tissue locations.

tubes (PMTs) (Hamamatsu Photonics R928) whose sensitivity is modulated by a 110.005-MHz signal (amplitude: ~32 dBm) applied to the second dynode. This heterodyne detection scheme down-converts the 110-MHz signal to a frequency of 5 kHz, which is called the cross-correlation frequency. The signal processing proceeds as shown in Fig. 7.1 to yield the average value, the amplitude, and the phase of the detected modulated signal. The choice of the laser diodes for tissue oximetry (case shown in Fig. 7.2) is dictated by the requirement of having two wavelengths on the opposite sides of the isosbestic point at 800 nm for maximal sensitivity (see Section 7.4.3). The choice of laser diodes emitting at 758 nm (Sharp LT030MD) and 830 nm (Sharp LT011MS) is ideal, as these wavelengths correspond to relatively flat portions of the absorption spectra of oxy-hemoglobin and deoxy-hemoglobin (see Fig. 7.4) (in particular, these wavelengths closely match a local maximum and a local minimum, respectively, in the deoxy-hemoglobin spectrum). However, the particular values of these wavelengths are not critical, so

that the 758-nm lasers (now discontinued) can be replaced by 690-nm lasers (for instance, Hitachi HL6738MG). Furthermore, the laser diodes are mounted on interchangeable boards, so that one can change the laser wavelength according to the specific application. For instance, one can use boards containing lasers emitting at eight different wavelengths for tissue spectroscopy (for instance, Fig. 7.5 reports data collected at 633, 670, 751, 776, 786, 814, 830, and 841 nm (Ref. [24])). Alternatively, one can use a laser board containing diodes emitting at the same wavelength to maximize the number of source locations in single-wavelength optical imaging. In general, the instrument provides 2 parallel detectors and 16 sources, resulting in 32 source-detector channels. The optical probes shown in Fig. 7.2 are designed to perform quantitative tissue oximetry. They implement the multidistance measurement scheme[10,25] that was found to be robust and accurate for *in vivo* applications. This scheme consists of placing multiple (in this case, four) source fibers at different distances from the single detector fiber. In this fashion, one measures the spatial dependence of the DC intensity, AC amplitude, and phase data, which is related to the tissue optical coefficients by a diffusion model (see Section 7.3.7). If two wavelengths are used, each illumination location consists of two source fibers (one per wavelength). One of the advantages of the multidistance scheme is its insensitivity to motion artifacts, which allows for measurement while the subject moves or exercises [see Fig. 7.6(c)]. Multiple laser diodes time-share the optical detector by means of a multiplexing circuit that turns the laser diodes on and off in sequence, so that only one laser is on at any given time. The multiplexing rate, which determines the on-time of each laser diode, is adjustable by software. A typical multiplexing rate of 100 Hz corresponds to a 10-ms on-time per diode. The laser rise time, determined by protection circuitry, is about 1 ms. Therefore, the data collected during the first 1 ms of the on-time period of each laser are discarded. During a typical 10-ms-long laser on-time, 45 cross-correlation periods are processed (the 5-kHz cross-correlation frequency corresponds to a period of 0.2 ms). As few as 25 cross-correlation periods (5 ms) can be processed per laser on-time, leading to a maximum multiplexing rate of about 170 Hz. Faster computers and higher cross-correlation frequencies may further increase the data acquisition rate. A number of multiplexing cycles (selected by software) can be averaged to increase the signal-to-noise ratio when fast measurements are not required.

The instrumental noise, which depends on the acquisition time, is typically much smaller than the physiological fluctuations observed *in vivo*. The noise can be estimated by the standard deviation of the temporal fluctuations of the measured data. Figure 7.3 shows typical temporal traces of the average intensity, amplitude, phase, absorption coefficient, and reduced scattering coefficient measured with an acquisition time per diode of 160 ms (average of sixteen 10-ms cycles) on a tissuelike solid phantom (made of silicone). The optical coefficients of the phantom [Fig. 7.3(d)] match typical optical properties of blood-perfused tissues in the near-infrared. The standard deviation errors in the various readings are reported in Table 7.1. The instrumental errors decrease for longer acquisition times.
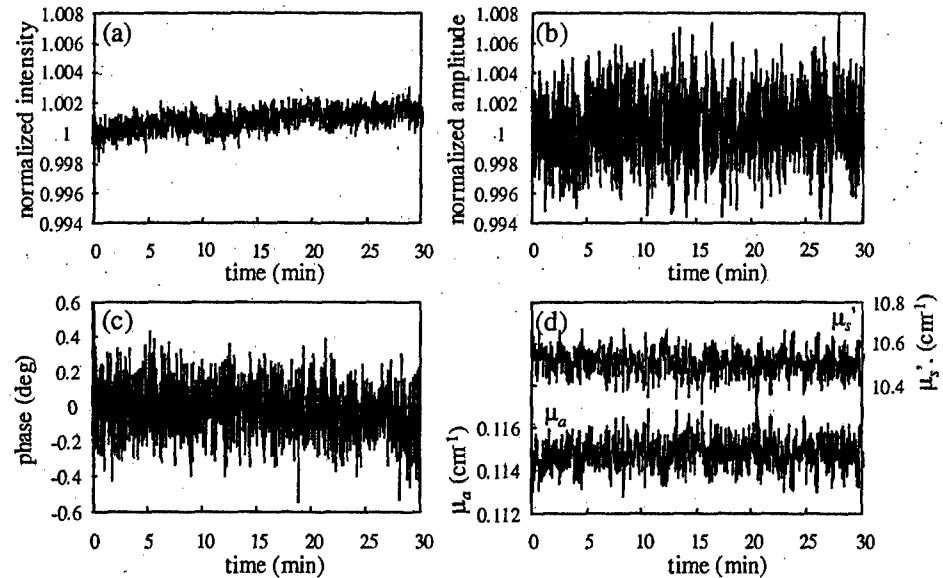
Figure 7.3 Temporal traces of the (a) normalized average intensity, (b) normalized amplitude, (c) phase, and (d) absorption (μ_a) and reduced scattering (μ_s') coefficients measured at 690 nm on a synthetic tissuelike phantom with the instrument of Fig. 7.2. The acquisition time for the average intensity, amplitude, and phase is 160 ms (10 ms on-time per laser diode, 16 multiplexing cycles averaged), and the source-detector separation is 2.5 cm. The four-distance measurement scheme of the absorption and reduced scattering coefficients (range of source-detector separations: 2.0–3.5 cm) determines an acquisition time of 640 ms (160 ms/diode × 4 diodes) for the optical coefficients.

Table 7.1 Instrumental noise estimated by the temporal standard deviation of the raw data (average intensity, amplitude, and phase) and the optical coefficients (absorption and reduced scattering) measured on a solid tissuelike phantom with the frequency-domain tissue spectrometer of Fig. 7.2. The acquisition time for the raw data (average intensity, amplitude, and phase) is 160 ms. Because the measurement of the optical coefficients at each wavelength requires the readings from four source locations (four source-detector separations), the acquisition time for μ_a and μ_s' is 160 ms × 4 = 640 ms).

Parameter	Acquisition time (ms)	Instrumental noise @ 690 nm	@ 830 nm
Average Intensity (DC)	160	0.05%	0.05%
Amplitude (AC)	160	0.2%	0.1%
Phase (Φ)	160	0.1°	0.1°
Absorption coefficient (μ_a)	640	0.0007 cm^{-1}	0.0006 cm^{-1}
Reduced scattering coefficient (μ_s')	640	0.05 cm^{-1}	0.04 cm^{-1}

7.3 Modeling Light Propagation in Scattering Media

7.3.1 The Boltzmann transport equation (BTE)

The Boltzmann transport equation (BTE) is a balance relationship that describes the flow of particles in scattering and absorbing media. The propagation of light in optically turbid media can be modeled by the transport equation, where the photons are treated as the transported particles. If we denote the angular photon density with $u(\mathbf{r}, \hat{\Omega}, t)$, which is defined as the number of photons per unit volume per unit solid angle traveling in direction $\hat{\Omega}$ at position $\mathbf{r}$ and time t, we can write the BTE as follows:[26]

$$\frac{\partial u(\mathbf{r}, \hat{\Omega}, t)}{\partial t} = -v\hat{\Omega} \cdot \nabla u(\mathbf{r}, \hat{\Omega}, t) - v(\mu_a + \mu_s)u(\mathbf{r}, \hat{\Omega}, t)$$

$$+ v\mu_s \int_{4\pi} u(\mathbf{r}, \hat{\Omega}', t)f(\hat{\Omega}', \hat{\Omega})d\hat{\Omega}' + q(\mathbf{r}, \hat{\Omega}, t), \qquad (7.1)$$

where v is the speed of light in the medium, μ_a is the absorption coefficient (units of cm^{-1}), μ_s is the scattering coefficient (units of cm^{-1}), $f(\hat{\Omega}', \hat{\Omega})$ is the phase function or the probability density of scattering a photon that travels along direction $\hat{\Omega}'$ into direction $\hat{\Omega}$, and $q(\mathbf{r}, \hat{\Omega}, t)$ is the source term. $q(\mathbf{r}, \hat{\Omega}, t)$ has units of $s^{-1} m^{-3} sr^{-1}$ and represents the number of photons injected by the light source per unit volume, per unit time, per unit solid angle at position $\mathbf{r}$, time t, and direction $\hat{\Omega}$. The left-hand side of Eq. (7.1) represents the temporal variation of the angular photon density. Each one of the terms on the right-hand side represents a specific contribution to this variation. The first term is the net gain of photons at position $\mathbf{r}$ and direction $\hat{\Omega}$ due to the flow of photons. The second term is the loss of photons at $\mathbf{r}$ and $\hat{\Omega}$ as a result of collisions (absorption and scattering). The third term is the gain of photons at $\mathbf{r}$ and $\hat{\Omega}$ due to scattering. Finally, the fourth term is the gain of photons due to the light sources. Let us now define some of the quantities used to describe photon transport.

Angular photon density: $u(\mathbf{r}, \hat{\Omega}, t)$
$u(\mathbf{r}, \hat{\Omega}, t)$ is defined such that $u(\mathbf{r}, \hat{\Omega}, t)dr d\hat{\Omega}$ represents the number of photons in dr that travel in a direction within $d\hat{\Omega}$ around $\hat{\Omega}$. The units of $u(\mathbf{r}, \hat{\Omega}, t)$ are $m^{-3} sr^{-1}$.

Photon radiance: $L(\mathbf{r}, \hat{\Omega}, t)$
$L(\mathbf{r}, \hat{\Omega}, t) = vu(\mathbf{r}, \hat{\Omega}, t)$. $L(\mathbf{r}, \hat{\Omega}, t)d\hat{\Omega}$ represents the number of photons traveling per unit time per unit area (perpendicular to $\hat{\Omega}$) in a range of directions within $d\hat{\Omega}$ around $\hat{\Omega}$. The units of $L(\mathbf{r}, \hat{\Omega}, t)$ are $s^{-1} m^{-2} sr^{-1}$.

Photon density: $U(\mathbf{r}, t)$
$U(\mathbf{r}, t) = \int_{4\pi} u(\mathbf{r}, \hat{\Omega}, t)d\hat{\Omega}$. The photon density is the number of photons per unit volume. The units are m^{-3}.

Photon fluence rate: $E_0(\mathbf{r}, t)$

$E_0(\mathbf{r}, t) = vU(\mathbf{r}, t) = \int_{4\pi} L(\mathbf{r}, \hat{\Omega}, t)d\hat{\Omega}$. The photon fluence rate is defined as the number of photons traveling per unit time per unit area (perpendicular to the direction of propagation) over all directions. The units are $s^{-1}\,m^{-2}$.

Photon current density, or photon flux: $\mathbf{J}(\mathbf{r}, t)$

$\mathbf{J}(\mathbf{r}, t) = \int_{4\pi} L(\mathbf{r}, \hat{\Omega}, t)\hat{\Omega}d\hat{\Omega}$. The photon flux is a vector that represents the net flow of photons. Its direction points in the direction of the net flux, while its amplitude gives the net number of photons transmitted per unit time per unit area in that direction. The units of $\mathbf{J}(\mathbf{r}, t)$ are $s^{-1}\,m^{-2}$.

The above definitions can be extended to describe radiant energy (instead of photon number) by replacing the word "photon" with "energy," and by introducing a factor $h\nu$ in all definitions ($h\nu$ is the energy per photon, where h is Planck's constant and ν is the light frequency). A complete nomenclature for quantities used in medical optics can be found in Ref. [27].

7.3.2 EXPANSION OF THE BOLTZMANN EQUATION IN SPHERICAL HARMONICS

To model light propagation in highly scattering media, as are most biological tissues, it is useful to expand the angular photon density $u(\mathbf{r}, \hat{\Omega}, t)$, the source term $q(\mathbf{r}, \hat{\Omega}, t)$, and the phase function $f(\hat{\Omega}', \hat{\Omega})$ into spherical harmonics $Y_l^m(\hat{\Omega})$.[28–30] The so-called P_N approximation to the Boltzmann equation (see Section 7.3.3) is based on such an expansion. As a result of the completeness property of the spherical harmonics, any function $h(\theta, \varphi)$ (with sufficient continuity properties) can be expanded in the Laplace series:[31]

$$h(\theta, \varphi) = \sum_{l=0}^{\infty} \sum_{m=-l}^{l} h_{lm} Y_l^m(\hat{\Omega}), \qquad (7.2)$$

where h_{lm} are coefficients independent of θ and φ, and the relationship among θ, φ, and $\hat{\Omega}$ is $\hat{\Omega} = \sin\theta \cos\varphi\hat{\mathbf{x}} + \sin\theta \sin\varphi\hat{\mathbf{y}} + \cos\theta\hat{\mathbf{z}}$. Accordingly, we expand $u(\mathbf{r}, \hat{\Omega}, t)$ and $q(\mathbf{r}, \hat{\Omega}, t)$ into spherical harmonics as follows:

$$u(\mathbf{r}, \hat{\Omega}, t) = \sum_{l=0}^{\infty} \sum_{m=-l}^{l} u_{lm}(\mathbf{r}, t)Y_l^m(\hat{\Omega}), \qquad (7.3)$$

$$q(\mathbf{r}, \hat{\Omega}, t) = \sum_{l=0}^{\infty} \sum_{m=-l}^{l} q_{lm}(\mathbf{r}, t)Y_l^m(\hat{\Omega}). \qquad (7.4)$$

We assume that the phase function $f(\hat{\Omega}', \hat{\Omega})$ only depends on $\hat{\Omega}' \cdot \hat{\Omega}$ (i.e., on the cosine of the scattering angle γ). We can thus expand $f(\hat{\Omega}', \hat{\Omega})$ in Legendre poly-

nomials, by recalling that a function $H(x)$ (which is sectionally continuous together with its derivative in the interval $[-1, 1]$) has the general Legendre series representation[31]

$$H(x) = \sum_{l=0}^{\infty} \frac{2l+1}{2} H_l P_l(x), \tag{7.5}$$

where $P_l(x)$ is the Legendre polynomial of order l, and $H_l = \int_{-1}^{1} H(x')P_l(x')dx'$. We then write

$$f(\hat{\Omega}' \cdot \hat{\Omega}) = \sum_{l=0}^{\infty} \frac{2l+1}{4\pi} f_l P_l(\hat{\Omega}' \cdot \hat{\Omega})$$

$$= \sum_{l=0}^{\infty} \sum_{m=-l}^{l} f_l Y_l^{m*}(\hat{\Omega}') Y_l^m(\hat{\Omega}), \tag{7.6}$$

where the last expression follows from the addition theorem for spherical harmonics,[31] namely $P_l(\hat{\Omega}' \cdot \hat{\Omega}) = 4\pi/(2l+1) \sum_{m=-l}^{l} Y_l^{m*}(\hat{\Omega}')Y_l^m(\hat{\Omega})$. Here, $f_l = 2\pi \int_{-1}^{1} f(\cos\gamma)P_l(\cos\gamma)d(\cos\gamma)$.

By substituting these expressions into Eq. (7.1), we obtain

$$\sum_{l=0}^{\infty} \sum_{m=-l}^{l} \left\{ \left[\frac{\partial}{\partial t} + v\hat{\Omega} \cdot \nabla + v(\mu_a + \mu_s) \right] u_{lm}(\mathbf{r}, t) Y_l^m(\hat{\Omega}) - q_{lm}(\mathbf{r}, t) Y_l^m(\hat{\Omega}) \right.$$

$$\left. - v\mu_s \int_{4\pi} u_{lm}(\mathbf{r}, t) Y_l^m(\hat{\Omega}') \sum_{l'=0}^{\infty} \sum_{m'=-l'}^{l'} f_{l'} Y_{l'}^{m'*}(\hat{\Omega}') Y_{l'}^{m'}(\hat{\Omega}) d\hat{\Omega}' \right\} = 0. \tag{7.7}$$

The integral in $d\hat{\Omega}'$ can be calculated using the orthogonality property of the spherical harmonics: $\int_{4\pi} Y_l^{m*}(\hat{\Omega}) Y_{l'}^{m'}(\hat{\Omega}) d\hat{\Omega} = \delta_{ll'} \delta_{mm'}$. The BTE thus becomes

$$\sum_{l=0}^{\infty} \sum_{m=-l}^{l} \left(\left\{ \frac{\partial}{\partial t} + v\hat{\Omega} \cdot \nabla + v[\mu_s(1 - f_l) + \mu_a] \right\} u_{lm}(\mathbf{r}, t) - q_{lm}(\mathbf{r}, t) \right) Y_l^m(\hat{\Omega}) = 0. \tag{7.8}$$

We then multiply this equation by $Y_L^{M*}(\hat{\Omega})$ and integrate over $\hat{\Omega}$ to obtain the relationship between the specific coefficients u_{LM} and q_{LM}, and all the coefficients of the spherical harmonic expansion of u, u_{lm}:

$$\frac{\partial}{\partial t} u_{LM}(\mathbf{r}, t) + v[\mu_s(1 - f_l) + \mu_a] u_{LM}(\mathbf{r}, t)$$

$$+ v \sum_{l=0}^{\infty} \sum_{m=-l}^{l} \int_{4\pi} \hat{\Omega} \cdot \nabla u_{lm}(\mathbf{r}, t) Y_l^m(\hat{\Omega}) Y_L^{M*}(\hat{\Omega}) d\hat{\Omega} = q_{LM}(\mathbf{r}, t). \tag{7.9}$$

The integral over $\hat{\Omega}$ can be evaluated by writing the x, y, and z components of the vector $Y_L^M(\hat{\Omega})\hat{\Omega}$ in terms of spherical harmonics. This can be done by using the recurrence relations for the associated Legendre functions $P_l^m(x)$. The result is the following:

$$
\begin{aligned}
Y_L^M(\hat{\Omega})\Omega_x = {} & Y_L^M(\hat{\Omega})\sin\theta\cos\varphi \\
= {} & -\frac{1}{2}\left[\frac{(L+M+1)(L+M+2)}{(2L+1)(2L+3)}\right]^{1/2} Y_{L+1}^{M+1}(\hat{\Omega}) \\
& +\frac{1}{2}\left[\frac{(L-M)(L-M-1)}{(2L-1)(2L+1)}\right]^{1/2} Y_{L-1}^{M+1}(\hat{\Omega}) \\
& +\frac{1}{2}\left[\frac{(L-M+1)(L-M+2)}{(2L+1)(2L+3)}\right]^{1/2} Y_{L+1}^{M-1}(\hat{\Omega}) \\
& -\frac{1}{2}\left[\frac{(L+M)(L+M-1)}{(2L-1)(2L+1)}\right]^{1/2} Y_{L-1}^{M-1}(\hat{\Omega}),
\end{aligned}
\tag{7.10}
$$

$$
\begin{aligned}
Y_L^M(\hat{\Omega})\Omega_y = {} & Y_L^M(\hat{\Omega})\sin\theta\sin\varphi \\
= {} & -\frac{1}{2i}\left[\frac{(L+M+1)(L+M+2)}{(2L+1)(2L+3)}\right]^{1/2} Y_{L+1}^{M+1}(\hat{\Omega}) \\
& +\frac{1}{2i}\left[\frac{(L-M)(L-M-1)}{(2L-1)(2L+1)}\right]^{1/2} Y_{L-1}^{M+1}(\hat{\Omega}) \\
& -\frac{1}{2i}\left[\frac{(L-M+1)(L-M+2)}{(2L+1)(2L+3)}\right]^{1/2} Y_{L+1}^{M-1}(\hat{\Omega}) \\
& +\frac{1}{2i}\left[\frac{(L+M)(L+M-1)}{(2L-1)(2L+1)}\right]^{1/2} Y_{L-1}^{M-1}(\hat{\Omega}),
\end{aligned}
\tag{7.11}
$$

$$
\begin{aligned}
Y_L^M(\hat{\Omega})\Omega_z = {} & Y_L^M(\hat{\Omega})\cos\theta \\
= {} & \left[\frac{(L-M+1)(L+M+1)}{(2L+1)(2L+3)}\right]^{1/2} Y_{L+1}^{M}(\hat{\Omega}) \\
& +\left[\frac{(L-M)(L+M)}{(2L-1)(2L+1)}\right]^{1/2} Y_{L-1}^{M}(\hat{\Omega}).
\end{aligned}
\tag{7.12}
$$

Using these expressions for the x, y, and z components of $Y_L^M(\hat{\Omega})\hat{\Omega}$, it is possible to calculate the integral using the orthogonality relations for spherical harmonics. We find that the relationship between the specific coefficients u_{LM} and q_{LM} does not involve all the coefficients of the spherical harmonic expansion of u, u_{lm}, but it only contains u_{lm} with indices l ranging from $L-1$ to $L+1$, and m ranging from $M-1$ to $M+1$:

$$\frac{\partial}{\partial t}u_{LM}(\mathbf{r},t) + v\big[\mu_s(1-f_L) + \mu_a\big]u_{LM}(\mathbf{r},t)$$

$$+ \frac{1}{2}\left[\frac{(L-M+1)(L-M+2)}{(2L+1)(2L+3)}\right]^{1/2}\left(\frac{\partial}{\partial x} - i\frac{\partial}{\partial y}\right)vu_{L+1}^{M-1}(\mathbf{r},t)$$

$$- \frac{1}{2}\left[\frac{(L+M)(L+M-1)}{(2L+1)(2L-1)}\right]^{1/2}\left(\frac{\partial}{\partial x} - i\frac{\partial}{\partial y}\right)vu_{L-1}^{M-1}(\mathbf{r},t)$$

$$- \frac{1}{2}\left[\frac{(L+M+2)(L+M+1)}{(2L+1)(2L+3)}\right]^{1/2}\left(\frac{\partial}{\partial x} + i\frac{\partial}{\partial y}\right)vu_{L+1}^{M+1}(\mathbf{r},t)$$

$$+ \frac{1}{2}\left[\frac{(L-M-1)(L-M)}{(2L+1)(2L-1)}\right]^{1/2}\left(\frac{\partial}{\partial x} + i\frac{\partial}{\partial y}\right)vu_{L-1}^{M+1}(\mathbf{r},t)$$

$$+ \left[\frac{(L+M+1)(L-M+1)}{(2L+1)(2L+3)}\right]^{1/2}\frac{\partial}{\partial z}vu_{L+1}^{M}(\mathbf{r},t)$$

$$+ \left[\frac{(L-M)(L+M)}{(2L-1)(2L+1)}\right]^{1/2}\frac{\partial}{\partial z}vu_{L-1}^{M}(\mathbf{r},t) = q_{LM}(\mathbf{r},t). \qquad (7.13)$$

7.3.3 THE P_N APPROXIMATION

The expansion of the BTE into spherical harmonics has led to an infinite set of equations with indices L (ranging from 0 to ∞) and M (ranging from $-L$ to L). Truncation of the Laplace series at $L = N$, leads to the so-called P_N approximation. The reason for this name is that the last term in the truncated Laplace series contains $Y_N^M(\hat{\Omega})$ which can be written in terms of the associated Legendre functions $P_N^M(x)$, which in turn can be written in terms of the Legendre polynomial $P_N(x)$. The relationships are the following:

$$Y_N^M(\hat{\Omega}) = (-1)^M\left[\frac{(2N+1)}{4\pi}\frac{(N-M)!}{(N+M)!}\right]^{1/2}P_N^M(\cos\theta)e^{iM\varphi}, \qquad (7.14)$$

$$P_N^M(x) = \left(1-x^2\right)^{M/2}\frac{d^M}{dx^M}P_N(x). \qquad (7.15)$$

7.3.4 THE P_1 APPROXIMATION

We now consider the P_1 approximation, which is often used to describe photon migration in tissues. In the P_1 approximation $u_{LM}(\mathbf{r},t)$ is set to 0 for $L > 1$. In the P_1 approximation, Eq. (7.13) is a set of four equations. The first, for $L = 0$, $M = 0$:

$$\frac{\partial}{\partial t}u_{0,0}(\mathbf{r},t) + v\big[\mu_s(1-f_0) + \mu_a\big]u_{0,0}(\mathbf{r},t) + \frac{1}{2}\sqrt{\frac{2}{3}}\left(\frac{\partial}{\partial x} - i\frac{\partial}{\partial y}\right)vu_{1,-1}(\mathbf{r},t)$$

$$- \frac{1}{2}\sqrt{\frac{2}{3}}\left(\frac{\partial}{\partial x} + i\frac{\partial}{\partial y}\right)vu_{1,1}(\mathbf{r},t) + \sqrt{\frac{1}{3}}\frac{\partial}{\partial z}vu_{1,0}(\mathbf{r},t) = q_{0,0}(\mathbf{r},t); \qquad (7.16)$$

the second, for $L = 1$, $M = -1$:

$$\frac{\partial}{\partial t}u_{1,-1}(\mathbf{r},t) + v[\mu_s(1-f_1)+\mu_a]u_{1,-1}(\mathbf{r},t)$$
$$+\frac{1}{2}\sqrt{\frac{2}{3}}\left(\frac{\partial}{\partial x}+i\frac{\partial}{\partial y}\right)vu_{0,0}(\mathbf{r},t) = q_{1,-1}(\mathbf{r},t); \qquad (7.17)$$

the third, for $L = 1$, $M = 0$:

$$\frac{\partial}{\partial t}u_{1,0}(\mathbf{r},t) + v[\mu_s(1-f_1)+\mu_a]u_{1,0}(\mathbf{r},t)$$
$$+\sqrt{\frac{1}{3}}\frac{\partial}{\partial z}vu_{0,0}(\mathbf{r},t) = q_{1,0}(\mathbf{r},t); \qquad (7.18)$$

and the fourth, for $L = 1$, $M = 1$:

$$\frac{\partial}{\partial t}u_{1,1}(\mathbf{r},t) + v[\mu_s(1-f_1)+\mu_a]u_{1,1}(\mathbf{r},t)$$
$$-\frac{1}{2}\sqrt{\frac{2}{3}}\left(\frac{\partial}{\partial x}-i\frac{\partial}{\partial y}\right)vu_{0,0}(\mathbf{r},t) = q_{1,1}(\mathbf{r},t). \qquad (7.19)$$

The coefficients $u_{0,0}(\mathbf{r},t)$ and $u_{1,M}(\mathbf{r},t)$ are related to the photon density $U(\mathbf{r},t)$ and to the photon flux $\mathbf{J}(\mathbf{r},t)$, respectively. In fact,

$$U(\mathbf{r},t) = \int_{4\pi} u(\mathbf{r},\hat{\Omega},t)d\hat{\Omega}$$
$$= \sum_{l=0}^{\infty}\sum_{m=-l}^{l} u_{lm}(\mathbf{r},t)\int_{4\pi} Y_l^m(\hat{\Omega})d\hat{\Omega} = \sqrt{4\pi}u_{0,0}(\mathbf{r},t), \qquad (7.20)$$

(since $\int_{4\pi}Y_l^m(\hat{\Omega})d\hat{\Omega} = 0$ for $m \neq 0$ and $Y_0^0(\hat{\Omega}) = 1/\sqrt{4\pi}$), and

$$\mathbf{J}(\mathbf{r},t) = \int_{4\pi} vu(\mathbf{r},\hat{\Omega},t)\hat{\Omega}d\hat{\Omega}$$
$$= \sum_{l=0}^{\infty}\sum_{m=-l}^{l} vu_{lm}(\mathbf{r},t)\int_{4\pi}(\sin\theta\cos\varphi\hat{\mathbf{x}}+\sin\theta\sin\varphi\hat{\mathbf{y}}+\cos\theta\hat{\mathbf{z}})Y_l^m(\hat{\Omega})d\hat{\Omega}$$
$$= \sum_{l=0}^{\infty}\sum_{m=-l}^{l} vu_{lm}(\mathbf{r},t)$$
$$\times \int_{4\pi}\sqrt{\frac{4\pi}{3}}\left\{\begin{array}{l}\sqrt{\frac{1}{2}}[-Y_1^{1*}(\hat{\Omega})+Y_1^{-1*}(\hat{\Omega})]\hat{\mathbf{x}}\\+\sqrt{\frac{1}{2}}\frac{1}{i}[Y_1^{1*}(\hat{\Omega})+Y_1^{-1*}(\hat{\Omega})]\hat{\mathbf{y}}+Y_1^0(\hat{\Omega})\hat{\mathbf{z}}\end{array}\right\}Y_l^m(\hat{\Omega})d\hat{\Omega}$$

$$= \sqrt{\frac{4\pi}{3}} v \bigg[\sqrt{\frac{1}{2}} (-u_{1,1}(\mathbf{r},t) + u_{1,-1}(\mathbf{r},t)) \hat{\mathbf{x}}$$

$$- i\sqrt{\frac{1}{2}} (u_{1,1}(\mathbf{r},t) + u_{1,-1}(\mathbf{r},t)) \hat{\mathbf{y}} + u_{1,0}(\mathbf{r},t) \hat{\mathbf{z}} \bigg]. \qquad (7.21)$$

The set of four Eqs. (7.16)–(7.19) of the P_1 approximation are thus equivalent to the following two equations (one scalar and one vectorial):

$$\frac{\partial}{\partial t} U(\mathbf{r},t) + v\big[\mu_s(1-f_0) + \mu_a\big] U(\mathbf{r},t) + \nabla \cdot \mathbf{J}(\mathbf{r},t) = \sqrt{4\pi} q_{0,0}(\mathbf{r},t), \quad (7.22)$$

$$\frac{1}{v}\frac{\partial}{\partial t}\mathbf{J}(\mathbf{r},t) + \big[\mu_s(1-f_1) + \mu_a\big]\mathbf{J}(\mathbf{r},t) + \frac{1}{3}v\nabla U(\mathbf{r},t)$$

$$= \sqrt{\frac{4\pi}{3}} \bigg[\sqrt{\frac{1}{2}} (q_{1,-1}(\mathbf{r},t) - q_{1,1}(\mathbf{r},t)) \hat{\mathbf{x}}$$

$$- i\sqrt{\frac{1}{2}} (q_{1,-1}(\mathbf{r},t) + q_{1,1}(\mathbf{r},t)) \hat{\mathbf{y}} + q_{1,0}(\mathbf{r},t) \hat{\mathbf{z}} \bigg]. \qquad (7.23)$$

The vectorial equation is obtained by combining Eqs. (7.17), (7.18), (7.19) according to the following formal relationship:

$$\sqrt{2\pi/3}[(7.17) - (7.19)]\hat{\mathbf{x}} - i\sqrt{2\pi/3}[(7.17) + (7.19)]\hat{\mathbf{y}} + \sqrt{4\pi/3}(7.18)\hat{\mathbf{z}}.$$

From the general definition of the coefficients f_l, we find that f_0 and f_1 are given by

$$f_0 = 2\pi \int_{-1}^{1} f(\cos\gamma) P_0(\cos\gamma) d(\cos\gamma) = 2\pi \int_{-1}^{1} f(\cos\gamma) d(\cos\gamma) = 1, \quad (7.24)$$

$$f_1 = 2\pi \int_{-1}^{1} f(\cos\gamma) P_1(\cos\gamma) d(\cos\gamma)$$

$$= 2\pi \int_{-1}^{1} f(\cos\gamma) \cos\gamma \, d(\cos\gamma) = \langle\cos\gamma\rangle, \qquad (7.25)$$

where in Eq. (7.24) we have used the fact that the scattering probability is normalized according to the condition $\int_{4\pi} f(\hat{\Omega}' \cdot \hat{\Omega}) d\hat{\Omega}' = 1$, which is equivalent to $2\pi \int_{-1}^{1} f(\cos\gamma) d(\cos\gamma) = 1$. Therefore f_0 is 1, whereas f_1 is the average cosine of the scattering angle γ ($\langle\cos\gamma\rangle$). The source terms in Eqs. (7.22) and (7.23) are formally a monopole term (spherically symmetric) and a dipole term, respectively.

We will indicate them with the symbols $S_0(\mathbf{r}, t)$ and $\mathbf{S}_1(\mathbf{r}, t)$, respectively. The final expressions for the P_1 equations are

$$\frac{\partial}{\partial t} U(\mathbf{r}, t) + v\mu_a U(\mathbf{r}, t) + \nabla \cdot \mathbf{J}(\mathbf{r}, t) = S_0(\mathbf{r}, t), \qquad (7.26)$$

$$\frac{1}{v} \frac{\partial}{\partial t} \mathbf{J}(\mathbf{r}, t) + \left[\mu_s (1 - \langle \cos\gamma \rangle) + \mu_a \right] \mathbf{J}(\mathbf{r}, t) + \frac{1}{3} v \nabla U(\mathbf{r}, t) = \mathbf{S}_1(\mathbf{r}, t). \quad (7.27)$$

7.3.5 THE REDUCED SCATTERING COEFFICIENT

Equations (7.26) and (7.27) show that, in the P_1 approximation, μ_s and $\cos\gamma$ only appear in the term $\mu_s(1 - \langle \cos\gamma \rangle)$. In this section, we give a physical meaning to this term on the basis of an analysis reported by Zaccanti et al.[32] Suppose that a photon is emitted at the point $P_0 \equiv (0, 0, 0)$ in direction $\hat{\mathbf{z}}$. This photon will first be scattered at a point $P_1 \equiv (x_1, y_1, z_1)$ after having traveled a distance r_1. Then it will be scattered at point $P_2 \equiv (x_2, y_2, z_2)$ after having traveled a distance r_2, and so on. In general, we refer to the scattering at point P_n as the n-th order scattering. We want to define the reduced scattering coefficient, μ_s', as the inverse of the average distance projected along the z axis that the photon has to travel to lose memory of the initial direction of propagation. In other words, $1/\mu_s'$ represents the average distance between what are effectively isotropic scattering events. In the derivation of μ_s', we neglect the absorption of the medium, since we are only interested in its scattering properties. The probability density, $g(r)$, of traveling a distance r without suffering a scattering event is defined as $g(r) = \mu_s e^{-\mu_s r}$. The first order scattering occurs at $P_1 \equiv (0, 0, r_1)$, whose average coordinates are[32]

$$\langle x_1 \rangle = \langle y_1 \rangle = 0,$$

$$\langle z_1 \rangle = \int_0^\infty r_1 g(r_1) dr_1 = \frac{1}{\mu_s}. \qquad (7.28)$$

The second order scattering occurs at $P_2 \equiv (r_2 \sin\theta_2 \cos\varphi_2, r_2 \sin\theta_2 \sin\varphi_2, z_1 + r_2 \cos\theta_2$. Since $r_1, r_2, \theta_2, \varphi_2$ are not statistically correlated, the average values of the coordinates of P_2 are[32]

$$\langle x_2 \rangle = \langle r_2 \rangle \langle \sin\theta_2 \rangle \langle \cos\varphi_2 \rangle = 0,$$

$$\langle y_2 \rangle = \langle r_2 \rangle \langle \sin\theta_2 \rangle \langle \sin\varphi_2 \rangle = 0, \qquad (7.29)$$

$$\langle z_2 \rangle = \langle r_1 \rangle + \langle r_2 \rangle \langle \cos\theta_2 \rangle = \frac{1}{\mu_s} \left(1 + \langle \cos\gamma \rangle \right).$$

The third order scattering occurs at $P_3 \equiv (x_3, y_3, z_3)$ where:

$$x_3 = x_2 + r_3(\sin\theta_3 \cos\varphi_3 \cos\theta_2 \cos\varphi_2 - \sin\theta_3 \sin\varphi_3 \sin\varphi_2 + \cos\theta_3 \sin\theta_2 \cos\varphi_2),$$

$$y_3 = y_2 + r_3(\sin\theta_3 \cos\varphi_3 \cos\theta_2 \sin\varphi_2 + \sin\theta_3 \sin\varphi_3 \cos\varphi_2 + \cos\theta_3 \sin\theta_2 \sin\varphi_2),$$

$$z_3 = z_2 + r_3(-\sin\theta_3 \cos\varphi_3 \sin\theta_2 + \cos\theta_3 \cos\theta_2). \qquad (7.30)$$

The average values of the coordinates of P_3 are[32]

$$\langle x_3 \rangle = \langle y_3 \rangle = 0,$$

$$\langle z_3 \rangle = \frac{1}{\mu_s}\left(1 + \langle \cos\theta \rangle + \langle \cos\theta \rangle^2\right). \tag{7.31}$$

In general, at the n-th order of scattering, the average values of the coordinates of the scattering point P_n are[32]

$$\langle x_n \rangle = \langle y_n \rangle = 0,$$

$$\langle z_n \rangle = \frac{1}{\mu_s}\sum_{k=0}^{n-1}\langle \cos\gamma \rangle^k = \frac{1 - \langle \cos\gamma \rangle^n}{\mu_s(1 - \langle \cos\gamma \rangle)}, \tag{7.32}$$

where we have used the result for the geometric series $\sum_{k=0}^{n-1} a^k = (1 - a^n)/(1 - a)$, with $a < 1$. In the limit of a high number of scattering events ($n \to \infty$), $\langle x_\infty \rangle = \langle y_\infty \rangle = 0$ and $\langle z_\infty \rangle = 1/[\mu_s(1 - \langle \cos\gamma \rangle)]$ give the coordinates of the center of symmetry of the statistical photon distribution. In particular, the coordinate $\langle z_\infty \rangle$ can be interpreted as the average distance between consecutive, effectively isotropic scattering events, and its inverse is defined as the reduced scattering coefficient μ_s':

$$\mu_s' = \mu_s\left(1 - \langle \cos\gamma \rangle\right). \tag{7.33}$$

In the case of isotropic scattering, $\langle \cos\gamma \rangle = 0$ and $\mu_s' = \mu_s$. In the case of forward scattering, $\langle \cos\gamma \rangle = 1$ and $\mu_s' = 0$.

7.3.6 THE P_1 EQUATION AND THE STANDARD DIFFUSION EQUATION (SDE)

We now reduce the P_1 approximation to a single equation for the photon density $U(\mathbf{r}, t)$. From Eq. (7.27) we obtain $\mathbf{J}(\mathbf{r}, t)$:

$$\mathbf{J}(\mathbf{r}, t) = -\frac{1}{v(\mu_s' + \mu_a)}\frac{\partial}{\partial t}\mathbf{J}(\mathbf{r}, t) - \frac{v}{3(\mu_s' + \mu_a)}\nabla U(\mathbf{r}, t) + \frac{1}{(\mu_s' + \mu_a)}\mathbf{S}_1(\mathbf{r}, t)$$

$$= -\frac{3D}{v^2}\frac{\partial}{\partial t}\mathbf{J}(\mathbf{r}, t) - D\nabla U(\mathbf{r}, t) + \frac{3D}{v}\mathbf{S}_1(\mathbf{r}, t), \tag{7.34}$$

where we have defined the diffusion coefficient $D = v/[3(\mu_s' + \mu_a)]$. By substituting this expression for $\mathbf{J}(\mathbf{r}, t)$ in Eq. (7.26), we get

$$\frac{\partial}{\partial t}U(\mathbf{r}, t) + v\mu_a U(\mathbf{r}, t) - \frac{3D}{v^2}\frac{\partial}{\partial t}\nabla \cdot \mathbf{J}(\mathbf{r}, t) - D\nabla^2 U(\mathbf{r}, t)$$

$$+ \frac{3D}{v}\nabla \cdot \mathbf{S}_1(\mathbf{r}, t) = S_0(\mathbf{r}, t). \tag{7.35}$$

From Eq. (7.26), $\nabla \cdot \mathbf{J}(\mathbf{r}, t) = S_0(\mathbf{r}, t) - \partial/\partial t(U(\mathbf{r}, t)) - v\mu_a U(\mathbf{r}, t)$. By substituting this expression and by rearranging the terms, we finally get the P_1 equation for the photon density:

$$\nabla^2 U(\mathbf{r}, t) = \frac{3}{v^2}\frac{\partial^2 U(\mathbf{r}, t)}{\partial t^2} + \frac{1}{D}\left(1 + \frac{3D}{v}\mu_a\right)\frac{\partial U(\mathbf{r}, t)}{\partial t} + \frac{v\mu_a}{D}U(\mathbf{r}, t)$$
$$- \frac{3}{v^2}\frac{\partial S_0(\mathbf{r}, t)}{\partial t} - \frac{1}{D}S_0(\mathbf{r}, t) + \frac{3}{v}\nabla \cdot \mathbf{S}_1(\mathbf{r}, t). \qquad (7.36)$$

By making a few assumptions, which are often satisfied in the case of light propagation in biological tissue, Eq. (7.36) reduces to the standard diffusion equation (SDE). The assumptions are the following:

(1) Strongly scattering regime, or $\mu_a \ll \mu_s'$. This condition means that a photon, on the average, will undergo many effectively isotropic scattering events before being absorbed. In this case, $3D\mu_a/v \equiv \mu_a/(\mu_a + \mu_s') \ll 1$, and the second term on the right-hand side of Eq. (7.36) reduces to $(1/D)\partial(U(\mathbf{r}, t))/\partial t$.

(2) Time scale of the variations of $U(\mathbf{r}, t)$ and $S_0(\mathbf{r}, t)$ are much greater than the average time between collisions $1/[v(\mu_a + \mu_s')]$. This condition can be expressed by the formal inequality $\partial/\partial t \ll v(\mu_a + \mu_s') \equiv v^2/(3D)$. Consequently,

$$\frac{3}{v^2}\frac{\partial^2 U(\mathbf{r}, t)}{\partial t^2} \ll \frac{1}{D}\frac{\partial U(\mathbf{r}, t)}{\partial t}, \qquad (7.37)$$

$$\frac{3}{v^2}\frac{\partial S_0(\mathbf{r}, t)}{\partial t} \ll \frac{1}{D}S_0(\mathbf{r}, t). \qquad (7.38)$$

In the frequency domain, where the harmonic time dependence is given by a factor $\exp(-i\omega t)$, the time derivative operator becomes a multiplication by $-i\omega$. Here, ω is the angular modulation frequency of the intensity modulation (which should not be confused with the frequency of light). Consequently, this condition poses an upper limit to the modulation frequency given by $\omega \gg v^2/(3D)$. In the case of biological tissues, the SDE usually breaks down at modulation frequencies on the order of 1 GHz.[16]

(3) The source term is isotropic; i.e., $\mathbf{S}_1(\mathbf{r}, t) = 0$.

With these assumptions, the P_1 equation (Eq. 7.36) reduces to the standard diffusion equation:

$$\frac{\partial U(\mathbf{r}, t)}{\partial t} = D\nabla^2 U(\mathbf{r}, t) - v\mu_a U(\mathbf{r}, t) + S_0(\mathbf{r}, t); \qquad (7.39)$$

and the photon flux $\mathbf{J}(\mathbf{r}, t)$ is related to the photon density $U(\mathbf{r}, t)$ by Fick's law:

$$\mathbf{J}(\mathbf{r}, t) = -D\nabla U(\mathbf{r}, t). \tag{7.40}$$

In the frequency domain, $\partial/\partial t \rightarrow -i\omega$ and the diffusion equation takes the form of the Helmholtz equation:

$$\left(\nabla^2 + k^2\right)U(\mathbf{r}) = -\frac{S_0(\mathbf{r})}{D}, \tag{7.41}$$

where $k^2 = (i\omega - v\mu_a)/D$.

7.3.7 SOLUTION OF THE STANDARD DIFFUSION EQUATION IN THE FREQUENCY DOMAIN

The solution to the diffusion equation for a homogeneous, infinite medium containing a harmonically modulated point source of power $P(\omega)$ at $\mathbf{r} = 0$ is given by[33]

$$U(r, \omega) = \frac{P(\omega)}{4\pi D}\frac{e^{ikr}}{r}. \tag{7.42}$$

The explicit expressions for the average photon density (U_{DC}), and for the amplitude (U_{AC}) and phase (Φ) of the photon-density wave are[25,34,35]

$$U_{DC}(r) = \frac{P_{DC}}{4\pi D}\frac{e^{-r(v\mu_a/D)^{1/2}}}{r}, \tag{7.43}$$

$$U_{AC}(r, \omega) = \frac{P(\omega)}{4\pi D}\frac{e^{-r(v\mu_a/2D)^{1/2}[(1+\frac{\omega^2}{v^2\mu_a^2})^{1/2}+1]^{1/2}}}{r}, \tag{7.44}$$

$$\Phi(r, \omega) = r(v\mu_a/2D)^{1/2}\left[\left(1 + \frac{\omega^2}{v^2\mu_a^2}\right)^{1/2} - 1\right]^{1/2} + \Phi_s, \tag{7.45}$$

where Φ_s is the source phase in radians. Analytical solutions in the frequency domain have also been reported for a semi-infinite medium,[25,35,36] infinite slab,[37] cylindrical, and spherical geometries.[37] Equations (7.39) and (7.41) refer to homogeneous media. For quantitative tissue spectroscopy and oximetry (Section 7.4), one typically assumes that tissues are macroscopically homogeneous, so that Eqs. (7.39) and (7.41) are applicable. By contrast, optical imaging of tissues (Section 7.5) aims at measuring the spatial distribution of the tissue optical properties, and Eq. (7.39) must be generalized to account for the spatial dependence of μ_a and D.

7.4 TISSUE SPECTROSCOPY AND OXIMETRY

7.4.1 OPTICAL PROPERTIES OF BIOLOGICAL TISSUE

As discussed in Section 7.3.1, the propagation of light inside biological tissues can be described in terms of the flow of photons. In this perspective, the light source injects a given number of photons per unit time, per unit volume, per unit solid angle into a specific tissue location, and these photons travel inside the tissue along certain trajectories. The collective motion of photons along these trajectories is called *photon migration*. While traveling inside tissues, photons can undergo a number of different processes, such as absorption, elastic scattering, inelastic scattering (for instance, dynamic light scattering and Raman Scattering), and fluorescence. In this Chapter, we consider only absorption (Section 7.4.1.1) and elastic scattering (Section 7.4.1.2) events. The scattering process from nonstationary scattering centers in tissues (cells, cellular organelles, etc.), which strictly speaking is an inelastic process, involves such small wavelength changes that it is also referred to as quasi-elastic scattering. Quasi-elastic scattering is the basis for dynamic light scattering,[38] diffusing-wave spectroscopy,[39] photon correlation spectroscopy,[40] and laser Doppler flowmetry.[41] When a photon is absorbed, it disappears and transfers its energy to the absorbing center. When a photon is elastically (or quasi-elastically) scattered, its direction of propagation changes, while its wavelength remains essentially unchanged. By contrast, Raman scattering and fluorescence processes cause larger photon wavelength changes related to the involvement of vibrational energy levels.

7.4.1.1 Absorption

The main absorbers of near-infrared (NIR) light in blood-perfused tissues are oxy-hemoglobin, deoxy-hemoglobin, and water. Their absorption spectra between 300 and 1500 nm are shown in Fig. 7.4, which is obtained from compiled absorption data for water[42] and hemoglobin.[43] In Fig. 7.4, the concentrations of oxy-hemoglobin and deoxy-hemoglobin are assumed to be 50 μM, which is a typical value in blood-perfused tissues. We observe that the absorption coefficients reported in Fig. 7.4 are defined to base e, and those for hemoglobin refer to a complete molecule (four heme groups). The so-called "medical spectral window" extends approximately from 700 to 900 nm, where the absorption of light shows a minimum (see Fig. 7.4). As a result, light in this spectral window penetrates deeply into tissues, thus allowing for noninvasive investigations. The optical penetration depth into tissues is limited, at shorter wavelengths, by the hemoglobin absorption, and at longer wavelengths by the water absorption. Other NIR absorbers in tissues that may be important in particular cases include myoglobin, cytochrome oxidase, melanin, and bilirubin.

The absorption properties of tissue are described by the absorption coefficient (μ_a), which is defined as the inverse of the average photon path length before absorption. From this definition, it follows that $1/\mu_a$ is the average distance traveled
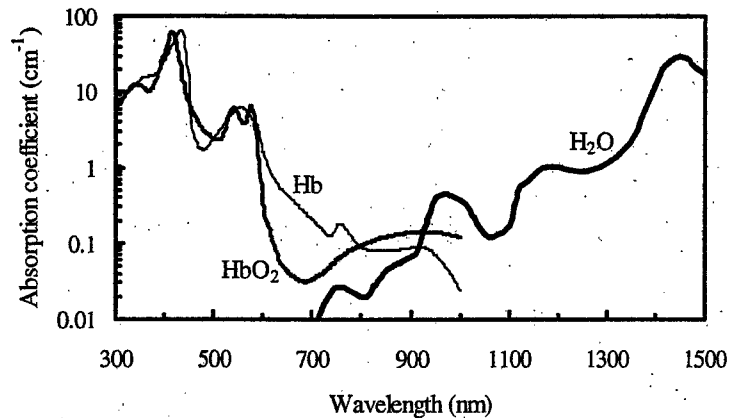
Figure 7.4 Absorption spectra of the three dominant near-infrared chromophores in tissues, namely oxy-hemoglobin (HbO_2), deoxy-hemoglobin (Hb), and water (H_2O). The absorption coefficient is defined to base e. The concentrations of Hb and HbO_2 are both assumed to be 50 μM, a typical value for blood-perfused tissues. These spectra are obtained from compiled absorption data for water[42] and hemoglobin.[43]

by a photon before being absorbed. In the NIR, typical values of μ_a in tissues range from 0.02 to 0.30 cm^{-1}. The photon mean free path for absorption thus ranges between about 3 and 50 cm.

7.4.1.2 Scattering

The scattering properties are determined mainly by the size of the scattering particles relative to the wavelength of light, and by the refractive index mismatch between the scattering particles and the surrounding medium. In biological tissues, the scattering centers are cells and cellular organelles. In the medical spectral window (700–900 nm), cellular organelles have dimensions comparable to the wavelength, and their index of refraction is relatively close to that of the cytosol and extracellular fluid. As a result, light scattering in tissue is mainly forward directed (i.e., the scattering angle γ introduced in Section 7.3.2 is less than 90 deg) and shows a weak wavelength dependence.

As discussed in Sections 7.3.1 and 7.3.5, the scattering properties of tissues are described by two parameters: (1) the scattering coefficient (μ_s), defined as the inverse of the average photon path length between successive scattering events; and (2) the average cosine of the scattering angle ($f_1 = \langle \cos \gamma \rangle$). From the definition of μ_s, it follows that $1/\mu_s$ is the average distance traveled by a photon between successive scattering events, as shown by Eq. (7.28). Even though each scattering event is mainly forward directed, after a number of collisions a photon loses memory of its original direction of propagation. Under these conditions, we can say that the photon has experienced an effectively isotropic scattering event. As discussed in Section 7.3.5, the reduced scattering coefficient [$\mu'_s = (1 - f_1)\mu_s$] represents

the inverse of the average distance over which the direction of propagation of a photon is randomized. In other words, we can say that $1/\mu_s'$ is the average distance between effectively isotropic scattering events. Note that μ_s' coincides with μ_s in the case of isotropic scattering ($f_1 = 0$). Typical values of μ_s' in biological tissues range from 2 to 20 cm^{-1}, while f_1 is typically 0.8–0.9 (so that μ_s' is about one order of magnitude smaller than μ_s).[44] The average distance traveled by a photon in tissues before losing memory of its initial direction of propagation is typically a few millimeters or less.

7.4.2 ABSORPTION SPECTROSCOPY OF TISSUES

Since μ_s' is typically much larger than μ_a, NIR light propagation in tissue is dominated by scattering. This is one of the conditions discussed in Section 7.3.6 for the validity of the diffusion equation [Eq. (7.39)]. The frequency-domain solution given by Eq. (7.42) provides a quantitative description of photon migration in an infinite medium with uniform optical properties. However, biological tissues are neither infinite, nor homogeneous. With regard to tissue inhomogeneity, Eq. (7.42) is a reasonable approximation as long as the characteristic size of the tissue inhomogeneities (for instance, muscle fibers, blood vessels, etc.) is small compared with the source-detector separation. A second problem is determined by the boundary conditions that are associated with the finite volume of the investigated tissue. In a reflectance geometry, where the source and the detector are located on the same side of the tissue, one typically applies the semi-infinite boundary condition. This condition implies that the tissue acts as an effective half-space, which is a reasonable assumption if the tissue depth is greater than the optical penetration depth (which is typically on the order of 2–3 cm or less). This assumption is not valid in a transmission geometry (where the source and the detector are located on opposite sides of the tissue), or in the case of a small tissue volume. In these cases, the application of more appropriate boundary conditions (such as a slab, cylinder, or sphere) may be needed.[37]

Tissue spectroscopy aims at determining certain properties of the investigated tissue volume (for example, the oxygenation or the hemoglobin concentration of a muscle) on the basis of measurement of the optical properties (absorption and scattering) of the tissue. Since the absorption coefficient of tissues is due to a number of chromophores (oxy-hemoglobin, deoxy-hemoglobin, water, cytochrome oxidase, melanin, bilirubin, lipids, etc.), multiwavelength measurements have been employed to determine the relative contributions of each chromophore. The basic idea is that the contribution to μ_a from the i-th chromophore can be written as the product of the extinction coefficient (ε_i) times the concentration (C_i) of that chromophore. As a result, in the presence of N chromophores, the absorption coefficient μ_a at wavelength λ_j is given by

$$\mu_a(\lambda_j) = \sum_{i=1}^{N} \varepsilon_i(\lambda_j) C_i. \tag{7.46}$$

If the extinction spectra $\varepsilon_i(\lambda)$ of all N species are known, the concentrations C_i can be determined by measuring μ_a at N or more wavelengths, so that the linear system of Eq. (7.46) is fully determined. This approach requires that μ_a be measured independently of μ_s'. In the frequency domain, Eqs. (7.43)–(7.45), or the corresponding equations for semi-infinite or other geometries, can be used to quantitatively measure μ_a and μ_s'.[36] The spatial[10] or the frequency[17] dependence of the DC intensity, AC amplitude, and phase can also be used effectively for *in- vivo* tissue spectroscopy. It is worth noting that this approach to tissue spectroscopy yields quantitative, absolute values of the concentration of chromophores in tissue.

7.4.3 NEAR-INFRARED TISSUE OXIMETRY

In many cases, the absorption spectra of tissues can be well described by considering only three chromophores; namely, oxy-hemoglobin, deoxy-hemoglobin, and water. For example, Fig. 7.5 shows the absorption coefficients of human muscle (forearm) and brain (forehead) measured at eight NIR wavelengths (squares) under resting conditions. The lines in Fig. 7.5 are the best fit absorption spectra corresponding to a linear combination of the water, oxy-hemoglobin, and deoxy-hemoglobin extinction spectra. The water concentration (by volume) is assumed to be 75% for the muscle, and 80% for the brain,[45] while the concentrations of oxy-hemoglobin ($[HbO_2]$) and deoxy-hemoglobin ($[Hb]$) are the parameters for fit. The best fit spectra of Fig. 7.5 yield values of $[HbO_2]$ and $[Hb]$ of 58 μM and
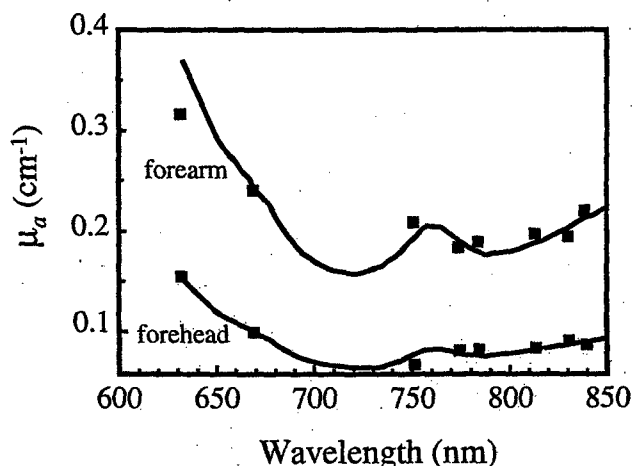

Figure 7.5 Quantitative absorption spectroscopy of tissues *in vivo*.[24,46] The squares represent the eight-wavelength spectra measured with frequency-domain spectroscopy in the skeletal muscle and in the forehead (according to the label) of human subjects. The lines are best fits using a linear combination of the extinction spectra of oxy-hemoglobin, deoxy-hemoglobin, and water.

26 μM, respectively, in the muscle, and 30 μM and 10 μM, respectively, in the brain. Consequently, the measured hemoglobin saturation in the muscle is 69%,[24] while in the brain it is 75%.[46] The good fit between the experimental data and the three-component absorption spectra indicates that oxy- and deoxy-hemoglobin are indeed the dominant absorbing species over the wavelength range considered (630–840 nm) (water absorption introduces only a relatively small correction at these wavelengths). This result allows for measurements of the oxygen saturation of hemoglobin in tissues using just two wavelengths. The possibility of using dual-wavelength optical measurements for blood oximetry have been known for a long time,[47] and it is exploited by pulse oximeters to measure the arterial saturation.[48] The novelty introduced by frequency-domain and time-domain spectroscopy is the capability of performing absolute tissue oximetry.[23,49]

The two wavelengths λ_1 and λ_2 for near-infrared oximetry are usually chosen such that $\lambda_1 < \lambda_{iso} \leq \lambda_2$, where λ_{iso} is the NIR isosbestic wavelength at which the extinction coefficients of oxy-and deoxy-hemoglobin have the same value (λ_{iso} is about 800 nm as can be seen in Fig. 7.4). This choice maximizes the sensitivity of the optical measurement to changes in the tissue oxygenation. The measurement of μ_a at two wavelengths translates Eq. (7.46) into a linear system of two equations (one per each wavelength) and two unknowns (namely, the concentrations of oxy-hemoglobin and deoxy-hemoglobin in the tissue). Its solution gives the oxy- and deoxy-hemoglobin concentrations, which in turn yield the total hemoglobin concentration (THC = [HbO$_2$] + [Hb]) and the tissue saturation (StO$_2$ = [HbO$_2$]/THC). Figures 7.6(a), (b), and (c) show typical traces of total hemoglobin concentration and tissue saturation measured with the frequency-domain tissue oximeter described in Section 7.2.6 (see Fig. 7.2). Panels (a) and (b) of Fig. 7.6 refer to measurements on the brachioradialis muscle (forearm) of a human subject during arterial and venous occlusion, respectively, while panel (c) refers to a measurement on the vastus lateralis muscle (thigh) during treadmill exercise.[50]

The two wavelengths employed in this particular case are 758 and 830 nm, and the acquisition time per data point is 1.28 s. The traces appear in real time on the computer screen during the examination. We stress again that the y-axes for hemoglobin concentration and saturation are quantitative and absolute. Figure 7.6(a) shows that the tissue desaturation during ischemia results from a rate of decrease of [HbO$_2$] that is equal to the rate of increase of [Hb] (because the total hemoglobin concentration THC remains constant during ischemia). The rate of conversion of HbO$_2$ to Hb can be used to quantify the muscle oxygen consumption.[51,52] The main effect of the venous occlusion [Fig. 7.6(b)] is to increase the hemoglobin concentration, as a result of blood accumulation. In fact, while the arterial inflow is unaffected by the venous occlusion, the venous outflow is blocked. The initial rate of increase of THC during venous saturation can be used to measure the muscle blood flow.[53–56] Figure 7.6(c) provides an example of an oxygenation and hemodynamics study *in vivo* during muscle exercise, with potential applications in the area of sports medicine.[50]
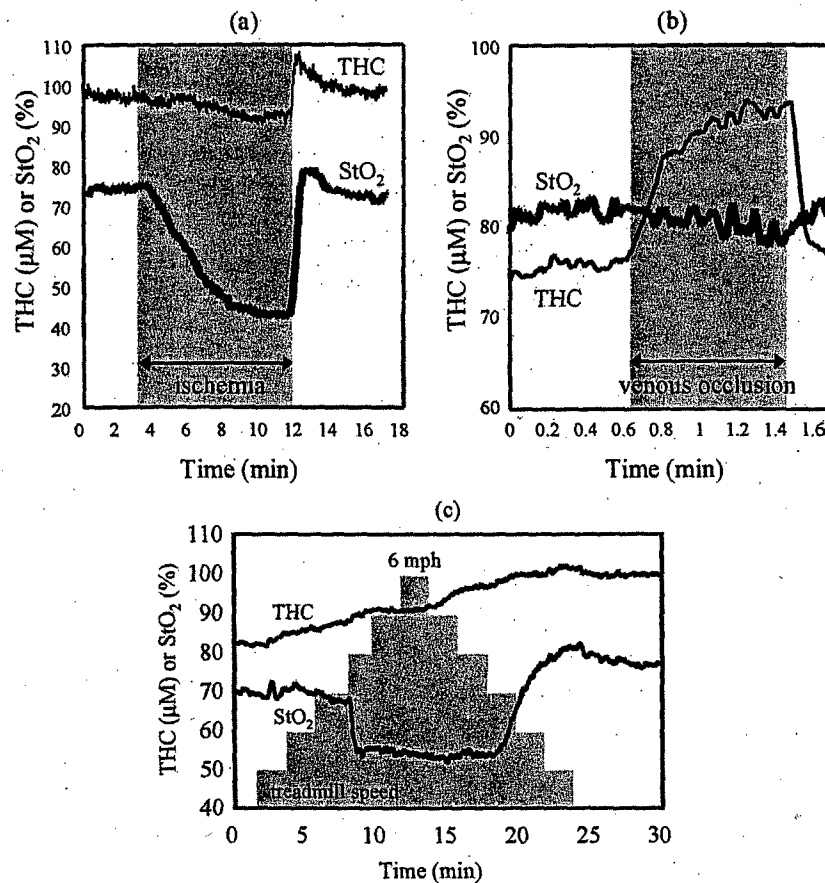
Figure 7.6 Temporal traces of optically measured total hemoglobin concentration (THC = [HbO$_2$] + [Hb]) and tissue saturation (StO$_2$) in human subjects. The measurements were conducted on a forearm muscle during (a) arterial or (b) venous occlusion, and (c) on a calf muscle during treadmill exercise. In panel (c), the step function represent the treadmill speed, which was changed by steps of 1 mph every 2 minutes.[50] Running started at a speed of 4 mph. The frequency-domain measurements allow for absolute y-axis readings

Near-infrared oximetry lends itself to measurements on the human head as well. Figure 7.7(a) shows the arrangement of optical fibers on the forehead of a human subject. The cerebral oxygenation may be varied by changing the fraction of oxygen inspired by the subject. The resulting changes in the cerebral tissue oxygenation (StO$_2$) are reported in Fig. 7.7(b). Figure 7.7(b) also shows a comparison between two traces of arterial saturation (SaO$_2$); one is measured with a commercial pulse oximeter, while the other is measured with a frequency-domain tissue oximeter.[46] Both instruments use the oscillatory components of the optical signals at the frequency of the heartbeat (which are directly associated with the arterial pulsation, and therefore with arterial blood volume). The key differ-
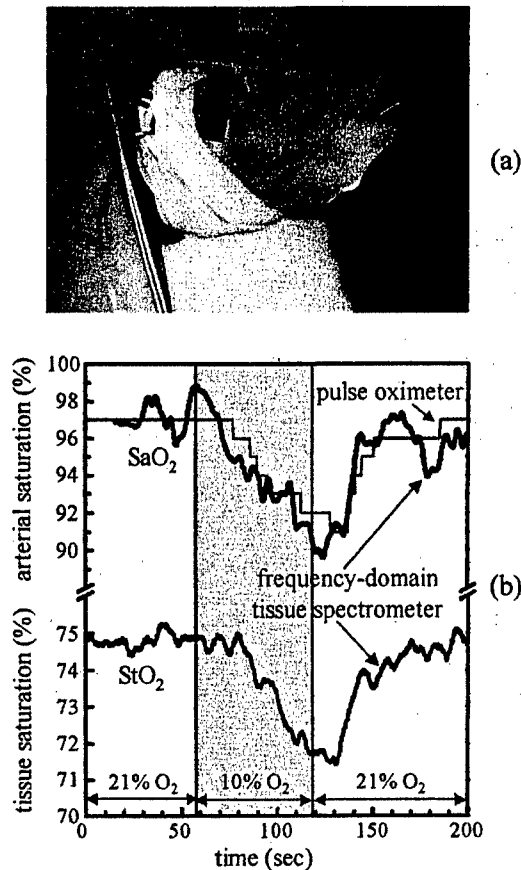
Figure 7.7 (a) Application of optical fibers to the forehead of a human subject for frequency-domain brain oximetry. (b) Temporal traces of arterial saturation (SaO_2) measured systemically (on a finger) by a pulse oximeter and locally (on the forehead) by a frequency-domain oximeter that also measured the cerebral tissue saturation (StO_2).[46] The fraction of oxygen inspired by the subject was varied between 21% and 10% (by volume) as indicated in the figure.

ence is that while the pulse oximeter applies an empirical calibration to translate the pulsatile components of the optical densities into a reading of arterial saturation, the frequency-domain oximeter directly measures the pulsatile components of the absorption coefficients and quantifies the arterial saturation by applying Eq. (7.46).[46]

The lack of discomfort associated with near-infrared measurements *in vivo*, and their noninvasive character, renders near-infrared tissue oximetry a suitable technique for newborn infants. For instance, Fig. 7.8 shows a comparison between the systemic reading of arterial saturation (with a pulse oximeter attached to a toe), and the cerebral oxygenation measured locally with a frequency-domain tissue oximeter. In this case, the decrease in the measured oxygenation was induced by a con-
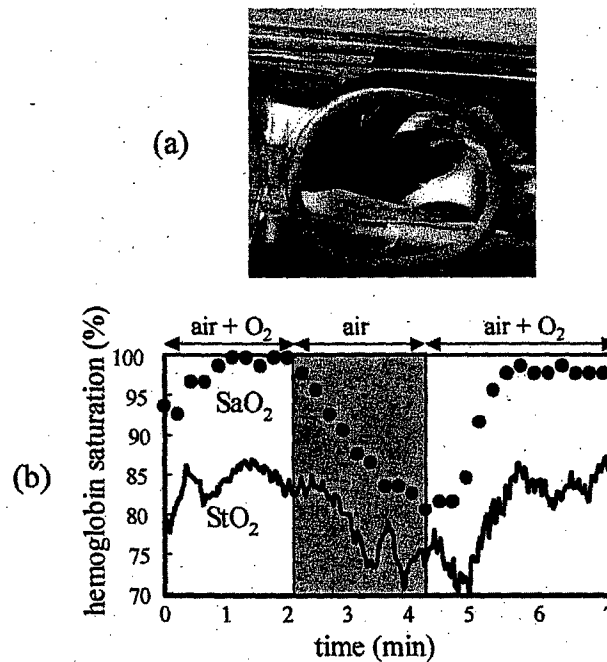
Figure 7.8 Frequency-domain, near-infrared oximetry of the newborn infant brain. (a) Photograph showing the application of a flexible optical probe to the infant's head. (b) Temporal traces of cerebral tissue saturation (StO_2) measured with frequency-domain optical oximetry, and systemic arterial saturation (SaO_2) measured with a pulse oximeter at an infant's toe. Deoxygenation is achieved by a controlled reduction in the fraction of inspired oxygen (in collaboration with G. P. Donzelli and S. Pratesi, University of Florence, Italy).

trolled decrease in the fraction of inspired oxygen. The arterial saturation and the cerebral saturation show a qualitatively similar trend. However, a local cerebral deoxygenation would be detected only by the NIR cerebral measurement. The manual application of the optical probe shown in Fig. 7.8(a) can be replaced by a flexible headband[57,58] or by an infant cap for continuous long-term monitoring.

7.4.4 MEASUREMENTS OF OPTICAL SCATTERING IN TISSUES

Traditionally, optical studies have been targeted at measurements of the absorption properties of tissues. The strong scattering of light in tissue constitutes a complication in quantitative absorption spectroscopy. However, it has recently been suggested that the reduced scattering coefficient itself may provide information about physiologically relevant parameters. For instance, it has been shown that mitochondria are the main source of light scattering in the liver, and possibly in other tissues as well.[59] Since a number of metabolic processes related to cellular respiration occur in the mitochondria, the reduced scattering coefficient may be

related to the cellular activity and viability. Furthermore, some studies have shown a correlation between blood glucose concentration and the reduced scattering coefficient of tissue.[60-62] This correlation is suggested by the fact that the scattering properties of tissues depend on the mismatch between the refractive indices of the scattering centers (cells, cellular organelles) and the host medium (extra-cellular fluid, cytosol). Since the index of refraction of the extracellular fluid is sensitive to glucose concentration, it is a plausible hypothesis that μ'_s would be affected by the blood glucose concentration. *In-vitro* studies have predicted that the sensitivity of μ'_s to the blood glucose level should be adequate to monitor glucose concentrations within the physiological range[61] (80–120 mg/dl in blood). This prediction is confirmed by Fig. 7.9, which shows a trace of μ'_s measured by frequency-domain NIR spectroscopy on the thigh muscle of a healthy 26-year-old male subject during a glucose tolerance test.[61] The reduced scattering coefficient decreases as the blood glucose increases, because of the glucose-induced reduction in the refractive index mismatch between the scattering centers and the host fluid. However, this kind of measurement yields only a relative determination of glucose concentration.

Furthermore, there are a number of additional factors, such as changes in temperature and pH, that yield variations in μ'_s that compete with the glucose-induced
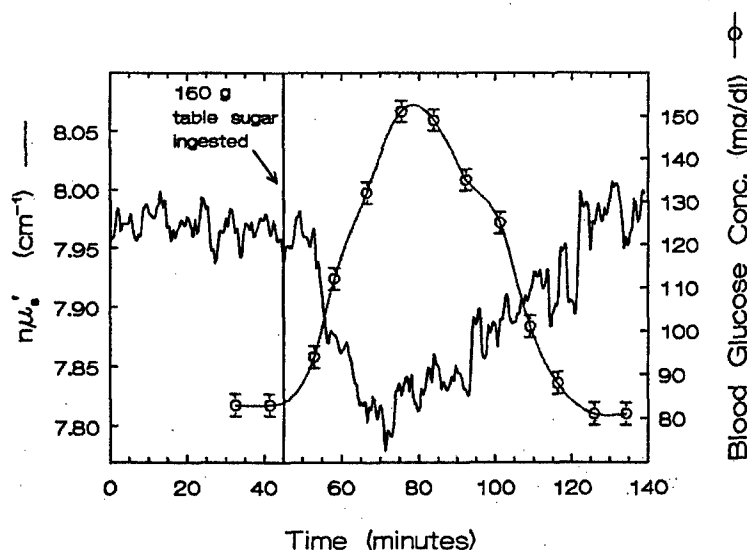
Figure 7.9 Comparison between the blood glucose concentration dynamics and the temporal evolution of the reduced scattering coefficient (μ'_s) measured on the thigh muscle by frequency-domain spectroscopy during a glucose tolerance test.[61] The diffusion model is not able to separate μ'_s from the refractive index n of the tissue [in Eq. (7.42) n and μ'_s are coupled in the expression for $D = v/[3(\mu'_s + \mu_a)] \cong c/(3n\mu'_s)$, where c is the speed of light in vacuum], so that the y-axis reports the product $n\mu'_s$.

effects. Theoretical and experimental studies of the optical properties of the human sclera (the white outer coat enclosing the eyeball) have also shown a significant scattering change induced by glucose and by other osmotically active species.[63] While the monitoring of glucose concentration by NIR spectroscopy is, at the present stage of development, far from being clinically applicable, it nevertheless points out the diversity of potential diagnostic applications of medical optics.

7.5 OPTICAL IMAGING OF TISSUES

7.5.1 GENERAL CONCEPTS

Optical imaging relies on its sensitivity to optical properties of tissues, namely absorption and scattering. Consequently, the contrast in NIR imaging originates from spatial variations in the optical absorption and scattering properties of the tissue. These spatial variations can be due to a local change in hemoglobin concentration or saturation (for instance, a hematoma or heterogeneous vascularization, blood flow, or oxygenation), a localized change in the tissue architecture (for example, a result of microcalcifications), or the concentration of cellular organelles. In any case, NIR imaging is sensitive to physical properties of tissues that are different than those probed by current diagnostic imaging modalities such as x-ray tomography (mass density, atomic number), ultrasound (acoustic impedance), magnetic resonance imaging (proton density, nuclear relaxation times), and positron emission tomography (accumulation of a radioactive tracer). In this sense, NIR imaging is not necessarily an alternative to these imaging modalities but could constitute an adjunct technique that complements existing methods. We point out here that the promise of optical tomography is not in achieving a high spatial resolution (which is intrinsically limited by the diffusive nature of light propagation in tissues), but rather in achieving high contrast and specificity.

NIR tissue imaging aims at generating spatial maps that display either structural or functional properties of tissues. Since optical imaging studies the spatial distribution of the optical properties, Eq. (7.39) must be replaced with the diffusion equation for inhomogeneous media:

$$\frac{\partial U(\mathbf{r}, t)}{\partial t} - \nabla \cdot D(\mathbf{r})\nabla U(\mathbf{r}, t) + v\mu_a(\mathbf{r})U(\mathbf{r}, t) = q(\mathbf{r}, t). \qquad (7.47)$$

Equation (7.47) can be used to solve the forward problem, which consists of finding the photon density $U(\mathbf{r}, t)$ corresponding to a given spatial distribution of the optical properties and of the photon sources. Analytical solutions of Eq. (7.47) are available only for a few inhomogeneous cases such as those of spherical[33] and cylindrical[64] inclusions. For arbitrary inhomogeneous cases, Eq. (7.47) can be solved using numerical methods such as the finite-difference method (FDM)[65] or the finite-element method (FEM).[66] Alternatively, a perturbation expansion in μ_a and D leads to a solution of Eq. (7.47) in terms of a volume integral involving

the appropriate Green's function.[67,68] Besides using diffusion theory, the case of inhomogeneous media can also be treated with stochastic methods such as Monte Carlo simulations[69,70] or lattice random walk models.[71]

The goal of imaging is to solve the inverse problem, which consists of determining the spatial distribution of μ_a and D (or μ_a and μ_s') within a volume V, from optical measurements at the boundary of V. Perturbation methods linearize the problem by keeping only the linear term in an expansion of the change in the measured quantities induced by a perturbation in the optical properties. The inverse problem reduces to inverting the Jacobian (i.e., the first derivative) matrix of the measured quantities with respect to the optical properties. The Jacobian matrix can be estimated using a Monte Carlo[72] or an analytical[67,68] model. The main practical disadvantage of the perturbation method is that it requires a difference between measurements with and without the perturbation. For *in vivo* applications, this is sometimes impractical, save the cases of dynamical perturbations such as those induced by evoked cerebral activity or by the injection of optical contrast agents.[73]

Nonlinear approaches are based on minimization of the distance (in measurement space) between the measured data and the projection of the distribution of optical properties onto the measurement space (according to the forward problem). The minimization process involves repeated iterations, so the computational speed of the forward model is a relevant factor. One example of a nonlinear approach is the Newton-Raphson scheme for minimization, which has been used in conjunction with an FEM forward model to do optical tomography.[74-76] The above-mentioned methods usually require relatively long computation times that render them unsuitable for real-time imaging. For applications where real-time information is important, simplified algorithms based on back projection[77-79] or on direct projection for 2D mapping[80] have been proposed. A recent and comprehensive review of medical optical imaging can be found in Ref. [30].

7.5.2 NONINVASIVE OPTICAL IMAGING OF THE HUMAN BRAIN

7.5.2.1 Detection of intracranial hematomas

Several studies have demonstrated that near-infrared light propagates through the intact skull.[81-83] One technique using continuous-wave (CW) light (wavelength: 760 nm, source-detector separation: 3.5 cm) has been used to detect intracranial hematomas in head-injured patients.[84] This is based on the fact that there is a greater concentration of hemoglobin in a hematoma with respect to normal brain tissue, resulting in a higher absorption of NIR light. A significant asymmetry between the optical signals collected over the two hemispheres will indicate a condition that could possibly be related to the presence of a hematoma. This technique is not aimed at displaying optical images of the brain. Rather, it involves a comparison of optical measurements at two different brain locations. In this sense, although this is not a true imaging technique, spatially resolved measurements are involved.

Another approach, using a hybrid of CW and frequency-domain techniques has been employed to perform real-time imaging (image acquisition rate: 5.2 Hz) of an experimental brain hemorrhage in a piglet model.[85] Figure 7.10 shows the optical image recorded noninvasively through the intact scalp and skull immediately following the subcortical injection (depth of injection: 1.2 cm) of 0.5 cc of autologous blood. In Fig. 7.10, a photograph of a brain slice obtained after autopsy is superimposed to the near-infrared image to show the geometrical relationship between the optical image and the piglet brain. The optical image was obtained by linearly combining the readings from 10 source-detector pairs according to a linear back-projection scheme.[85] While this scheme is computationally fast, it does not lead to quantitative readings, so that the absorption scale in Fig. 7.10 is qualitative (i.e., the image gives reliable spatially resolved information on whether the absorption increases or decreases, but the absorption changes are not accurately

$\Delta\mu_a$ @ 830 nm (cm^{-1})
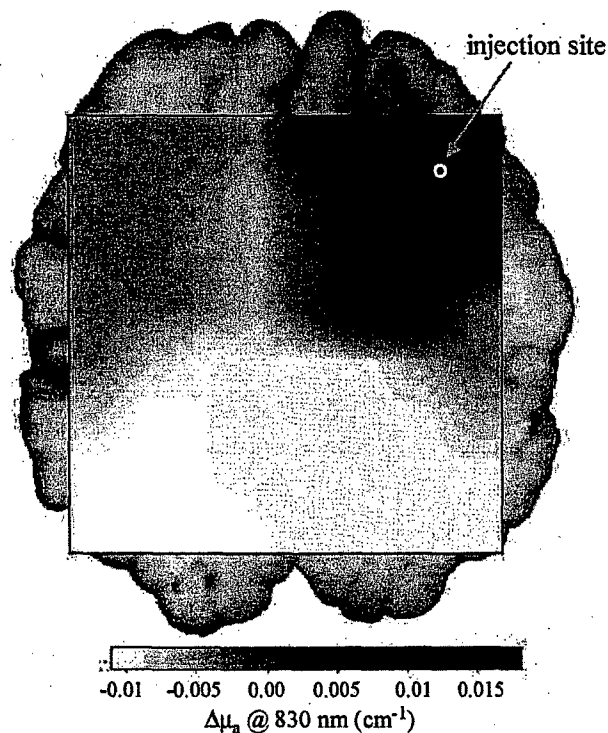
Figure 7.10 Optical absorption image of a 4 × 4 cm^2 area of the piglet brain, measured non-invasively immediately after the subcortical injection of 0.5 cc of blood.[85] The injection site is indicated by the white circle. A picture of a brain slice taken after autopsy is superimposed to the optical image to show the geometrical relationship between the imaged area and the piglet brain. One can see the increased optical absorption over the area surrounding the injection site, which corresponds to the subcortical hemorrhage.

quantified). The lack of quantitative capabilities in optical imaging of tissues is a general shortcoming of back-projection schemes.

7.5.2.2 Functional imaging of the brain

The relationship between neuronal activation and local cerebral hemodynamics is provided by neurovascular coupling.[86,87] In the brain, local blood flow is continuously adjusted according to functional activity and metabolic demand. This adjustment occurs due to the vasomotor action of the cerebral arteries and arterioles. Both of the leading methods in functional neuroimaging, positron emission thomography (PET) and functional magnetic resonance imaging (fMRI), use neurovascular coupling to asses brain activity. Electro-encephalography (EEG) and magneto-encephalography (MEG), on the other hand, can measure the fast (latency: 50–100 ms) electrical and magnetic signals directly related to neural activation. The spatial localization of the signals detected by EEG and MEG is problematic, however, because these techniques are sensitive to the whole brain. Near-infrared (NIR) imaging shows promise of being a unique technique, since it is the only existing modality that is sensitive to both ends of the neurovascular coupling, namely the neuronal activity and the vascular response. *In vitro* optical measurements on neurons have shown that neuronal activity is associated with an increase in light scattering, induced by a change in the index of refraction of the neuronal membranes.[88,89] In the last few years, several attempts have been made to measure such light scattering changes in human subjects *in vivo* and noninvasively. Using a frequency-domain system, G. Gratton et al.[90] have reported a transient increase in the pathlength of light in the visual cortex with a latency of 50–100 ms following the onset of visual stimulation. This signal shows a time course consistent with the electrophysiological response measured with EEG.

It has been proven that the hemodynamic changes monitored with NIR spectroscopy correlate with the activation state of the cortex in response to a stimulus. In fact, studies combining PET and fMRI with NIRS were able to demonstrate that the optically measured oxy- and total hemoglobin changes correspond to regional cerebral blood flow increases as measured by PET,[91,92] whereas deoxy-hemoglobin changes correspond to the BOLD signal measured by fMRI.[93,94] The circulatory effect of functional activation is an increase in cerebral blood flow (CBF) (higher blood volume and blood velocity) resulting from an increase in oxygen consumption. An increase in CBF that overcompensates the increase in oxygen consumption accounts for the observed decrease in the cerebral deoxy-hemoglobin concentration.[95]

Local cerebral studies are just a first step toward optical brain imaging. The key to functional brain imaging is a fast acquisition rate, which is required by the relatively short latency of the neural activation (~0.1 s) and the evoked hemodynamic signal (1–5 s). For structural brain imaging, the requirement of a fast acquisition time is not as important as for functional imaging. Several groups have reported noninvasive optical brain imaging with acquisition times per image of 3–5 s,[96,97]

<30 s,[98] 2.5 min,[99] several hours,[57,58] and not-quantified "slow data acquisition rate"[100] and "long measurement times."[94] Faster optical imaging approaches, suitable for noninvasive functional brain imaging, have been reported recently with image acquisition times of 500 ms[101] and 160 ms.[79] Noninvasive optical studies of the brain are reviewed in Ref. [102].

Figure 7.11 shows the results of a functional brain imaging study that used a multichannel frequency-domain optical instrument (a modified version of Model No. 96208, ISS, Inc., Champaign, IL, shown in Fig. 7.2).[79] The optically measured maps of cerebral deoxy-hemoglobin concentration show the activated cortical area during voluntary hand tapping. Image reconstruction was based on a linear superposition of the optical signals from 10 source-detector pairs. The fast image acquisition rate (6.25 Hz) leads to online, continuous optical mapping of the cerebral cortex during the examination. Figure 7.11 shows one optical image every 10 measurements (i.e., every 1.6 s) for space reasons. The real-time movie of the cerebral activation recorded with near-infrared imaging can be viewed in Ref. [79].

Currently, most optical functional studies of the brain have been based on continuous-wave (CW) spectroscopy. Even Fig. 7.11 shows results based on the DC component of the measured amplitude-modulated signal. The reason for the more common use of CW data in optical brain imaging is twofold. (1) The study of cerebral activation requires the measurement of changes in the optical signals that correlate with brain activity. Therefore, even relative readings, i.e., changes from an arbitrary initial value, yield meaningful information. (2) The absolute measurement capability afforded by time-resolved methods requires the application of a physical model for light propagation inside tissues. An accurate model for the highly inhomogeneous and geometrically irregular case of the human head is yet to be achieved. However, there are a few exceptions to the use of CW spectroscopy for optical studies of the brain.[98,99,103,104] These studies show that even without absolute measurements, time-resolved data can be extremely valuable in optical studies of the human brain. In fact, the additional information content of time-resolved data (the phase in the frequency-domain, the time-of-flight distribution in the time-domain) may lead to more effective approaches to human brain studies, for instance by affording the optimization of the spatial region of sensitivity, and the maximization of the sensitivity to localized absorption and scattering changes.

7.5.3 OPTICAL MAMMOGRAPHY

From a practical point of view, the human breast lends itself to near-infrared tissue spectroscopy and imaging. In fact, it is easily accessible and its relatively low hemoglobin concentration (10–20 μM)[105,106] determines near-infrared absorption coefficients ($\sim$0.02–0.04 cm^{-1}) that account for a deep optical penetration depth and the optical transmission through the whole breast. Furthermore, there is much appeal in the possibility of detecting breast cancer using a noninvasive method that
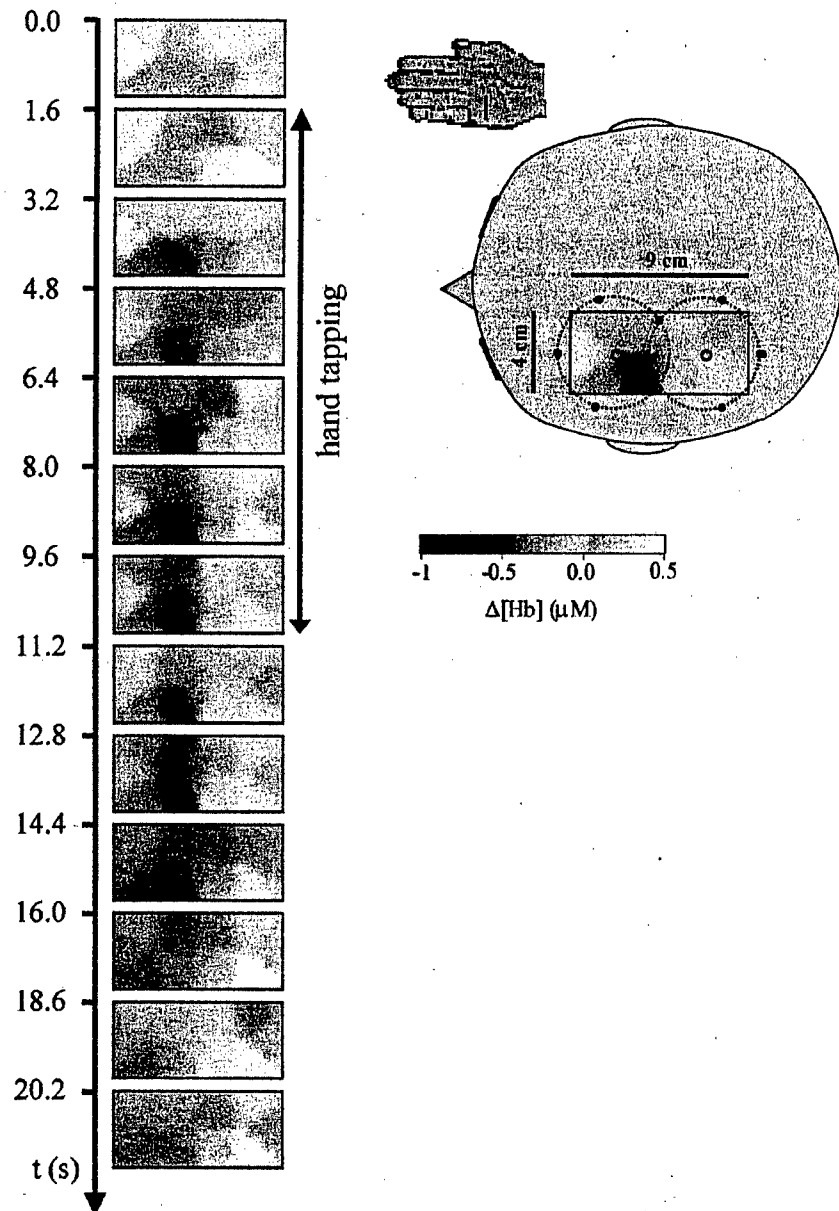
Figure 7.11 Real-time, noninvasive functional imaging of the brain using near-infrared light.[79] The schematic diagram of the head shows the locations of the illuminating optical fibers (eight small circles) and the collecting optical fibers (two large circles). A linear back-projection scheme reconstructs an optical image of the 4×9 cm^2 area indicated by the rectangle. The motor cortex activation is induced by voluntary hand tapping. The sequence of optical images of the brain collected over a period of 20 s is shown to the left (the sequence actually shows one image every ten images acquired, as the image acquisition time was 160 ms per image). One can see the localized decrease in the cerebral deoxy-hemoglobin concentration observed during hand tapping, and the recovery following the end of hand tapping.

does not involve ionizing radiation. The optical detection of breast cancer may rely on the perturbations induced by cancer on the host tissue rather than on a direct detection of optical signatures associated with cancer cells.[107] These perturbations include angiogenesis,[107,108] alterations to the blood flow and oxygenation,[108] and fibroblast proliferation,[107] which may yield modifications to the optical scattering and absorption properties. However, it is not known whether these cancer-induced optical perturbations can lead to an effective optical approach to breast cancer detection over the wide range of cases observed in the clinical and screening practice (different types and stages of cancer, various benign tumors, different levels of tissue heterogeneity, etc.). *In vitro* optical studies of normal and diseased breast tissues have not found significant differences between their optical properties.[109,110] This result further suggests that the optical contrast induced by cancer may result only from modifications to the vascularization, oxygenation, or tissue architecture, which are significantly altered for the measurements *in vitro*. In fact, *in vivo* measurements have indicated that cancerous breast tissue has a significantly larger absorption coefficient and a marginally larger reduced scattering coefficient with respect to normal breast tissue.[111–113] Since it is yet to be demonstrated that optical mammography can rely solely on the intrinsic optical contrast associated with cancer, it has recently been proposed to use dyes as optical contrast agents.[73,114,115]

The first clinical tests of breast transillumination for diagnostic purposes were performed by Cutler in 1929.[116] This approach was soon abandoned because of the poor sensitivity and specificity of the method. In the 1970s and 1980s, technical developments led to two new optical techniques called *diaphanography*[117] and *lightscanning*,[118] which induced a renewed enthusiasm for optical mammography. These approaches employed a broad beam of visible and NIR continuous-wave light that illuminated one side of the breast. On the opposite side of the breast, the examiner visually inspected the light transmission pattern and used a video camera for image recording. The examination had to be performed in a dark room, and the examiner's eyes needed to be dark-adapted. Despite some encouraging initial results,[119] several clinical studies conducted in the late 1980s have shown that diaphanography and lightscanning are inferior to x-ray mammography both as a screening and as a clinical tool.[120,121] As a result, medical acceptance of diaphanography and lightscanning has been subdued.

The introduction of time-resolved methods for tissue imaging has yielded new instrumental tools for optical mammography. Furthermore, the application of the diffusion equation [Eq. (7.47)] provides a mathematical model that allows for a more rigorous approach to optical mammography with respect to the mainly empirical studies of the past. As a result, new time-domain[73,112,122–124] and frequency-domain[18,105,113,125–128] approaches for optical mammography have recently been developed. Siemens AG, Medical Engineering (Erlangen, Germany) has recently designed and clinically tested a frequency-domain prototype for optical mammography.[129] Figure 7.12 shows a block diagram of this prototype and two representative optical mammograms obtained on a patient affected by breast cancer. The optical mammograms shown in Fig. 7.12 are 2D projection images ob-
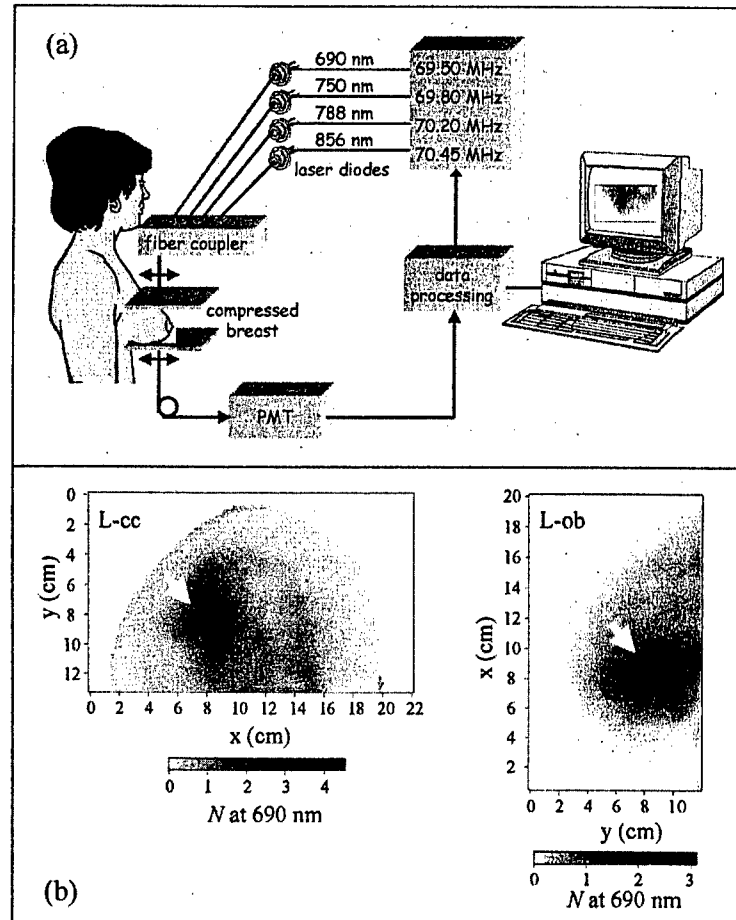
Figure 7.12 (a) Schematic diagram of the prototype for frequency-domain (70 MHz) optical mammography developed by Siemens AG, Medical Engineering.[129] The slightly compressed breast is optically scanned to obtain 2D projection images at four wavelengths (690, 750, 788, and 856 nm). The optical detector is a photomultiplier tube (PMT). The scanning time is about 2 minutes per image. The optical image of the breast is displayed in real time during the examination. (b) Craniocaudal (cc) and oblique (ob) views of the left (L) breast of a 72-year-old patient (patient No. 197) affected by invasive ductal carcinoma. Cancer size is 2.5 cm. The cancer, indicated by arrows, appears with high contrast in both views of the breast. The imaged parameter (N at 690 nm) is related to the optical absorbance of breast tissue,[80] so that the higher value of N at the cancer location indicates a higher optical absorption with respect to healthy tissue.

tained by scanning two collinear optical fibers (one for illumination, one for light collection) placed on the opposite sides of the slightly compressed breast. The total time required to scan the breast is 2–3 min. The frequency-domain optical data have been processed with an algorithm designed to enhance tumor contrast

by minimizing the effects of the breast geometry on the optical data.[80] As in x-ray mammography, the breast is imaged in two directions, leading to a craniocaudal (cc) and an oblique (ob) view. Figure 7.12 shows that breast cancer can be detected with excellent contrast using optical methods. However, optical mammography still needs to improve its performance in the detection of small tumors and in the discrimination between malignant tumors and benign breast lesions. A preliminary analysis based on the criterion that an optical mammogram is positive if it shows a region of abnormal absorbance in both the craniocaudal and oblique views, has led to a sensitivity (fraction of cancerous breasts successfully detected) of 72% and a specificity (fraction of noncancerous breasts correctly evaluated as negative) of 52% on a clinical population of 131 patients.[130] This result is consistent with the sensitivity of 73% obtained on 69 patients[131] with a similar frequency-domain prototype developed independently by the research laboratories of Carl Zeiss (Oberkochen, Germany).[132] It must be stressed that these results, which are based on optical mammograms like the ones shown in Fig. 7.12(b), rely on 2D projection data at a single wavelength. The potential of optical mammography goes beyond these capabilities, so that there are a number of possibilities for developing more effective approaches. For instance, testing nonplanar geometries without (or with minimal) breast compression, exploiting the spectral information, quantifying and discriminating the breast absorption and scattering coefficients, achieving a true 2D or 3D spatial reconstruction of the breast optical properties, performing oxygenation or blood flow imaging, and developing imaging approaches based on dynamic perturbations (such as periodic light compression and decompression of the breast), are some of the areas currently under investigation by research groups worldwide.

7.6 FUTURE DIRECTIONS

The key difference between continuous-wave and frequency-domain spectroscopy is the phase measurement capability afforded by the frequency-domain. For optical studies of tissues, the phase information can be exploited in at least two ways.

First, by combining the phase measurement with the DC intensity, AC amplitude, or modulation measurement, one can separately measure the absorption and the reduced scattering coefficients of tissues. This is of paramount importance for quantitative tissue spectroscopy, imaging, and oximetry. In this chapter, we have illustrated the capability of frequency-domain spectroscopy to quantify the absorption and the reduced scattering coefficients [Figs. 7.3(d), 7.5, and 7.9], and to perform absolute tissue oximetry (Figs. 7.6–7.8).

The second relevant aspect of the phase measurement is that the phase is sensitive to a different tissue volume with respect to the DC intensity and AC amplitude. The region of sensitivity can be evaluated by the effect on the measured quantities of a small perfectly absorbing object located at r. In particular, the DC, AC, and phase sensitivities can be expressed by the parameters $e_{DC}(r) = DC(r)/DC_0$, $e_{AC}(r) = AC(r)/AC_0$, and $e_F(r) = \Phi(r) - \Phi_0$, respectively, where DC_0, AC_0, Φ_0,

are the measured values in the absence of the absorbing object, and DC($\mathbf{r}$), AC($\mathbf{r}$), $\Phi(\mathbf{r})$ are the measured values in the presence of the absorbing object at point $\mathbf{r}$. The theoretical and experimental regions of sensitivities for the DC, AC, and phase are illustrated in Fig. 7.13 for an infinite medium (other conditions are listed in the
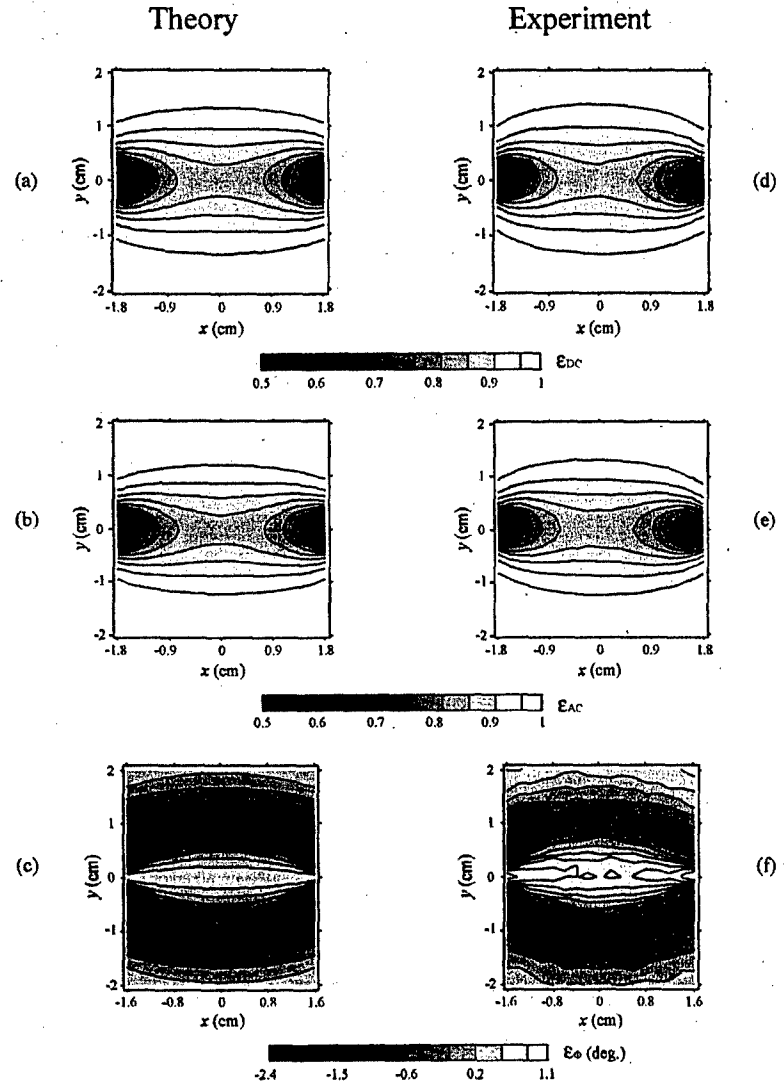
Figure 7.13 Regions of sensitivity for the DC (panels (a) and (d)), AC (panels (b) and (e)), and phase (panels (c) and (f)) in an infinite medium. The source and the detector (not shown) are located respectively in $(-2, 0)$ and $(2, 0)$. The optical properties of the medium are $\mu_a = 0.03$ cm^{-1}, $\mu'_s = 19$ cm^{-1}, and the source modulation frequency is 120 MHz. The gray scales represent the parameters e_{DC}, e_{AC}, and e_F, which are defined in the text. The left panels are theoretical predictions based on diffusion theory, while the right panels are experimental results.[133]

figure caption).[133] Figure 7.13 shows that the DC and AC measurement are most sensitive to the region along the line joining the source and the detector, which, by contrast, is not the highest region of sensitivity for the phase. In a noninvasive tissue measurement, which is better modeled by a semi-infinite geometry, where the illuminating and collecting optical fibers are located on the tissue/air interface, the phase measurement is typically less sensitive to the superficial tissue layer with respect to the DC and AC measurements. As a result, the phase information may contribute to achieving depth discrimination in optical imaging of tissues.

Future applications of frequency-domain techniques to the optical study of biological tissues will exploit the two above-mentioned features, with the objective of developing innovative approaches for medical imaging and diagnosis.

ACKNOWLEDGMENTS

REFERENCES

1. D. T. Delpy, M. Cope, P. van der Zee, S. Arridge, S. Wray, and J. Wyatt, "Estimation of optical pathlength through tissue from direct time of flight measurement," *Phys. Med. Biol.* Vol. 33, pp. 1433–1442 (1988).
2. M. S. Patterson, B. Chance, and B. C. Wilson, "Time resolved reflectance and transmittance for the non-invasive measurement of optical properties," *Appl. Opt.* Vol. 28, pp. 2331–2336 (1989).
3. B. Chance, M. Cope, E. Gratton, N. Ramanujam, and B. Tromberg, "Phase measurement of light absorption and scatter in human tissue," *Rev. Sci. Instrum.* Vol. 69, pp. 3457–3481 (1998).
4. E. Gratton and M. Limkeman, "A continuously variable frequency-domain cross-correlation phase fluorometer with picosecond resolution," *Biophys. J.* Vol. 44, pp. 315–324 (1983).
5. R. D. Spencer and G. Weber, "Measurement of subnanosecond fluorescence lifetimes with a cross-correlation phase fluorometer," *Ann. NY Acad. Sci.* Vol. 158, pp. 361–376 (1969).
6. D. W. Piston, G. Marriott, T. Radivoyevich, R. Clegg, T. M. Jovin, and E. Gratton, "Wide-band acousto-optic light modulator for frequency-domain fluorometry and phosphorimetry," *Rev. Sci. Instrum.* Vol. 60, pp. 2596–2600 (1989).

7. J. R. Alcala, E. Gratton, and D. M. Jameson, "A multifrequency phase fluorometer using the harmonic content of a mode-locked laser," *Anal. Instrum.* Vol. 14, pp. 225–250 (1985).

8. E. Gratton, D. M. Jameson, N. Rosato, and G. Weber, "Multifrequency cross-correlation phase fluorometer using synchrotron radiation," *Rev. Sci. Instrum.* Vol. 55, pp. 486–493 (1984).

9. G. De Stasio, N. Zema, F. Antonangeli, A. Savoia, T. Parasassi, and N. Rosato, "Plastique: a synchrotron radiation beamline for time resolved fluorescence in the frequency domain," *Rev. Sci. Instrum.* Vol. 62, pp. 1670–1671 (1991).

10. S. Fantini, M. A. Franceschini, J. B. Fishkin, B. Barbieri, and E. Gratton, "Quantitative determination of the absorption spectra of chromophores in strongly scattering media: a light-emitting-diode based technique," *Appl. Opt.* Vol. 33, pp. 5204–5213 (1994).

11. E. Gratton, W. W. Mantulin, M. J. van de Ven, and J. B. Fishkin, "A novel approach to laser tomography," *Bioimaging* Vol. 1, pp. 40–46 (1993).

12. A. Knüttel, J. M. Schmitt, and J. R. Knutson, "Spatial localization of absorbing bodies by interfering diffusive photon-density waves," *Appl. Opt.* Vol. 32, pp. 381–389 (1993).

13. E. M. Sevick, J. K. Frisoli, C. L. Burch, and J. R. Lakowicz, "Localization of absorbers in scattering media by use of frequency-domain measurements of time-dependent photon migration," *Appl. Opt.* Vol. 33, pp. 3562–3570 (1994).

14. B. Guan, Y. Zhang, and B. Chance, "A new multi-wavelength phase modulation system for photon diffusion studies," *Proc. SPIE* Vol. 2979, pp. 838–846 (1997).

15. J. R. Lakowicz and K Berndt, "Frequency-domain measurements of photon migration in tissues," *Chem. Phys. Lett.* Vol. 166, pp. 246–252 (1990).

16. J. B. Fishkin, S. Fantini, M. J. vandeVen, and E. Gratton, "Gigahertz photon density waves in a turbid medium: theory and experiments," *Phys. Rev. E* Vol. 53, pp. 2307–2319 (1996).

17. S. J. Madsen, E. R. Anderson, R. C. Haskell, and B. J. Tromberg, "Portable, high-bandwidth frequency-domain photon migration instrument for tissue spectroscopy," *Opt. Lett.* Vol. 19, pp. 1934–1936 (1994).

18. X. D. Li, T. Durduran, A. G. Yodh, B. Chance, and D. N. Pattanayak "Diffraction tomography for biochemical imaging with diffuse-photon density waves," *Opt. Lett.* Vol. 22, pp. 573–575 (1997).

19. K. W. Berndt and J. R. Lakowicz, "Detection and localozation of absorbers in scattering media using frequency-domain principles," *Proc. SPIE* Vol. 1431, pp. 149–160 (1991).

20. T. E. French, "The development of fluorescence lifetime imaging and an application in immunology," Ph.D. Thesis, Dept. of Physics, University of Illinois at Urbana-Champaign (1996).

21. B. A. Feddersen, D. W. Piston, and E. Gratton, "Digital parallel acquisition in frequency domain fluorometry," *Rev. Sci. Instrum.* Vol. 60, pp. 2929–2936 (1989).

22. R. N. Bracewell, *The Fourier Transform and Its Applications*, pp. 189–194, McGraw-Hill, Singapore (1986).

23. S. Fantini, M. A. Franceschini, J. S. Maier, S. A. Walker, B. Barbieri, and E. Gratton, "Frequency-domain multichannel optical detector for non-invasive tissue spectroscopy and oximetry," *Opt. Eng.* Vol. 34, pp. 32–42 (1995).

24. M. A. Franceschini, E. Gratton, D. Hueber, and S. Fantini, "Near-infrared absorption and scattering spectra of tissues *in vivo*," *Proc. SPIE* Vol. 3597, pp. 526–531 (1999).

25. S. Fantini, M. A. Franceschini, and E. Gratton, "Semi-infinite-geometry boundary problem for light migration in highly scattering media: a frequency-domain study in the diffusion approximation," *J. Opt. Soc. Am. B* Vol. 11, pp. 2128–2138 (1994).

26. J. J. Duderstadt and L. J. Hamilton, *Nuclear Reactor Analysis*, p. 113, Wiley, New York, NY (1976).

27. F. Hetzel, M. Patterson, L. Preuss, and B. Wilson, "Recommended nomenclature for physical quantities in medical applications of light," AAPM Report No. 57, American Institute of Physics, Woodbury, NY, pp. 1–6 (1996).

28. J.-M. Kaltenbach and M. Kaschke, "Frequency- and time-domain modelling of light transport in random media," in *Medical Optical Tomography: Functional Imaging and Monitoring*, G. J. Muller et al. (eds.), pp. 65–86, SPIE, Bellingham, Washington (1993).

29. D. A. Boas, "Diffuse Photon Probes of Structural and Dynamical Properties of Turbid Media: Theory and Biomedical Applications," Ph.D. Thesis, Dept. of Physics, University of Pennsylvania (1996).

30. S. R. Arridge, "Optical tomography in medical imaging," *Inverse Problems* Vol. 15, pp. R41–R93 (1999).

31. H. W. Wyld, *Mathematical Methods for Physics*, Chapter 3, Addison-Wesley, Reading, MA (1994).

32. G. Zaccanti, E. Battistelli, P. Bruscaglioni, and Q. Wei, "Analytic relationships for the statistical moments of scattering point coordinates for photon migration in a scattering medium," *Pure Appl. Opt.* Vol. 3, pp. 897–905 (1994).

33. D. A. Boas, M. A. O'Leary, B. Chance, and A. G. Yodh, "Scattering of diffuse photon density waves by spherical inhomogeneities within turbid media: analytic solution and applications," *Proc. Natl. Acad. Sci. USA* Vol. 91, pp. 4887–4891 (1994).

34. J. B. Fishkin and E. Gratton, "Propagation of photon-density waves in strongly scattering media containing an absorbing semi-infinite plane bounded by a straight edge," *J. Opt. Soc. Am. A* Vol. 10, pp. 127–140 (1993).

35. R. C. Haskell, L. O. Svaasand, T. T. Tsay, T. C. Feng, M. S. McAdams, and B. J. Tromberg, "Boundary conditions for the diffusion equation in radiative transfer," *J. Opt. Soc. Am. A* Vol. 11, pp. 2727–2741 (1994).

36. M. S. Patterson, J. D. Moulton, B. C. Wilson, K. W. Berndt, and J. R. Lakowicz, "Frequency-domain reflectance for the determination of the scattering and absorption properties of tissue," *Appl. Opt.* Vol. 30, pp. 4474–4476 (1991).

37. S. R. Arridge, M. Cope, and D. T. Delpy, "The theoretical basis for the determination of optical pathlengths in tissue: temporal and frequency analysis," *Phys. Med. Biol.* Vol. 37, pp. 1531–1560 (1992).

38. J. Ricka, "Dynamic light scattering with single-mode and multimode receivers," *Appl. Opt.* Vol. 32, pp. 2860–2875 (1993).

39. D. J. Pine, D. A. Weitz, P. M. Chaikin, and E. Herbolzheimer, "Diffusing-wave spectroscopy," *Phys. Rev. Lett.* Vol. 60, pp. 1134–1137(1988).

40. D. A. Boas and A. G. Yodh, "Spatially varying dynamical properties of turbid media probed with diffusing temporal light correlation," *J. Opt. Soc. Am. A* Vol. 14, pp. 192–215 (1997).

41. I. M. Braverman, "Anatomy and Physiology of the Cutaneous Microcirculation," in *Bioengineering of the Skin: Cutaneous Blood Flow and Erythemia*, E. Berardesca, P. Elsner, and H. I. Maibach (eds.), CRC Press, Boca Raton, FL (1995).

42. G. M. Hale and M. R. Querry, "Optical constants of water in the 200 nm to 200 µm wavelength region," *Appl. Opt.* Vol. 12, pp. 555–563 (1973).

43. S. Prahl (of the Oregon Medical Laser Center, Portland, OR) has tabulated the molar extinction coefficients for oxy-hemoglobin and deoxy-hemoglobin using data from W. B. Gratzer and N. Kollias. These tabulated data are available at http://omlc.ogi.edu/spectra/hemoglobin/summary.html.

44. W. F. Cheong, S. A. Prahl, and A. J. Welch, "A review of the optical properties of biological tissues," *IEEE J. Quantum Electron.* Vol. 26, pp. 2166–2185 (1990).

45. F. A. Duck, *Physical Properties of Tissues: A Comprehensive Reference Book*, Academic Press, San Diego, CA (1990).

46. M. A. Franceschini, E. Gratton, and S. Fantini, "Non-invasive optical method to measure tissue and arterial saturation: an application to absolute pulse oximetry of the brain," *Opt. Lett.* Vol. 24, pp. 829–831 (1999).

47. G. A. Millikan, "The oximeter, an instrument for measuring continuously the oxygen saturation of arterial blood in man," *Rev. Sci. Instr.* Vol. 13, pp. 434–444 (1942).

48. Y. Mendelson, "Pulse oximetry: theory and applications for noninvasive monitoring," *Clin. Chem.* Vol. 38, pp. 1601–1607 (1992).

49. M. Miwa, Y. Ueda and B. Chance, "Development of time resolved spectroscopy system for quantitative non-invasive tissue measurement," *Proc. SPIE* Vol. 2389, pp. 142–149 (1995).

50. V. Quaresima, M. A. Franceschini, S. Fantini, E. Gratton, and M. Ferrari, "Difference in leg muscles oxygenation during treadmill exercise by a new near infrared frequency-domain oximeter," in *Photon Propagation in Tissues III*, D. A. Benaron, B. Chance, and M. Ferrari (eds.), *Proc. SPIE* Vol. 3194, pp. 116–120 (1998).

51. T. R. Cheatle, L. A. Potter, M. Cope, D. T. Delpy, P. D. Coleridge Smith, and J. H. Scurr, "Near-infrared spectroscopy in peripheral vascular disease," *Br. J. Surg.* Vol. 78, pp. 405–408 (1991).

52. R. A. de Blasi, M. Cope, and M. Ferrari, "Oxygen consumption of human skeletal muscle by near-infrared spectroscopy during tourniquet-induced ischemia in maximal voluntary contraction," *Adv. Exp. Med. Biol.* Vol. 317, pp. 771–777 (1992).

53. R. A. de Blasi, M. Ferrari, A. Natali, G. Conti, A. Mega, and A. Gasparetto, "Noninvasive measurement of forearm blood flow and oxygen consumption by near-infrared spectroscopy," *J. Appl. Physiol.* Vol. 76, pp. 1388–1393 (1994).

54. S. Homma, H. Eda, S. Ogasawara, and A. Kagaya, "Near-infrared estimation of O_2 supply and consumption in forearm muscles working at varying intensity," *J. Appl. Physiol.* Vol. 80, pp. 1279–1284 (1996).

55. M. C. P. van Beekvelt, W. N. J. M. Colier, B. G. M. van Engelen, M. T. E. Hopman, R. A. Wevers, and B. Oeseburg, "Validation of measurement protocols to assess oxygen consumption and blood flow in the human forearm by near-infrared spectroscopy," *Proc. SPIE* Vol. 3194, pp. 133–144 (1998).

56. C. Casavola, L. A. Paunescu, S. Fantini, and E. Gratton, "Blood flow and oxygen consumption with near-infrared spectroscopy and venous occlusion: spatial maps and the effect of time and pressure of inflation," *J. Biomed. Opt.* Vol. 5, pp. 269–276 (2000).

57. S. R. Hintz, D. A. Benaron, J. P. van Houten, J. L. Duckworth, F. W. H. Liu, S. D. Spilman, D. K. Stevenson, and W.-F. Cheong, "Stationary headband for clinical time-of-flight optical imaging at the bedside," *Photochem. Photobiol.* Vol. 68, pp. 361–369 (1998).

58. S. R. Hintz, W.-F. Cheong, J. P. van Houten, D. K. Stevenson, and D. A. Benaron, "Bedside imaging of intracranial hemorrhage in the neonate using light: comparison with ultrasound, computed tomography, and magnetic resonance imaging," *Pediatr. Res.* Vol. 45, pp. 54–59 (1999).

59. B. Beauvoit, T. Kitai, and B. Chance, "Contribution of the mitochondrial compartment to the optical properties of the rat liver: a theoretical and practical approach," *Biophys. J.* Vol. 67, pp. 2501–2510 (1994).

60. M. Kohl, M. Cope, M. Essenpreis, and D. Böcker, "Influence of glucose concentration on light scattering in tissue-simulating phantoms," *Opt. Lett.* Vol. 19, pp. 2170–2172 (1994).

61. J. S. Maier, S. A. Walker, S. Fantini, M. A. Franceschini, and E. Gratton, "Possible correlation between blood glucose concentration and the re-

duced scattering coefficient of tissues in the near infrared," *Opt. Lett.* Vol. 19, pp. 2062–2064 (1994).

62. J. T. Bruulsema, J. E. Hayward, T. J. Farrel, M. S. Patterson, L. Heinemann, M. Berger, T. Koschinsky, J. Sandahl-Christiansen, H. Orskov, M. Essenpreis, G. Schmelzeisen-Redeker, and D. Böcker, "Correlation between blood glucose concentration in diabetics and noninvasively measured tissue optical scattering coefficient," *Opt. Lett.* Vol. 22, pp. 190–192 (1997).

63. V. V. Tuchin, I. L. Maksimova, D. A. Zimnyakov, I. L. Kon, A. H. Mavlutov, and A. A. Mishin, "Light propagation in tissues with controlled optical properties," *J. Biomed. Optics* Vol. 2, pp. 304–321 (1997).

64. S. A. Walker, D. A. Boas, and E. Gratton, "Photon density waves scattered from cylindrical inhomogeneities: theory and experiments," *Appl. Opt.* Vol. 37, pp. 1935–1944 (1998).

65. B. W. Pogue, M. S. Patterson, H. Jiang, and K. D. Paulsen, "Initial assessment of a simple system for frequency domain diffuse optical tomography," *Phys. Med. Biol.* Vol. 40, pp. 1709–1729 (1995).

66. S. R. Arridge, M. Schweiger, M. Hiraoka, and D. T. Delpy, "A finite element approach to modelling photon transport in tissue," *Med. Phys.* Vol. 20, pp. 299–309 (1993).

67. S. R. Arridge, P. van der Zee, M. Cope, and D. T. Delpy, "Reconstruction methods for infra-red absorption imaging," *Proc. SPIE* Vol. 1431, pp. 204–215 (1991).

68. M. A. O'Leary, D. A. Boas, B. Chance, and A. G. Yodh, "Experimental images of heterogeneous turbid media by frequency-domain diffusing photon tomography," *Opt. Lett.* Vol. 20, pp. 426–428 (1995).

69. L. H. Wang, S. L. Jacques, "Hybrid model of Monte-Carlo simulation and diffusion theory for light reflectance by turbid media," *J. Opt. Soc. Am. A* Vol. 10, pp. 1746–1752 (1993).

70. I. V. Yaroslavsky, A. N. Yaroslavsky, V. V. Tuchin, and H.-J. Schwarzmaier, "Effect of the scattering delay on time-dependent photon migration in turbid media," *Appl. Opt.* Vol. 36, pp. 6529–6538 (1997).

71. A. H. Gandjbakhche, R. F. Bonner, R. Nossal, and G. H. Weiss, "Absorptivity contrast in transillumination imaging of tissue abnormalities," *Appl. Opt.* Vol. 35, pp. 1767–1774 (1996).

72. H. L. Graber, J. Chang, J. Lubowsky, R. Aronson, and R. L. Barbour, "Near-infrared absorption imaging of dense scattering media by steady-state diffusion tomography," *Proc. SPIE* Vol. 1888, pp. 372–386 (1993).

73. V. Ntziachristos, A. G. Yodh, M. Schnall, and B. Chance, "Concurrent MRI and diffuse optical tomography of breast after indocyanine green enhancement," *Proc. Natl. Acad. Sci. USA* Vol. 97, pp. 2767–2772 (2000).

74. S. R. Arridge, M. Schweiger, M. Hiraoka, and D. T. Delpy, "Performance of an iterative reconstruction algorithm for near-infrared absorption imaging," *Proc. SPIE* Vol. 1888, pp. 360–371 (1993).

75. H. Jiang, K. D. Paulsen, U. L. Osterberg, B. W. Pogue, and M. S. Patterson, "Simultaneous reconstruction of optical absorption and scattering maps in turbid media from near-infrared frequency-domain data," *Opt. Lett.* Vol. 20, pp. 2128–2130 (1995).

76. B. W. Pogue, T. O. McBride, J. Prewitt, U. L. Österberg, and K. D. Paulsen, "Spatially variant regularization improves diffuse optical tomography," *Appl. Opt.* Vol. 38, pp. 2950–2961 (1999).

77. D. A. Benaron. D. C. Ho, S. Spilman, J. P. Van Houten, and K. D. Stevenson, "Non-recursive linear algorithms for optical imaging in diffusive media," *Adv. Exp. Med. Biol.* Vol. 361, pp. 215–222 (1994).

78. S. A. Walker, S. Fantini, and E. Gratton, "Image reconstruction using back-projection from frequency-domain optical measurements in highly scattering media," *Appl. Opt.* Vol. 36, pp. 170–179 (1997).

79. M. A. Franceschini, V. Toronov, M. E. Filiaci, E. Gratton, and S. Fantini, "On-line optical imaging of the human brain with 160-ms temporal resolution," *Opt. Express* Vol. 6, pp. 49–57 (2000).

80. S. Fantini, M. A. Franceschini, and E. Gratton, "Effective source term in the diffusion equation for photon transport in turbid media," *Appl. Opt.* Vol. 36, pp. 156–163 (1997).

81. F. F. Jöbsis "Noninvasive, infrared monitoring of cerebral and myocardial oxygen sufficiency and circulatory parameters," *Science* Vol. 198, pp. 1264–1267 (1977).

82. P. W. McCormick, M. Stewart, G. Lewis, M. Dujovny, and J. I. Ausman, "Intracerebral penetration of infrared light. technical note," *J. Neurosurg.* Vol. 76, pp. 315–318 (1992).

83. G. Gratton, J. S. Maier, M. Fabiani, W. W. Mantulin, and E. Gratton, "Feasibility of intracranial near-infrared optical scanning," *Psychophysiology* Vol. 31, pp. 211–215 (1994).

84. S. P. Gopinath, C. S. Robertson, R. G. Grossman, and B. Chance, "Near-infrared spectroscopic localization of intracranial hematomas," *J. Neurosurg.* Vol. 79, pp. 43–47 (1993).

85. S. Fantini, M. A. Franceschini, E. Gratton, D. Hueber, W. Rosenfeld, D. Maulik, P. G. Stubblefield, and M. R. Stankovic, "Non-invasive optical mapping of the piglet brain in real time," *Opt. Express* Vol. 4, pp. 308–314 (1999).

86. C. S. Roy and C. S. Sherrington, "On the regulation of the blood supply of the brain," *J. Physiol.* Vol. 11, pp. 85–108 (1890).

87. A. Villringer and U. Dirnagl, "Coupling of brain activity and cerebral blood flow: basis of functional neuroimaging," *Cerebrovasc. Brain Metab. Rev.* Vol. 7, pp. 240–276 (1995).

88. B. M. Salzberg and A. L. Obaid, "Optical studies of the secretory event at vertebrate nerve terminals," *Exp. Biol.* Vol. 139, pp. 195–231 (1988).

89. R. A. Stepnoski, A. LaPorta, F. Raccuia-Behling, G. E. Blonder, R. E. Slusher, and D. J. Kleinfeld, "Noninvasive detection of changes in membrane

potential in cultured neurons by light scattering," *Proc. Natl. Acad. Sci. USA* Vol. 88, pp. 9382–9386 (1991).

90. G. Gratton, P. M. Corballis, E. Cho, M. Fabiani, and D. C. Hood, "Shades of gray matter: noninvasive optical images of human brain responses during visual stimulation," *Psychophysiology* Vol. 32, pp. 505–509 (1995).

91. Y. Hoshi, H. Onoe, Y. Watanabe, J. Andersson, M. Bergstrom, A. Lilja, B. Langsrom, and M. Tamura, "Non-synchronous behavior of neuronal activity, oxidative metabolism and blood supply during mental tasks in man," *Neurosci. Lett.* Vol. 172, pp. 129–133 (1994).

92. K. Villringer, A. Villringer,S. Minoshima, S. Ziegler, M. Herz, S. Schuh-Hofer, H. Obrig, C. Hock, U. Dirnagl, and M. Schwaiger, "Frontal brain activation in humans: a combined near infrared spectroscopy and positron emission tomography study," *Soc. Neurosci. Abst.* Vol. 120, p. 1355 (1994).

93. S. Punwani, C. E. Cooper, M. Clemence, J. Pernice, P. Amess, J. Thornton, and R. J. Ordidge, "Correlation between absolute deoxyhaemoglobin [dHb] measured by near infrared spectroscopy (NIRS) and absolute R2' as determined by magnetic resonance imaging (MRI)," *Adv. Exp. Med. Biol.* Vol. 413, pp. 129–137 (1997).

94. C. Hirth, K. Villringer, A. Thiel, J. Bernarding, W. Mühlnickl, H. Obrig, U. Dirnagl, and A. Villringer, "Towards brain mapping combining near-infrared spectroscopy and high resolution 3D MRI," *Adv. Exp. Med. Biol.* Vol. 413, pp. 139–147 (1997).

95. A. Villringer, "Functional neuroimaging optical approaches," *Adv. Exp. Med. Biol.* Vol. 413, pp. 1–18 (1997).

96. A. Maki, Y. Yamashita, Y. Ito, E. Watanabe, Y. Mayanagi, and H. Koizumi, "Spatial and temporal analysis of human motor activity using noninvasive NIR topography," *Med. Phys.* Vol. 22, pp. 1997–2005 (1995).

97. A. M. Siegel, J. J. A. Marota, and D. Boas, "Design and evaluation of a continuous-wave diffuse optical tomography system," *Opt. Express* Vol. 4, pp. 287–298 (1999).

98. B. Chance, E. Anday, S. Nioka, S. Zhou, L. Hong, K. Worden, C. Li, T. Murray, Y. Ovetsky, D. Pidikiti, and R. Thomas, "A novel method for fast imaging of brain function, non-invasively, with light," *Opt. Express* Vol. 2, pp. 411–423 (1998).

99. R. M. Danen, Y. Wang, X. D. Li, W. S. Thayer, and A. G. Yodh, "Regional imager for low-resolution functional imaging of the brain with diffusing near-infrared light," *Photochem. Photobiol.* Vol. 67, pp. 33–40 (1998).

100. Y. Shinohara, M. Haida, N. Shinohara, F. Kawaguchi, Y. Itoh, and H. Koizumi, "Towards near-infrared imaging of the brain," *Adv. Exp. Med. Biol.* Vol. 413, pp. 85–89 (1997).

101. H. Koizumi, Y. Yamashita, A. Maki, T. Yamamoto, Y. Ito, H. Itagaki, and R. Kennan, "Higher-order brain function analysis by trans-cranial dynamic near-infrared spectroscopy imaging," *J. Biomed. Opt.* Vol. 4, pp. 403–413 (1999).

102. A. Villringer and B. Chance, "Non-invasive optical spectroscopy and imaging of human brain function," *Trends Neurosci.* Vol. 20, pp. 435–442 (1997).

103. G. Gratton, M. Fabiani, D. Friedman, M. A. Franceschini, S. Fantini, P. M. Corballis, and E. Gratton, "Rapid changes of optical parameters in the human brain during a tapping task," *J. Cognitive Neuroscience* Vol. 7, pp. 446–456 (1995).

104. K. A. Kang, D. F. Bruley, and B. Chance, "Feasibility study of a single- and multiple-source near-infrared phase-modulation device for characterizing biological systems," *Biomed. Instrum. Technol.* Vol. 31, pp. 373–386 (1997).

105. B. J. Tromberg, O. Coquoz, J. B. Fishkin, T. Pham, E. R. Anderson, J. Butler, M. Cahn, J. D. Gross, V. Venugopalan, and D. Pham, "Non-invasive measurements of breast tissue optical properties using frequency-domain photon migration," *Phil. Trans. R. Soc. Lond. B* Vol. 352, pp. 661–668 (1997).

106. V. Quaresima, S. J. Matcher, and M. Ferrari, "Identification and quantification of intrinsic optical contrast for near-infrared mammography," *Photochem. Photobiol.* Vol. 67, pp. 4–14 (1998).

107. S. Thomsen and D. Tatman, "Physiological and pathological factors of human breast disease that can influence optical diagnosis," *Ann. NY Acad. Sci.* Vol. 838, pp. 171–193 (1998).

108. P. Vaupel, F. Kallinowski, and P. Okunieff, "Blood flow, oxygen and nutrient supply, and metabolic microenvironment of human tumors: a review," *Cancer Res.* Vol. 49, pp. 6449–6465 (1989).

109. V. G. Peters, D. R. Wyman, M. S Patterson, and G. L. Frank, "Optical properties of normal and diseased human breast tissues in the visible and near-infrared," *Phys. Med. Biol.* Vol. 35, pp. 1317–1334 (1990).

110. T. L. Troy, D. L. Page, and E. Sevick-Muraca, "Optical properties of normal and diseased breast tissues: prognosis for optical mammography," *J. Biomed. Opt.* Vol. 1, pp. 342–355 (1996).

111. S. Fantini, S. A. Walker, M. A. Franceschini, M. Kaschke, P. M. Schlag, and K. T. Moesta, "Assessment of the size, position, and optical properties of breast tumors *in vivo* by non-invasive optical methods," *Appl. Opt.* Vol. 37, pp. 1982–1989 (1998).

112. D. Grosenick, H. Wabnitz, H. H. Rinneberg, K. T. Moesta, and P. M. Schlag, "Development of a time-domain optical mammograph and first *in vivo* applications," *Appl. Opt.* Vol. 38, pp. 2927–2943 (1999).

113. B. J. Tromberg, N. Shah, R. Lanning, A. Cerussi, J. Espinoza, T. Pham, L. Svaasand, and J. Butler, "Non-invasive *in vivo* characterization of breast tumors using photon migration spectroscopy," *Neoplasia* Vol. 2, pp. 26–40 (2000).

114. B. Riefke, K. Licha, and W. Semmler, "Contrast media for optical mammography," *Radiologe* Vol. 37, pp. 749–755 (1997).

115. S. Nioka, S. B. Colak, X. Li, Y. Yang, and B. Chance, "Breast tumor images of hemodynamic information using a contrast agent with back projection and FFT enhancement," *OSA Trends in Optics and Photonics Vol. 21, Advances*

in Optical Imaging and Photon Migration, J. G. Fujimoto and M. S. Patterson (eds.), pp. 266–270, Optical Society of America, Washington, DC (1998).

116. M. Cutler, "Transillumination of the breast," *Surg. Gynecol. Obstet.* Vol. 48, pp. 721–727 (1929).

117. C. M. Gros, Y. Quenneville, Y. Hummel, "Diaphanologie mammaire," *J. Radiol. Electrol. Med. Nucl.* Vol. 53, pp. 297–306 (1972).

118. E. Carlsen, "Transillumination light scanning," *Diagn. Imaging* Vol. 4, pp. 28–34 (1982).

119. R. J. Bartrum and H. C. Crow, "Transillumination lightscanning to diagnose breast cancer: a feasibility study," *AJR* Vol. 142, pp. 409–414 (1984).

120. E. A. Sickles, "Breast cancer detection with transillumination and mammography," *AJR* Vol. 142, pp. 841–844 (1984).

121. A. Alveryd et al., "Lightscanning versus mammography for the detection of breast cancer in screening and clinical practice," *Cancer* Vol. 65, pp. 1671–1677 (1990).

122. K. Wells, J. C. Hebden, F. E. W. Schmidt, and D. T. Delpy, "The UCL multi-channel time-resolved system for optical tomography," *Proc. SPIE* Vol. 2979, pp. 599–607 (1997).

123. V. Ntziachristos, X. H. Ma, and B. Chance, "Time-correlated single photon counting imager for simultaneous magnetic resonance and near-infrared mammography," *Rev. Sci. Instrum.* Vol. 69, pp. 4221–4233 (1998).

124. R. Cubeddu, A. Pifferi, P. Taroni, A. Torricelli, and G. Valentini, "Noninvasive absorption and scattering spectroscopy of bulk diffusive media: an application to the optical characterization of human breast," *Appl. Phys. Lett.* Vol. 74, pp. 874–876 (1999).

125. M. A. Franceschini, K. T. Moesta, S. Fantini, G. Gaida, E. Gratton, H. Jess, W. W. Mantulin, M. Seeber, P. M. Schlag, and M. Kaschke, "Frequency-domain techniques enhance optical mammography: initial clinical results," *Proc. Natl. Acad. Sci. USA* Vol. 94, pp. 6468–6473 (1997).

126. S. Zhou, C. Xie, S. Nioka, H. Liu, Y. Zhang, and B. Chance, "Phased array instrumentation appropriate to high precision detection and localization of breast tumor," in *Optical Tomography and Spectroscopy of Tissue: Theory, Instrumentation, Model, and Human Studies II*, B. Chance and R. R. Alfano (eds.), *Proc. SPIE* Vol. 2979, pp. 98–106 (1997).

127. B. W. Pogue, M. Testorf, T. McBride, U. Osterberg, and K. Paulsen, "Instrumentation and design of a frequency-domain diffuse optical tomography imager for breast cancer detection," *Opt. Expr.* Vol. 1, pp. 391–403 (1997).

128. K. T. Moesta, S. Fantini, H. Jess, S. Totkas, M. A. Franceschini, M. Kaschke, and P. M. Schlag, "Contrast features of breast cancer in frequency-domain laser scanning mammography," *J. Biomed. Opt.* Vol. 3, pp. 129–136 (1998).

129. L. Götz, S. H. Heywang-Köbrunner, O. Schütz, and H. Siebold, "Optische Mammographie an präoperativen Patientinnen," *Akt. Radiol.* Vol. 8, pp. 31–33 (1998).

130. S. Fantini, E. L. Heffer, M. A. Franceschini, L. Götz, A. Heinig, S. Heywang-Köbrunner, O. Schütz, and H. Siebold, "Optical mammography with intensity-modulated light," Proceedings Volume from In Vivo Optical Imaging Workshop (September 16-17, 1999, National Institutes of Health, Bethesda, MD), A. Gandjbakhche (ed). (Optical Society of America 2000), *in press*.

131. H. Jess, H. Erdl, K. T. Moesta, S. Fantini, M. A. Franceschini, E. Gratton, and M. Kaschke, "Intensity-modulated breast imaging: technology and clinical pilot study results," *OSA Trends in Optics and Photonics on Advances in Optical Imaging and Photon Migration*, R. R. Alfano and J. G. Fujimoto (eds.), Vol. 2, pp. 126–129, Optical Society of America, Washington, DC (1996).

132. M. Kaschke, H. Jess, G. Gaida, J. M. Kaltenbach, and W. Wrobel, "Transillumination imaging of tissue by phase modulation techniques," in *Advances in Optical Imaging and Photon Migration*, R. R. Alfano (ed.), *Proc. OSA* Vol. 21, pp. 88–92 (1994).

133. S. Fantini, M. A. Franceschini, S. A. Walker, J. S. Maier, and E. Gratton, "Photon path distributions in turbid media: applications for imaging," *Proc. SPIE* Vol. 2389, pp. 340–349 (1995).

REPLY TO
ATTENTION OF

MCMR-RMI-S   (70-1y)   1 July 03

MEMORANDUM FOR Administrator, Defense Technical Information
Center (DTIC-OCA), 8725 John J. Kingman Road, Fort Belvoir,
VA 22060-6218

SUBJECT: Request Change in Distribution Statement

1. The U.S. Army Medical Research and Materiel Command has
reexamined the need for the limitation assigned to technical
reports written for this Command. Request the limited
distribution statement for the enclosed accession numbers be
changed to "Approved for public release; distribution
unlimited." These reports should be released to the National
Technical Information Service.

2. Point of contact for this request is Ms. Kristin Morrow at
DSN 343-7327 or by e-mail at Kristin.Morrow@det.amedd.army.mil.

FOR THE COMMANDER:

Encl   PHYLIS M. RINEHART
                                  Deputy Chief of Staff for
                                  Information Management

ADB274518
ADB287328
ADB277943
ADB288221
ADB248332
ADB265760
ADB287619
ADB281577
ADB287600
ADB288422
ADB288375
ADB268297